

VANDETANIB-ELUTING BEADS FOR THE
TREATMENT OF LIVER TUMOURS

ALICE HAGAN

A thesis submitted in partial fulfilment of the
requirements for the University of Brighton for
the degree of Doctor of Philosophy

June 2018

ABSTRACT

Drug-eluting bead trans-arterial chemo-embolisation (DEB-TACE) is a minimally invasive interventional treatment for intermediate stage hepatocellular carcinoma (HCC). Drug loaded microspheres, such as DC Bead™ (Biocompatibles UK Ltd) are selectively delivered via catheterisation of the hepatic artery into tumour vasculature. The purpose of DEB-TACE is to physically embolise tumour-feeding vessels, starving the tumour of oxygen and nutrients, whilst releasing drug in a controlled manner. Due to the reduced systemic drug exposure, toxicity is greatly reduced. Embolisation-induced ischaemia is intended to cause tumour necrosis, however surviving hypoxic cells are known to activate hypoxia inducible factor (HIF-1) which leads to the upregulation of several pro-survival and pro-angiogenic pathways. This can lead to tumour revascularisation, recurrence and poor treatment outcomes, providing a rationale for combining anti-angiogenic agents with TACE treatment. Local delivery of these agents *via* DEBs could provide sustained targeted therapy in combination with embolisation, reducing systemic exposure and therefore toxicity associated with these drugs.

This thesis describes for the first time the loading of the DEB DC Bead and the radiopaque DC Bead LUMI™ with the tyrosine kinase inhibitor vandetanib. Vandetanib selectively inhibits vascular endothelial growth factor receptor 2 (VEGFR2) and epidermal growth factor receptor (EGFR), two signalling receptors involved in angiogenesis and HCC pathogenesis. Physicochemical properties of vandetanib loaded beads such as maximum loading capacity, effect on size, radiopacity and drug distribution were evaluated using various analytical techniques. Drug release was characterised using multiple *in vitro* models and compared with other traditional TACE drugs and *in vivo* pharmacokinetics. A hypoxic chamber was used to mimic embolisation induced ischaemia in order to assess the effect of hypoxia on the response of both HCC and endothelial cells to vandetanib. Finally, vandetanib loaded beads were evaluated in preclinical models of HCC.

The feasibility and characteristics of loading and release of vandetanib from radiopaque DEBs were demonstrated, and the product was shown to meet specifications in terms of physical properties, handling and performance. Vandetanib suppresses proliferation and induces apoptosis in HCC cells and endothelial cells *in vitro*, without signs of hypoxia-induced drug resistance. Vandetanib-eluting beads have been evaluated in pre-clinical studies and found to be safe with durable drug release from beads. The data produced in this thesis has supported the transition of the product to first-in-human clinical trials.

TABLE OF CONTENTS

Abstract	i
Table of Contents	iii
List of figures	ix
List of abbreviations and definitions.....	xiii
Acknowledgements	xvii
Declaration	xix
1 Chapter One: Introduction	1
1.1 Hepatocellular Carcinoma: epidemiology and risk factors.....	1
1.2 The liver in health and disease	1
1.2.1 Cirrhosis	3
1.2.2 Mechanisms of hepatocarcinogenesis	3
1.2.3 Angiogenesis	3
1.2.4 The EGFR pathway.....	5
1.2.5 Physiology of liver tumours	6
1.3 Treatment for intermediate unresectable HCC: TACE.....	7
1.4 Novel DEB platforms: radio-opaque beads	12
1.5 Towards development of an anti-angiogenic DEB – drug candidate selection 13	
1.5.1 Vandetanib	14
1.6 The challenge of hypoxia.....	19
1.6.1 Hypoxia related drug resistance	19
1.6.2 Modelling hypoxia in vitro.....	23
1.7 Methods of pre-clinical evaluation of drug-eluting beads: <i>in vitro</i> and <i>in vivo</i> models of HCC.....	23
1.7.1 Cell culture	23

1.7.2	Mouse models	24
1.7.3	Woodchuck model	25
1.7.4	Rabbit VX2 model	25
1.8	Summary	25
1.9	Aims of the thesis.....	26
2	Chapter Two: Physicochemical characterisation of vandetanib loaded beads	29
2.1	Introduction.....	29
2.1.1	Drug loading capacity and bead interactions	30
2.1.2	Size/compressibility.....	33
2.1.3	Radiopacity	34
2.1.4	Summary	35
2.1.5	Aims of this chapter	37
2.2	Materials and Methods.....	37
2.2.1	Materials.....	37
2.2.2	Physicochemical analysis methods	37
2.3	Results.....	43
2.3.1	Maximum vandetanib loading capacity in DC Bead and DC Bead LUMI	43
2.3.2	Effect of vandetanib loading on bead size and morphology.....	44
2.3.3	Bead penetration testing.....	46
2.3.4	Vandetanib distribution within beads	47
2.3.5	Evaluation of drug-bead interactions using FTIR spectroscopy.....	50
2.3.6	Radio-opacity of vandetanib loaded beads	50
2.3.7	Suspension, handling and delivery of vandetanib loaded DC Bead LUMI	51
2.4	Discussion	52
2.4.1	Influence of vandetanib charge states on bead properties.....	52
2.4.2	Prototype selection – radiopaque or non-radiopaque?.....	53
2.4.3	Properties of radiopaque vandetanib beads.....	54

2.5	Conclusion	55
2.6	Supplementary figures	56
3	Chapter Three: Evaluation and comparison of <i>in vitro</i> models of drug release from beads.....	59
3.1	Introduction	59
3.1.1	Modelling drug release from DEB <i>in vitro</i>	59
3.1.2	Existing models for measuring <i>in vitro</i> drug release from DEB.....	61
3.1.3	Aims of this chapter	64
3.2	Materials and Methods	64
3.2.1	Materials.....	64
3.2.2	Basic <i>in vitro</i> drug release assay	64
3.2.3	Drug leaching in contrast agent	65
3.2.4	Vascular Flow System elution	66
3.2.5	Extended release flow through model.....	67
3.2.6	Pre-clinical procedure and <i>in vitro in vivo</i> correlation (IVIVC).....	68
3.3	Results	71
3.3.1	Vandetanib release from beads in the basic USP-II type model.....	71
3.3.2	Early phase drug release (contrast suspension and VFS model).....	74
3.3.3	Drug release from beads in the flow through cell.....	77
3.3.4	<i>In vivo</i> pharmacokinetics	78
3.3.5	IVIVC.....	80
3.4	Discussion	85
3.4.1	Effect of DEB properties on vandetanib release	85
3.4.2	Evaluation of early and late phase elution modelling	86
3.5	Conclusions	89
4	Chapter Four: Effect of hypoxia on vandetanib activity <i>in vitro</i>	91
4.1	Introduction	91

4.1.1	Vandetanib as an anti-cancer agent.....	91
4.1.2	Vandetanib and hypoxia.....	92
4.1.3	Aims of this chapter	94
4.2	Materials and Methods.....	94
4.2.1	Cell lines	94
4.2.2	Cell culture protocols	95
4.2.3	Hypoxic incubation	95
4.2.4	Preparation of drug solutions	96
4.2.5	Cell viability assays	97
4.2.6	Detection of apoptosis and cell cycle analysis.....	99
4.2.7	Detection of phospho and total EGFR by western blotting	100
4.2.8	Measurement of VEGF in cell culture supernatants	102
4.2.9	Measurement of HIF-1 α levels	102
4.2.10	MAPK phosphorylation antibody array.....	102
4.2.11	Growth factor antibody array.....	103
4.3	Results.....	103
4.3.1	Effect of vandetanib on HCC cell viability in normoxic and hypoxic conditions.....	103
4.3.2	Effect of vandetanib on HUVEC viability in normoxic and hypoxic conditions.....	106
4.3.3	Effects of vandetanib and hypoxia on HCC and HUVEC cell cycle and apoptosis	107
4.3.4	Effect of hypoxia, vandetanib and doxorubicin on VEGF secretion from HCC cells.....	108
4.3.5	Effect of hypoxia, vandetanib and doxorubicin on HIF-1 α levels in HCC cells	109
4.3.6	Phosphorylation of EGFR.....	110
4.3.7	MAPK pathway activation.....	112

4.3.8	Growth factor secretion.....	114
4.4	Discussion	115
4.4.1	Vandetanib induces cell cycle arrest and apoptosis in HCC cells and HUVECs with equipotency in normoxia and hypoxia	115
4.4.2	Vandetanib reduces hypoxia induced VEGF secretion from HCC cells independently of HIF-1 α	117
4.4.3	Insights into potential mechanisms of resistance to vandetanib in the setting of TACE.....	118
4.5	Conclusion	120
5	Chapter Five: <i>In vivo</i> evaluation of vandetanib loaded beads	123
5.1	Introduction.....	123
5.1.1	Potential pre-clinical models.....	124
5.1.2	Aims of this chapter	126
5.2	Materials and methods	126
5.2.1	Preparation of vandetanib loaded beads.....	126
5.2.2	Evaluation of bead formulations for subcutaneous injection.....	126
5.2.3	Animal study	127
5.3	Results and Discussion.....	132
5.3.1	Xenograft study 1 – 15 mg/mL dose.....	132
5.3.2	Toxicity/Mouse body weight	133
5.3.3	Evaluation of bead formulations and alternative vehicles	134
5.3.4	Xenograft study 2 – 100 mg/mL dose.....	135
5.3.5	Toxicity/ Mouse Body weight.....	137
5.3.6	Limitations of the model – Potential reasons for lack of anti-tumoural activity	138
5.3.7	Cutaneous toxicity.....	140
5.3.8	Alternative models for assessing treatment efficacy.....	142
5.4	Conclusion	142

6	General discussion	145
	References	150
	Appendices	171
	Micro-CT protocol (RSSL)	171
	Publications & presentations.....	173

LIST OF FIGURES

Figure 1.1 Anatomy of the liver.....	2
Figure 1.2 The VEGF pathway.	4
Figure 1.3 The Barcelona Clinic for Liver Cancer Staging System / treatment algorithm.	7
Figure 1.4 Schematic of TACE using Drug-eluting Beads.....	8
Figure 1.5 The chemical structure of vandetanib.....	15
Figure 1.6 Mechanism of action of vandetanib.....	16
Figure 1.7 Results of a feasibility study of vandetanib-loaded DC Bead in rabbits bearing VX2 liver tumours.....	18
Figure 1.8 Summary of HIF-1 mediated mechanisms of drug resistance and implicated proteins.....	20
Figure 2.1 Ionic interaction between DC Bead (L groups are present in DC Bead LUMI) and vandetanib	30
Figure 2.2 300-500 μm DC Bead loaded with A) 25 mg/mL doxorubicin, B) 20 mg/mL mitoxantrone.	32
Figure 2.3 Comparison of DC Bead (marketed as LC Bead in USA) and radiopaque Beads (DC/LC Bead LUMI) preparation and appearance.	35
Figure 2.4 The embolisation model.	40
Figure 2.5 Maximum vandetanib loading capacity of DC Bead and DC Bead LUMI...43	
Figure 2.6 DC Bead (70-150 μm) before (A) and after (B) loading with 30 mg/mL vandetanib; DC Bead LUMI (70-150 μm) before (C) and after (D) loading with 100 mg/mL vandetanib..	45
Figure 2.7 Frequency histograms of A) DC Bead and B) DC Bead LUMI size range after maximum vandetanib loading at various pH.	46
Figure 2.8 DC Bead LUMI penetration distance in the embolisation model.	47
Figure 2.9 Optical micrographs of sectioned DC Bead LUMI in OCT compound.	48
Figure 2.10 SEM-EDX analysis of vandetanib loaded beads.....	49
Figure 2.11 Effect of vandetanib loading dose on the S=O stretching frequency from bead sulfonate groups as determined by FTIR spectroscopy.....	50

Figure 2.12 Effect of vandetanib loading into DC Bead LUMI on radiopacity of the beads.....	51
Figure 3.1 Optical micrographs of DC Bead LUMI loaded with A) doxorubicin, B) vandetanib and C) irinotecan, and their respective chemical structures.	60
Figure 3.2 Phases of the embolization process	61
Figure 3.3 <i>In vitro</i> set-ups for modelling drug release from DEB.....	62
Figure 3.4 Vascular flow model set up for evaluating drug release from DEB.....	66
Figure 3.5 Schematic of the slow flow through cell elution model.	68
Figure 3.6 Vandetanib release from DC Bead and DC Bead LUMI	71
Figure 3.7 Effect of the vandetanib loading solution pH on drug release.	72
Figure 3.8 Effect of bead size range on drug release..	72
Figure 3.9 Effect of vandetanib loading dose on drug release.....	73
Figure 3.10 The effect of the pH of the elution medium on the released fraction of vandetanib from DC Bead LUMI.	74
Figure 3.11 Drug release in the VFS model.....	75
Figure 3.12 Effect of elution medium pH on vandetanib elution in the VFS model.....	76
Figure 3.13 Drug dose release profile with time during the later phase using the open loop flow through model.....	77
Figure 3.14 Plasma pharmacokinetic data from pre-clinical studies in swine using LUMIDOX, LUMIRI and LUMIVAN.	79
Figure 3.15 Log plasma concentration of irinotecan, vandetanib and doxorubicin in swine plasma over time.....	80
Figure 3.16 IVIVC of plasma AUC for LUMIDOX AND LUMIRI in healthy swine against <i>in vitro</i> cumulative % drug release obtained in the VFS model.....	81
Figure 3.17 Assessment of IVIVC between <i>in vitro</i> and <i>in vivo</i> AUC from raw LUMIVAN flow through elution data.	83
Figure 3.18 IVIVC using flow through elution model data.....	84
Figure 4.1 Simplified representation of the molecular pathways likely to be implicated in vandetanib-TACE	92
Figure 4.2 The InvivO ₂ Hypoxia chamber.....	96
Figure 4.3 WST-1 Assay plate layout.....	98
Figure 4.4 HepG2 viability in response to increasing doses of vandetanib as determined by the WST-1 assay..	104

Figure 4.5 Hep3B cell viability in response to increasing doses of vandetanib as determined by the WST-1 assay.	105
Figure 4.6 JHH6 cell viability in response to increasing doses of vandetanib as determined by the WST-1 assay.	105
Figure 4.7 HUVEC viability in response to increasing doses of vandetanib as determined by the WST-1 assay.	106
Figure 4.8 Cell cycle analysis of cells treated with vandetanib in normoxic or hypoxic conditions.	107
Figure 4.9 Normalised VEGF levels in cell culture supernatant.(Vandetanib)	108
Figure 4.10 Normalised VEGF levels in cell culture supernatant.(Doxorubicin).....	109
Figure 4.11 Normalised HIF-1 α levels in cell lysates after treatment with vandetanib or doxorubicin.	109
Figure 4.12 Western blots using antibodies against phospho-EGFR, total EGFR and beta-actin in HCC cell lysates.	111
Figure 4.13 Relative spot signal intensities in JHH6 cell lysates analysed with a membrane antibody array for MAPK signalling.....	113
Figure 4.14 Relative spot signal intensities of selected growth factors analysed in the supernatant of HepG2 cells using a membrane antibody array.....	114
Figure 5.1 Small scale diffusion model of vandetanib release from trial bead formulations..	127
Figure 5.2 Planned study schedule and location of weekly injection of beads around HepG2 tumour xenografts.....	129
Figure 5.3 Study 1: HepG2 tumour volume over time during treatment with vandetanib loaded beads.....	133
Figure 5.4 Study 1: Mouse body weight over time.....	134
Figure 5.5 The effect of delivery vehicles on vandetanib release in a diffusion model.	135
Figure 5.6 Study 2: HepG2 tumour volume over time during treatment with vandetanib loaded beads.....	136
Figure 5.7 Study 2: Mouse body weight over time.....	137
Figure 6.1 Interventional Radiologists and BTG team in theatre following the first clinical vandetanib bead procedure.....	149

LIST OF ABBREVIATIONS AND DEFINITIONS

Akt	protein kinase B
ATP	adenosine tri-phosphate
AUC	area under curve
BSA	bovine serum albumin
C _{max}	maximum drug concentration in plasma/elution profile
CMC	carboxymethyl cellulose
CREB	camp response element binding protein
μ-CT	micro computed-tomography
DAPI	4',6-diamidino-2-phenylindole
DEB	drug-eluting bead
DNA	deoxyribonucleic acid
DOX	doxorubicin
EBM/EGM	endothelial basal/growth medium
EDTA	ethylenediaminetetraacetic acid
EDX	energy-dispersive x-ray spectroscopy
EGF(R)	epidermal growth factor (receptor)
ELISA	enzyme-linked immunosorbent assay
ERK	extracellular signal-regulated kinase
FBS	fetal bovine serum
FDA	US Food and Drug Administration
FEG SEM	field emission gun scanning electron microscope
FGF(R)	fibroblast growth factor (receptor)
FTIR	Fourier-transform infrared spectroscopy
GLUT-1	glucose transporter 1
GSK3α	glycogen synthase kinase-3 alpha
HCC	hepatocellular carcinoma
HCl	hydrochloric acid

HEPA	high efficiency particulate air
HER2	human epidermal growth factor receptor 2
HIF	hypoxia-inducible factor
HPLC/UPLC	high/ultra-performance liquid chromatography
HRE	hypoxia response element
HRP	horseradish peroxidase
HUVEC	human umbilical vein endothelial cell
IC ₅₀	concentration inhibiting response by half
IGF(R)	insulin-like growth factor (receptor)
IRI	irinotecan
IVIVC	<i>in vitro in vivo</i> correlation
k _e	elimination constant
LC-MS	liquid chromatography-mass spectrometry
MAPK	mitogen-activated protein kinase
MEK/MKK	mitogen-activated protein kinase kinase
MET	tyrosine-protein kinase Met
MSK2	mitogen and stress activated kinase 2
mTKI	multiple tyrosine kinase inhibitor
Mtor	mechanistic target of rapamycin
MTT	(3-(4,5-dimethylthiazol-2-yl)-2,5-diphenyltetrazolium bromide)
NAD(P)H	nicotinamide adenine dinucleotide (phosphate)
NaOH	sodium hydroxide
NSCLC	non-small cell lung cancer
OCT	optimum cutting temperature
PBS	phosphate buffered saline
PDGF(R)	platelet derived growth factor (receptor)
P-GP	p-glycoprotein transporter
PI3K	phosphoinositide 3-kinase

PK	pharmacokinetics
PTEN	phosphatase and tensin homolog
PVA	poly-vinyl alcohol
QT interval	measure of the time between the start of the Q wave and the end of the T wave in the heart's electrical cycle
RAF	rapidly accelerated fibrosarcoma kinase
REDD	regulated in development and DNA damage responses
RIPA	radioimmunoprecipitation assay buffer
RTK	receptor tyrosine kinase
SDS-PAGE	sodium dodecyl sulfate polyacrylamide gel electrophoresis
$T_{1/2}$	half life
TACE	transarterial chemoembolisation
TBST	tris-buffered saline with tween
TFA	trifluoroacetic acid
TGF	transforming growth factor
T_{last}	time of final quantifiable sample (PK)
T_{max}	time of maximum observed drug concentration (plasma/elution profile)
USP	United States Pharmacopeia
UV	ultraviolet
VAN	vandetanib
V_d	volume of distribution (PK)
VEGF(R)	vascular endothelial growth factor (receptor)
VFS	vascular flow system
WST-1	water soluble tetrazolium salt 1

ACKNOWLEDGEMENTS

I want to start by thanking Professor Andy Lewis – your belief in me, constant encouragement and guidance have got me to this point and pushed me to achieve things I didn't think I was capable of. My supervisory team may have changed a lot, but I value everyone who has been a part of it, especially Dr Gary Phillips, Professor Andrew Lloyd and Dr Wendy Macfarlane, who were always there for support during my time at the University of Brighton. Thanks also to the staff and fellow students in Brighton who helped me settle in to a new environment, and especially Dr Sandeep Kumar who patiently taught me many new techniques and often helped me out of a tight spot.

A huge thank you to numerous colleagues and friends at BTG/Biocompatibles, who have not only listened to my concerns, complaints and chemistry questions over the years but have also made my time inside and outside work so enjoyable. Special thanks to Damien, Jade, Jon and Alex – wherever we end up, you'll always be my 'BTG crew'.

Thank you to the Royal Commission for the Exhibition of 1851 for awarding me an Industrial Fellowship, it has made a huge difference to my experience and given me so many unique opportunities – I never dreamed I would be visiting Buckingham palace, hearing lectures from Nobel Prize winners and even presenting my research to a member of the royal family! I am proud to be an 1851 alumnus for life.

Finally, thank you to my parents Russ and Terry and the rest of my family for the range of physical, emotional and even scientific support throughout the last four years, I couldn't have done this without you.

DECLARATION

I declare that the research contained in this thesis, unless otherwise indicated within the text, is the original work of the author. The thesis has not been previously submitted to this or any other university for a degree, and does not incorporate any material already submitted for a degree.

Signed

Dated

1 CHAPTER ONE: INTRODUCTION

1.1 Hepatocellular Carcinoma: epidemiology and risk factors

Primary liver cancer, or hepatocellular carcinoma (HCC), is the 6th most common human tumour type worldwide, causing an estimated 746,000 deaths in 2012 [1]. Whilst the incidence of many cancer types has been either stable or declining in recent years, liver cancer incidence and mortality rose between 2003 and 2012 among American men and women [2]. The greatest risk factor for developing HCC is chronic infection with hepatitis B and C viruses. The disease is prevalent in eastern Asia and sub-Saharan Africa due to high incidence of hepatitis B virus (HBV) infection, alongside exposure to aflatoxin, a carcinogenic contaminant found on staple foods of these regions. Incidence of HCC in the USA and UK is increasing in parallel with the spread of hepatitis C (HCV) infection. Other risk factors include heavy consumption of alcohol leading to alcoholic liver disease, smoking tobacco, diabetes, and more rarely, metabolic disorders such as Wilson's disease [3]. The sustained liver damage caused by these factors can lead to cirrhosis over time. The exact molecular mechanism by which these risk factors lead to HCC remains only partly understood, however the presence of cirrhosis in the liver is strongly linked to the development of cancer; an established background of liver disease is present within 70-90% of HCC patients [4]. Prevention of cirrhosis caused by hepatitis viruses using antiviral therapy can in turn prevent the onset of HCC, however once cirrhosis is established, the use of antivirals has no effect on HCC development [5].

1.2 The liver in health and disease

The liver is a large, heterogeneous organ that provides a multitude of essential functions to the human body, including the uptake and metabolism or storage of proteins, amino acids, carbohydrates, lipids, vitamins, cholesterol, and bile acids [6]. It receives a dual blood supply from the hepatic artery and portal vein, whose arterioles and venules along with bile ducts feed into hexagonal lobules (Figure 1.1) [7]. Liver tissue is comprised of many cell types, of which the majority are hepatocytes, providing most of the liver's functionality. Hepatocytes are separated from the various ducts and blood vessels by specialised sinusoidal endothelial cells (SEC) that filter incoming blood with the help of small pores named fenestrae. Other biologically important cell types include phagocytic

Kupffer cells, biliary epithelial cells, and hepatic stellate cells (HSC). Both SEC and HSC are known to play major roles in liver pathology, including cirrhosis [8].

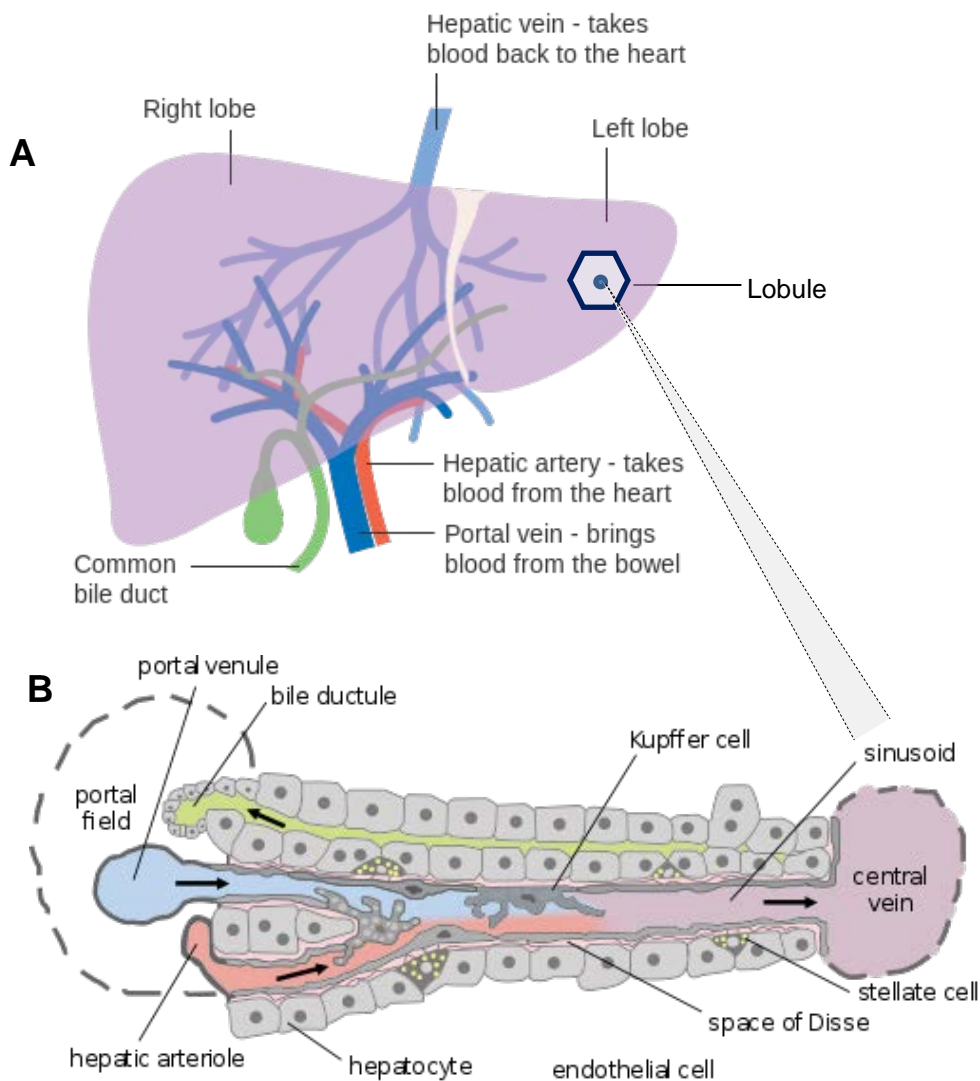


Figure 1.1 Anatomy of the liver. A) Gross anatomy showing dual blood supply. B) Histological view of a sinusoid. Multiple sinusoids form a hexagonal lobule that drains into the central vein. Adapted from Cancer Research UK/Wikimedia commons; Frevert *et al.* (2005) [9] under creative commons license.

<https://creativecommons.org/licenses/by/2.5/legalcode> Original in colour.

1.2.1 Cirrhosis

Cirrhosis is an often irreversible scarring of the liver tissue as a result of sustained liver damage, due to excessive alcohol intake, viral hepatitis infection, non-alcoholic steatohepatitis (NASH), aflatoxin exposure or certain genetic disorders. Activation of HSC induces fibrosis, which in turn leads to reduced liver function as a consequence of architectural distortion and decreased hepatocellular mass [10]. The continued cycles of liver damage and repair increases the likelihood that a cancer causing mutation will arise. Cirrhosis is present in 80-90% of HCC cases, although the relative risk of developing HCC depends on the underlying cause of the cirrhosis [11]. Screening of cirrhotic patients is therefore critical in the early detection of HCC and the best chance of administering curative therapy.

1.2.2 Mechanisms of hepatocarcinogenesis

Several signalling pathways have been implicated in the pathogenesis of HCC. In a summary by Whittaker and colleagues, growth factor mediated angiogenic signalling, the mitogen-activated protein kinase (MAPK) pathway, the mechanistic target of rapamycin (mTOR) pathway and the Wnt/ β -catenin pathway are among the major players identified [12]. Of these, there has been a great deal of interest in angiogenic factors such as vascular endothelial growth factor (VEGF) and epidermal growth factor (EGF) and the pathways they stimulate as potential therapeutic targets for many tumour types [13, 14].

1.2.3 Angiogenesis

Angiogenesis is the process of formation of new blood vessels from cellular elements of pre-existing vessels. All mammalian cells require access to the vascular network for delivery of oxygen, nutrients and the removal of metabolic wastes. As such, the maximum distance between a healthy cell and a blood vessel is 200 μm – limited by the diffusion distance of oxygen [15]. Tumours too require a supply of oxygen to sustain neoplastic growth, however the speed of this growth is often greater than the rate at which cells can effectively respond to the need for oxygen and induce angiogenesis. Heterogeneous regions of hypoxia are common within solid tumours, which poses a challenge in terms of treatment as hypoxia confers a resistance to radiotherapy and chemotherapy and can promote the survival of aggressive phenotypes [16].

Tumour cells respond to hypoxia by activating a family of transcription factors known as hypoxia inducible factors (HIF). HIF is a highly conserved, heterodimeric DNA

binding protein, consisting of two subunits, α and β [17]. The activity of HIF is regulated by levels of the HIF- α subunit. Three isoforms of HIF- α have been identified in mammals, of which HIF-1 α is the best characterised. HIF-1 α is constitutively expressed, but is subject to oxygen-dependent hydroxylation and ubiquitination that leads to its degradation in the proteasome. In the absence of sufficient oxygen, HIF-1 α is stabilised, and translocates to the nucleus where it becomes transcriptionally active. Along with other members of the HIF family, HIF1- α is responsible for the regulation of over half of the hundreds of genes that respond to hypoxia [18].

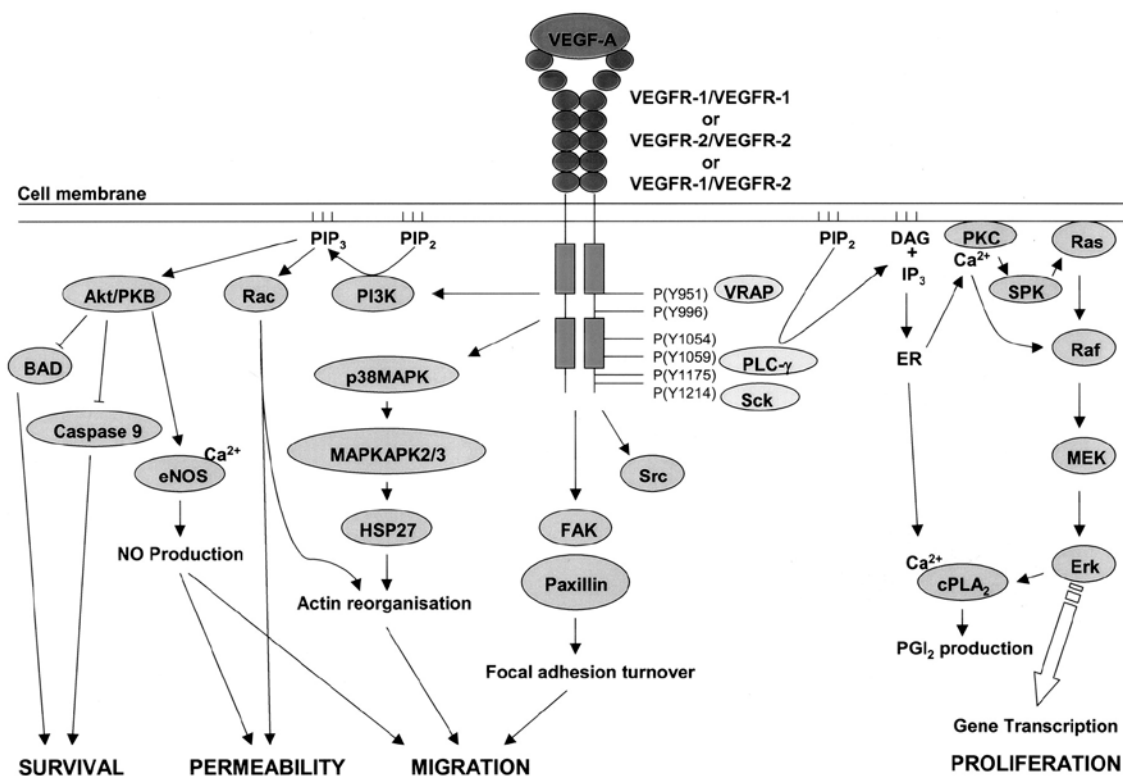


Figure 1.2 The VEGF pathway. Reproduced with permission from Hoeben *et al.* (2004).

VEGF is one of the genes influenced by HIF-1 α . It encodes a family of pro-angiogenic factors, of which VEGF-A is the most important. VEGF-A is a heparin-binding homodimeric glycoprotein, which binds to specific tyrosine kinase receptors, VEGFR-1, VEGFR-2 and VEGFR-3 (Figure 1.2). Binding of VEGF to VEGFR-2 results in the autophosphorylation of tyrosine residues, creating binding sites for additional proteins, including phospholipase C (PLC γ 1). This leads to the activation of protein kinase C, which in turn activates Ras. The Ras/Raf/MEK/Erk pathway leads to activation of transcription factors involved in increasing cell proliferation. VEGFR-2 phosphorylation also leads to the activation of the Akt/PKB pathway, promoting cell

survival and permeability, and the MAPK pathway, leading to increased cell migration [15].

With pathological angiogenesis playing an important role in cancer, a concentrated research effort into anti-angiogenic therapy has yielded the discovery of several agents which have proven efficacious in clinical trials (Table 1.1). The rationale for this type of approach in the context of HCC has been justified with several studies looking into the expression of VEGF, EGF and their receptors in liver tumours. VEGF has been shown to be expressed in human HCC cell lines, and the expression is significantly increased in hypoxic conditions [19]. Furthermore, liver expression of VEGF mRNA was found to be increased in HCC compared to other liver diseases, and in cancerous tissue compared to extra-tumoural tissue [20].

Table 1.1 Examples of currently approved cancer therapies targeting the VEGFR pathway

Drug name	Approved indications	Mechanism of action
Bevacizumab (Avastin®)	Metastatic colorectal cancer, non-small cell lung cancer	Monoclonal antibody: Binding to VEGF
Sorafenib (Nexavar®)	Unresectable HCC, advanced renal cell carcinoma	Inhibition of VEGFR, Platelet derived growth factor (PDGFR), Raf kinases
Sunitinib (Sutent®)	Advanced renal cell carcinoma, gastrointestinal stromal tumour	Inhibition of VEGFR, PDGFR, c-KIT
Vandetanib (Caprelsa®)	Medullary thyroid cancer	Inhibition of VEGFR-2, EGFR, RET proto-oncogene

1.2.4 The EGFR pathway

EGF and its receptor EGFR are overexpressed in several cancer types, including HCC [21], which is associated with a poor prognosis [22]. Binding of ligands to EGFR causes homo-dimerisation or hetero-dimerisation of the receptor followed by tyrosine trans-phosphorylation of the receptor subunits. This allows binding of proteins *via* their Src homology 2 (SH2) domains, which in turn induces downstream signalling pathways involved in the stimulation of cell growth, proliferation, survival and differentiation. Increases in cell proliferation and survival are mediated by the RAS/ERK pathway and the PI3 kinase/AKT pathway, which lead to the activation of proteins that facilitate mitosis and protein synthesis, as well as increased expression of inhibitor of apoptosis proteins (IAPs) [23]. Stimulation of HCC cell lines with EGF has been shown to increase their proliferative ability and invasive properties [22].

Whilst EGFR mutations are common in non-small cell lung cancer (NSCLC) and may confer susceptibility to EGFR inhibitors [24], such mutations are rare in HCC [25, 26]. The EGFR inhibitors erlotinib and gefitinib have been evaluated in human HCC cell lines, inducing growth inhibition, cell cycle arrest and apoptosis, possibly as a consequence of ERK1/2 and AKT inhibition and suppression of anti-apoptotic proteins Bcl-2 and Bcl-X(L) [27-29].

1.2.5 Physiology of liver tumours

Primary HCCs are heterogeneous, and often poorly differentiated. They may be massive, multinodular, diffuse, or pedunculated in macroscopic appearance. Whilst variations in tumour histology do not usually offer a prognostic indication, microvascular infiltration is highly predictive of a poor outcome [16]. HCCs are usually asymptomatic until the tumour has grown to a significant size in terms of available treatment options. There are several staging systems available for assessing the stage of HCC progression and guiding potential therapeutic approaches, usually named after their place of origin, for example Cancer of the Liver Italian Program (CLIP), Hong Kong Liver Cancer (HKLC) or The Barcelona Clinic for Liver Cancer (BCLC). Whilst there is ongoing debate as to which of these provides the most accurate staging in terms of prognosis and suitability of the indicated treatment, the BCLC system (Figure 1.3) is the most widely used [30]. It integrates elements of the Child-Turcotte-Pugh (CTP) score, a measure of the degree of liver dysfunction based on biochemical and clinical markers, and the Okuda system, which takes into account tumour size.

Whilst early-stage HCCs may respond well to surgical resection, orthotopic liver transplantation (OLT) or percutaneous ablation, intermediate to advanced stage HCC is much more difficult to treat. The BCLC system here recommends a shift towards more palliative treatments, aimed at decreasing tumour burden and prolonging survival of the patient (Figure 1.3).

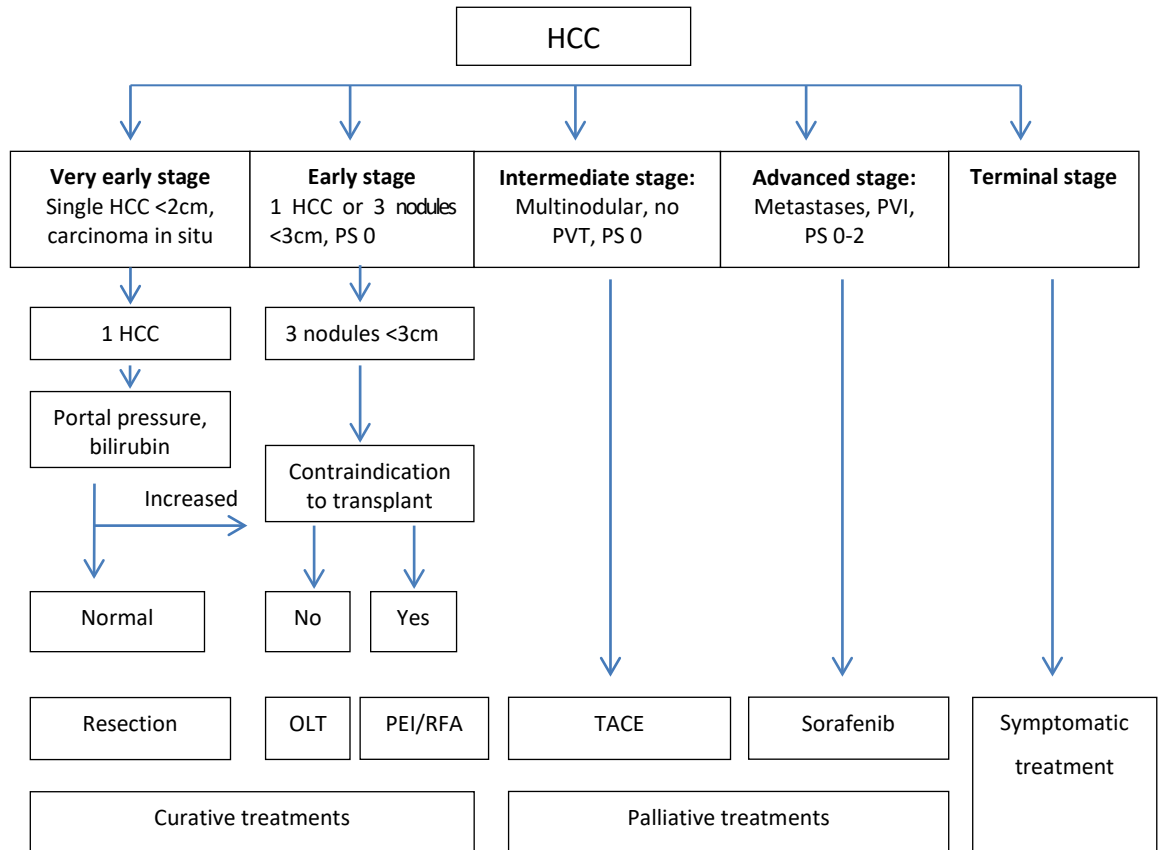


Figure 1.3 The Barcelona Clinic for Liver Cancer Staging System / treatment algorithm. PS = performance status; PVT = portal vein thrombosis; PVI = portal vein invasion; OLT = orthotopic liver transplant; PEI = percutaneous ethanol infusion; RFA = radiofrequency ablation; TACE = Transarterial chemoembolization.

1.3 Treatment for intermediate unresectable HCC: TACE

Trans-arterial (chemo)-embolisation (TA(C)E) is a technique commonly used to treat unresectable HCC. It is an image-guided procedure in which an interventional radiologist injects a chemotherapeutic agent along with an embolic material *via* the hepatic artery to the blood vessels feeding the liver tumour, blocking off its blood supply and delivering a targeted dose of drug to the tumour site (Figure 1.4). The benefits to this treatment are many-fold, exploiting the fact that many liver tumours are hypervascular [31], yet embolization of the blood vessels supplying them does not damage the healthy tissue thanks to the liver's dual blood supply. Up to 90% of HCC tumours are supplied by the hepatic artery [32, 33]. TACE can be performed by infusing a mixture of ethiodised oil (Lipiodol®) and chemotherapeutic drug followed by embolic particles such as poly(vinyl alcohol) (PVA) fragments or gelfoam, however more recently TACE using specifically designed Drug-eluting Beads (DEB) has become a popular treatment choice. DEB are size calibrated particles, usually spherical, capable of

incorporating chemotherapeutic drugs either mechanically or by ionic interaction, and of releasing the drug in a sustained, local manner once delivered to the tumour. This allows embolisation and drug delivery in a single step, with reduced systemic toxicity [34].

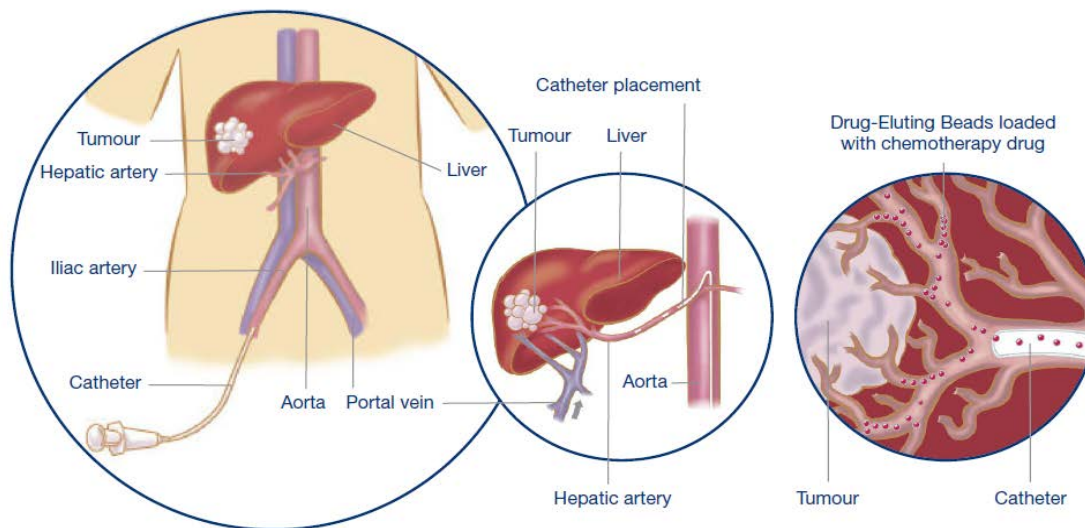


Figure 1.4 Schematic of TACE using Drug-eluting Beads. Reproduced with permission from Biocompatibles UK Ltd. Original in colour.

Table 1.2 lists a selection of drug-loadable microsphere products currently available in Europe for the treatment of hypervascular tumours (HCC or liver metastases). These microspheres are non-absorbable, permanent medical devices, therefore they must be composed of biocompatible materials, which should be somewhat compressible (low elastic modulus) in order to facilitate delivery of the product through microcatheters. The size range of the microsphere can be selected based on the diameter of the vessel to be embolised. Microspheres are supplied unloaded or “bland”, allowing the physician the choice of performing embolisation without drugs or loading their choice of drug into the beads (most commonly doxorubicin for HCC or irinotecan for colorectal carcinoma liver metastases) [35].

Table 1.2 Composition and properties of drug-eluting embolic microspheres on the market in Europe.

Product Name (Manufacturer)	Composition	Sizes (μm)	Specific properties
Embozene Tandem (Boston Scientific Corporation)	Drug-loadable microspheres, HydroGel core with Polyzene-F coating	40, 75, 100 Tightly size calibrated. 9% size decrease after dox loading [36]	50mg/ml dox/iri loading capacity
HepaSphere Microspheres (Merit Medical Systems, Inc.)	Sodium acrylate alcohol copolymer, drug-eluting microspheres	30–60 (120–240 reconstituted*), 50–100 (200–400), 100–150 (400–600), 150–200 (600–800)	*Dry microspheres swell 4x after reconstitution (drug solution or saline) Loads 75mg dox per vial (25mg microspheres). Irregular appearance after loading [36]. Elastic modulus 9.64 ± 2.46 kPa [37]
LifePearl (Terumo Europe)	Polyethylene glycol drug-eluting microspheres	100, 200, 400 24% size decrease after dox loading [36]	37.5mg/mL dox, 50mg/mL iri loading capacity
DC Bead (Biocompatibles UK Ltd.)	PVA hydrogel microspheres	70-150, 100–300, 300–500, 500–700 20% size decrease after dox loading [36]	37.5mg/mL dox, 50mg/mL iri loading capacity Elastic modulus 0.58 ± 0.21 MPa [38]
DC Bead LUMI (Biocompatibles UK Ltd.)	Iodinated PVA hydrogel microspheres	70-150, 100-300 No significant size change after drug loading [38]	X-ray visible 37.5mg/mL dox, 50mg/mL iri loading (recommended doses) Elastic modulus 28.8 ± 2.8 MPa [38]

DC Bead®, a DEB manufactured by Biocompatibles UK Ltd, are microspheres composed of a PVA hydrogel, with size ranges available from 70 – 700 μm . The hydrogel is modified to contain negatively charged sulfonate groups, which allow the beads to be ‘loaded’ by forming interactions with oppositely-charged drugs, for example the hydrochloride salts of doxorubicin or irinotecan [39]. These interactions are strong enough so that the drug will not be released from the bead in de-ionised water,

however in the presence of ions (for example blood and tissue) an ion exchange mechanism allows the drug to exit the bead slowly. This allows for a targeted combination of ischaemia caused by the occlusion of the blood vessels and a controlled and sustained dose of cytotoxic drug as it elutes from the bead, helping to control tumour growth.

In the PRECISION V trial, DEB-TACE has shown a benefit over conventional TACE in terms of improved objective response in patients with Child-Pugh class B bilobar disease and recurrent disease [40]. Additionally, due to the beads' efficiency in sequestering doxorubicin from solution and the subsequent slow release, the amount of drug reaching circulation is reduced. This leads to significant reductions in serious liver toxicity compared to conventional TACE, with significantly increased local drug concentrations at the tumour site [41]. However, tumour regrowth after treatment remains an issue. The hypoxia caused by embolisation induces an angiogenic response, encouraging the revascularisation of tumours and a possible gain in metastatic potential [42].

In studies conducted in both animal models and human HCC patients, increased HIF-1 α levels in plasma and in liver tumour tissue samples have been reported following TACE treatment. This is thought to be a consequence of embolisation-induced hypoxia [43, 44]. A study on HCC treated by TACE [45] identified an increased proliferation of endothelial and tumour cells correlated with ischaemic necrosis. Increased levels of VEGF in both liver tumours and plasma samples after TACE treatment has been widely documented [43, 46, 47]. Elevated levels of VEGF in plasma post-TACE are associated with the development of metastases [48], as well as other adverse prognostic outcomes such as poor treatment response and shorter survival times [49-51].

In terms of systemic treatment, conventional cytotoxic drugs such as doxorubicin have shown little effectiveness in the treatment of HCC [52]. Attention has been focussed therefore on the development of targeted drug therapies that specifically interfere with molecular processes implicated in the disease [53]. At present, the only targeted drug therapy approved for HCC is sorafenib, a multi-targeted tyrosine kinase inhibitor. Its primary mechanism of action is *via* the inhibition of VEGFR, and consequent disruption of angiogenic processes in the tumour. Sorafenib has shown significant benefits to progression free survival (PFS) and overall survival (OS) compared to placebo in

clinical trials [54]. Several other small molecule tyrosine kinase inhibitors are currently under investigation as systemic treatments for HCC. Similarly, monoclonal antibodies targeted against VEGF are being evaluated as treatment candidates [55]. However, the use of these agents is associated with some significant toxicity, including an increased risk of haemorrhage [56].

It is perhaps unsurprising that the combination of TACE with targeted therapies, specifically anti-angiogenic drugs, is being evaluated by several groups [57-60]. Its prospective benefits come from the evidence that TACE induces a strong hypoxic response, including an upregulation of angiogenic factors such as VEGF. Research indicates that this effect can take place within a few hours after a procedure [61]. Concurrent or post-treatment administration of anti-angiogenic drugs could counteract this surge of VEGF, in theory slowing down the re-vascularisation process and improving treatment outcomes.

At present, the angiogenesis inhibitors are administered orally to give a systemic therapy. There has been some discussion as to the optimal timing of systemic therapy in relation to the TACE procedure. In a study where sorafenib was given 1-3 months after TACE, there was no significant improvement to survival, whereas the results of a phase 2 trial where sorafenib treatment was delivered sooner after TACE (1 week) response rates were improved [62]. Recently, results of an exploratory phase 2 trial again examining the combination of sorafenib with TACE have been published (the SPACE trial). Oral sorafenib treatment or placebo started on day 1, and DEB-TACE with doxorubicin loaded beads (DEBDOX) was performed 3–7 days later. There was no difference in the primary endpoint of median time to progression (TTP), however the authors noted that duration of sorafenib treatment in this setting may be critical to improving treatment outcomes, as subgroup analysis saw a link between longer sorafenib treatment and improved TTP [63, 64]. Observations from the GIDEON registry (Global Investigation of Therapeutic Decisions in Hepatocellular Carcinoma and of Treatment with Sorafenib), a prospective, observational study, have shown a link between improved response and having TACE and sorafenib concurrently, compared with separately [65]. A future randomised trial of TACE plus sorafenib administered continuously *versus* sequentially will help to validate these findings, but evidence suggests that anti-angiogenic therapy delivered *via* DEBs could provide the benefits of

the combination therapy in the optimal timeframe whilst reducing toxicity that can cause some clinical trial patients to discontinue treatment.

1.4 Novel DEB platforms: radio-opaque beads

Radiopacity (or radiodensity) refers to the absorption of x-rays by elements, and is related to the density and atomic number of the element – heavier atoms absorb more x-rays. Contrast agents incorporating the radiodense atoms iodine or barium are commonly used in medical imaging to provide contrast in x-ray or CT scans, to visualise vasculature for example. DEB-TACE is an image guided procedure, in which interventional radiologists employ the use of a non-ionic iodinated contrast agent to visualise the blood vessels feeding the tumour, and give an indication of the endpoint of angiographic stasis. However, the embolic microspheres themselves are not visible under x-ray, meaning the exact delivery site and embolic endpoint cannot be completely visualised, something that had been identified as a limitation by physicians carrying out TACE procedures. This motivated the development of inherently radiopaque embolic materials by a number of methods: adsorption of Lipiodol (an ethiodised oil commonly used as a contrast agent in cTACE) into beads [66, 67], precipitation of radiopaque substances within a polymer matrix [68], and covalent attachment of iodinated species [69].

Biocompatibles UK Ltd has developed a radiopaque version of the existing DC Bead platform, marketed as DC Bead LUMI® (LC Bead LUMI® in the USA) which at the time of writing is approved in Europe, Canada and the US for intra-arterial embolisation treatment of liver tumours. After the PVA microspheres are synthesised, they undergo an acetylation reaction with a triiodinated benzyl moiety [70]. This renders the beads inherently radiopaque, meaning intra- and post-procedural imaging feedback is made possible. This could lead to improvements in delivery and post-procedure follow-up and reduce the risk of off-target embolisation.

The addition of the iodinated moiety also alters the properties of the beads in terms of their capacity to load drugs [38]. The increased solid content of the bead leads to a higher density of binding sites that has been shown to significantly increase the loading capacity of DC Bead LUMI with doxorubicin and irinotecan, compared with DC Bead. This gives the possibility of achieving higher intratumoral doses alongside imageability,

making DC Bead LUMI an attractive platform in the development of novel drug-eluting devices for TACE.

1.5 Towards development of an anti-angiogenic DEB – drug candidate selection

Small molecule multi-tyrosine kinase inhibitors have attracted a lot of interest recently, given the approval of sorafenib (Nexavar®, Bayer-Onyx) for the treatment of HCC. Table 1.3 outlines a selection from a broad list of options that have been considered for mTKI loading into DEBs, taking into account drug structure, properties and mode of action.

Sorafenib drug-eluting peptide nanocomposites [71] and poly(lactide-co-glycolide) microspheres [72, 73], both with magnetic resonance imaging (MRI) capability have been described for intra-arterial delivery to treat HCC. Poly(D,L-lactic acid) microspheres have also been prepared and loaded with either sorafenib or together with cisplatin and showed that the drug combination had a faster release rate [74] and was more efficacious in cell assays [75] compared to either drug alone. Lahti *et al.* (2015, 2017) described the off-label loading of LC Bead with both sorafenib [76] and sunitinib [77] but both processes were inefficient. Fuchs *et al.* (2015) have reported on a much more comprehensive appraisal of sunitinib loading into DC Bead [78], correlation of *in vitro* release with *in vivo* pharmacokinetics [79] and evaluation of anti-tumour effects in a rabbit VX2 embolisation model [80]. Whilst these studies show great promise and demonstrate feasibility for the locoregional delivery of mTKIs from DEBs, concerns remain over the severe toxicity of sunitinib in the liver [81] and alternative suitable mTKI candidates have been sought.

Table 1.3 Selection of mTKIs and their mode of action and properties
(*information sourced from www.drugbank.ca or individual drug FDA labels)

Compound	Mode of Action	Properties*
Axitinib	Potent VEGF inhibitor, inhibits breast cancer growth, prevents neoangiogenesis in 9L tumours, activity in refractory met renal cell	DMSO + DMF soluble Solubility of over 0.2 µg/mL in aq media with a pH 1.1-7.8, pK _a 4.8
Bosutinib	Active inhibitor of Bcr-Abl, inhibits tumour cell growth, angiogenesis, growth factor expression	DMSO + EtOH soluble, poorly water soluble Basic pK _a s 8.04, 4.80, 3.77
Canertinib diHCl	Potent pan-erbB tyrosine kinase inhibitor, irreversible TK inhibitor, radiosensitiser	10 mg/mL water solubility, DMSO ≥ 5.6 mg/mL, logPc 3.05
Dasatinib	SRC and BCR/ABL tyrosine kinase inhibitor, Lyn & Src kinase inhibitor	Very poorly water soluble (0.0128 mg/mL), pK _a s 3.1, 6.8, log P 1.8

Compound	Mode of Action	Properties*
Dovitinib	mTKI of fibroblast growth factor receptor (FGFR) 3, inhibits tumour growth in xenograft models of colon cancer	DMSO soluble, poorly EtOH soluble
Erlotinib HCl	Targets EGFR TK, potent inhibitor of JAK2-V617F. "Tarceva" approved for NSCLC, pancreatic and others	Slight water and methanol solubility, pK _a 5.42, logP 2.7
Gefitinib	EGFR TK inhibitor. "Iressa" approved for NSCLC	Solubility 0.027 mg/mL, sparingly water soluble at pH3, pK _a s 5.4, 7.2, logP 3.2
Imatinib methane-sulfonate	Inhibits particular TK enzymes, used to decrease bcr-abl TK activity. Gleevec®, indicated for chronic myelogenous leukemia, GI stromal tumours	DMSO and water soluble, poorly EtOH soluble, logP 3
Lapatinib toluene-sulfonate	EGFR and HER2/neu dual TK inhibitor, potent EGFR kinase inhibitor, can restore tamoxifen sensitivity. "Tykerb®" for advanced met breast cancer	Poorly water soluble (0.0223 mg/mL), DMSO soluble, logP 5.4
Nilotinib	Selective BCR-ABL inhibitor and of proliferation of haematopoietic cells in CML and ALL. TK inhibitor Ph I in CML "Tasigna®"	Poorly water (0.00201 mg/mL) and poorly EtOH soluble, DMSO soluble, logPc 4.51
Pazopanib	Selective multi-targeted TK inhibitor, targets VEGFR, PDGFR and c-kit	Limited solubility in warm DMSO, poorly water soluble (0.0433 mg/mL) logPc 3.59
Sorafenib toluene-sulfonate	Biaryl urea inhibits ERK pathway and angiogenesis by targeting VEGFR-2 and PDGFR-b. "Nexavar®" approved renal cell carcinoma and HCC	Poorly water (0.00171 mg/mL) and EtOH soluble, DMSO soluble, log P 3.8
Sunitinib Malate	Selective inhibitors of MTKs, inhibits FLT3-ITD phosphorylation, CSF-1 rK. "Sutent®" for renal cell carcinoma	Water soluble at pH 1.2-6.8, fluorescent, weak base pK _a 8.95, logP 5.2
Vandetanib	VEGFR-dependent tumor angiogenesis inhibitor, EGFR & RET-dependent proliferation inhibitor. "Zactima®" for follicular, medullary, anaplastic, adv/met papillary thyroid cancer	DMSO soluble, poorly water soluble (0.008 mg/mL), soluble at lower pHs, logPc 5.01
Vatalanib DiHCl	Selective inhibitor for VEGFR-1&2 TK+ PDGFR-b, c-KIT & c-FMS	Water soluble (10 mg/mL), DMSO soluble (85 mg/mL)

1.5.1 Vandetanib

When selecting a targeted agent for evaluation in a DEB product, vandetanib, developed by AstraZeneca, emerged as a candidate following technical and *in vivo* feasibility studies in collaboration with Biocompatibles. As a novel multiple tyrosine kinase inhibitor (mTKI), vandetanib has a desirable pharmacological profile, targeting two known pathways implicated in liver cancer: VEGFR and EGFR.

The molecule, an orally bioavailable 4-anilinoquinazoline, has at least one positively charged amine group at physiological pH which enables its interaction with the negatively charged sulfonate group within DC Bead (Figure 1.5). Vandetanib has a long half-life of 19 days [82], which is a benefit for sustained local delivery. Furthermore, vandetanib exposure is unaffected in patients with mild to severe hepatic impairment and the drug is well tolerated in these patients, meaning it is suitable for patients with liver damage which often accompanies HCC [83].

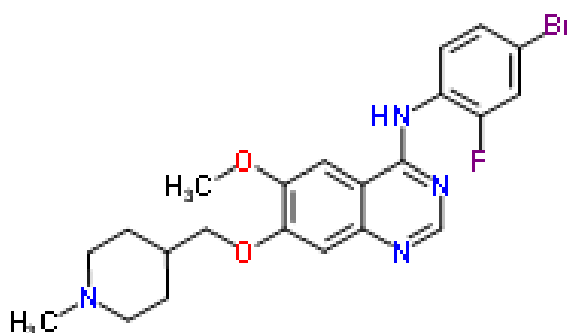


Figure 1.5 The chemical structure of vandetanib.

1.5.1.1 Mechanism of action

Vandetanib selectively inhibits vascular endothelial growth factor receptor 2 (VEGFR-2), epidermal growth factor receptor (EGFR), and rearranged during transfection (RET) tyrosine kinase (Figure 1.6) [82]. Vandetanib forms key hydrogen bonds with the ATP binding pocket competitively displacing ATP, and interacts with an adjacent hydrophobic pocket that also provides potency and selectivity. As a consequence target kinase activity and downstream signalling is inhibited [84].

Vandetanib is considered to be an angiogenesis inhibitor, given its activity in the VEGF pathway, interrupting key processes required for formation of blood vessels such as endothelial cell migration and proliferation. EGFR is also implicated in angiogenesis, and has been identified as an oncogene owing to its involvement in cell proliferation, inhibition of apoptosis, migration, adhesion and invasion [85]. The RET proto-oncogene encodes a tyrosine kinase protein, which is necessary for correct development of the nervous system and kidneys. Mutations in RET that cause the protein to be constitutively active can lead to neuroendocrine tumours, of which medullary thyroid cancer is the most common [86].

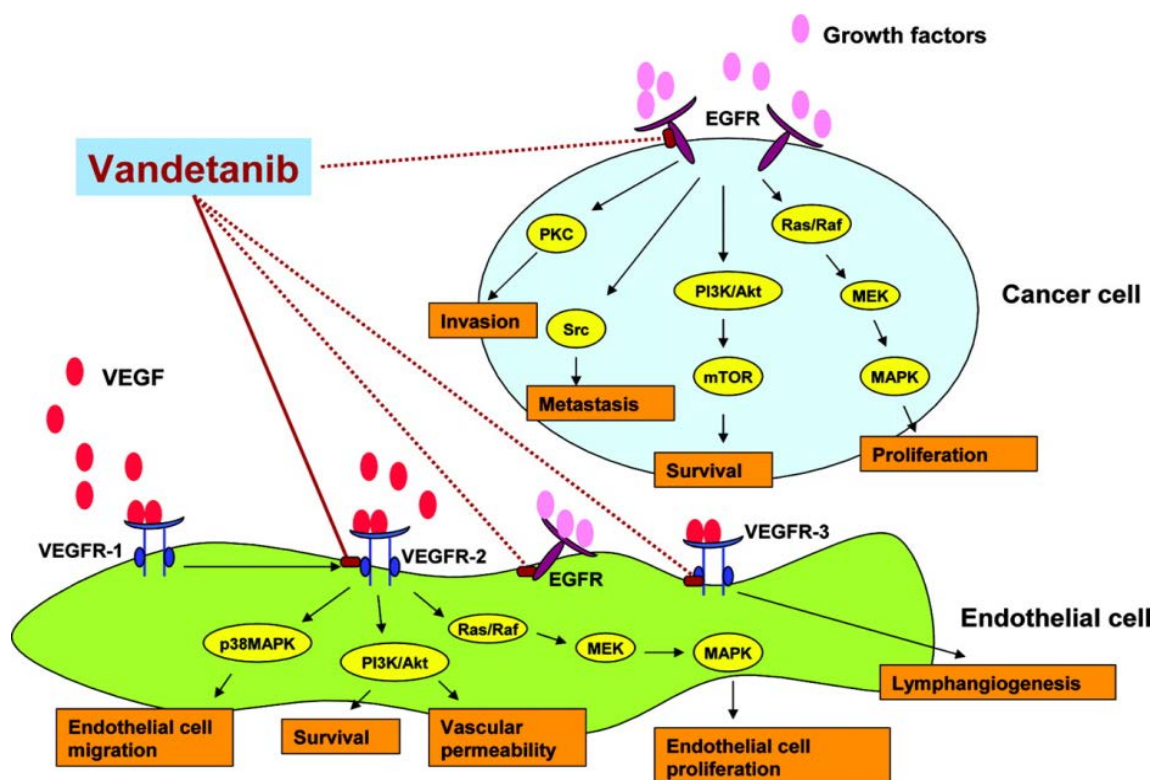


Figure 1.6 Mechanism of action of vandetanib. Vandetanib potently inhibits (solid line) VEGFR-2 and also has been shown to inhibit, with lower affinity (dashed lines) VEGFR-3 and EGFR.

Abbreviations: EGFR, epidermal growth factor receptor; MAPK, mitogen-activated protein kinase; MEK, MAPK/extracellular signal-related kinase kinase; mTOR, mammalian target of rapamycin; PI3K, phosphatidylinositol 3 kinase; PKC, protein kinase C; VEGFR, vascular endothelial growth factor receptor. Reproduced with permission from Morabito *et al.*, 2009. Original in colour.

1.5.1.2 *In vitro* and *in vivo* evaluation in hepatocellular carcinoma

Vandetanib potently inhibits VEGF EGF and bFGF-stimulated endothelial cell proliferation *in vitro*, as well as endothelial tubule formation [84, 87, 88]. Vandetanib also inhibits the proliferation of a range of HCC cell lines *in vitro*, including HepG2 cells, and induces apoptosis as determined by cell cycle analysis. Furthermore, it has been demonstrated to inhibit the migration and invasion of HCC cells, which could have implications in preventing metastasis [27, 87].

Inoue *et al.* (2012) investigated the effects of vandetanib on tumour progression and survival in mice bearing liver tumours [87]. Vandetanib treatment not only significantly

suppressed tumour growth and tumour vascularity in a dose dependent manner, but also seemed to have an inhibitory effect on intrahepatic metastasis, with drug treated mice having significantly fewer tumour nodules compared to control mice. Tumour bearing mice receiving 75 mg/kg vandetanib treatment had a significantly prolonged survival time compared to control, however all mice eventually perished as a result of tumour growth [87].

Recently, vandetanib-complexed biodegradable nanoparticles have been described [89] which showed *in vitro* activity against human umbilical vein endothelial cells (HUVECs). The nanoparticles were conjugated with a tumour-homing peptide motif and more effectively inhibited growth of HCC xenografts when given intravenously, as compared with oral vandetanib at 30 mg/kg. This work demonstrated the potential for improved outcomes using targeted delivery of vandetanib, which could potentially be augmented when combined with the embolic effect of DEBs.

Vandetanib is currently approved for the treatment of advanced medullary thyroid cancer, however clinical trials have taken place to assess its efficacy in other cancer types such as NSCLC, breast cancer, kidney cancer and HCC [90-92]. In a randomised, phase II, double-blind, placebo-controlled study, the efficacy and safety of vandetanib in patients with unresectable advanced HCC was evaluated. Whilst there was no statistically significant difference in tumour stabilisation rate (total of complete response, partial response and stable disease rates after 16 weeks), there was a suggestion of improvement in progression –free survival (PFS) and overall survival (OS) [93].

Common adverse events associated with the oral delivery of vandetanib include diarrhoea and rash, which can occasionally be severe. Prolongation of the QT interval (alteration in cardiac rhythm) has also been observed [94]. Significant side effects limit the oral use of vandetanib in cancer treatment, however local delivery of vandetanib *via* DEB could reduce the concentration of vandetanib in the plasma, thereby minimising the associated risks. Biocompatibles UK Ltd have carried out preliminary feasibility studies using vandetanib-loaded DC Bead in a rabbit VX2 liver cancer model [95]. Compared to rabbits treated with oral vandetanib, the concentration of the drug in the plasma of rabbits treated with vandetanib-eluting beads was significantly reduced

throughout the duration of the experiment. This was coupled with an equivalent anti-tumour effect to both oral drug and doxorubicin-eluting beads (Figure 1.7).

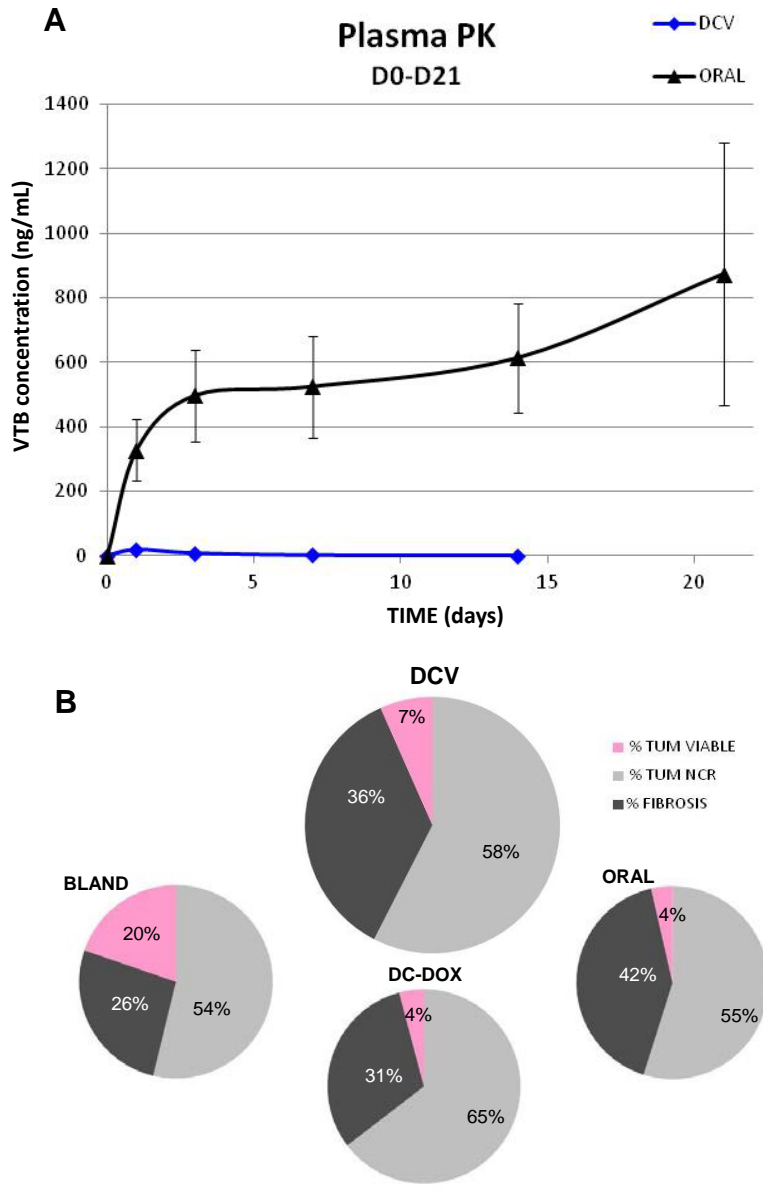


Figure 1.7 Results of a feasibility study of vandetanib-loaded DC Bead in rabbits bearing VX2 liver tumours. A) Vandetanib plasma concentrations in animals given oral vandetanib vs vandetanib beads. B) Average proportions of viable (pink), necrotic (grey) or fibrotic (black) tumour in each treatment group. DCV= vandetanib loaded DC Bead; Bland = unloaded dc Bead; DC-DOX = doxorubicin loaded DC Bead. Hagan *et al.*, (2016). Original in colour.

Furthermore, histological analysis of vandetanib-bead treated liver showed that the region of necrosis extended outside the tumour capsule. This is a result not previously seen with DEBDOX, but has been observed with DC Bead loaded with sunitinib,

another mTKI [80]. This characteristic could provide added benefit to vandetanib-bead therapy by encompassing zones where micro-metastases are located, addressing common sites of tumour recurrence. Indeed, ablation zones created by radiofrequency ablation that extend past the tumour margin are known to reduce tumour recurrence [96]. Caution would be needed in establishing a safe dose of vandetanib that does not compromise healthy liver tissue.

This potent anti-tumour activity of vandetanib combined with embolisation warrants further investigation. Exploiting hypoxia in cancer is a topic which has received a lot of attention. Treatment with drugs that exhibit elevated potency in hypoxic conditions or interact with the molecular pathways involved in hypoxia is a desirable and selective approach.

1.6 The challenge of hypoxia

Hypoxia is a deficiency in the supply of oxygen to tissues, the threshold of which depends on the normal oxygen tension of the organ in question. In the healthy liver, a range of oxygen tensions are found depending on distance from the source of oxygen rich blood: the branches of the hepatic artery. In fact, this oxygen gradient contributes to the zonation of the liver parenchyma and differentiation of hepatocytes to create the heterogeneous structure and function of the lobules [97]. In perivenous regions of the normal healthy liver the oxygen tension can be as low as 4%, however despite this a hypoxic response is not triggered [98]. In disease states such as HCC, hypoxia can be an inherent feature of the tumour and results in stabilisation of HIF [99]. Treatment by embolotherapy will then further deprive the target tissues of oxygen. Hypoxia is a stressful condition for cells which therefore activates pathways involved in survival. For tumour cells, whose controls over growth and apoptosis are already deregulated, these conditions can further promote switching on of aggressive phenotypes, leading to poor prognosis [100]. As well as upregulation of angiogenic factors as described previously, hypoxia can promote metastasis, proliferation, radioresistance, and importantly, chemoresistance [101].

1.6.1 Hypoxia related drug resistance

The observation that hypoxia contributes to resistance to chemotherapeutics has been documented for some time. More recently, the mechanisms behind the cellular changes

responsible for this resistance have been elucidated, and HIF has been found to be responsible for several of these changes [102], summarised in Figure 1.8.

Of importance to HCC and this study are the mechanisms of resistance to doxorubicin, the current drug of choice for DEB combination therapy, and mechanisms of resistance to tyrosine kinase inhibitors.

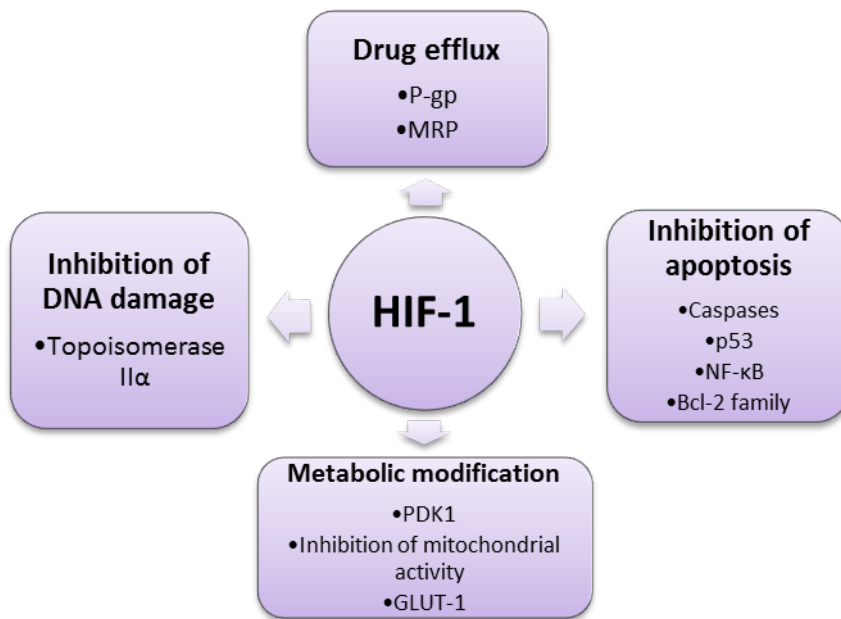


Figure 1.8 Summary of HIF-1 mediated mechanisms of drug resistance and implicated proteins. P-glycoprotein (P-gp) and Multi-drug resistance protein (MRP) are ABC transporters which pump drugs out of cells. Topoisomerase II (TOP2) enzymes are required for successful DNA replication and are the target of anthracycline drugs such as doxorubicin. In resistant cells, TOP2 may be reduced in content or mutated such that its inhibitors are no longer effective. HIF-1 can downregulate pro-apoptotic proteins via tyrosine kinase signalling cascades. Finally, HIF-1 can regulate a shift to anaerobic metabolism, activating proteins involved in glycolysis such as pyruvate dehydrogenase kinase 1 (PDK1) and the glucose transporter GLUT-1. Glycolytic activity has been associated with increased resistance to chemotherapy in several cancer types.

1.6.1.1 Hypoxia and resistance to doxorubicin

Doxorubicin is an anthracycline antibiotic whose mechanism of action is intercalation with DNA and disruption of DNA replication *via* interference with the topoisomerase II enzyme [103]. One possible mechanism of doxorubicin resistance in cancer cells is drug efflux by the P-glycoprotein (P-gp) transporter [104]. This transporter is encoded by the multi-drug resistance gene (MDR1), which has been shown to be directly regulated by HIF-1. Interference with HIF-1 attenuated hypoxia-induced MDR1 expression *in vitro* [105]. However, whilst primary HCC cell lines previously untreated with

chemotherapeutic agents showed resistance to doxorubicin *in vitro* [106] low levels of the P-gp transporter were found in these cell lines pointing to additional mechanisms of resistance. Bowyer demonstrated for the first time that culturing HepG2 cells in hypoxic conditions bestowed added resistance to doxorubicin [107], and that combining doxorubicin with rapamycin (an agent known to interfere with HIF-mediated signalling pathways) in DEB was more effective in controlling tumour growth in a mouse xenograft model of HCC than either treatment alone.

In a review summarising mechanisms of HCC resistance to doxorubicin [108] it is mentioned that both the PI3/Akt and MEK/ERK pathways could be implicated. As previously stated, these are pathways downstream of the targets of many tyrosine kinase inhibitors including vandetanib. Indeed, erlotinib, an EGFR tyrosine kinase inhibitor, enhanced sensitivity to doxorubicin in HCC cell lines [29]. However, this was not the case with sorafenib, which when combined with doxorubicin produced an antagonistic effect on toxicity in Hep3B cells [109]. Vandetanib has been shown to interfere with P-gp transporters, reversing doxorubicin resistance in certain cells [110]. Further studies combining doxorubicin with vandetanib in HCC cells, in both normoxic and hypoxic conditions, could demonstrate whether there is any synergism between the two drugs against HCC and in the setting of TACE. However the literature has shown that the mechanisms of doxorubicin resistance and cross-talk between signalling pathways are complex and researchers/clinicians should be cautious of antagonistic effects.

1.6.1.2 Hypoxia and tyrosine kinase inhibitors

The proposed benefit of tyrosine kinase inhibitors targeting angiogenic pathways is that they diminish the ability of tumours to respond to inherent hypoxia by inhibiting neovascularisation [111]. It has been demonstrated that the drugs may themselves induce hypoxia in tumours by this mechanism [112]. Combined with the ischaemic effect of TACE, this means that it is extremely important that a TKI-DEB candidate is effective in hypoxic conditions.

There are few studies available in the literature that examine the effect of hypoxia on the activity of TKIs, however Ahmadi and colleagues set out to test the effects of several TKIs on a panel of cancer cell lines including colorectal cancer, non-small cell lung cancer, breast and renal carcinomas [113]. The study identified that some TKIs showed either increased or reduced inhibitory activity in hypoxic conditions, however

this varied considerably depending on the cell line. Across the cell line panel vandetanib was shown to be either equipotent or mildly more effective in hypoxia. Of note, sorafenib was significantly less effective in hypoxia, but this was not associated with the degree of hypoxia-induced changes in RAF/MEK/ERK signalling [113]. Hypoxia consistently conferred resistance to sorafenib across a panel of HCC cell lines, coupled with increased expression of VEGF, GLUT-1 and P-gp. Sensitivity was restored by treatment with an inhibitor of HIF-1 α accumulation. Evidence of hypoxia-induced resistance to sorafenib was also seen in a clinical setting in HCC, with sorafenib resistant tumours having significantly higher HIF-1 α nuclear expression compared with untreated and sorafenib sensitive tumours [114].

Other VEGFR inhibitors, including vandetanib, have been found to suppress HIF-1 α expression *via* inhibition of Akt and ERK signalling pathways [115, 116]. Similarly, the EGFR inhibitor gefitinib was found to suppress HIF-1 α induction in hypoxia by inhibiting PI3/Akt mediated protein translation [117]. Nevertheless, this effect has not been studied in HCC cell lines.

In an orthotopic rat model of HCC, hypoxia of the liver was induced by hepatic artery ligation (HAL) and combined with valatanib, a VEGFR inhibitor under development. Those rats receiving the combination of HAL and valatanib had significantly better survival times and reduced tumour growth. Hypoxic conditions were also shown to sensitise endothelial cells to the inhibitory effects of valatanib on tubular-structure formation [118].

Whilst in general it seems that tyrosine kinase inhibitors show good anti-tumour activity in hypoxia, the literature shows that this is dependent on the cell line and the targets of the drug. Despite sorafenib being the only of these candidates to be clinically approved for HCC and thus perhaps the obvious candidate, evidence of hypoxia-induced resistance is cause for concern and could be one possible explanation for the lack of success in clinical trials combining TACE and sorafenib [63]. Examining the effect of vandetanib on HCC cell lines in both normoxic and hypoxic conditions will allow screening of potential mechanisms of resistance (or sensitivity) and provide information on its suitability. Although the preliminary rabbit VX2 study on vandetanib eluting beads has already shown promising results, *in vitro* studies will allow a deeper

understanding of the mechanisms of vandetanib and hypoxia in combination on cells derived from human HCC.

1.6.2 Modelling hypoxia in vitro

The standard condition for culturing cells is 21% oxygen. However, this does not reflect the true oxygen concentration in tissues. In normal healthy liver, oxygen tension (pO₂) is significantly lower than atmospheric oxygen tension, such that 5% oxygen may be considered 'physoxic' (physiological normoxia) [119]. In liver tumours, pO₂ can be as low as 6 mmHg (<1% O₂) [120]. In order to examine the effect of embolisation-induced hypoxia and provide better translational data from *in vitro* to *in vivo* and beyond, it is necessary to culture cells at relevant oxygen tensions. One option for modelling hypoxia is by using cobalt chloride, which chemically stabilises HIF-1/2 α in normoxia. True hypoxic conditions are made possible with incubators or sealed glove boxes that allow the control of oxygen concentration [121].

1.7 Methods of pre-clinical evaluation of drug-eluting beads: *in vitro* and *in vivo* models of HCC

1.7.1 Cell culture

Several immortalised cell lines derived from HCC tumours are available for use in *in vitro* studies, differing in their characteristics in terms of morphology and biology. For the purposes of this work, the cells described below were used.

HepG2 cells were derived from a 15 year old Caucasian male. There is a lack of consensus in the literature as to whether the tumour of origin was a true HCC or a hepatoblastoma (a pediatric hepatic malignancy), however HepG2 are frequently used to model HCC *in vitro* due to an absence of viral infection. The cells are adherent and have an epithelial morphology, a mutation in the β -catenin gene as well as deregulation of cell growth and survival pathways [122]. Reported expression of EGFR in HepG2 cells is variable, but in general seems to be low in comparison with other HCC cells [123, 124]. Expression of EGFR and VEGFA genes has been found to be downregulated in HepG2 cells compared to hepatocytes [125]. Despite this, treatment with EGF enhances HepG2 proliferation, migration and promotes survival of drug resistant cells [85, 126], and constitutive activation of EGFR in HepG2 cells has been

observed [127]. Due to phenotypic differences between HepG2 and other HCC cell lines [128], it is important to include other cell lines in the evaluation of drug response.

Hep3B cells are an HCC cell line derived from an 8 year old male, and are adherent and epithelial in nature. These cells produce polypeptides of the hepatitis B virus surface antigen [129]. Hypoxic conditions are known to stimulate VEGF expression in Hep3B cells [130], and they are thought to stimulate their own growth in an autocrine manner *via* EGF expression [131].

JHH6 cells are an undifferentiated HCC cell line derived from a 57 year old Japanese female. The morphology is undifferentiated compared to HepG2, and as such represents a more aggressive model of HCC [132].

An obvious limitation of using HCC cells alone to examine the response to an anti-angiogenic drug is that most of their inhibitory effects are exerted upon endothelial cells expressing VEGFR, with the disruption of blood supply to tumour cells as an indirect consequence. In the case of vandetanib, the inhibition of EGFR also directly affects the tumour cells, impeding proliferation [87]. Human umbilical vein endothelial cells (HUVECs) can also be used in culture as a model of endothelial cell response to anti-angiogenic drugs. However, to evaluate the full effect of the drug, the effect on tumour growth in the proper environment must be studied. 3D cell culture models may be employed to more accurately model the tumour microenvironment, for example tumour cell spheroids are more representative of *in vivo* tumours in terms of their cell morphology, heterogeneity, and presence of hypoxic gradients [133]. 3D models of HCC cells incorporating co-culture with HUVECs have demonstrated differences in aggressiveness, cellular signalling, and response to anti-angiogenic drugs compared with 2D cultures [134, 135]. Ultimately, investigational treatments should be evaluated in animal models to provide the best indication of response in a representative tumour environment.

1.7.2 *Mouse models*

Mice are one of the most commonly used species for early *in vivo* studies, and there are several methods available to model HCC. As summarised in a review by Heindryckx *et al.*, mice may develop HCC by chemical induction, genetic modification (allowing analysis of the effect of over-expression of various oncogenes) or they may be

implanted with human HCC cells in order to create an ectopic or orthotopic xenograft [136].

Mouse models are most suitable when evaluating compounds intended for systemic delivery. Selective intra-arterial interventions such as TACE are impossible to perform due to the size of the animal. However, ectopic xenograft models have been used in the past to demonstrate control of tumour growth *via* subcutaneous tumour-adjacent application of DEB [137, 138]. Despite the obvious limitations of this model, it is relatively inexpensive and easy to set up as it does not require anaesthesia or surgical procedures. It can give information about the efficacy of drugs when released locally from a DEB and allows post-mortem analysis of excised treated tumours. In order to evaluate the combination of embolisation (and therefore hypoxia) and local drug release in an orthotopic model, a larger animal must be used to model treatment of HCC by TACE.

1.7.3 Woodchuck model

The eastern woodchuck can be infected with the Woodchuck hepatitis virus (WHV) which can cause chronic hepatitis and subsequent HCC in these animals. The woodchuck is a useful model for studying viral carcinogenesis and has been used to evaluate both anti-angiogenic therapies and embolotherapy [139-141].

1.7.4 Rabbit VX2 model

VX2 tumours are derived from a virus-induced papilloma of rabbits, first described by Shope and Hurst in 1933. When VX2 cells or tumour fragments are injected into the rabbit liver, they produce fast-growing, hypervascular malignancies which due to their similarities to HCC have been used extensively as a model for this disease. Furthermore, VX2 cells and HepG2 cells have been shown to respond in a similar manner to several chemotherapeutic agents, including doxorubicin and tyrosine kinase inhibitors [142]. As the rabbit is large enough to be successfully catheterised *via* the hepatic artery, VX2 liver tumours have also been treated by TACE in numerous studies [143-145].

1.8 Summary

In summary, intermediate HCC is a disease with a poor prognosis and a severe lack of effective therapies. The current standard of care, TACE, yields poor response rates which may be due in part to hypoxic regions within the tumour. Hypoxia can be both

inherent and induced by embolisation and is associated with chemoresistance (including doxorubicin) and poor outcome. Targeted therapies such as mTKIs may provide improved treatment responses but are limited by significant systemic toxicities. Vandetanib is a multi-tyrosine kinase inhibitor which targets two pathways implicated in HCC, the VEGFR pathway and the EGFR pathway. Delivery of vandetanib *via* drug-eluting beads could result in a high, sustained dose of vandetanib local to the tumour coupled with embolisation induced necrosis. The anti-angiogenic and anti-proliferative effects of vandetanib could have benefits in controlling tumour growth and recurrence, therefore investigation into its mechanism of action when delivered locally *via* DEB is warranted.

1.9 Aims of the thesis

This thesis aims to investigate whether delivering the TKI vandetanib locally *via* DEB in a TACE procedure is feasible and effective to treat liver tumours, despite hypoxic conditions induced by embolisation. This will require development of an optimised vandetanib-loaded bead prototype, evaluation of its characteristics and performance as an embolic product, and assessment of the effect of embolization induced hypoxia on the efficacy of vandetanib in the setting of HCC.

The ideal DEB candidate will be:

- Easily produced, handled and delivered *via* microcatheter
- Visible under CT
- An efficient and predictable embolic
- Sustained release of the drug which is active in hypoxia
- Well tolerated with negligible systemic side effects
- Effective at killing tumours and inhibiting angiogenesis

In order to evaluate the DEB formulations, the *in vitro* loading and release of vandetanib from beads of different sizes and chemical formulations will be profiled using HPLC to detect vandetanib in elution medium. Vandetanib loaded beads will be characterised for size changes, handling, drug-bead interaction, and drug distribution using tests developed at Biocompatibles UK Ltd. Data generated on novel, more representative *in vitro* elution models will be compared with *in vivo* PK data as it becomes available.

To assess the activity of vandetanib in hypoxic conditions, cell viability assays and apoptosis detection assays will be carried on a panel of HCC cell lines and endothelial cells at 1% and 21% oxygen. Changes in protein expression in these cells will be measured by Western blot and other molecular biology techniques to give insight into the mechanism of action. Finally, vandetanib loaded beads will be evaluated in a mouse xenograft model of HCC for efficacy and assessment of biological response.

In summary, the aims of the thesis are to:

- Characterise the physicochemical properties of vandetanib loaded DEBs in order to find the optimal formulation;
- Evaluate the mechanism of vandetanib release from beads in various elution models and assess similarities to *in vivo* pharmacokinetics;
- Examine the effects of vandetanib on HCC and endothelial cell proliferation and apoptosis in hypoxia and normoxia;
- Analyse changes in expression of relevant proteins in these cells;
- Test vandetanib beads in a mouse xenograft model of HCC.

2 CHAPTER TWO: PHYSICOCHEMICAL CHARACTERISATION OF VANDETANIB LOADED BEADS

2.1 Introduction

As a treatment for hepatic malignancies, Drug-eluting Beads (DEB) have a dual mechanism of action: the physical embolisation of blood vessels leading to ischaemic insult to the target lesion, and the delivery of the chemotherapeutic agent to the tumour site [39]. The balance of which function is the primary mode of action (PMOA) may vary depending on the drug used and the way in which the product is delivered. For example, interventional radiologists may aim to achieve full stasis of blood flow when injecting beads, suggesting a high degree of embolisation, or they may aim to leave a small amount of residual flow in order to facilitate the release of the drug from the beads or leave the opportunity for retreatment [146-148]. In either case, the functions of the DEB should complement each other. Therefore, when creating a drug loaded bead it is important to establish that the process of loading the drug does not have a significant negative impact on the physical properties of the bead that allow it to perform as an embolic device [149, 150]. Furthermore, it must be ensured that the drug will perform as intended when loaded and released from the bead. Kerr (1987) was one of the first to propose the ideal attributes of a drug-eluting microparticle for regional cancer treatment [151]. The features to be considered were:

- Particle delivery
- Particle size
- Particle composition
- Drug – particle compatibility
- Drug type
- Drug dose
- Drug release profile.

Interplay between these factors affects the final characteristics of the product, as will be discussed in greater detail below.

2.1.1 Drug loading capacity and bead interactions

Maximum drug loading capacity can depend on the chemical structure of the bead and the size and chemical properties of the drug molecule, for example the number of positively charged sites. As an example, DC Bead is capable of loading approximately 45 mg of doxorubicin per mL of beads. Doxorubicin HCl has one positive charge at pH 7, and also may exhibit pi-pi stacking which could influence its interactions within the beads [152].

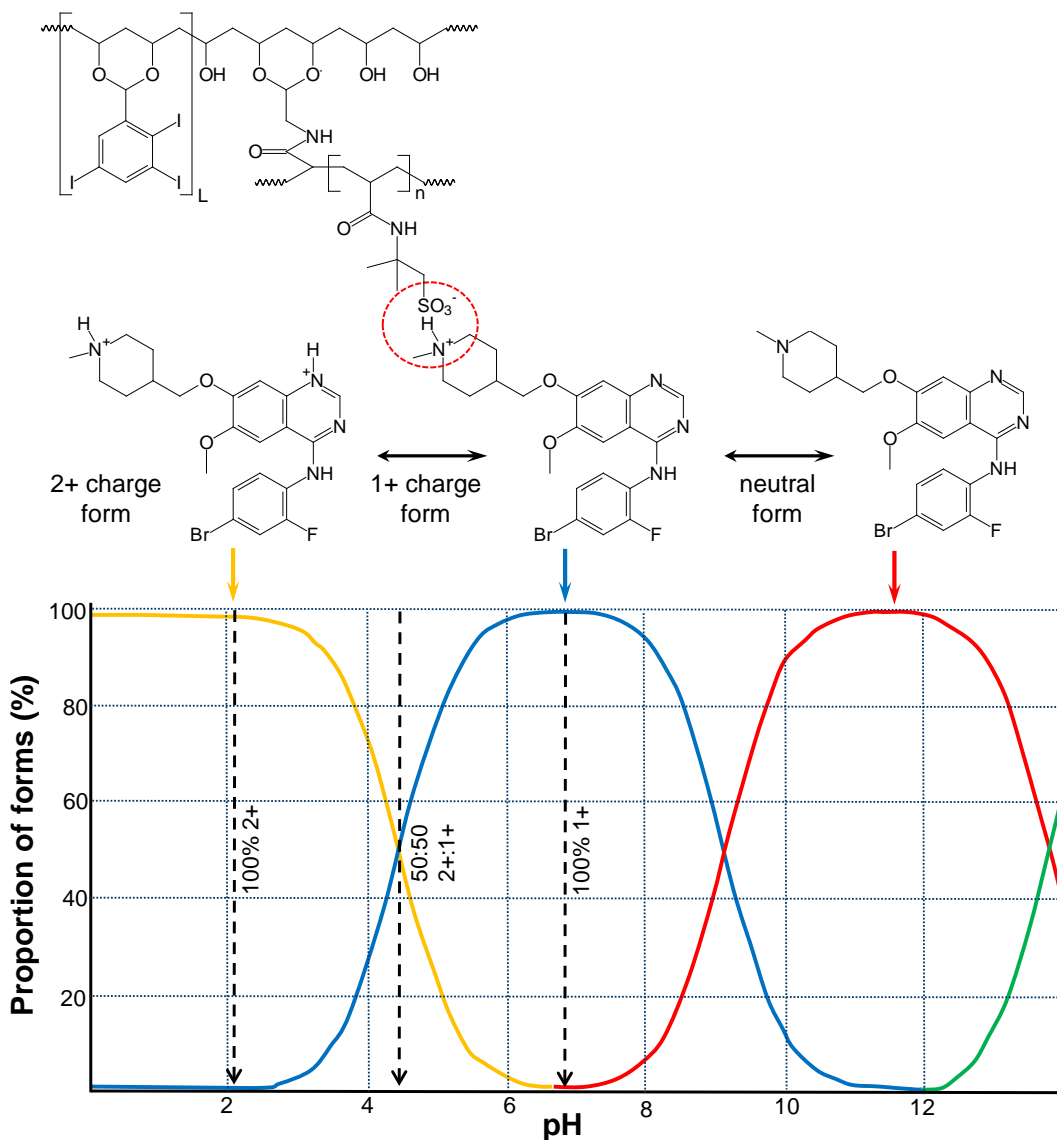
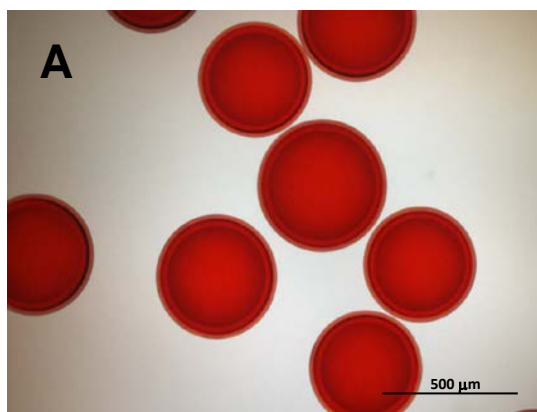


Figure 2.1 Ionic interaction between DC Bead (L groups are present in DC Bead LUMI) and vandetanib (top); structure of the ionised forms of vandetanib at different pH (middle); theoretical proportion of the various forms of vandetanib present with pH (bottom). Adapted from chemicalize.org. Original in colour.

Figure 2.1 shows the proposed interaction between the structure of DC Bead and the protonated vandetanib molecule. During the loading process, drug molecules are adsorbed into the bead and form ionic interactions between positively charged sites and negatively charged sulfonate groups present on the DC Bead polymer structure. This also leads to the displacement of water from the beads which may lead to a decrease in bead size [152].

The theoretical maximum binding capacity of DEB may be estimated knowing the percentage content of sulfur by elemental analysis of beads and converting this to a value in moles. Assuming a 1:1 (mol:mol) binding ratio, as was observed with irinotecan and DC Bead [153], the theoretical drug binding capacity is equivalent to the amount of sulfonate present in 1 mL of beads. DC Bead LUMI has a significantly higher solid content than DC Bead (~35% vs ~5% respectively), and therefore has a much higher theoretical maximum capacity due to the presence of a greater weight percent of sulfonate binding groups incorporated per unit volume of hydrated beads [38]. However, not all binding sites may be accessible due to the cross-linked structure and reduced interstitial water content of the beads, thus the theoretical maximum capacity is likely an overestimation. Additionally, the binding ratio may not always be 1:1. Mitoxantrone, an anthraquinone antineoplastic, possesses two positively charged amines, which means each drug molecule has the potential to occupy two binding sites in the bead [39]. This has several implications: not only is the maximum loading capacity decreased compared with doxorubicin, but this stronger interaction retards drug elution rate and decreases bead diameter to a greater extent than singly charged drugs (Figure 2.2) [39, 154].



Doxorubicin 25 mg/mL



Mitoxantrone 20 mg/mL

Figure 2.2 300-500 μm DC Bead loaded with A) 25 mg/mL doxorubicin, B) 20 mg/mL mitoxantrone. Mitoxantrone binds to two sulfonate groups in the hydrogel structure, pulling the network closer together and decreasing bead diameter. Reproduced with permission from Biocompatibles UK Ltd., data on file. Original in colour.

Drugs that do not possess a positive charge may also be loaded into beads, but the process is more complex. Sorafenib loading into DC Bead has been reported but the low solubility of the drug in aqueous media requires a loading process of several sequential sessions of loading from low drug concentration solution to achieve sufficient quantities of loaded drug [155]. This can be overcome by use of a DMSO swelling process in which drug dissolved in DMSO can be used to swell the beads, followed by a precipitation step as the drug swollen beads are immersed in water [156]. This however, leaves the drug in a microprecipitated form in which its elution is dependent upon the dissolution of the particulates. The partial ethanol solubility of sorafenib can be used to produce suitable loading solutions in ethanol:water mixtures in which the drug can be exchanged into the bead matrix. Sorafenib however, unlike, many other mTKIs, is not protonated at neutral pH and relies upon strong hydrogen bonding of the amines on the urea group to interact with carboxylate residues at its target site. This may also provide a source of interaction between drug and bead to ensure controlled release.

Vandetanib exhibits pH-dependent solubility, meaning that in order to prepare vandetanib solution for loading into DEB, the pH must be acidic. This alters the charge state of the molecule as can be seen in Figure 2.1: as pH decreases below 6.8, the proportion of vandetanib molecules with two positive charges will increase, thereby shifting the bead-binding ratio to 2:1 and decreasing drug loading capacity. Finding an

optimum balance between capacity and solubility will be an important task when developing the formulation of a vandetanib loaded DEB.

The distribution of drugs within beads following loading is something that can be visualised under optical microscopy in the case of coloured compounds such as doxorubicin, or confocal microscopy for fluorescent drugs [157, 158]. Distribution and quantitation of drugs in DEB has also been analysed by using Fourier-transform infrared spectroscopy (FTIR) *in vivo* [159]. In an ideal scenario, the drug will be evenly distributed throughout the bead, indicating efficient loading, and a more gradual and sustained release compared to a bead for which only its surface is coated. Vandetanib is mostly colourless in solution and therefore loaded beads cannot be distinguished from unloaded beads under optical microscopy. Furthermore, it does not possess a fluorophore hence cannot be mapped using confocal microscopy. Alternative methods will need to be sought to map vandetanib distribution in beads, for example FTIR or scanning electron microscopy coupled with elemental analysis (SEM-EDX).

2.1.2 Size/compressibility

Bead size range is an important factor in several aspects of DEB-TACE therapy including effects on elution rate, tumour penetration efficiency and potential adverse events [66, 160]. In initial clinical evaluations of DC Bead, larger sized beads (500-700 μm) were favoured due to similarity in size with other commonly used embolic particles in cTACE as well as safety concerns, as small particles are known to present a greater risk of extrahepatic distribution, for example to the spleen or lung [40, 161, 162]. In recent years there has been a trend amongst interventional radiologists to opt for the smaller size ranges (100-300 μm) when performing DEB-TACE [163]. This is due to clinical observations of more distal penetration of smaller beads into the tumour vasculature which would suggest a greater coverage in terms of embolic effect and drug release, a concept which has been demonstrated *in vivo* with DC Bead M1 (70-150 μm) [66, 164]. There is some discrepancy in the literature as to whether use of smaller bead sizes leads to fewer or more adverse events [164], however it has been observed that particles of around 40 μm pose a risk of potentially fatal complications resulting from off-target embolisation [165, 166]. This highlights the requirement for careful angiographic planning and good delivery technique when using smaller size microspheres.

As previously mentioned, loading DC Bead with drugs displaces water from the beads leading to a reduction in diameter [39], and the extent of this shrinkage can vary depending on the structure of the drug being loaded [152]. Moreover, the water loss caused by drug loading also affects the elastic modulus of the beads, rendering them less compressible as drug dose increases [149, 153, 167]. As well as penetration efficiency, this characteristic may have implications for the delivery for larger size microspheres, as less compressible beads may be more prone to blockage in smaller internal diameter microcatheters. When considering the compressibility of the DEB, it has been shown that due to its increased solid content, DC Bead LUMI is about 100-fold less compressible than DC Bead; however this did not cause a significant difference in penetration efficiency in an *in vitro* embolisation model [70]. It will be important to investigate the extent to which DC Bead and DC Bead LUMI size range changes when loaded with vandetanib, and if penetration efficiency is affected, when considering prototype selection.

2.1.3 Radiopacity

The concept and prospective benefits of the radiopaque version of DC Bead, DC Bead LUMI, have been previously introduced in the first chapter of this thesis. Figure 2.3 demonstrates the alterations performed in order to render DC Bead inherently radiopaque. Instead of the blue dye RB4, a 2,3,5-triiodobenzyl moiety is added to the beads, resulting in a beige coloured microsphere visible under X-Ray imaging [70].

DC Bead LUMI has been previously optimised in terms of iodine content and resulting radiopacity to allow visualisation of embolised vessels *in vivo* [70]. Therefore, it is important to ensure that loading of DC Bead LUMI with vandetanib does not exhibit any quenching effect on the radiopacity of the beads, or any detrimental effect on their handling and administration, perhaps due to a further increase in rigidity or density.

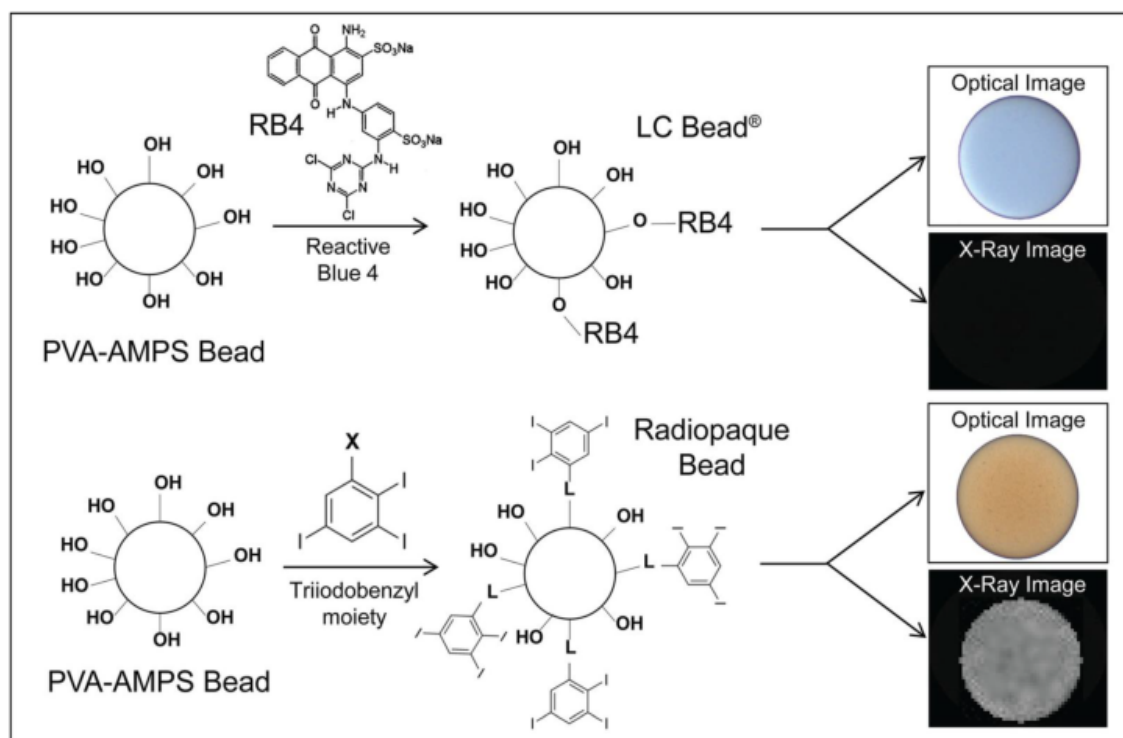


Figure 2.3 Comparison of DC Bead (marketed as LC Bead in USA) and radiopaque Beads (DC/LC Bead LUMI) preparation and appearance. Reproduced from Duran *et al.*, Theranostics (2016). Original in colour. <https://creativecommons.org/licenses/by-nc/4.0/legalcode>

2.1.4 Summary

Table 2.1 summarises the physicochemical characteristics that should be evaluated and considered in the development of a vandetanib eluting bead, and common methods of *in vitro* evaluation. Drug release will be investigated in detail in chapter three of this thesis.

Table 2.1 Desired characteristics of DEBs and their evaluation methods.

Characteristic	Description	Evaluation methods
Maximum loading capacity	The maximum amount of drug that can be loaded per unit volume of beads (usually mg/mL). Must be adequate to deliver a sustained therapeutic dose to the target tissue.	Beads are loaded in excess. Residual drug in the depleted loading solution is quantified by the appropriate analytical method.
Drug release	The rate at which drug is released from the beads. The drug should be capable of being close to, if not completely released from the beads in an appropriate time frame to attain a consistent therapeutic dose in the tissue.	Drug release into elution medium (usually PBS) over time is measured with sequential sampling and analysis to give a dissolution profile. Different <i>in vitro</i> set-ups resulting in varied hydrodynamic conditions alter the release kinetics to suit requirements (confirming batch uniformity vs prediction of <i>in vivo</i> release) (See chapter 3)
Size/compressibility	Bead size range and compressibility has an effect on the penetration efficiency of the product. Smaller beads will embolise more distal blood vessels, but they can also present a risk of off-target embolisation.	Optical microscopy is used in combination with calibrated sizing software to obtain size distribution of a bead sample. Compressibility (elastic modulus) of a single bead can be determined using a nanoindentation system, or bespoke <i>in vitro</i> models can estimate penetration distance.
Radiopacity (DC Bead LUMI)	DC Bead LUMI has been designed to aid interventional radiologists in visualising the product during and after the DEB-TACE procedure. Beads must be visible under X-Ray/CT.	Micro-CT can be used to quantify attenuation of beads when embedded in agarose 'phantoms'.
Handling and deliverability	Aspects related to the handling of the product by the physician and the delivery during the DEB-TACE procedure. Beads should have a sufficiently long suspension time in contrast agent, and be able to be delivered through a suitable catheter without blockage.	Handling studies in the lab aim to simulate the preparation and use of beads in the clinic. Suspension time in contrast agent and ease of catheter delivery is tested against specifications and may be confirmed by several operators.

2.1.5 Aims of this chapter

- Establish the maximum vandetanib loading capacity of DC Bead and DC Bead LUMI.
- Assess changes in bead size following vandetanib loading.
- Examine drug-bead interactions and drug distribution within beads.
- Quantify the radiopacity of vandetanib loaded DC Bead LUMI by micro-CT analysis.
- Identify the optimal formulation of a vandetanib loaded DEB in terms of its physicochemical properties.

2.2 Materials and Methods

2.2.1 Materials

Table 2.2: List of materials, suppliers and storage conditions.

Material	Supplier	Storage
Vandetanib powder (C₂₂H₂₄BrFN₄O₂)	Astra Zeneca	-20°C, protected from light
0.1M Hydrochloric acid (HCl)	Fluka	Ambient
1M Sodium Hydroxide (NaOH)	Fisher Scientific	Ambient
DC Bead™	Biocompatibles	4°C in PBS
DC Bead LUMI™	Biocompatibles	4°C in 0.9% NaCl
Trifluoroacetic acid (CF₃COOH)	Sigma Aldrich	Ambient
Methanol (CH₃OH)	Romil	Ambient
Agarose	Sigma Aldrich	Ambient
OCT compound (Tissue Tek)	Sakura	Ambient
Omnipaque™ 350 contrast agent (Iohexol)	GE healthcare	Ambient
Phosphate buffered serology saline (PBSS)	Source Bioscience	Ambient

2.2.2 Physicochemical analysis methods

2.2.2.1 HPLC method for quantification of vandetanib concentration in solution

Quantification of vandetanib in aqueous solutions (drug loading solution, elution medium etc.) was performed on Waters Acquity HPLC/UPLC systems with UV detection using the parameters listed in Table 2.3.

Table 2.3 Instrument parameters for the analysis of vandetanib by HPLC.

Column	Thermo Scientific Hypersil GOLD C18 3µm 4.6 x 150 mm			
Detector wavelength	254 nm			
Mobile Phase	Mobile Phase A: 0.1% v/v TFA in purified water Mobile Phase B: 0.1% v/v TFA in methanol			
Mobile phase flow rate	1.0 mL/min			
Method Type	Gradient			
Gradient Parameters	Time (min)	%A	%B	Curve
	Initial	70	30	Initial
	22	48	52	6
	22.1	70	30	6
	30	70	30	6
Injection volume:	5 µL			
Run Time	30 minutes			
Wash solvent	Methanol			
Purge solvent	Methanol:Water (50:50)			

For each run, duplicate injections of two standards of $100 \pm 10 \mu\text{g/mL}$ were used to calculate a calibration factor using the following equation:

Standard Calibration Factor

$$= \frac{\text{Concentration of Standard } (\mu\text{g/mL})}{\text{Mean peak area of Vandetanib Calibration Standard}}$$

Thereby allowing the calculation of the concentration of vandetanib in the unknown sample:

Concentration of Vandetanib in sample solution (µg/mL)

$$= \text{Mean peak area of Vandetanib} \times \text{Standard Calibration Factor}$$

The method was validated previously at Biocompatibles for accuracy, precision, specificity, limit of detection, limit of quantitation, linearity, range and robustness.

2.2.2.2 Vandetanib solution preparation

Vandetanib has an isoelectric point (pI) of 11.46 and is poorly soluble in water, however solubility can be increased by decreasing the pH. Drug solutions were prepared at a concentration of 15-20 mg/mL in acidified water, with the exception of solutions prepared at pH 6.8 where the maximum concentration achieved was 5 mg/mL. Vandetanib powder was weighed into a volumetric flask. 0.1 M HCl was added to 70% (to target pH 4.8 or below) or 50% (to target pH 6.8) of the total desired volume of solution to dissolve the vandetanib powder. The pH was adjusted to the desired value by dropwise addition of 1 M NaOH and checked using a calibrated pH meter (Orion Star). Vandetanib precipitate was re-dissolved with the aid of sonication in an ultrasonic bath (Fisher) if necessary. The solution was made up to the final volume with ultra-pure deionised water. The concentration was confirmed by HPLC using the method described in section 2.2.2.1.

2.2.2.3 Drug loading into beads

The desired amounts (settled volume) of DC Bead or DC Bead LUMI were measured using a graduated measuring tube and transferred into glass vials for drug loading. Prior to loading, any packing solution (saline) present was carefully removed from the beads using a glass pipette, leaving only hydrated beads. The appropriate amount of vandetanib solution was added directly into the vials containing the beads. During drug loading, beads were placed on a shaker plate (IKA Basic) at 420 rpm for a minimum of 2 hours. In order to calculate the dose successfully loaded into the beads, the depleted loading solution was collected and the beads were washed 3 times in 5 mL deionised water. The washing solution was collected and combined with the depleted solution, then analysed by HPLC to quantify total unbound drug using the method described in section 2.2.2.1.

2.2.2.4 Bead size determination

Bead size analysis was performed on a sample of beads on a microscope slide using an optical microscope (Olympus BX50) with an attached camera (Colorview III). Images were taken of beads at 4x or 10x magnification depending on bead size range. Stream software (Olympus) had been previously calibrated to convert pixels to micrometres at each magnification, and was used to manually draw horizontal lines across each bead,

n=200 per sample. The line lengths (converted to μm) were exported to Microsoft Excel for data processing.

2.2.2.5 Bead penetration testing

The embolisation model (Figure 2.4) is an in-house benchtop test system developed at Biocompatibles UK, previously described by Lewis *et al.* (2016) [164]. It consists of a specially milled Delrin® base with a shallow gradient, over which a glass plate is secured resulting in an interstitial space whose height decreases gradually. Beads may be injected into the system *via* a Y haemostasis port at the widest end of the taper, which is also supplied with a flow of saline or water from a reservoir of calibrated height that generates a pressure of approximately 40 mmHg, which is equivalent to average pressure in arterioles feeding tumours [168].

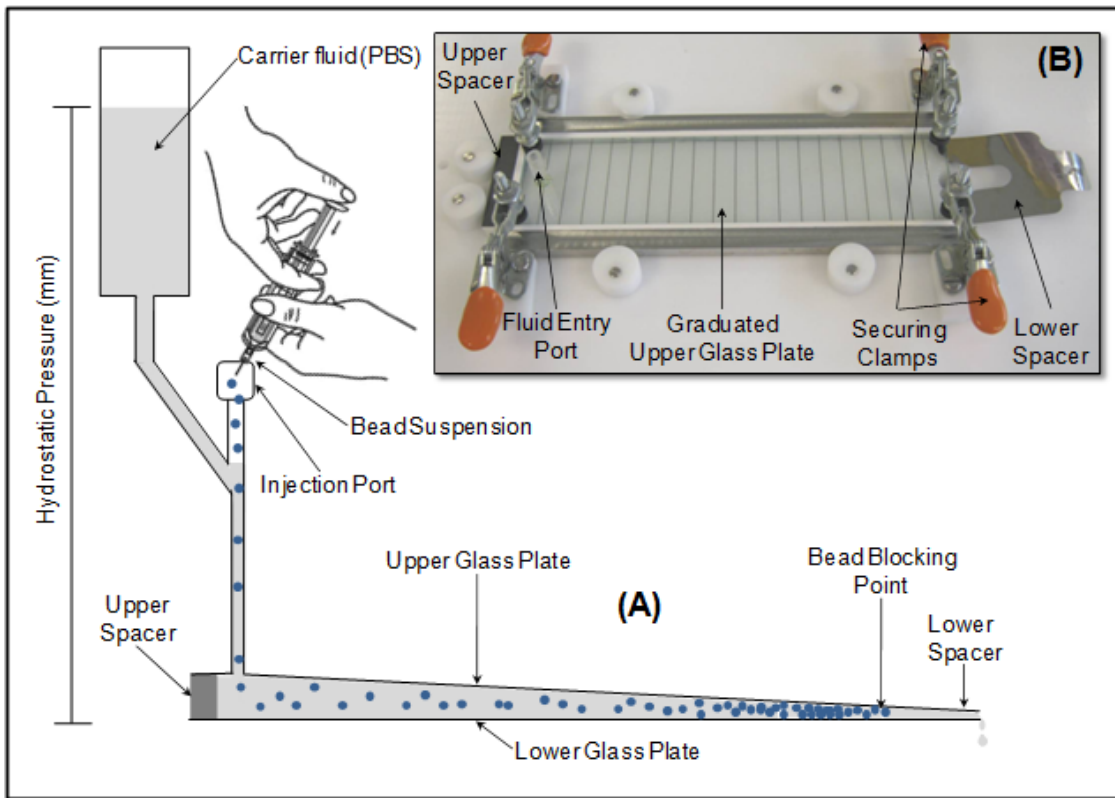


Figure 2.4 The embolisation model. A) Schematic of operation. Flow at a pressure of 40 mmHg is maintained by an elevated reservoir. Interstitial space between the Delrin block and the glass plate ranges from 555 μm to 25 μm . Beads are injected slowly via an injection port and are propelled by flow to a blocking point determined by size and mechanical properties. B) (Inset) General overview of the model.

The purpose of the model is to compare both size range and to a certain extent compressibility of different bead samples. Beads are injected under flow and pass through the model until they are trapped by the decreasing height of the gap. Knowing the gradient of the base, it is possible to calculate the height of the gap in the model at a given distance from the injection point. This was also previously confirmed using incompressible basalt microspheres of known diameter.

The embolisation model was used to compare the penetration efficiency of DC Bead LUMI loaded with vandetanib at different doses (30 mg/mL and 100 mg/mL) to unloaded DC Bead LUMI. Lyophilised product was used in keeping with the final product format selected for *in vivo* models. Beads were hydrated in 5 mL of purified water for 30 minutes. 3 mL of water was then removed and the remaining bead slurry was suspended in 18 mL of Omnipaque 350 contrast agent. 3 mL of bead suspension was transferred into a 3 mL syringe via 3-way connector. With purified water as the flowing phase to avoid drug elution, small amounts of the bead suspension were injected into the embolisation model using an 18G needle. When a clear band of beads was observed in the model, the flow was stopped and the distance was measured of the distal and proximal embolisation endpoints. Two injections were performed for each sample.

2.2.2.6 X-ray Micro-Computer Tomography for radio-opacity analysis

Unloaded LUMI and LUMI loaded with vandetanib at concentrations of 30, 60 and 100 mg/mL were uniformly suspended in 1% agarose solution in nunc tubes. μ -CT 3D scanning was performed to quantify individual bead radiopacity in Hounsfield units (HU) of each bead in the sample (minimum 6000 beads). μ -CT analysis was performed by Reading Scientific Services Ltd., Reading, UK. The full protocol and instrument parameters are detailed in the appendix.

2.2.2.7 Mapping drug distribution – SEM-EDX

Scanning electron microscopy coupled with energy dispersive x-ray spectroscopy (SEM-EDX) was used to map vandetanib distribution in DC Bead LUMI. To prepare beads for analysis, they were embedded in Tissue-Tek optimum cutting temperature compound (Sakura, USA) on liquid nitrogen and transferred to -80°C to ensure thorough freezing. Embedded samples were sectioned in a cryostat (Leica) in 10 μ m thick sections. For SEM, sections were mounted on stubs with carbon pads, then coated with 4nm platinum using a Quorum Q150T turbo molecular-pumped sputter coating

system. SEM imaging was carried out on a Zeiss SIGMA FEG-SEM scanning electron microscope equipped with an Oxford Instruments 80mm² X-Max energy dispersive X-ray analysis system. Elemental mapping and spectra were acquired for iodine, bromine, fluorine and sulfur on radiopaque unloaded beads and radiopaque beads loaded with vandetanib at maximum capacity.

2.2.2.8 FTIR analysis of drug loaded beads

DC Bead LUMI loaded with vandetanib at 15, 30, 45, 60 or 95 mg/mL were embedded and sectioned into 10 µm slices as described in section 2.2.2.7. The sections were mounted on zinc selenide crystal windows. These were subjected to FTIR microscopy point analysis at the centre of 10-15 different beads per sample using a Spotlight 400 FTIR system (Perkin Elmer). The spectra (from 4000-750 cm⁻¹) were collated and the position of the S=O stretching frequency around 1040-1050 cm⁻¹ was averaged for each sample. The effect of differing concentrations of drug loading on the stretching absorption of the sulfonate binding groups on the beads could then be evaluated.

2.2.2.9 Evaluation of suspension, handling and delivery of vandetanib loaded DC Bead LUMI

A series of evaluations were conducted to ensure that loading of vandetanib into the beads did not adversely affect their handling and delivery through a microcatheter. DC Bead LUMI (70-150 µm) was loaded with 100 mg/mL of vandetanib as described in section 2.2.2.3, excess loading solution removed with a glass pipette and the bead slurry (1 mL) mixed with 9 mL of contrast agent (Omnipaque™ 350, GE Healthcare, Oslo, Norway). After transferring into a 20 mL Luer-lok™ syringe (BD Plastipak, Temse, Belgium) a three-way stopcock (Discofix®, B.Braun, Melsungen, Germany) was attached to the syringe and another syringe attached to enable transfer between them to allow suspension of the beads. The beads were then transferred 20 times between two syringes to form a uniform suspension of beads in contrast agent. Suspension time was measured by the time it took for 25 % of the solution to be free from beads, i.e. time taken for the top of the bead suspension to fall to 75 % of the internal height of the syringe (n=3). The suspension was passed through a 2.4 Fr catheter (Progreat®, Terumo Corp., Tokyo, Japan) and the beads assessed visually for any signs of deformation of their shape or presence of fragmentation using optical microscopy as described in section 2.2.2.4.

2.2.2.10 Statistical analysis

Statistical analysis was carried out in Excel, Graphpad Prism, or Minitab. Student's t-test or ANOVA was used to compare groups of normally distributed data, Mann Whitney test was used to compare non-Gaussian data.

2.3 Results

2.3.1 Maximum vandetanib loading capacity in DC Bead and DC Bead LUMI

At acidic pH, positively charged amines on vandetanib molecules interact with negatively charged sulfonate groups within the microsphere hydrogel network, enabling drug loading. From the theoretical prediction shown in Figure 2.1, the major vandetanib microspecies, a 2+ charged form and a 1+ charged form, are predominant at pH 2.1 and pH 6.8 respectively, with a 50:50 proportion of each form predicted at pH 4.4. Vandetanib solutions were prepared at each of these pHs and added to beads in excess to assess the effect on maximum loading capacity.

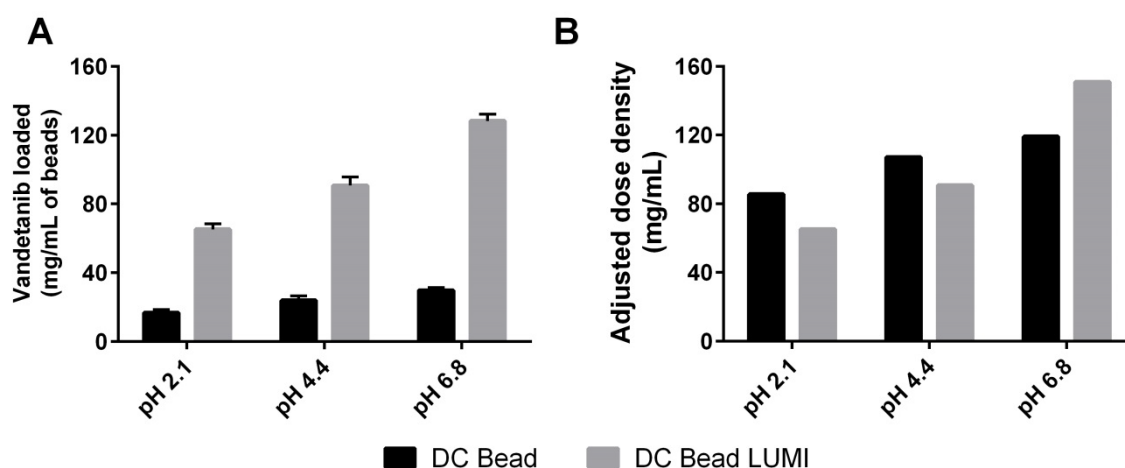


Figure 2.5 Maximum vandetanib loading capacity of DC Bead (black bars) and DC Bead LUMI (grey bars). A) Amount of vandetanib loaded into 1 mL of beads (starting volume) Mean \pm SD, N=5; B) Mean vandetanib dose density (mg/mL of beads) after adjustment for loading-induced bead volume changes.

Maximum vandetanib capacity increased with pH (proportion of 1+ form) as expected, with maximum capacity at 30 mg/mL for DC Bead and 135 mg/mL for DC Bead LUMI (Figure 2.5). Initial analysis of depleted loading solution from DC Bead showed a higher than expected loading efficiency, but with subsequent washes in water the actual loading dose was found to be lower suggesting that some drug was weakly associated with the bead surface and able to be removed with water. This effect was less pronounced with DC Bead LUMI. Below maximum capacity, a loading efficiency of >

99 % was achieved after 2 hours of incubation with loading solution suggesting fast adsorption of vandetanib into beads. <0.5% of the dose was recovered in water washing steps suggesting efficient binding below maximum capacity. When considering the respective chemical compositions of both beads, the theoretical maximum loading capacity based upon the content of sulfonic acid drug binding residues is higher for both DC Bead and DC Bead LUMI than the actual experimentally determined maximum drug binding capacity. For DC Bead, the maximum amount of drug loaded varied from 81-91.2 % of the theoretical, compared to 74.5-80.4 % for DC Bead LUMI, both dependent upon the pH of the loading solution (Table 2.4).

Table 2.4 Comparison of theoretical and experimental vandetanib maximum loading capacity (max. cap.) for DC Bead and DC Bead LUMI. Estimated binding site occupation = experimental / theoretical max. cap. %

pH	DC Bead			DC Bead LUMI		
	Theoretical max. cap. (mg/mL)	Experimental max. cap. (mg/mL)	Estimated binding site occupation (%)	Theoretical max. cap. (mg/mL)	Experimental max. cap. (mg/mL)	Estimated binding site occupation (%)
2.1	18.4	16.8	91	81.2	65.3	80
4.4	27.6	23.9	87	121.9	90.8	74
6.8	37	29.8	81	162.5	128.4	79

2.3.2 Effect of vandetanib loading on bead size and morphology

After loading with vandetanib, beads retained a smooth, spherical appearance (Figure 2.6). Average bead diameters before and after loading are displayed in Table 2.5. Loading DC Bead at maximum vandetanib capacity caused a significant decrease in mean diameter of 35 % (Mann Whitney test, $p < 0.0001$) as well as a narrowing of the size distribution (Figure 2.7). The size reduction corresponded with a reduction in settled bead volume of over 60 %. The size decrease showed a trend with decreasing pH, resulting in beads loaded at pH 2.1 being significantly smaller than beads loaded at pH 6.8 (Mann Whitney test, $p < 0.0001$). In contrast, the mean diameter of DC Bead LUMI loaded at maximum capacity did not significantly decrease at any pH (Figure 2.7), despite a 15 % reduction in the settled bead volume at pH 6.8 only.

Table 2.5 Average bead diameters (μm) and standard deviation of the mean of DC Bead and DC Bead LUMI before and after loading with maximum capacity of vandetanib. p value denotes outcome of Mann Whitney test between diameter of unloaded beads and loaded beads, n = 200 per sample.

	DC Bead diameter (μm)				DC Bead LUMI diameter (μm)			
	Unloaded	pH 2.1	pH 4.4	pH 6.8	Unloaded	pH 2.1	pH 4.4	pH 6.8
Median	121.8	75.1	79.5	83.6	100.9	105.6	106.3	99.5
Mean	122.4	77.2	80.2	83.1	102.5	104.4	107	101
Standard deviation	18.8	12.4	11.2	10.5	17.3	17.1	16	15.57
p value	-	<0.0001	<0.0001	<0.0001	-	0.438	0.021	>0.999

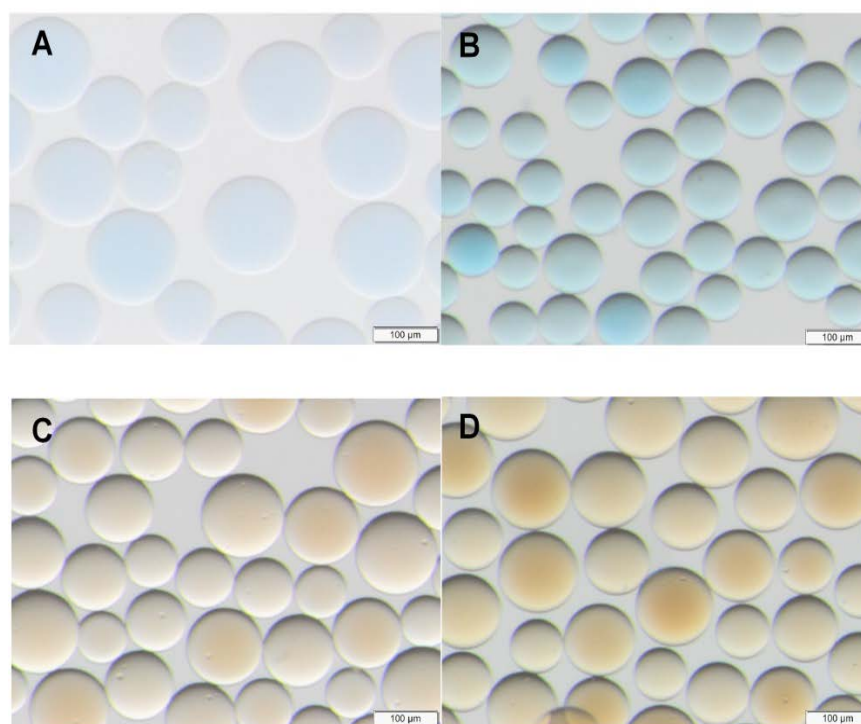


Figure 2.6 DC Bead (70-150 μm) before (A) and after (B) loading with 30 mg/mL vandetanib; DC Bead LUMI (70-150 μm) before (C) and after (D) loading with 100 mg/mL vandetanib. Scale bars 100 μm . Original in colour.

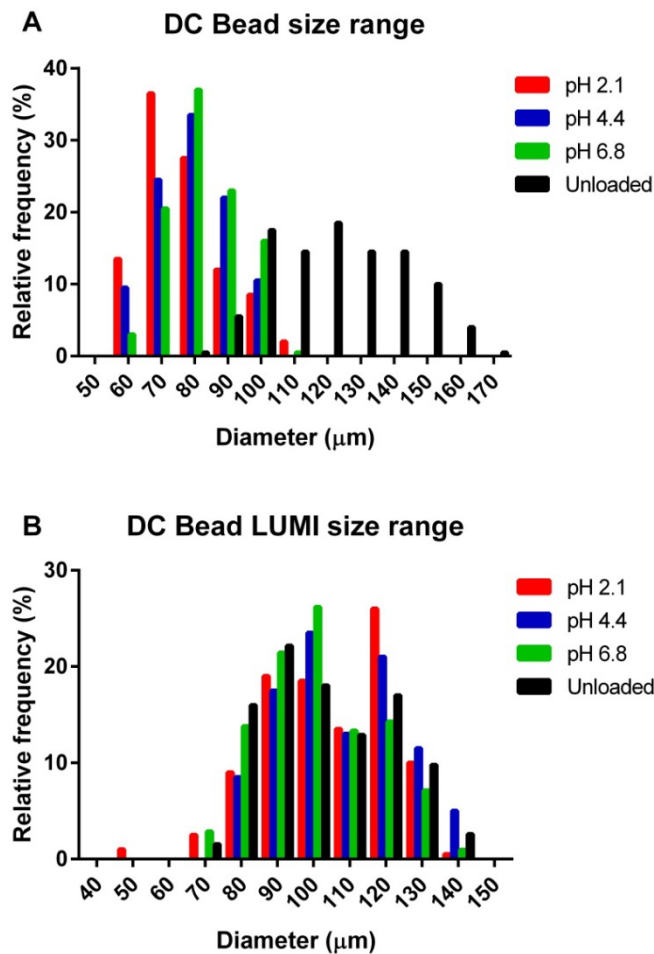


Figure 2.7 Frequency histograms of A) DC Bead and B) DC Bead LUMI size range after maximum vandetanib loading at various pH. N=200 beads per sample. Original in colour.

2.3.3 Bead penetration testing

Unloaded DC Bead LUMI, and LUMI loaded with vandetanib at 30 or 100 mg/mL were assessed for penetration distance in the embolisation model. Unloaded beads and 30 mg/mL vandetanib beads had a similar penetration range, whereas 100 mg/mL beads penetrated slightly further in the model (Figure 2.8). This is consistent with a slight decrease in size of DC Bead LUMI when loaded at a 100mg/mL dose (range, 60-130 μm). A representative image of beads in the model is shown in supplementary Figure S1.

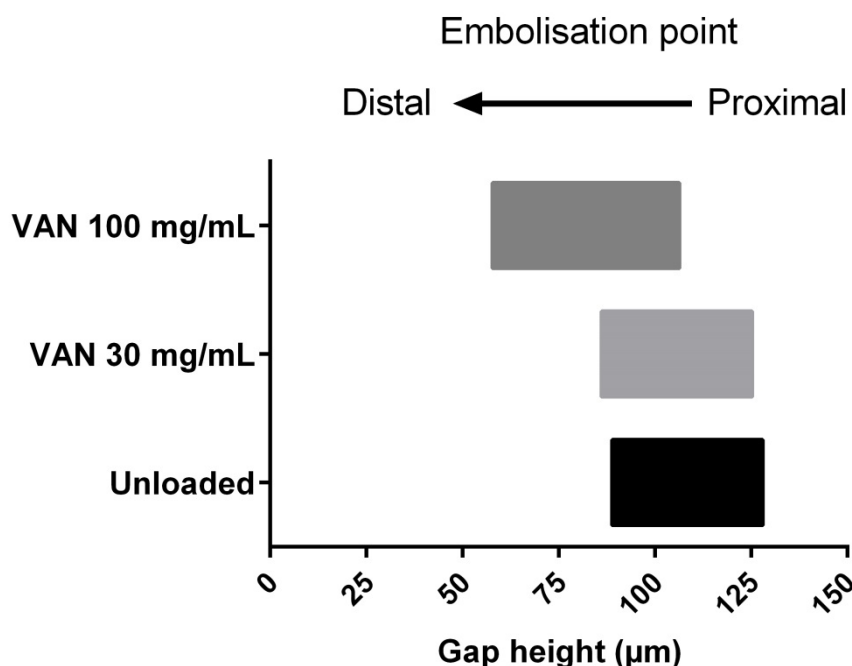


Figure 2.8 DC Bead LUMI penetration distance in the embolisation model. Unloaded beads and beads loaded with 30 or 100 mg/mL vandetanib were injected between two glass plates of decreasing gap height under hydrostatic pressure. The gap height was recorded at the stopping point of the front edge of the beads (distal embolisation point) and the rear edge (proximal embolisation point). Bars represent the range of the bead distribution (average of 2 injections per sample).

2.3.4 Vandetanib distribution within beads

Attempts to analyse vandetanib distribution in DC Bead LUMI by FTIR were not validated due to deformation of bead sections during analysis leading to ‘edge-effect’ artefacts (see Figure 2.9). Dehydration of the sample over time led the edges of bead sections to curl inwards, which would have given a false intensity of any drug related signal in this area due to increased density. Several approaches were taken in an attempt to prevent bead shrinkage, including coating slides in poly-L-lysine to promote adhesion, quick freezing in liquid N₂ vs gradual freezing, varying bead size or section thickness, and passing water vapour over the section during analysis, but unfortunately none were successful. Therefore, the technique of SEM-EDX was used to study drug distribution.

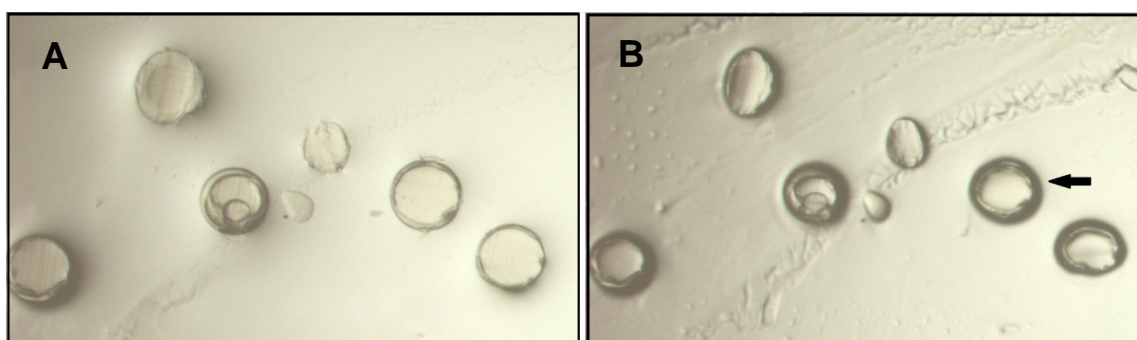


Figure 2.9 Optical micrographs of sectioned DC Bead LUMI in OCT compound. A) Shortly after sectioning, B) the same beads within minutes after sectioning demonstrating curling of bead edges (black arrow).

Scanning electron microscopy showed the sectioned internal structure of DC Bead LUMI to be homogeneous and devoid of any visible pores (Figure 2.10 (a)). SEM-EDX analysis was used to detect vandetanib distribution in sectioned sample loaded at maximum capacity of 135 mg/mL. Bromine was selected as the element of interest for the drug distribution, being present in vandetanib molecules but not in DC Bead LUMI. The sulfur and iodine distributions were also mapped to gain insight into the bead internal structure. Elemental mapping revealed that bromine was evenly distributed throughout the sectioned beads (Figure 2.7(b)), the bromine peak seen in the EDX spectrum (arrow, Figure 2.7(e)) being absent in the spectrum for control (unloaded) beads (supplementary Figure S1). Sulfur and iodine distributions also appeared to be evenly distributed within the bead structure (Figure 2.7(c) and (d)). The table insert in Figure 2.7(e) shows there is an excellent agreement between the measured weight percent of elements by EDX compared with the theoretical calculated weight percentage expected based upon 135 mg/mL loading of vandetanib into DC Bead LUMI, the latter which possesses 177 mg/mL iodine [70].

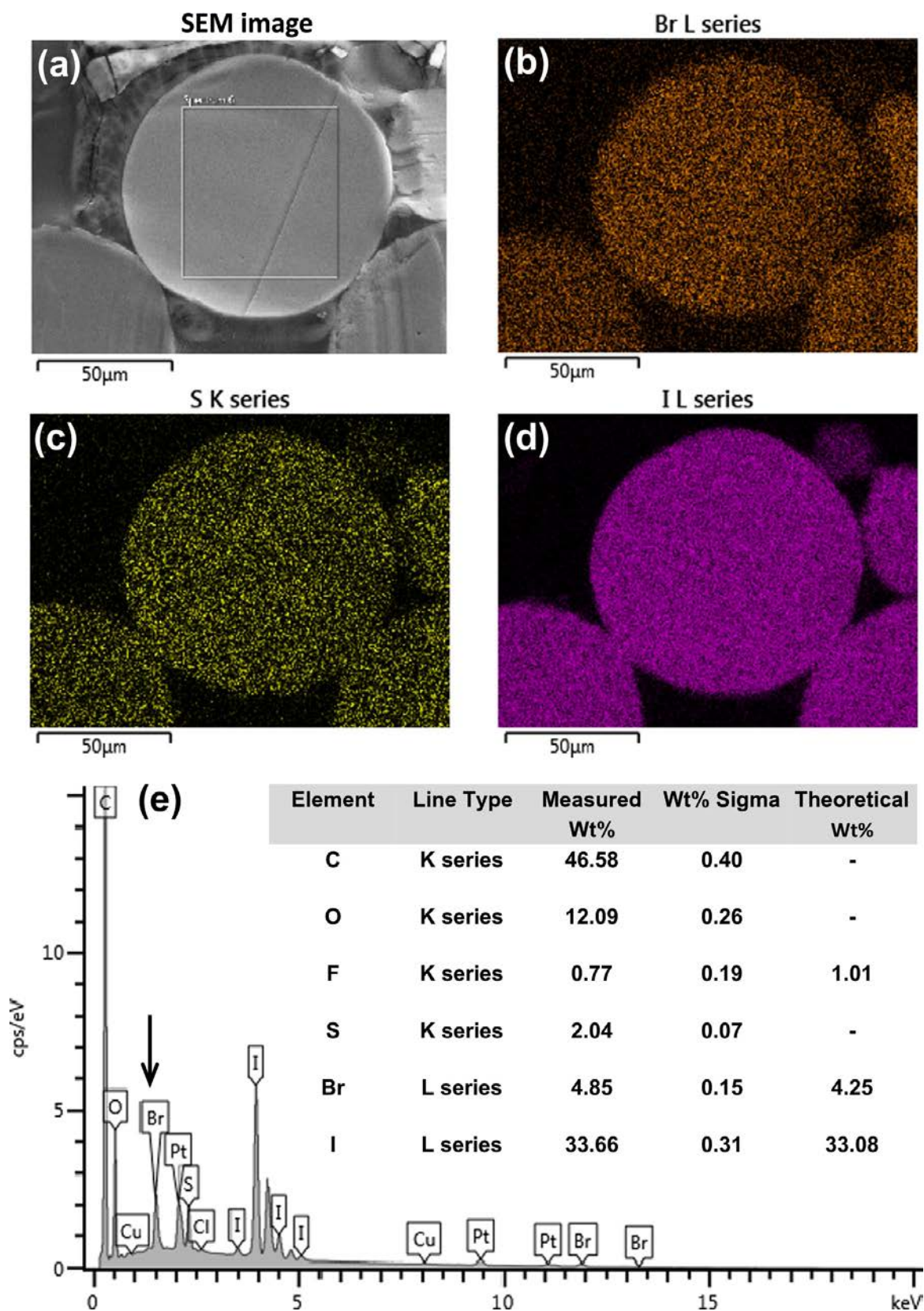


Figure 2.10 (a) Scanning electron microscopy image of a sectioned vandetanib-loaded DC Bead LUMI sample; (b) bromine elemental mapping distribution image; (c) sulfur elemental mapping distribution image; (d) iodine elemental mapping distribution image; (e) EDX elemental spectrum showing bromine peak for the vandetanib loaded bead and elemental analysis (table inset). Original in colour.

2.3.5 Evaluation of drug-bead interactions using FTIR spectroscopy

FTIR spectroscopy was used to investigate the interaction between vandetanib and DC Bead LUMI. As the dose of vandetanib loaded into DC Bead LUMI was increased, the frequency of the S=O stretch from the sulfonate groups of the beads was seen to shift steadily to lower wavenumber (Figure 2.11). This is indicative of an increasing interaction between drug and bead as all of the bead binding sites become progressively occupied. Samples loaded using a target loading of 60 mg/mL at pH 6.8, 4.4 and 2.1 gave rise to similar S=O stretching frequencies at 1041.6 cm⁻¹, 1040.3 cm⁻¹ and 1040.4 cm⁻¹ respectively.

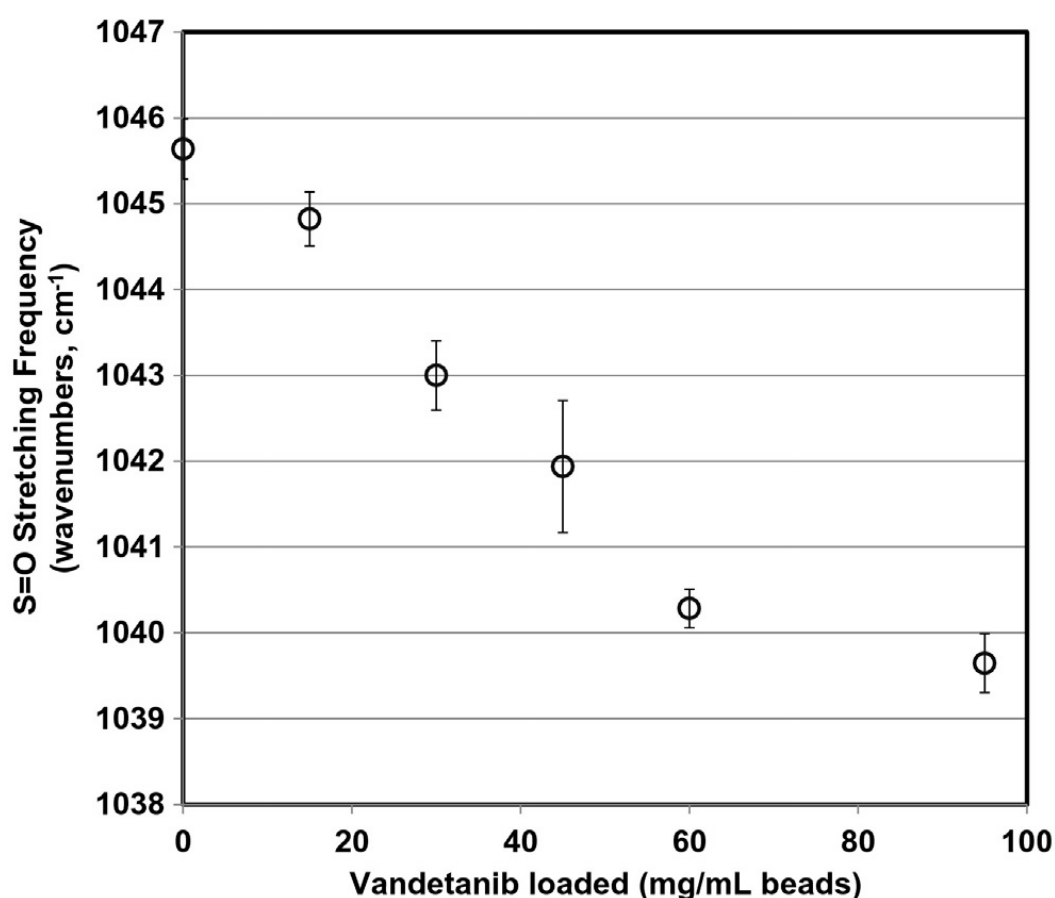


Figure 2.11 Effect of vandetanib loading dose on the S=O stretching frequency from bead sulfonate groups as determined by FTIR spectroscopy. Mean of at least 10 beads per sample \pm SEM.

2.3.6 Radio-opacity of vandetanib loaded beads

Micro-CT analysis of DC Bead LUMI shows it to possess an inherent radiopacity due to the triiodobenzyl moieties attached to the bead structure [70], giving rise to a baseline radiopacity of 4454 ± 225 Hounsfield Units. The level of radiopacity is seen to increase

linearly with increasing loading of vandetanib into the beads (Figure 2.12) until at a loading of 100 mg/mL of vandetanib, the radiopacity is seen to have increased by 621 Hounsfield Units.

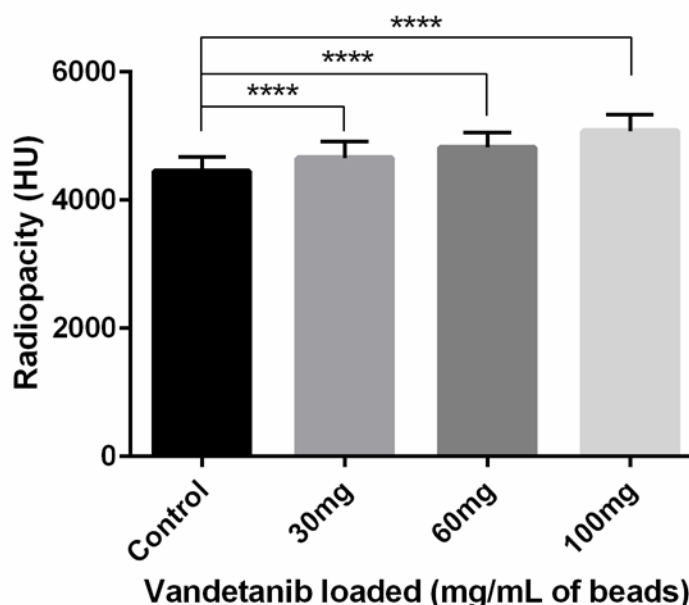


Figure 2.12 Effect of vandetanib loading into DC Bead LUMI on radiopacity of the beads. μ -CT 3D scanning was performed to quantify individual bead radiopacity in Hounsfield units (HU) of beads suspended in agarose. Bars represent mean of all beads in a single scan of the sample (>6000 beads per sample) \pm SD. **** = $p < 0.0001$ by 1 way ANOVA + Holm-Sidak's multiple comparisons test between doses.

2.3.7 Suspension, handling and delivery of vandetanib loaded DC Bead LUMI

When DC Bead LUMI loaded with 100 mg of vandetanib was suspended in Omnipaque 350 (section 2.2.2.8) the beads formed a uniform suspension and showed no signs of bead agglomeration. The bead suspension did not adhere onto the surface of the vial and was easily transferred into a syringe for delivery. The average time in suspension within the syringe was >6.5 mins which is more than sufficient for practical usage. The bead suspension was delivered through a 2.4 Fr microcatheter with ease and there was no occurrence of catheter blockage during bead delivery. The beads remained spherical with no signs of fragmentation post-delivery (Supplementary Figure S3).

2.4 Discussion

Drug candidates that have been loaded into DC Bead have conventionally been water soluble cationic salt forms that allow for diffusion and ion-exchange into the anionically-charged hydrogel matrix of the bead [137, 149, 150, 169, 170]. MTKIs represent a group of small molecules with widely differing structures that impact drug solubility, lipophilicity and ionization potential. Different process strategies may therefore be required when considering how to load sufficient amounts of these compounds in an efficient way into the bead matrix, and subsequently what intermolecular drug-bead interactions will control the release of the molecule.

2.4.1 Influence of vandetanib charge states on bead properties

Vandetanib is prepared in acidic solution in order to solubilise the drug for DEB loading. Based on the theoretical ionisation of vandetanib in solution at different pH (Figure 2.1) and therefore the relative concentrations of different vandetanib charge forms, the drug loading maximum capacity should be influenced by the pH of the loading solution, which was confirmed in this study (Figure 2.5). For both DC Bead and DC Bead LUMI, there was a positive relationship between pH of the loading solution and the maximum amount of vandetanib that could be loaded into the beads. This is due to the fact that as pH decreases, a greater proportion of vandetanib molecules in solution have 2 positive charges, and can therefore occupy 2 sulfonate binding sites within the beads, shifting towards a 2:1 binding ratio. This reduction in availability of sulfonate groups results in a reduced maximum loading capacity at low pH.

This effect also played a role in bead morphology. Shrinkage upon loading is expected as a consequence of water displacement and would usually be correlated with the loaded dose. However, when DC Bead was loaded with excess vandetanib, beads loaded at pH 2.1 had a significantly smaller median diameter than those loaded at pH 6.8, despite containing less vandetanib. This is in keeping with previously observed effects of loading mitoxantrone, which has 2 positively charged sites, and thus exerts an increased shrinking effect on DC Bead which is suggested to be an effect of contraction of the hydrogel network by interacting with multiple sites [39].

The drug-bead charge-charge interaction through the sulfonate groups was confirmed by the shift of the S=O stretching frequency to lower wavenumber with increasing drug dose, a phenomenon also observed for both doxorubicin and irinotecan binding to DC

Bead [152, 171, 172]. Interestingly, when 60 mg/mL loading was performed at pH 2.1, 4.4 and 6.8, the S=O frequency was seen not to change significantly, even though at this dose DC Bead LUMI is only at about 50% binding capacity. At pH 2.1, the second charge residing on the quinazoline ring system would not be expected to interact as strongly as that on the piperidine ring as indicated by the lack of change in the S=O stretching frequency.

2.4.2 Prototype selection – radiopaque or non-radiopaque?

Initially both DC Bead and DC Bead LUMI were considered as candidate platforms for a vandetanib DEB. DC Bead is widely used and information and experience about its use in chemoembolisation is well documented in the literature giving a good understanding of the platform [173]. However, there are some limitations of using DC Bead to create a preloaded DEB product. DC Bead had a lower maximum capacity than DC Bead LUMI, but significant bead shrinkage upon drug loading lead to a high final dose density. Between 13.5 and 34 % of vandetanib loaded DC Beads were below 70 μm in diameter, which would not meet specification for a 70-150 μm product, whereas > 98 % of LUMI beads fell within the 70-150 μm diameter range. Fatal pulmonary embolisms have been previously reported as a result of off target embolisation with 40-120 μm microspheres [166], so having a large proportion of small microspheres may represent a safety concern. To account for bead shrinkage, the volume of starting material for DC Bead would need to be at least double that of DC Bead LUMI to produce an equivalently dosed product, making the process somewhat inefficient. DC Bead LUMI proved to be largely resistant to loading induced size changes regardless of dose or pH, leading to a predictable loading process.

In terms of handling, DC Bead LUMI is denser and less compressible than DC Bead, however this has not been shown to negatively impact ease of use [38]. The higher density of LUMI necessitates suspension in pure contrast agent rather than the 50:50 contrast/water mix traditionally used for DC Bead, but similar suspension times are achieved for both products [36, 38].

Basic comparative *in vitro* drug release evaluation between DC Bead and DC Bead LUMI was also performed during the optimisation phase of vandetanib DEB development, which will be discussed in depth in the following chapter. Considering the existing advantages discussed for the radiopaque platform, including improved intra and

post procedural feedback [38, 174, 175], it was decided that this platform would be taken forward for the development of the vandetanib DEB.

2.4.3 *Properties of radiopaque vandetanib beads*

The data presented in this study has confirmed that DC Bead LUMI has desirable physicochemical characteristics suitable for use as a DEB delivering an anti-angiogenic compound. Firstly, maximum vandetanib loading capacity is high, reaching maximum doses of 135 mg/mL at pH 6.8 and even when decreasing pH to maintain vandetanib solubility doses of 100 mg/mL are still feasible. The oral dose that showed an improvement in overall survival in a Phase 2 trial on advanced HCC was 100 mg per day [93]. With the localised release made possible with DEB, this drug dose should in theory be sufficient to reach therapeutic concentrations within the liver, and retreatment with subsequent doses of vandetanib beads is possible with reduced risk of systemic exposure.

SEM-EDX elemental mapping of bromine revealed that vandetanib appeared to be evenly distributed throughout the bead structure, showing homogenous loading. In theory, this should promote controlled release of the drug, *via* gradual diffusion of vandetanib molecules from the centre of the beads. It would be of interest to repeat the elemental mapping periodically throughout the drug release process to confirm if drug remains homogeneously distributed (film diffusion control) or forms a concentration gradient from the centre (internal depletion layer model) [176]. However, this may require use of a more sensitive detection method as it was only possible to detect bromine from vandetanib in maximally loaded bead samples by SEM-EDX.

In terms of vandetanib bead imageability, increasing loading of vandetanib also leads to a proportional increase in the radiopacity of the DC Bead LUMI (Figure 2.12) which is not attributable to a densification of the internal structure as the mean diameter of the beads are essentially unchanged with drug loading (Figure 2.7). The existence of a bromine atom on the vandetanib structure is the likely source of the added radiopacity [177], which increases by approximately 25-26 Hounsfield units per mg of radiodense atom (iodine and bromine) present.

The handling properties of the radiopaque vandetanib beads were evaluated and found to be suitable for its use as an embolic agent, having a suspension time of over 5 minutes in Omnipaque 350 contrast agent and no instances of catheter blockage.

Evaluation in alternative contrast agent formulations will be necessary in the future to confirm compatibility. Structural integrity was maintained throughout the suspension and delivery process; the beads remained spherical with no signs of fragmentation. The effect of vandetanib loading on bead compressibility was not directly measured with a nanoindentation system, however the embolisation model showed that bead penetration distance was not decreased with drug loading inferring a similar compressibility. In fact, 100 mg/mL beads penetrated slightly further in the model than unloaded beads, which rather than being due to increased compressibility is more likely to be due to a slight decrease in size range in vandetanib beads that had been previously lyophilised, gamma sterilised and rehydrated, in keeping with preparation protocols for *in vivo* studies. The effect of this sterilisation method on other final product properties has not been discussed in this thesis, but has since been shown to be minimal (Biocompatibles unpublished data).

2.5 Conclusion

The data presented in this chapter together with clinical trends have guided the development of the final vandetanib DEB product in terms of its chemistry, preparation, dose and size range. Optimisation of the loading process and the final dose density of the product were performed by gradually increasing the pH of the loading solution to increase the proportion of singly charged vandetanib molecules, until the solution was no longer stable. By this method, an optimum pH range was selected of 4.6-4.8. Knowing the maximum loading capacity of DC Bead LUMI in this range, a target dose of 100 mg/mL was selected. The size range selected for the product is 60-160 μm . This is in following with current trends in DEB-TACE as previously mentioned and positive clinical experience with smaller bead sizes, including improved rates of complete response [178] and favourable safety profile [179]. More distal tumour penetration of vandetanib DEB is desirable for optimum tumour coverage of the drug.

DC Bead LUMI can be efficiently loaded with vandetanib whilst maintaining bead integrity and properties suitable for use as an embolisation agent, which warrants its further characterisation as an anti-angiogenic DEB.

2.6 Supplementary figures

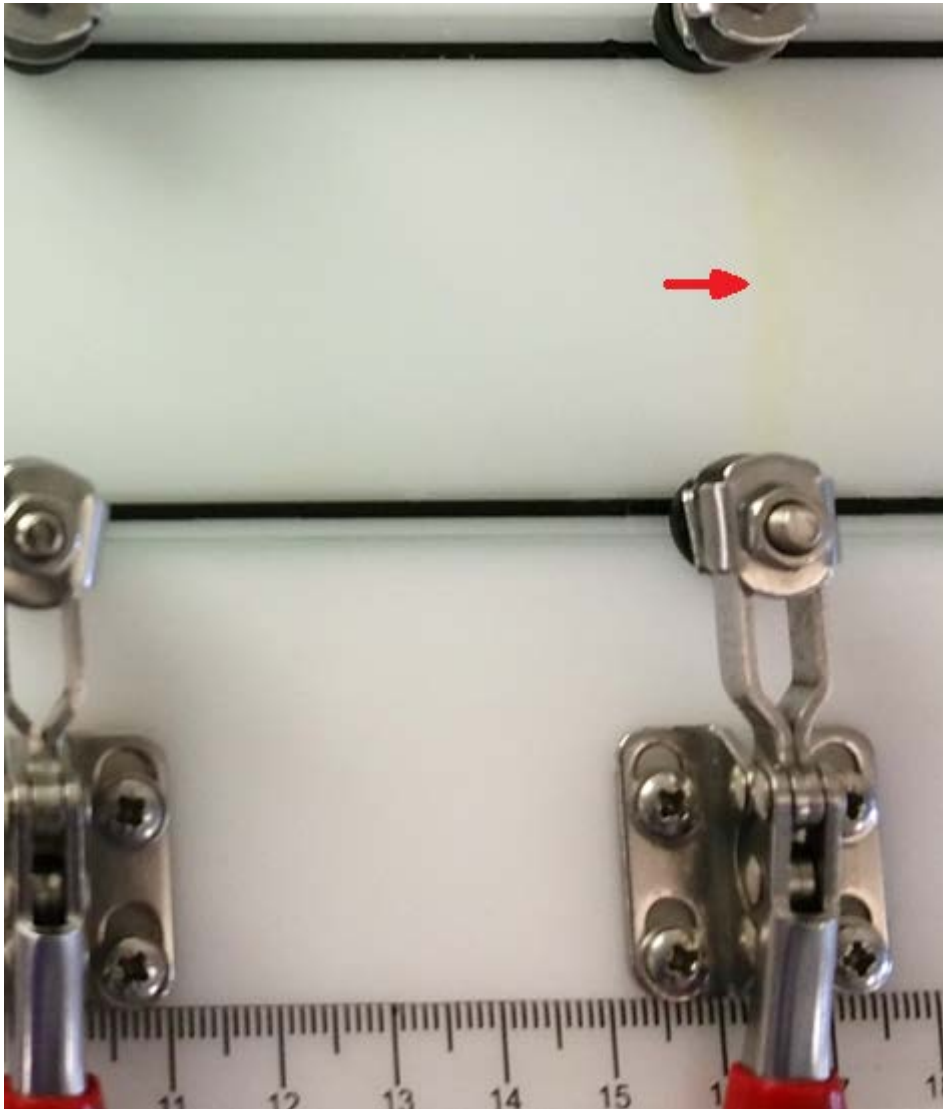


Figure S 1 Vandetanib loaded DC Bead LUMI in the embolisation model. The beige coloured beads are faintly visible as a band (red arrow). Future versions of the embolisation model may be crafted with black material to aid contrast with radiopaque beads, which lack a brightly coloured dye. Original in colour.

Unloaded DC Bead LUMI SEM-EDX

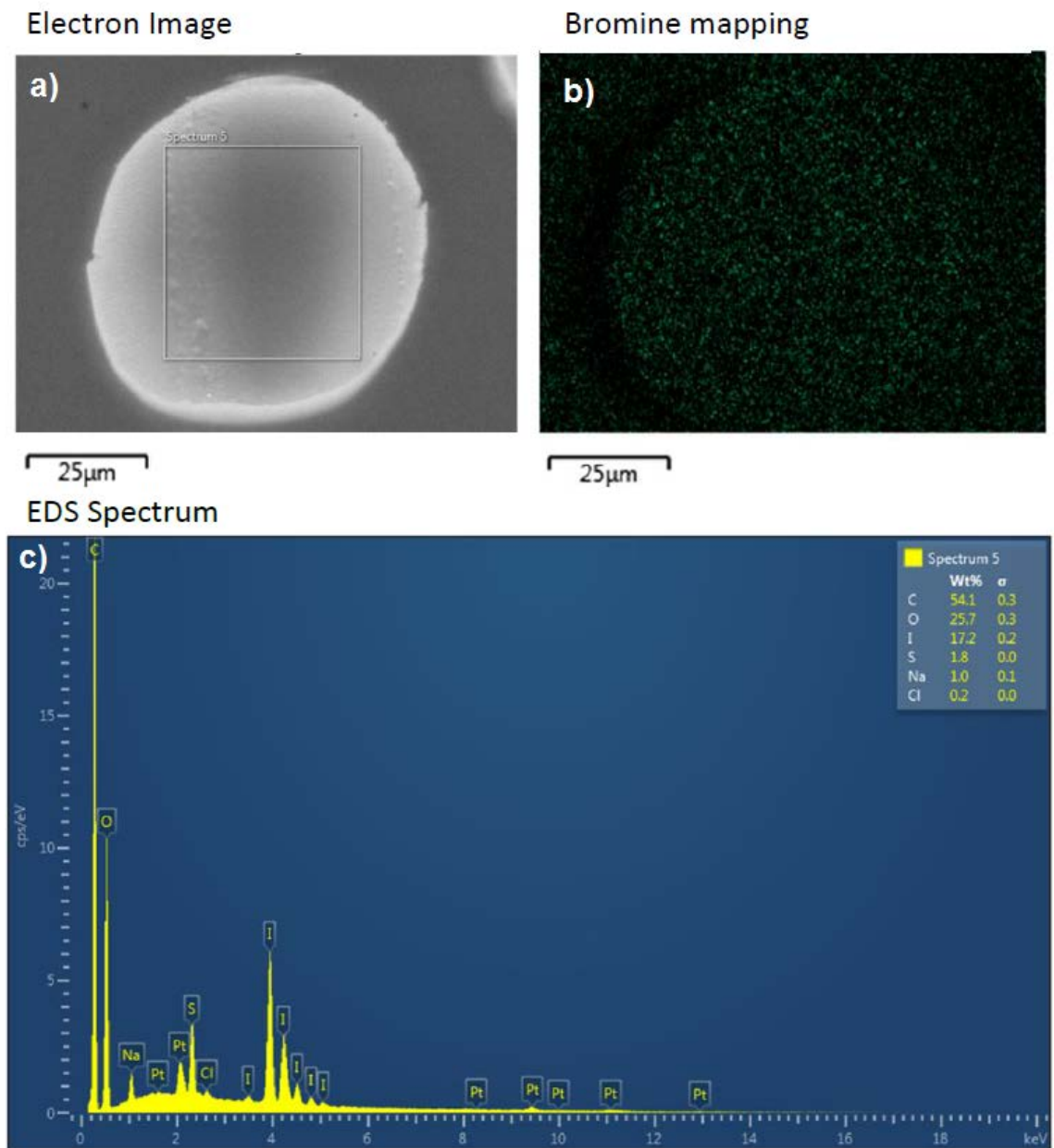


Figure S 2 SEM-EDX analysis of unloaded DC Bead LUMI. A) Electron microscopy image of bead section showing region of interest for EDX spectrum. B) Elemental analysis of bromine distribution showed some background signal. C) EDX spectrum for unloaded beads, showing absence of bromine peak. Original in colour.

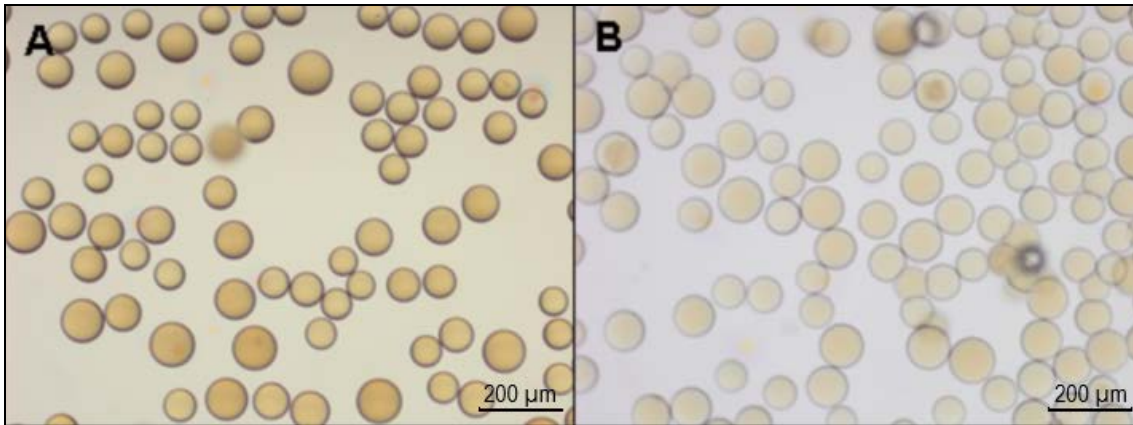


Figure S 3 Vandetanib loaded radiopaque beads (100 mg/mL) A) Before handling B) After contrast suspension and delivery through a 2.4 Fr catheter as detailed in section 2.2.2.9. Beads remain intact and spherical after delivery. Original in colour.

3 CHAPTER THREE: EVALUATION AND COMPARISON OF *IN VITRO* MODELS OF DRUG RELEASE FROM BEADS

3.1 Introduction

3.1.1 Modelling drug release from DEB in vitro

Chapter 711 of the United States Pharmacopeial convention provides guidance on standardised methods to provide information about drug release from oral dosage forms, such as the USP II or IV dissolution apparatus. However, as yet no standardised *in vitro* method exists for determining drug release from parenteral dosage forms such as drug-eluting beads. The drug release profile from DEB has implications in both the safety and efficacy of the product, and yet remains one of the most difficult aspects to model *in vitro* in a representative manner. A single centre, randomised trial comparing doxorubicin loaded beads with bland beads for embolisation treatment of 92 HCC patients recently reported no significant benefit in overall survival when adding doxorubicin [180]. The study sparked debate in the interventional radiology community as to the robustness of the findings, due to a small patient population and heterogeneity of patients in terms of previous treatments and disease stage [181]. However, it remains necessary to elucidate potential reasons for ambiguity in the treatment benefit of chemo-embolisation, whether it be a poor choice of drug (doxorubicin) [182] or an incomplete or slow release of drug from beads *in vivo* leading to sub-clinical concentrations of drug reaching tumour cells as has been previously suggested [138].

Drug release from DC Bead and DC Bead LUMI is based on ion exchange [183]. Upon contact with biological fluids, small cations exchange with the positively charged drug molecules in the microsphere matrix. The rate controlling mechanisms for different drugs, for example doxorubicin and irinotecan, have been found to vary based on differing molecular interactions between drug and bead [184], which explains differences in release rates observed *in vitro* and *in vivo*. Figure 3.1 shows the appearance of DC Bead LUMI after loading with each drug, and their chemical structures. Doxorubicin binds via a primary amine group, which is expected to interact

more strongly with the beads than irinotecan's tertiary amine. As discussed in chapter 2, vandetanib possesses two potential binding sites, which affects drug loading capacity in DEB and may affect drug release rate. Detailed investigation and modelling on release mechanisms has not as yet been carried out on the radiopaque DC Bead LUMI, whose increased hydrophobicity and solid content have been shown to slightly retard drug release compared with standard DC Bead [38]. Determining the mechanism and kinetics of release of the candidate compound, vandetanib, from DC Bead and DC Bead LUMI will aid in predicting *in vivo* pharmacokinetic behaviour under varied hydrodynamic conditions.

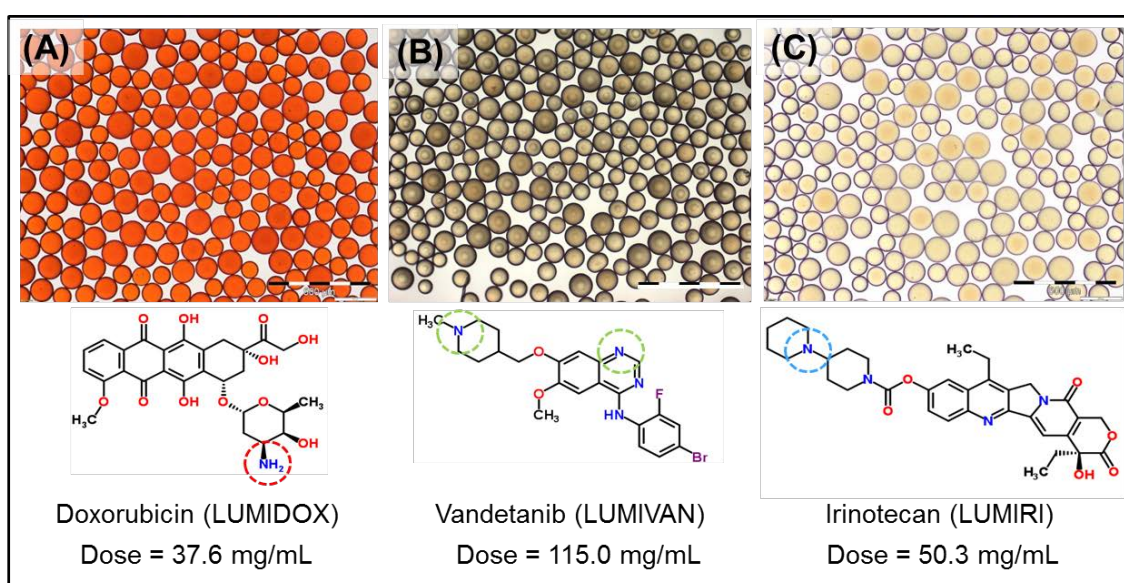


Figure 3.1 Optical micrographs of DC Bead LUMI loaded with A) doxorubicin, B) vandetanib and C) irinotecan, and their respective chemical structures. Circled amine groups represent ionic bead-binding sites for each drug. Scale bar = 500 μ m. Original in colour.

In vitro DEB release models were the topic of a paper investigating DC Bead loaded with sunitinib seeking to compare *in vitro* release with *in vivo* pharmacokinetic data [78]. The findings that not one *in vitro* model corresponded perfectly to the *in vivo* situation points to the fact that drug release from DEB during TACE is a multiphasic process (Figure 3.2). Many *in vitro* elution set-ups begin with a ‘pre-occluded system’ representing the post administration phase of DEB-TACE, which does not account for the drug that may be released during the delivery phase. The beads must be mixed with contrast agent before delivery, which in itself can induce a small degree of drug elution from the surface layers of the beads. The bead/contrast suspension is then slowly delivered in small bursts at a rate of around 1mL of suspension per minute in order that

the beads are carried by the blood into the high flow areas (normally the tumour when it is hypervascular in nature) and distribute into the distal arterioles without premature proximal blockage (phase 1). If the drug-bead interaction is weak there may be a burst of drug release during this phase as the beads are surrounded by ion-rich blood which is an effective medium for the sequestration of drug. Beads will fill vessels distally and compact until they form a cast within the vessel architecture and flow between and around the beads is slowed to near stasis (phase 2). Finally the stagnated blood between the beads will eventually clot to form an occlusive mass, and ions from the surrounding tissues will diffuse into the mass and exchange for the drug bound to the bead reservoirs, leaving the drug to diffuse into the surrounding tissues by mass transfer (phase 3).

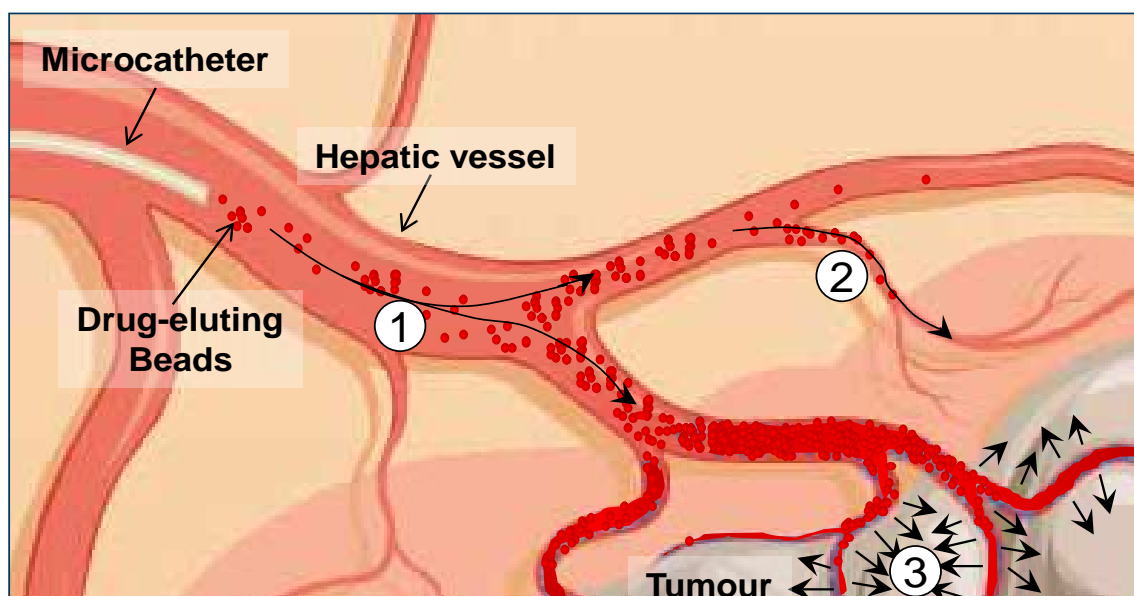


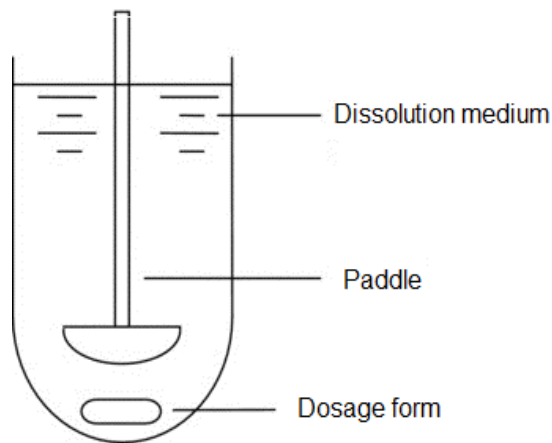
Figure 3.2 Phases of the embolization process from leaving the catheter and free flowing in the blood stream (1) to distribution and bead compaction into the tumour arteriole network (2), to formation of an occlusive mass, with near blood stasis and longer-term drug diffusion from the beads, through the vessels and into the tumour and surrounding parenchyma (3). Original in colour.

3.1.2 Existing models for measuring *in vitro* drug release from DEB

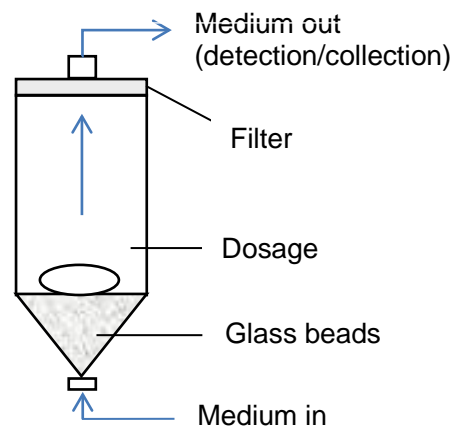
The most commonly used methods for evaluating drug release from microspheres are systems based on USP apparatus, namely USP II (paddle) and USP IV (flow through cell) types. Figure 3.3 displays schematic diagrams of each apparatus. DEBs are placed in vessels containing an elution medium, usually PBS, which is sampled periodically and drug content quantified by UV spectroscopy or HPLC. In USP II type apparatus, beads are free flowing, and therefore drug release is rapid. Full drug release may be

limited by the elution medium becoming saturated, which can be avoided by using pseudo-sink conditions, e.g. replacing saturated medium periodically with fresh medium. This method has little similarity in terms of hydrodynamics to the *in vivo* situation, therefore the release profile is unlikely to correlate well with pharmacokinetic data. In USP IV flow through cells, beads are not stirred and rest on top of a layer of glass beads, which create laminar flow. Flow of elution medium is not restricted, leading to similar release profiles to USP II type apparatus [78]. These methods are capable of discriminating between different bead chemistries, sizes and drug types, and are useful in a quality control setting to test batch to batch uniformity.

A) USP II - Paddle



B) USP IV - Flow through cell



cell

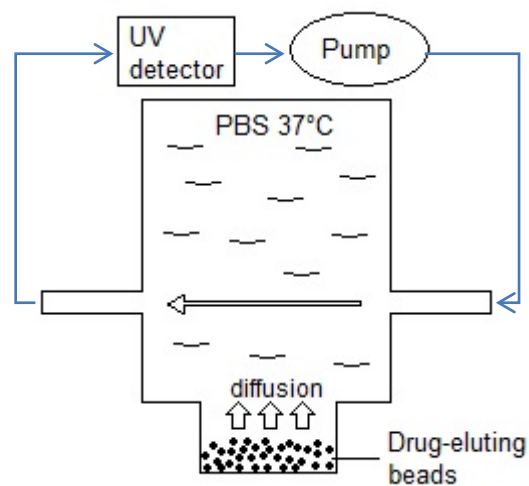


Figure 3.3 *In vitro* set-ups for modelling drug release from DEB. A) USP II, B) USP IV and C) T cell dissolution apparatus.

Attempts at improving *in vitro in vivo* correlation (IVIVC) for DEB release models have led to the conception of the T cell method (Figure 3.3C) [185-187] whereby beads are

contained in a reservoir at the base of a 'T' apparatus and as such are not directly exposed to the flowing phase of medium, instead, the drug release is more diffusion based, with the flow of medium above also creating a convection zone that mimics distant blood vessels. With this method, level A IVIVC was achieved with clinical doxorubicin-loaded DC Bead (DEBDOX) pharmacokinetic data, however this was only for the first 24 hours post-embolisation. Indeed, DEBDOX clinical data show that doxorubicin in plasma is at very low levels at 24 hours post embolisation [41] after which it is expected that release occurs primarily through diffusion into the target liver tissue. Swaine *et al.* (2016) have recently described a flow through method that has been adapted to mimic tight packing of beads in a blood vessel, with a very low (0.1 mL/ min) flow rate, which may enable closer correlation with phase 2 of drug release [188].

As plasma drug levels are not representative of actual drug release from DEB in the final phase (phase 3), drug concentration in the target tissue following DEB-TACE *in vivo* may be estimated by homogenising tissue samples and subjecting them to analytical techniques such as liquid chromatography - mass spectrometry (LC-MS), but results are usually heterogeneous and are limited in their accuracy due to the difficulty of distinguishing between true tissue drug concentrations and drug that still remains within implanted beads in the sample. Obtaining spatiotemporal information on phase 3 drug distribution is also a challenge due to the destructive nature of the analysis, therefore there has been interest in developing alternative techniques to assess drug distribution in tissue. Namur *et al.* (2010), was the first to attempt to quantify doxorubicin concentrations in tissue sections following implantation of DEB and demonstrate the spatial distribution of doxorubicin over time [159]. This method was based on fluorescence microscopy, exploiting the fact that doxorubicin has intrinsic fluorescence. These studies indicated that doxorubicin had a diffusion distance from a single implanted DEB of at least 600 μ m. This work was repeated by Dreher *et al.* (2012), who studied the temporal changes in drug distribution with greater resolution, finding that maximum doxorubicin concentrations in embolised tissue were reached at 1 hour post embolisation and decreasing thereafter [66]. Despite this early peak, doxorubicin has been detected in embolised swine liver up to 90 days after administration, highlighting the longevity of drug release from beads (or perhaps preferential drug retention in necrotic tissues) [159, 189]. Alternative methods for

detection of non-fluorescent drugs include mass spectrometry imaging [158] and Raman spectroscopy. The ability to model tissue drug distribution *in vitro* would avoid the need for costly animal studies, however mimicking tissue diffusion *in vitro* can be challenging due to the multitude of biological effects that can influence drug behaviour: protein binding, elimination, efflux, and biological barriers. A preliminary model using an alginate agarose gel was recently used to model doxorubicin elution from DEB *via* confocal microscopy [190], with promising results.

3.1.3 Aims of this chapter

The aim of this chapter is to carry out an investigation into the drug release properties of the proposed vandetanib loaded radiopaque beads, using simple USP type apparatus as well as more novel bespoke set-ups aimed at modelling early phase and later phase elution. Vandetanib release profiles were compared with other commonly used drugs, doxorubicin and irinotecan, to investigate the effect of chemical properties on drug release. The *in vitro* models were evaluated for their ability to predict *in vivo* pharmacokinetics through comparison with available pre-clinical data.

In summary, the aims of the work described in this chapter were:

- Examine the effect of prototype parameters (dose, size, pH) on vandetanib elution rate
- Use different *in vitro* elution models to examine early and late phase release for different drugs
- Evaluate the suitability of the models for *in vitro in vivo* correlation (IVIVC)

3.2 Materials and Methods

3.2.1 Materials

Unless otherwise specified, beads used in the experiments were DC Bead or DC Bead LUMI (radiopaque bead) in the size range 70-150 μm (Biocompatibles UK Ltd). Beads were drug loaded at the required dose as previously described by immersion and agitation in solutions of vandetanib (Astra Zeneca, UK), irinotecan (ScinoPharm, Taiwan) or doxorubicin (Hisun, China).

3.2.2 Basic *in vitro* drug release assay

In order to characterise vandetanib release from beads, a model similar to the USP II apparatus was used. Beads were added to amber jars containing PBS (Source

Bioscience, Nottingham, UK), stirring *via* magnetic stirrer bar at 200 rpm. At determined time points, stirring was stopped to allow beads to settle before removing a 5 mL sample of PBS for vandetanib quantification by HPLC as described in section 2.2.2.1. 5 mL of fresh PBS was replaced after each time point. Variables studied included bead chemistry, dose, loading pH, bead size and pH of the PBS.

Statistical comparison of elution curves was performed by calculating the f_1/f_2 difference/similarity factors, in the DDSolver excel add in [191]. The difference factor f_1 is a measure of the relative error between two curves, while the similarity factor f_2 is a measure of the similarity in the percent of dissolution between two curves. These two factors can be respectively defined by:

$$f_1 = \left[\frac{\sum_{t=1}^n |R_t - T_t|}{\sum_{t=1}^n R_t} \right] \times 100$$

$$f_2 = 50 \cdot \log \left\{ \left[1 + \frac{1}{n} \sum_{t=1}^n (R_t - T_t)^2 \right]^{-0.5} \times 100 \right\}$$

where R_t , T_t are the percentage dissolved of the reference and test profile respectively at time point t and n is the number of sampling points. Current FDA guidelines [192] suggest that two profiles can be considered similar if f_1 is less than 15 (0–15) and f_2 is greater than 50 (50–100), which is equivalent to an average difference of 10% at all sampling time points.

3.2.3 Drug leaching in contrast agent

Drug elution from vandetanib loaded DC Bead LUMI (70–150 μm) suspended in contrast agent (Omnipaque 350, GE Healthcare) was investigated by taking aliquots of the delivery media supernatant over a period of 24 h and analysing them using the HPLC method described in section 2.2.2.1 to determine the amount of vandetanib eluted ($n=3$). The chromatographic peak was also analysed to determine if there was any drug degradation during this period. Data for doxorubicin and irinotecan loaded DC Bead LUMI using similar methodology was accessed from Biocompatible's data on file.

3.2.4 Vascular Flow System elution

A silicon vascular cast, termed the vascular flow system (VFS), had been previously designed and produced at Biocompatibles for the purposes of demonstrating DEB delivery (Figure 3.4). The internal diameter of the channels diminishes from 4000 to 900 μm . The size of DEB used were 70-150 μm , so in order to create the effect of embolisation, inserts of 65 μm mesh (Sefar AG) were placed at the end of target channels during delivery. Pre-warmed PBS (Source Bioscience) was constantly pumped through the system *via* a peristaltic pump at 120 mL/min, representing the lower range

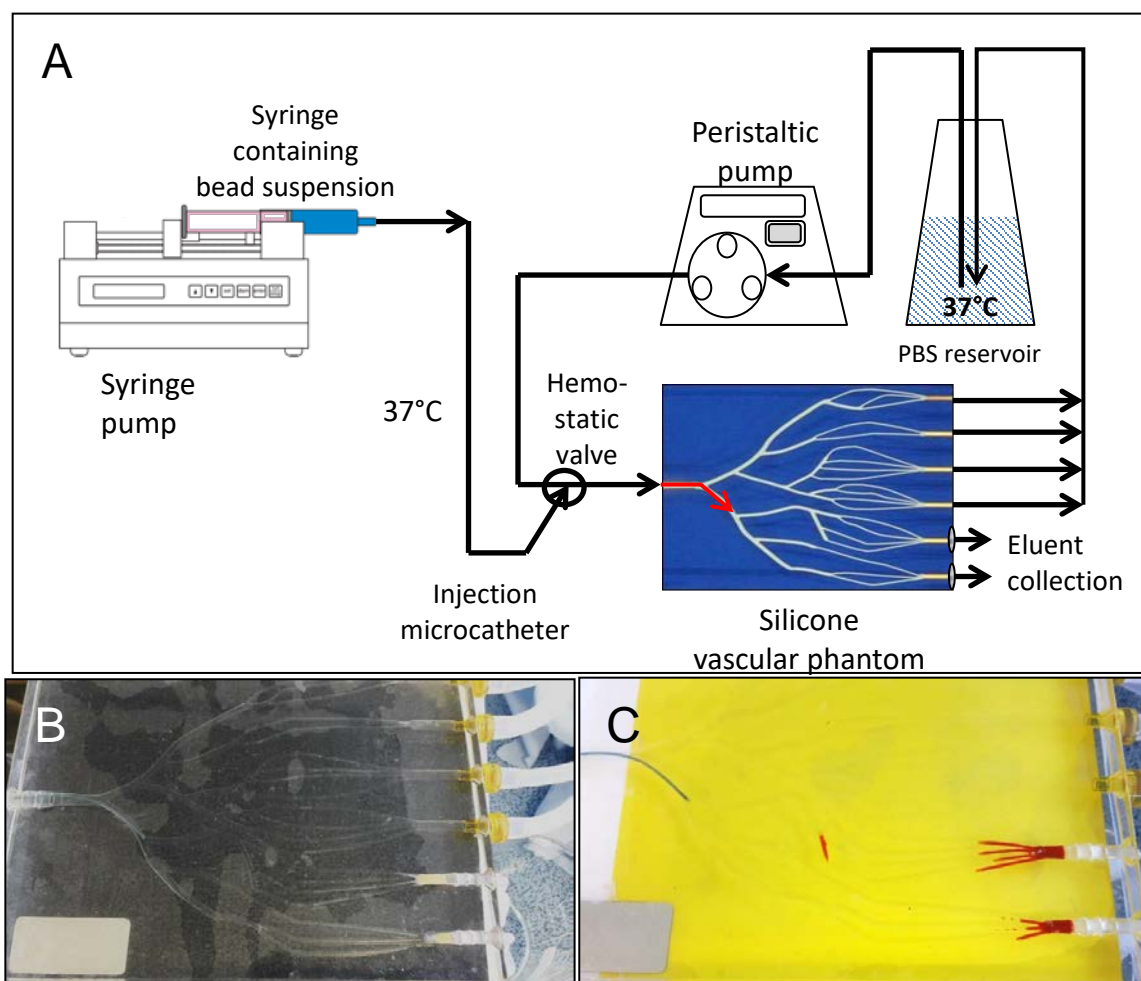


Figure 3.4 Vascular flow model set up for evaluating drug release from DEB. A) Schematic depicting the elution model. Bead suspensions are delivered at a constant rate via syringe pump and microcatheter into the vascular flow model. The catheter is positioned to selectively target the lower two channels, which are blocked at the end with microporous mesh. PBS from a reservoir maintained at 37°C is pumped through the model via peristaltic pump, and is either collected from the outlets of the blocked channels for drug content analysis, or recirculates through the remaining channels back to the reservoir. B) Vandetanib loaded beads delivered into the model. C) Doxorubicin loaded beads in the model. Original in colour.

of hepatic arterial flow rate. A microcatheter (Progreat® 2.4 F, Terumo, Belgium) was steered in one of the channels prior to its first bifurcation (red arrow, Figure 3.4A), whereby the outlet filters became the target embolisation sites, the remainder of the outlets being recirculated back into the PBS reservoir. The beads were prepared for delivery *via* the microcatheter into the model following parameters used in pre-clinical studies. 0.15 mL of drug loaded beads was suspended in contrast agent (Omnipaque 350, GE Healthcare) in a 3 mL syringe immediately prior to delivery. Bead drug doses and suspension ratios are listed in Table 3.1 and were selected based on pre-clinical study protocols to facilitate comparison. A syringe pump was used to inject the bead suspension at 1 mL/minute to ensure reproducible delivery times. Delivery was paused to mix and re-suspend beads in the syringe when necessary. After delivery was complete, the delivery syringe and catheter were flushed three times with deionised water to ensure the full dose was delivered. At set time points, eluent passing through the occluded channels was collected in pre-weighed glass vials for 5 seconds (or 10 seconds in the case of a low flow rate). Between sampling times, eluent was allowed to flow into a separate container. After eluent collection, the vials were weighed to determine the eluent volume, which allowed calculation of the flow rate at each time point. The eluent was then analysed by UV spectroscopy (483 nm, DOX; 369 nm, IRI) or HPLC (VAN) to quantify drug content. The total amount of drug collected in the separate container was also calculated.

Drug	Dose density	Suspension ratio
Doxorubicin	37.5 mg/mL	1:10
Irinotecan	50 mg/mL	1:10
Vandetanib	100 mg/mL	1:20

Table 3.1 Dose densities and contrast suspension ratios of drug loaded radiopaque DEB used in the vascular flow elution model

3.2.5 *Extended release flow through model*

Drug release from radiopaque beads was also profiled in a slow rate, flow through cell open loop system as described in [188] (Figure 3.5). Beads were loaded at the same dose densities as described in Table 3.1. Drug loaded beads (1 mL settled volume) were sandwiched between two filter membranes in an elution cell, submerged in a water bath maintained at 37 °C. PBS was pumped through the system at a flow rate of 0.1 mL/minute, in order to mimic slow residual blood flow after embolisation. Detection of

drug concentration in the eluent over time was performed by automated UV spectroscopy of eluent passing through a flow through cuvette. (Dox, 483 nm; Iri, 369 nm; Van, 330 nm) Drug concentration was calculated from absorbance data using standards of known concentration for each drug.

3.2.6 Pre-clinical procedure and in vitro in vivo correlation (IVIVC)

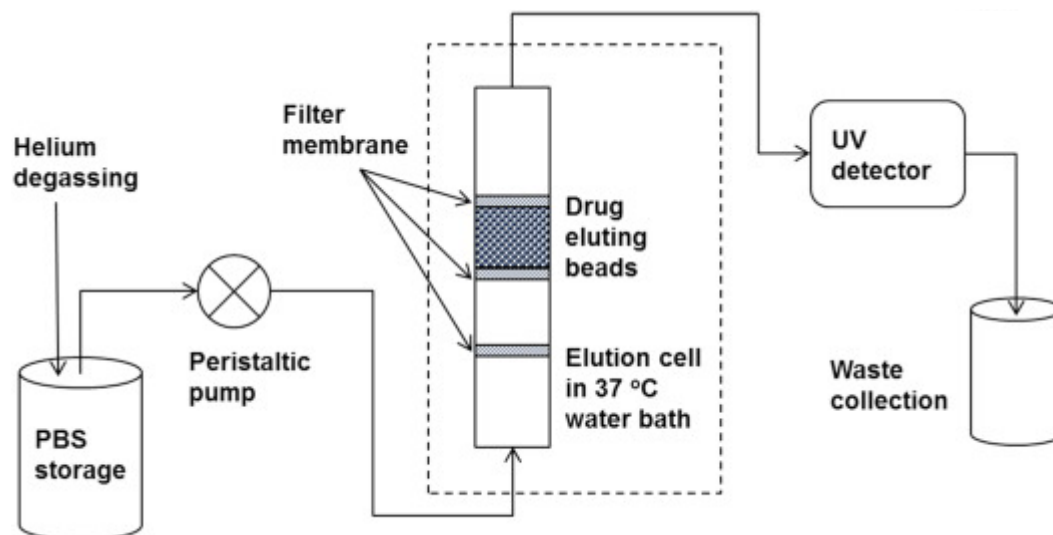


Figure 3.5 Schematic of the slow flow through cell elution model.

3.2.6.1 In vivo studies

For IVIVC, pharmacokinetic data was used from pre-clinical studies of radiopaque DEB-TACE in healthy swine, sponsored by Biocompatibles UK Ltd and conducted by staff at MPI Research (Mattawan, Michigan, USA). Embolisation procedures were performed by a CAQ trained radiologist in experimentally naïve male domestic Yorkshire crossbred swine (farm pigs, weights 53.5 – 66.5 kg at randomisation), as previously described [193]. The research centre is AAALAC accredited and the study conformed to USDA Animal Welfare Act (9 CFR parts 1, 2 and 3) and the ‘Guide for the Care and Use of Laboratory Animals’, Institute of Laboratory Animal Resources, National Academy Press, Washington, D.C, 2011. The protocols were approved by the Institutional Animal Care and Use Committee (IACUC).

Study Number	Test articles	Number of Animals
MPI 2279-008	1mL LUMIVAN 100mg/mL	8
MPI 2279-010	1mL LUMIDOX 37.5 mg/mL	3
	1mL LUMIRI 50 mg/mL	3

Table 3.2 Study details of evaluation of drug loaded radiopaque beads in swine.

In brief, each DEB under investigation as detailed in Table 3.2 was mixed with Omnipaque 350 and suspended by transferring between two syringes through a 3-way stopcock. Bead suspension was aliquoted into a 3 mL syringe for delivery through the microcatheter to allow for better control and re-suspended regularly to prevent sedimentation. Access and selection of the main hepatic artery was achieved using a 2.7 Fr microcatheter (Progreat®, Terumo Japan). An arterial branch that fed around 50% of the liver volume was identified and an angiogram of the lobe(s) taken. With the catheter in position at the target location, the selected DEB was administered slowly under continuous fluoroscopy, evaluating changes in vascular flow rate and appearance of reflux or non-target embolisation of the beads (inferred from visible contrast flow). The maximum volume was administered for all animals (target volume 1 mL of sedimented beads). Dosing occurred in the left lateral lobe or left median lobe for all animals. After all images were obtained, all guides, catheters, and the sheath were removed and the femoral artery ligated; the muscle and subcutaneous tissues were closed with absorbable sutures and the skin was closed with skin glue.

Blood samples were collected from all animals via the jugular or ear vein for determination of the plasma concentrations of doxorubicin, irinotecan, or vandetanib. Drug quantification in plasma was performed by World Wide Clinical Trials (WWCT, Texas, USA) or York Bioanalytical Solutions (YBS, York, UK) using validated liquid chromatography and tandem mass spectrometry (LC-MS/MS) methods. Samples were collected pre-dose and at selected intervals following administration, up to 14 days. Individual doxorubicin, irinotecan, and vandetanib plasma concentration-time profiles from treated animals were analysed using model independent methods in Phoenix® WinNonLin® software (Certara, USA). For each animal, the following toxicokinetic parameters were determined: maximum observed plasma concentration (C_{max}), time of maximum observed plasma concentration (T_{max}), and area under the plasma concentration-time curve (AUC). The AUC from time 0 to 336hr ($AUC_{0-336hr}$), the AUC from time 0 to the time of the final quantifiable sample (AUC_{Tlast}), and the AUC from time 0 to infinity (AUC_{INF}) were calculated by the linear trapezoidal method for all animals with at least three consecutive quantifiable concentrations. Half-life values ($T_{1/2}$) were reported for each plasma concentration-time profiles that had sufficient plasma concentrations in the terminal elimination phase (at least three samples not including T_{max}) and an adjusted R^2 of ≥ 0.9 .

3.2.6.2 *In vitro in vivo* correlation methods

Two approaches for IVIVC were used depending on the elution model being evaluated. For the early phase VFS model, the effect of drug elimination was considered less important due to the short duration (30 minutes) of the experiment. Therefore, a simple point to point comparison was made between plasma AUC calculated with the trapezoidal method, plotted against % cumulative release *in vitro*, in order to assess correlation.

For the later phase flow through elution data, a convolution method was used to convert *in vitro* dissolution profile to a predicted plasma profile using the method described by Qureshi [194]. The amount of drug released between time points (amt (mg)) was calculated and a first order elimination model was applied to determine drug elimination over time using the following equations:

$$\text{Elimination rate constant } k_e = \frac{0.693}{t_{1/2}}$$

$$\text{drug remaining at time (t)} = \text{amt} \times e^{-k_e \times t}$$

The sum of the drug amount remaining (in mg) for each time point was then converted to a predicted plasma concentration (C) in ng/mL:

$$C = \frac{\text{amt} \times 1000}{V_d \times \text{body weight}}$$

Where V_d is the volume of distribution of the drug expressed in L/kg. Volume of distribution refers to the ratio between the total amount of drug in the body and the concentration of drug seen in the plasma, which varies according to the degree of uptake into various tissues. Bioavailability was considered to be 100% due to intra-arterial administration, therefore was not accounted for in the equation.

$T_{1/2}$ and V_d for vandetanib and irinotecan in swine were obtained from calculated values reported in the pre-clinical study reports for LUMIVAN and LUMIRI. These values were not able to be calculated for LUMIDOX, therefore $T_{1/2}$ and V_d for doxorubicin in swine were obtained from the literature [195]. Average pig body weights in kg were obtained from the pre-clinical study reports.

AUC of the predicted and actual plasma profiles between t=0 and the last shared time point for which C>0 were calculated using the trapezoidal method in Prism software.

3.3 Results

3.3.1 Vandetanib release from beads in the basic USP-II type model

3.3.1.1 Effect of bead chemistry

The elution of vandetanib from DC Bead and DC Bead LUMI into PBS was analysed using an *in vitro* USP type II dissolution model, using 0.3 mL aliquots of beads that had been loaded at equivalent dose densities of 40 mg/mL at pH 4.4 (12 mg per aliquot). This was taking into account bead shrinkage in the case of DC Bead and represents the final dose density per volume rather than the target loading dose. Drug release showed a rapid burst phase in the first 2 hours, after which it began to plateau (Figure 3.6). The total percentage release of vandetanib over the test period was higher from DC Bead than from DC Bead LUMI, achieving on average 85 % drug release in 24 hours, compared to an average of 50 % from DC Bead LUMI. Due to DC Bead LUMI being selected as the preferred platform for reasons discussed in chapter 2, subsequent studies were focused on the parameters affecting vandetanib release from these radiopaque beads.

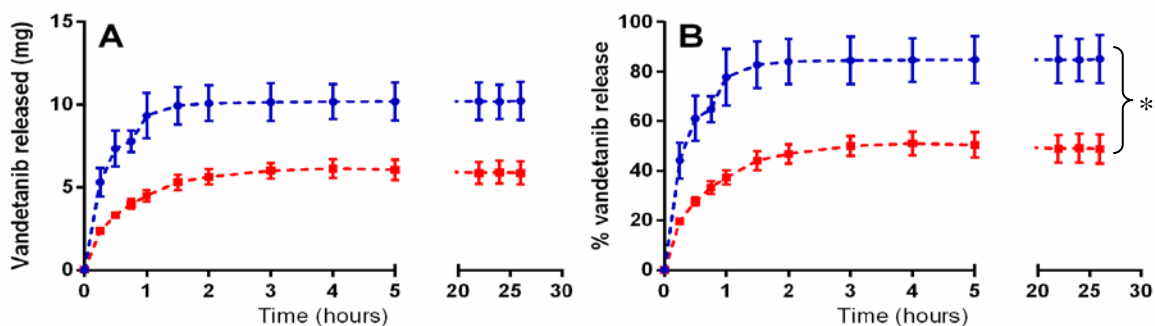


Figure 3.6 Vandetanib release from DC Bead [●] and DC Bead LUMI [■] as A) amount released in mg; B) percentage of available dose. 0.3 mL aliquots of beads (70-150 μm) containing equivalent of 12 mg vandetanib were stirred in 1 L PBS, pH 7. Mean ± SD, n=3. *The curves are significantly different by f1/f2 test (f1=48.12, f2=24.44). Original in colour.

3.3.1.2 Effect of loading pH – DC Bead LUMI

There was not a significant difference in elution rate when comparing DC Bead LUMI that had been loaded at the same dose but at different pH, as confirmed by f_1 test ($f_1 < 15$ for all comparisons). All samples reached plateau at approximately 60 % elution, after 26 hours (Figure 3.7).

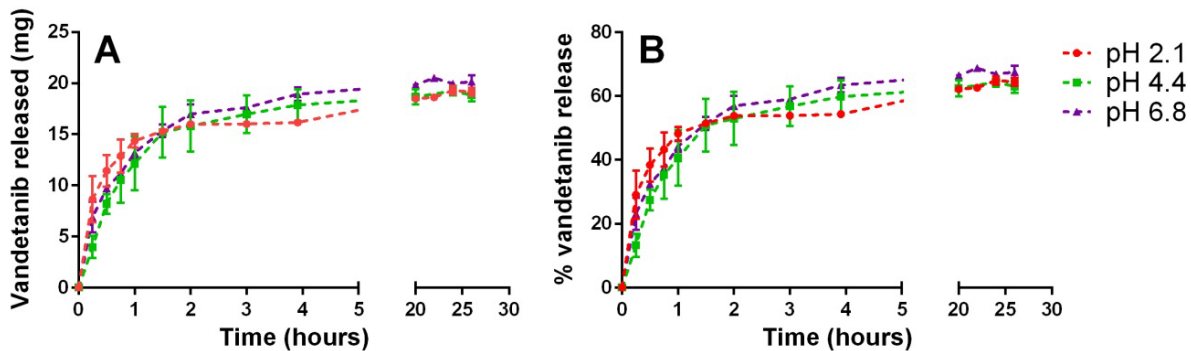


Figure 3.7 Effect of the vandetanib loading solution pH on A) amount B) percentage drug release. 0.5 mL of beads were loaded with 30 mg vandetanib (60 mg/mL) at pH 2.1 [●], 4.4 [■] or 6.8 [▲]. Mean \pm SD, n=3. Original in colour.

3.3.1.3 Effect of bead size range – DC Bead LUMI

As expected due to a lower surface area to volume ratio, the initial rate of vandetanib release was slower from DC Bead LUMI of a larger size range (300-500 μm , mean diameter 350 μm) compared to 100-300 μm or 70-150 μm (Figure 3.8). However, the percentage release at 24 hours was similar for each size range (~60%). There was not a significant difference in elution rate between 100-300 μm and 70-150 μm beads, whose mean diameters are 130 μm and 100 μm respectively ($f_1 = 7.67$).

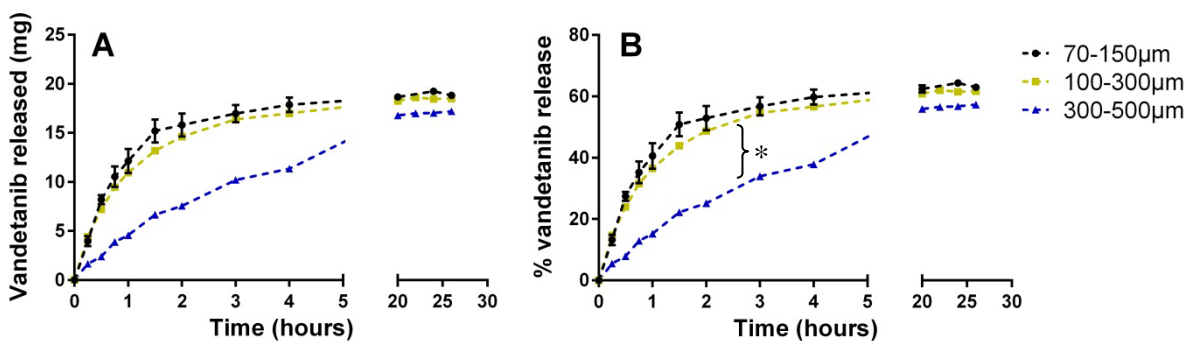


Figure 3.8 Effect of bead size range on A) amount B) percentage drug release. 0.5 mL of beads of diameter range 70-150 μm [●], 100-300 μm [■] or 300-500 μm [▲] were loaded with 30 mg vandetanib (60 mg/mL). Mean \pm SD, n=3. *300-500 μm elution curve is significantly different to 100-300 μm ($f_1=41.68$, $f_2=38.14$). Original in colour.

3.3.1.4 Effect of vandetanib dose density – DC Bead LUMI

The vandetanib loading dose of DC Bead LUMI was positively correlated with the release rate (Figure 3.9). High dose vandetanib beads released drug more quickly than lower dose beads, but also released a greater proportion of the available dose in the given time frame, suggesting that a high drug concentration gradient between the DEB and the elution medium encouraged drug transport. It is noted that the overall percentage release achieved in this experiment was lower than previous results with similar doses, which is likely due to minor protocol differences; fewer early sampling points were taken and a smaller sampling volume of 1 mL was used therefore less fresh PBS was replaced during the experiment, which may have led to increased medium saturation.

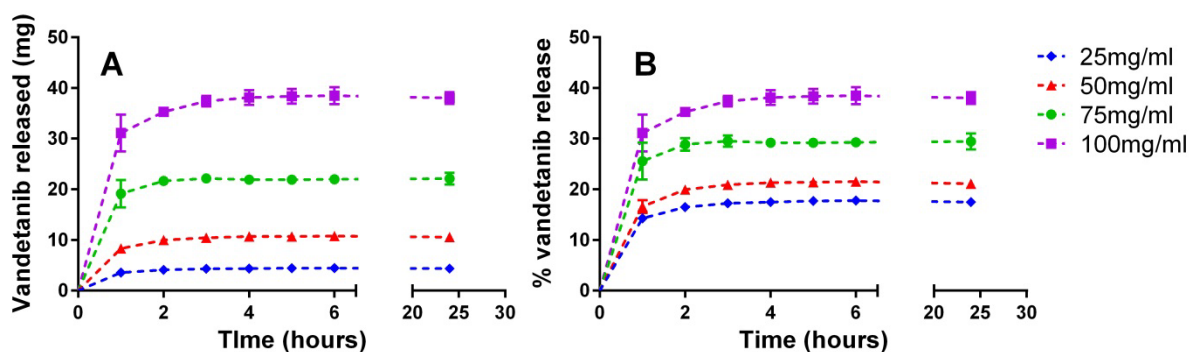


Figure 3.9 Effect of vandetanib loading dose on A) amount and B) percentage drug release. 1 mL of beads (70-150 μm) were loaded with 25, 50, 75 or 100 mg vandetanib. Mean \pm SD, n=3. Original in colour.

3.3.1.5 Effect of elution medium pH – DC Bead LUMI

In order to assess whether incomplete vandetanib elution was a result of poor drug solubility in PBS, the experiment was repeated using PBS that was adjusted to pH 5 using HCl. Reducing the pH of the elution medium to 5 slightly increased the elution rate of vandetanib from DC Bead LUMI, achieving on average 60% total release compared with 48% at neutral pH. The release profiles were compared using f_1/f_2 analysis and revealed to be significantly different ($f_1=29.76, f_2=47.56$).

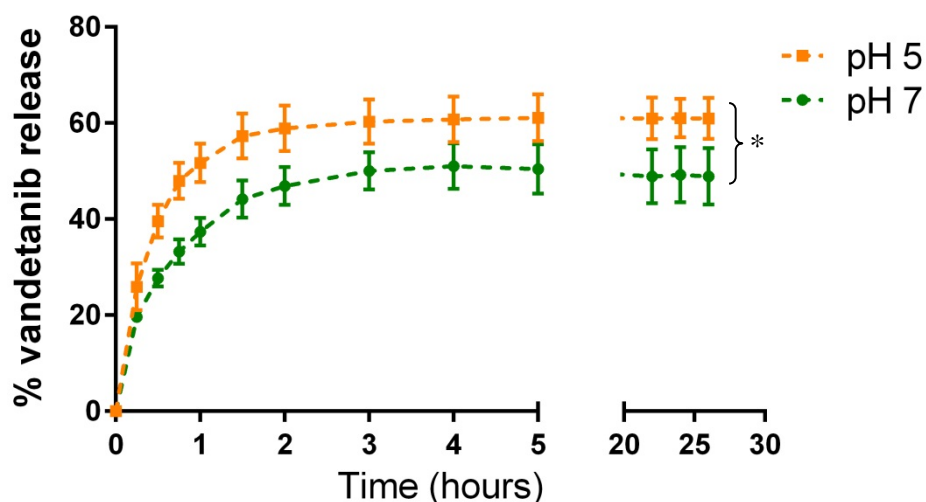


Figure 3.10 The effect of the pH of the elution medium on the released fraction of vandetanib from DC Bead LUMI. 0.3 mL beads containing 12 mg vandetanib (40 mg/mL) were stirred in 1 L of PBS at pH 5 [■] or pH 7 [●]. Mean \pm SD, n=3. *Curves are significantly different by f1/f2 test ($f_1=29.76$, $f_2=47.56$). Original in colour.

3.3.2 Early phase drug release (contrast suspension and VFS model)

The drug release profile obtained using the VFS elution model representing the first 30 minutes of bead administration is shown in Figure 3.11(A-B). The elution rate peaks within the first 5 minutes, demonstrating a ‘burst’ effect which is clearly more pronounced with irinotecan than with vandetanib or doxorubicin. The accumulation of beads in the channel ends led to a dramatic decrease in eluent flow rate passing through the occlusive bead mass, which corresponded with the drop in elution rate (Figure 3.11(C)). The flow rate profile was similar for each DEB tested. The amount of drug released over 30 minutes corresponded to approximately 9% of the total dose for irinotecan, 2.6% for doxorubicin and 2.1% for vandetanib.

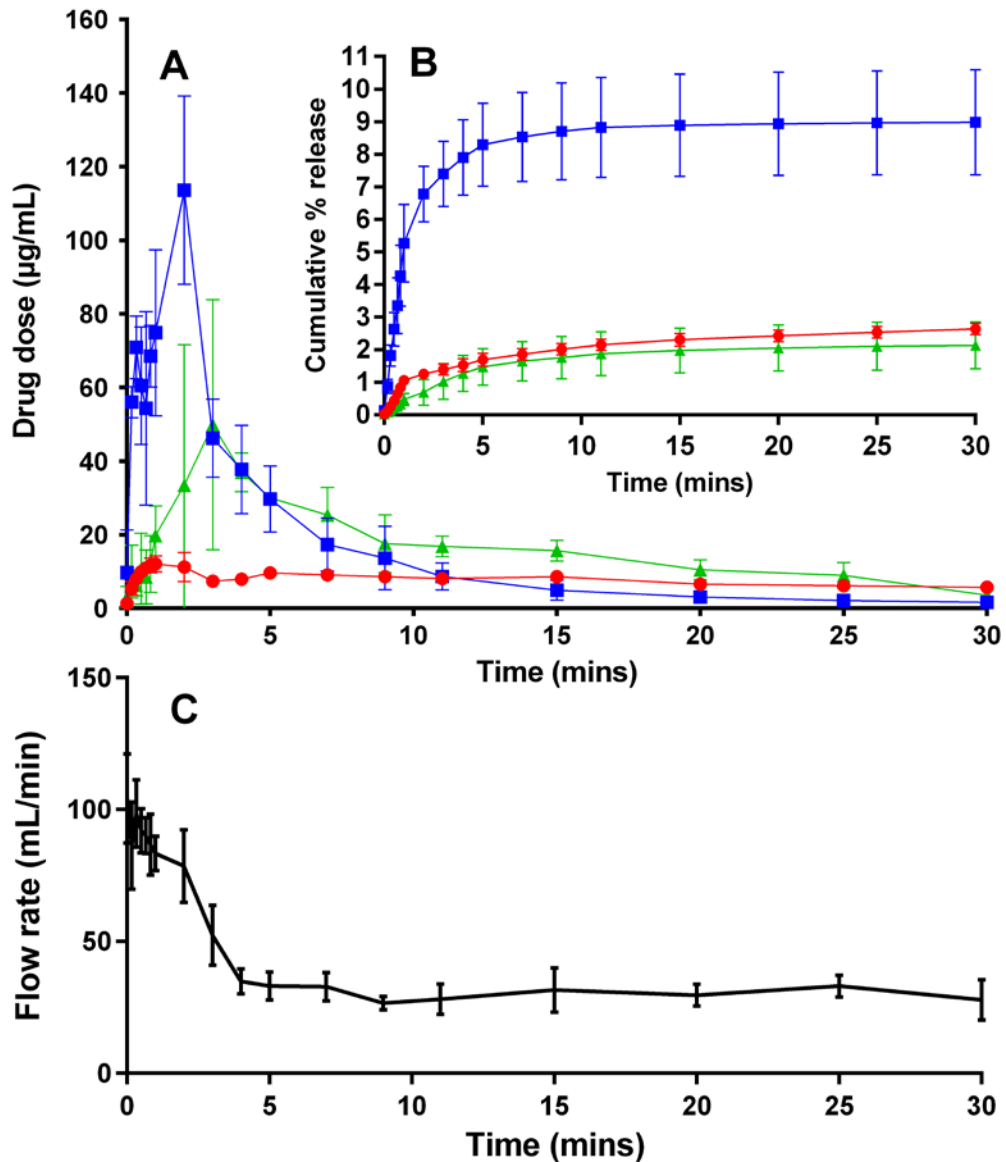


Figure 3.11 (A) Drug dose release profile with time during the administration phase using the VFS; (B, inset) Data expressed as cumulative percentage release; (C) Representative flow rate profile as measured by volume of eluent exiting occluded channels over time – data from LUMIVAN. Mean \pm SD, n=3. Original in colour.

In order to examine the relationship between early phase elution kinetics and drug leaching in contrast agent, the beads were suspended in Omnipaque 350 and drug concentration in the supernatant was quantified. The amount of vandetanib released from the beads into the contrast medium 15 min after mixing was 3.3 mg, which

increased to just 3.5 mg in total after 24 h storage representing 3.5% of the loaded dose. The drug was seen to be unaltered and remained within specification, >98.0% purity with no single impurity >0.2%. This shows that a bead suspension could be potentially prepared in advance and stored overnight without significant elution of drug into the delivery medium and without risk of drug degradation. On the other hand, irinotecan is quickly leached from the beads upon mixing with contrast agent, and the amount released continues to increase with extended storage, from 1.9% (t=0) to 10.8% (t=4h). Therefore, irinotecan loaded beads are recommended to be used immediately after suspension. Doxorubicin loaded beads are stable in contrast agent and eluted only 0.2% of their dose in up to 4 hours of storage. The size of the AUC for the burst phase in the VFS elution profile seems to correlate with the respective susceptibility of the drugs to leach in contrast agent, which suggests this effect contributes to the initial burst of drug release in the VFS.

In keeping with the results obtained in the USP II type model, when vandetanib elution was repeated in the VFS using PBS adjusted to pH 5, there was an increase in release rate evident in the early time points (Figure 3.12). Total drug fraction released was 6.2% compared to 2.1% in pH 7 PBS. In addition, drug release did not appear to reach plateau for the duration of the elution run at pH 5, despite a comparable reduction in flow rate. Statistical comparison of curves via f1/f2 could not be reliably calculated due to high variability in the early timepoints (<5min), however dissolution % were significantly different between pH conditions from 4min onwards (multiple t-tests, p<0.05).

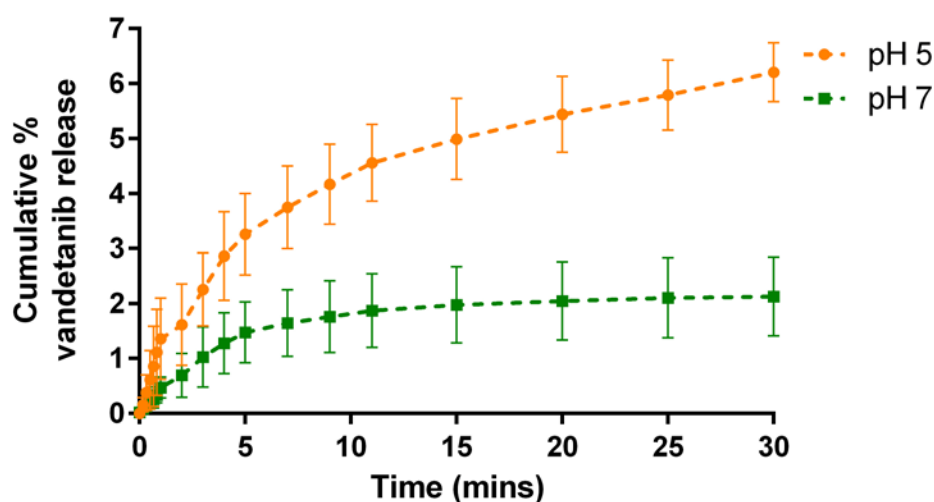


Figure 3.12 Effect of elution medium pH on vandetanib elution in the VFS model. Mean \pm SD, n=3. Original in colour.

3.3.3 Drug release from beads in the flow through cell

Evaluation of the later phase drug release (post formation of an occlusive mass of beads) from the various DEBs was modelled using the open-loop flow through model described in section 3.2.5. Data is shown in Figure 3.13(A) as concentration in the eluent over time (expansion inset Fig. 3.12(B)), and Fig. 3.12(C) as cumulative percentage dose released. Using this method, irinotecan is still seen to release relatively rapidly compared to the other drugs with complete release achieved in around 2 days. Doxorubicin displays a sustained and slow elution, with around 45% of the dose eluted within 16 days and continuing at a slow rate. Vandetanib displays an interesting release pattern, with a linear zero order release phase over the first 5 days that plateaus after 90% is eluted.

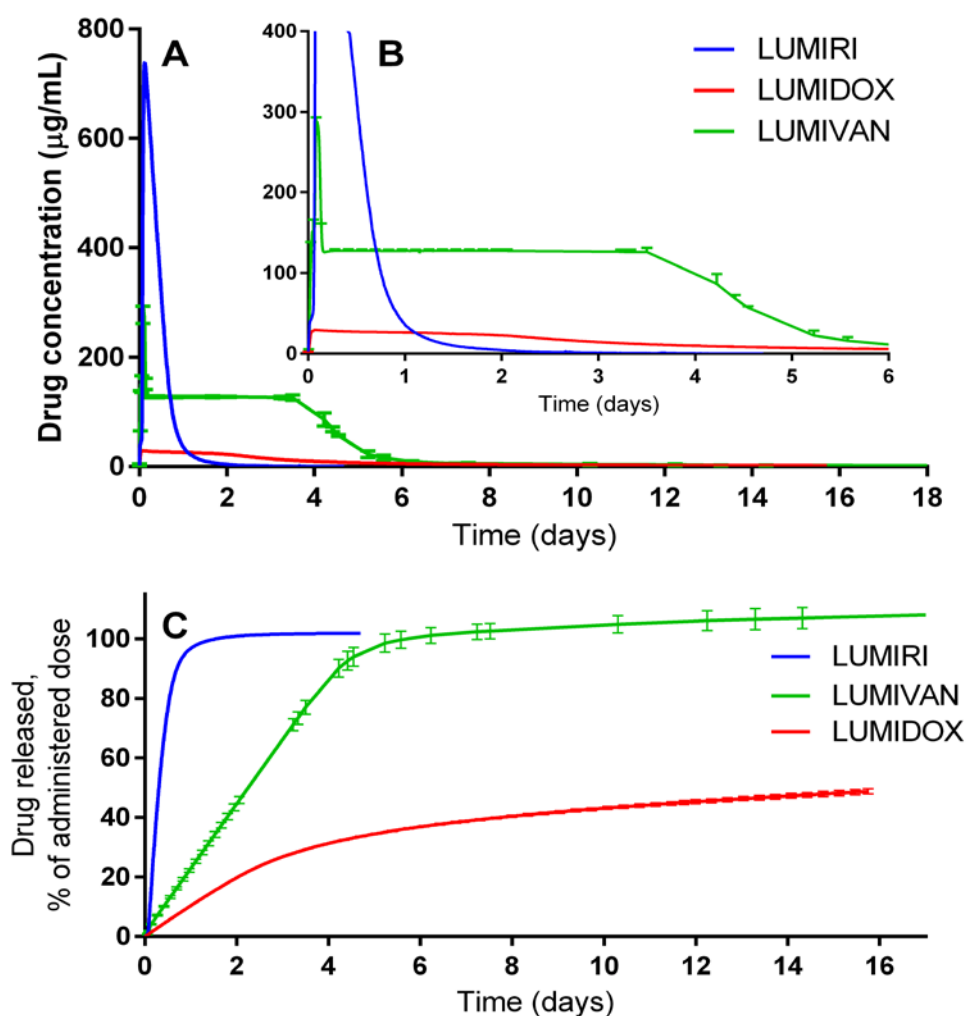


Figure 3.13 (A): Drug dose release profile with time during the later phase using the open loop flow through model; (B) inset: expanded view of the first 6 days; (C) data expressed as cumulative percentage release. LUMIRI = irinotecan beads, LUMIVAN = vandetanib beads, LUMIDOX = doxorubicin beads. Mean \pm SD, n=3. Original in colour.

3.3.4 *In vivo pharmacokinetics*

The pharmacokinetic profiles for the three DEBs are seen to be different in each case when comparing the curve shapes in Figure 3.14(A), which is plotted on a log scale in order to allow the visualisation of the curves together. The C_{max} (see also Table 3.2) for LUMIRI is much higher than for LUMIDOX and LUMIVAN as shown in Figure 3.14(B) where the curves are plotted on a standard scale to provide the direct comparison of the relative doses of the drugs released from the different DEB over the first 24 hours post administration. LUMIDOX reaches C_{max} within minutes and declines rapidly, whereas LUMIRI takes between 1-2 hours and declines over the next 24 hours. LUMIVAN shows a very minor C_{max} at about 1 hour and persists in the plasma with a slow decline over several days. Figure 3.14(C) provides an alternative 24 hour plot whereby double Y axes are used to allow the LUMIRI to be scaled to the same order of magnitude as the other DEBs, and Figure 3.14(D) is the comparator graph only scales over 170 hour period to demonstrate the long time over which vandetanib can be detected in the plasma post administration.

DEB	Drug Dose (mg)	C_{max} (ng/mL)	$C_{max}/Dose$ (ng/mL/mg)	T_{max} (hr)	AUC_{Tlast} (hr*ng/mL)	$AUC_{Tlast}/Dose$ (hr*ng/mL/mg)	$T_{1/2}$ (hr)
LUMIDOX	37.6	74.6 ± 27.7	1.99 ± 0.738	0.067 (0.067 - 0.15)	185 ± 24.6	4.93 ± 0.657	N/A *
LUMIRI	50.3	474 ± 138	9.47 ± 2.77	1.067 (0.4- 2.2)	2860 ± 278	57.3 ± 5.57	3.67 ± 0.74
LUMIVAN	100	23.8 ± 9.13	0.238 ± 0.091	2 (0.333 -4)	535 ± 150	5.35 ± 1.5	22.8 ± 4.15

Table 3.3 Pharmacokinetic parameters obtained from the pre-clinical embolisation studies in healthy swine liver. * $T_{1/2}$ could not be calculated due to insufficient plasma-concentration time data.

Plotting the \log_{10} of plasma concentrations (C_p) vs time resulted in different slopes for the different drugs (Figure 3.15). Vandetanib and irinotecan showed a linear relationship between $\log C_p$ and time, indicating that the pharmacokinetics of these drugs are best fit by a one compartment model. On the other hand, doxorubicin pharmacokinetics appeared to be more multi-phasic, which suggests a multi-compartment model may be applicable, as has been previously suggested [196, 197].

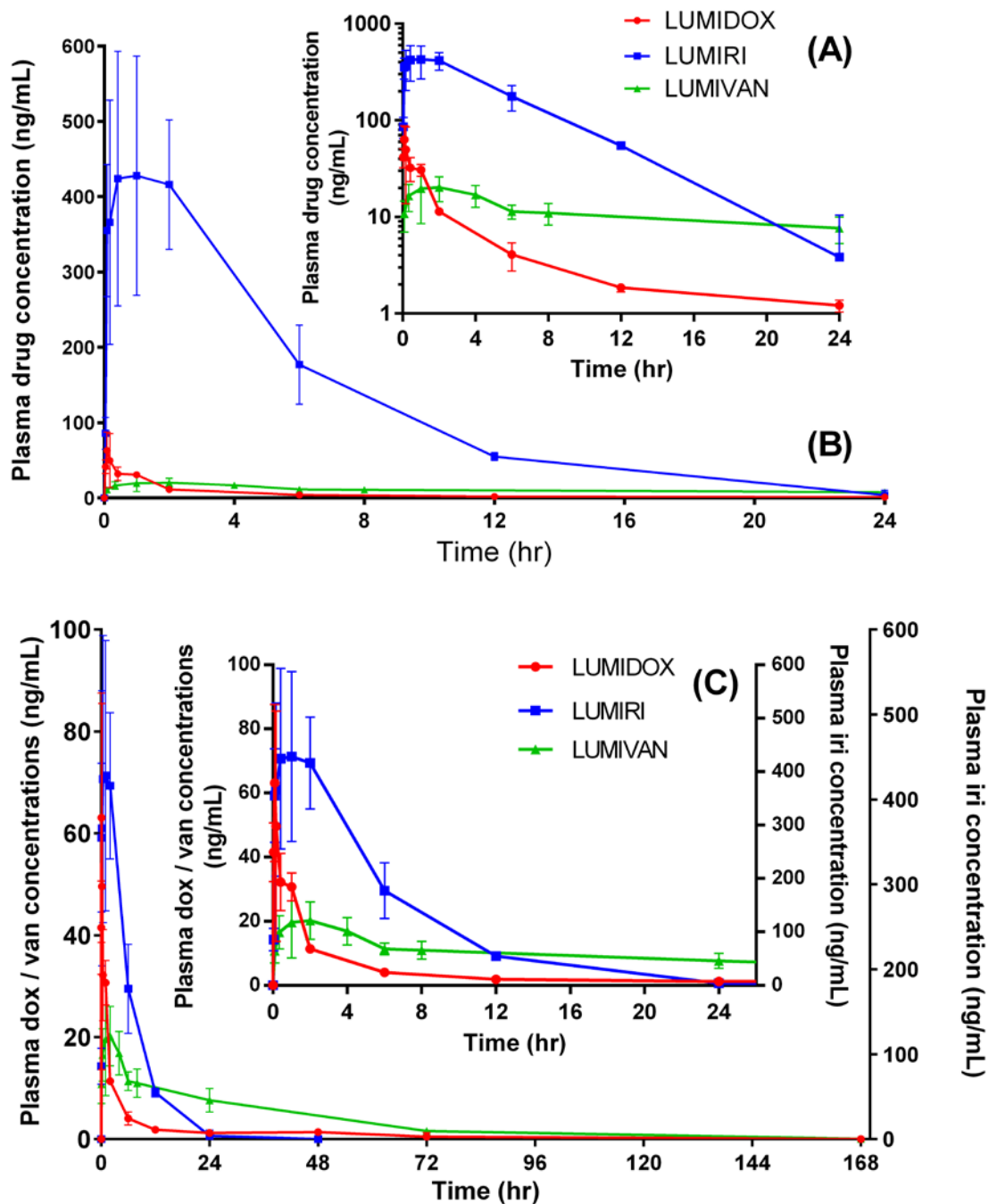


Figure 3.14 Plasma pharmacokinetic data from pre-clinical studies in swine using LUMIDOX, LUMIRI and LUMIVAN. Plasma concentration-time profiles for the first 24 hours are depicted in A) log:linear, B) linear:linear, C) Dual Y axes with irinotecan plotted on the right axis. D) Extended plasma concentration time profile again on dual Y axes up to 170 h. Data shows mean of $n \geq 3$ animals \pm SD. Original in colour.

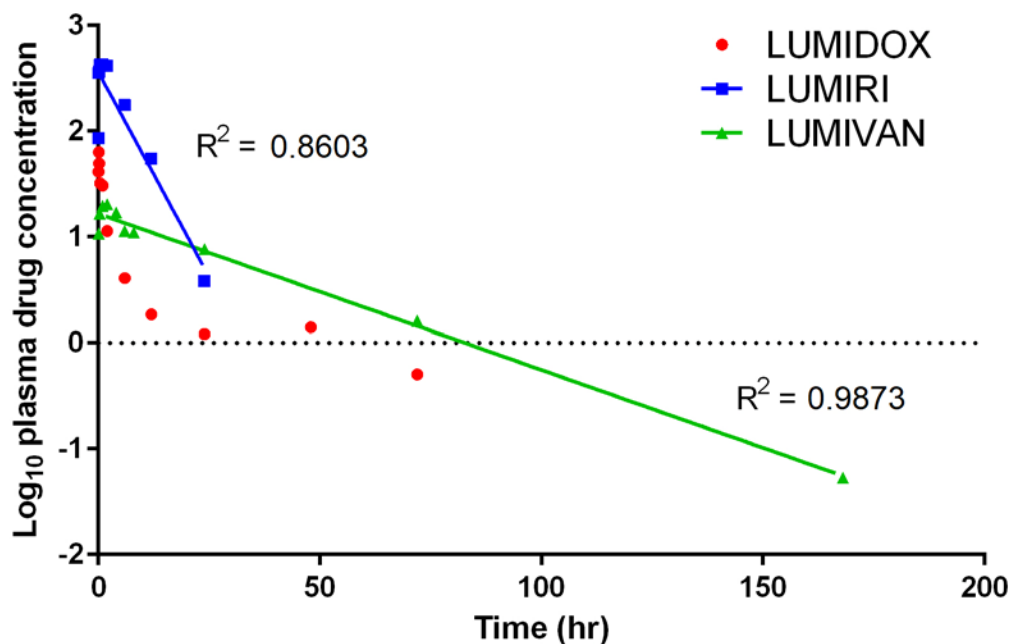


Figure 3.15 Log plasma concentration of irinotecan, vandetanib and doxorubicin in swine plasma over time. Linear relationships (IRI and VAN) are suggestive of a one compartment model. Original in colour.

3.3.5 IVIVC

3.3.5.1 Early phase

The AUC of doxorubicin and irinotecan plasma profiles were calculated using the trapezoidal method, and plotted against cumulative % release from the VFS elution data at corresponding timepoints (2, 5, 11, 25 mins from start of bead administration), shown in Figure 3.16.

For Level A IVIVC as specified by FDA guidance [198], a linear correlation is required between the *in vivo* parameter (AUC) and the *in vitro* dissolution profile. A better correlation was achieved with doxorubicin than irinotecan, however the VFS model predicted a faster release than the actual *in vivo* profile for both drugs. T_{max} for doxorubicin were in a similar timeframe *in vitro* and *in vivo* ($t=0.9$ mins vs $t=4$ mins respectively). The difference was greater for irinotecan, with the VFS showing T_{max} to be 2 mins, whereas maximal plasma concentrations were seen at approximately 1 hour in the swine model.

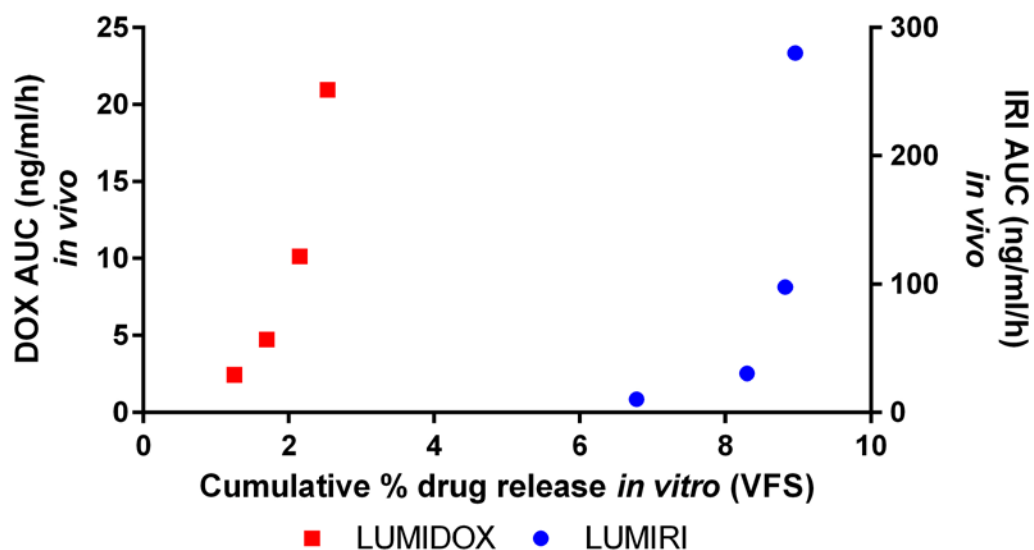


Figure 3.16 IVIVC of plasma AUC for LUMIDOX (left Y axis) AND LUMIRI (right Y axis) in healthy swine against *in vitro* cumulative % drug release obtained in the VFS model (X axis). Original in colour.

The frequency of blood draws in the vandetanib bead swine pre-clinical study was not sufficient to allow a point to point correlation with VFS data. However T_{max} were compared and found also to differ significantly, with the VFS model showing T_{max} at 3 mins compared with 2 hours *in vivo*. The dose adjusted C_{max} were not drastically different between *in vivo* and *in vitro*, indicating that similar proportions of the drug dose were released in the early phase set up, albeit at an accelerated time course. The compared C_{max} and T_{max} for each drug are summarised in Table 3.3.

	$C_{max}/\text{dose } in vivo$ (ng/mL/mg)	$C_{max}/\text{dose VFS}$ (ng/mL/mg)	$T_{max} in vivo$	$T_{max} in VFS$
LUMIRI	9.47	15.15	1h	2min
LUMIDOX	1.99	0.94	4min	0.9min
LUMIVAN	0.238	3.33	2h	3min

Table 3.4 Comparison between pharmacokinetic/dissolution parameters *in vivo* (swine) and *in vitro* (VFS model)

3.3.5.2 Late phase

Comparing the raw concentration-time data for the flow through model with the *in vivo* PK data, we see that the T_{max} are fairly similar to their *in vivo* counterparts for vandetanib and irinotecan (3 h vs 1 h, 2.2 h vs 2 h respectively), but the duration of drug release in the model persists longer than the presence of drug in plasma. However, the concentrations cannot be directly compared with the *in vivo* data as they represent the concentrations of drug in eluent passing directly from the beads to the UV detector at a given moment, without taking into account dilution and accumulation in the blood, distribution in tissues and elimination. Therefore, the data was convoluted as described in section 3.2.6.

The convoluted flow through data for vandetanib and irinotecan LUMI beads showed similarity in curve shape to the plasma profiles, predicting a similar elimination time course for the drugs from the plasma (Figure 3.18 A&B). The convolution was not extended past 48 hours due to the infrequency of comparable data points beyond this time: the average T_{last} for LUMIRI, LUMIDOX and LUMIVAN were 12 h, 48 h and 72 h respectively. The predicted maximum plasma concentrations as well as AUC for all DEBs were between 5.2 and 66.3 fold lower than the actual values, however at later stages (24-48 h) the predicted and actual concentrations begin to converge. The *in vitro* T_{max} in all cases occurred several hours later compared with *in vivo*. For doxorubicin, the convoluted elution profile did not correlate well in terms of curve shape with the actual plasma profile, predicting a much lower C_{max} and slower elimination of the drug. However, from 12 hours onwards, the predicted and actual doxorubicin concentrations are within 1-2 ng/mL of each other, which may explain why the compared AUCs were less disparate than the C_{max} .

In order to achieve level A IVIVC, a linear correlation would be expected between compared parameters over the time course. Interestingly, despite differing by an order of magnitude, when *in vitro* and *in vivo* AUC were plotted against each other, a linear correlation was achieved for LUMIVAN but not for LUMIRI or LUMIDOX. AUC calculated from the raw concentration time data from the flow through model correlated better than the convoluted data in this case, but both fits had an $r^2 > 0.9$ (Figure 3.17). The steep slopes of the compared AUCs for doxorubicin and irinotecan in the first hour

is indicative of the drug being observed in the plasma *in vivo* much faster than it was observed in the *in vitro* test (data not shown).

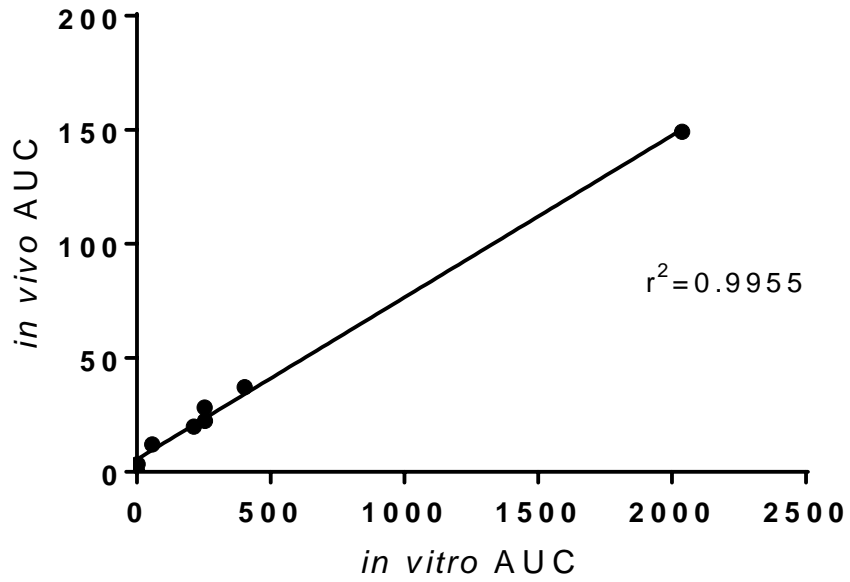


Figure 3.17 Assessment of IVIVC between *in vitro* and *in vivo* AUC from raw LUMIVAN flow through elution data.

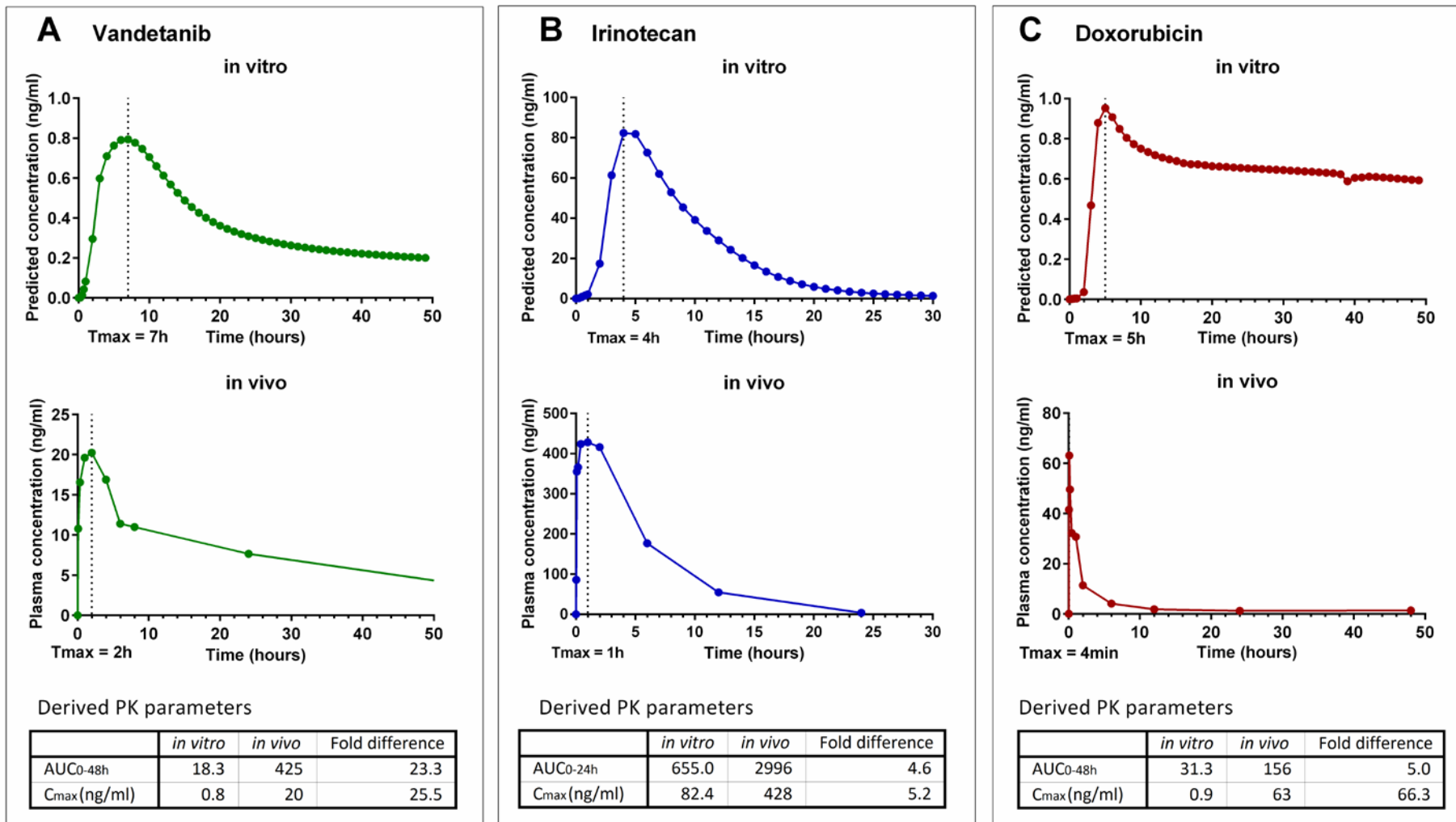


Figure 3.18 IVIVC using flow through elution model data. A) LUMIVAN, B) LUMIRI, and C) LUMIDOX elution profiles were convoluted with a first order elimination model (upper graphs) and compared with the *in vivo* plasma profiles (lower graphs). Predicted (*in vitro*) and actual (*in vivo*) PK parameters are reported in the tables. Original in colour.

3.4 Discussion

Three different methods of modelling drug release from beads *in vitro* were employed, with the goal of distinguishing between vandetanib bead prototypes, and accurately modelling release kinetics in the early phase and late phase of drug elution.

3.4.1 Effect of DEB properties on vandetanib release

Bead chemistry and size range had predictable effects on vandetanib release, with the increased solid content and hydrophobicity of LUMI likely impeding diffusion of ions and drug molecules throughout the bead matrix [38]. The increased elution rate from smaller beads is explained simply by a larger surface area to volume ratio. There is a trend towards using smaller bead size ranges in clinical practice due to their ability to penetrate tumours more distally, and we could expect that this may be associated with a more rapid availability of the drug in plasma and tissue compared with larger size ranges. Several studies have reported increased response rates and similar or even decreased adverse event rates with smaller bead size ranges, which suggests that a potential increased plasma exposure does not necessarily contribute to increased systemic side effects [146, 178, 179, 199].

Although it could be expected that doubly charged vandetanib molecules occupying 2 binding sites may be released more slowly in an elution model, the release profile of vandetanib from DC Bead LUMI did not vary significantly depending on the pH of the loading solution and therefore the charge state. Possible reasons for this are that the ionic interactions are not strong enough to be affected in this manner, or perhaps the neutral pH of the elution medium negates this pH dependent effect as soon as the ion exchange process begins.

In the USP-II type model, release of vandetanib from DC Bead LUMI was incomplete, despite maximum concentrations reached in the elution vessel remaining lower than the theoretical solubility of 0.008 mg/mL (Figure 3.5). By adjusting the pH of the PBS elution medium to 5, vandetanib release rate from LUMI was slightly increased with total drug release increasing by 12%. This effect was also seen in the short term VFS elution model, suggesting that drug solubility may be a rate-limiting factor in vandetanib release. Hypoxic tumours are known to be acidotic due to production of lactic acid by anaerobic glycolysis. Moreover efficient arterial embolisation will impede clearance of lactic acid from tumoural tissues, contributing to the acidic

microenvironment [200], which may somewhat facilitate release in the case of acid-soluble drugs. Similarly to doxorubicin [201], vandetanib binding to DEB has been shown to be fully reversible in appropriate solvents as the total dose can be extracted using a solution of potassium chloride and ethanol. Furthermore, the total vandetanib dose was released in the slow flow through model, suggesting that maintaining a fresh supply of ions is necessary to sustain vandetanib release, which has been previously reported for other DEB combinations [186].

The effect of increasing the vandetanib dose density in DC Bead LUMI was that of an increased release rate and overall release fraction. This relationship is opposite to what has been previously observed with doxorubicin loaded DC Bead, in which increased dose hinders drug release due to the effects of water displacement: DEB shrinking leads to increased proximity of doxorubicin molecules therefore more drug-drug interactions (π stacking), and increased hydrophobicity hampers water transport and ion exchange [184]. Since DC Bead LUMI are more resistant to size changes after drug loading, it is possible that bead shrinkage no longer hinders drug and ion transport and instead increased loading dose leads to an increased drug concentration gradient which encourages drug release. In addition, vandetanib is not known to have strong self-interactions. These may play an important role when it comes to doxorubicin, as it has been observed in preclinical models that hepatic embolisation using LUMI loaded with 75 mg/mL dox yielded a lower C_{\max} in plasma than the 37.5 mg/mL dose despite minimal bead size variation (Biocompatibles UK Ltd unpublished data). This was not the case for irinotecan, where the C_{\max} for a 100 mg/mL dose was approximately double that of the 50 mg/mL dose; again, irinotecan has weaker self-interactions than doxorubicin.

3.4.2 Evaluation of early and late phase elution modelling

3.4.2.1 VFS model

The VFS model allows the reproduction of many phenomena experienced during administration of DEB in the clinic: suspension in contrast agent, gradual (rather than instantaneous) DEB delivery, exposure to high rate pulsatile flow of elution medium, and eventual packing of beads in a confined channel. The presence of these features is a vast improvement in representativeness of the *in vivo* situation, in comparison to the basic USP type set ups. This may have been the key to the achievement of good correlation of the elution data with the first 30 minutes of *in vivo* plasma concentration

data in the case of LUMIDOX. For LUMIRI and LUMIVAN the model predicted a shorter T_{max} than the *in vivo* value, however the dose adjusted C_{max} were in a similar range to the *in vivo* values for all three drugs suggesting that the model is capable of making a fair estimation of the proportion of drug that will be released from the beads in this burst phase. The accelerated release time course observed in the VFS may simply be a function of the condensed nature of the model – the volume of bead suspension delivered is a tenth of what is used in the swine model, therefore delivery of the entire dose does not take as long, and the channels are blocked quickly as beads reach the filters leading to the reduction of drug release. Another key difference is that since the VFS is a semi-open loop system, the drug concentration that is recorded at each time point provides a snapshot of what has been released in that moment, in other words the drug does not have the opportunity to accumulate as it would in the plasma prior to the start of elimination. Doxorubicin has a very short distribution half-life of 5 minutes [202], in other words it is quickly taken up by the tissues which is reflected in its early disappearance from the plasma compared to irinotecan and vandetanib. This may be why a better correlation is achieved with doxorubicin in the VFS, where the eluted drug is also quickly removed from the system.

Owing to the complexity of the VFS model, there are several potential variables in its operation which may have contributed to relatively large standard deviations in some data sets. Improvements may need to be made to the operation of the system in order to reduce error, and tighter standardisation of the protocol will aid reproducibility between runs and operators.

3.4.2.2 Flow through model

The flow through cell model employed in this study mimics tight packing of beads in blood vessels with a very slow flow rate, which makes it suitable for modelling the mid to late phase of drug release from DEB. The volume and drug dose of beads used in the model are the same as those used in the swine pre-clinical studies, allowing a direct comparison of the achieved concentration-time profiles. The flow through system was capable of distinguishing between the three drug types, showing the same pattern as the *in vivo* data in terms of the relative release rate of irinotecan, vandetanib and doxorubicin as a consequence of drug binding strength and interactions. A linear point to point correlation was achieved when comparing the AUC derived from the flow through data and *in vivo* plasma data for vandetanib only, whereas doxorubicin and

irinotecan had differential release rates *in vitro* compared to *in vivo*. The convoluted *in vitro* data showed only similarities in elimination phase curve shape for vandetanib and irinotecan. In contrast to the VFS model, the predicted T_{\max} were this time several hours later than the actual *in vivo* T_{\max} . However, this can be explained by the fact that the flow through elution process is started with the beads already in an occlusive mass, therefore the burst effect is not modelled and the drug will take longer to reach a peak concentration. FDA guidance states that time-scaling or time shift correction may be applied to the *in vitro* profile to improve the alignment [198], which has been successfully implemented in developing IVIVC in non-IV microsphere formulations using modified USP IV apparatus [203]. Doxorubicin IVIVC was not improved by implementing a simple time shift correction to account for the slow initial release rate, therefore further investigation is required to establish if time-scaling may be appropriate. If the time-scaling factor is found to be non-linear, the lack of consistency between release rates should be treated as a limitation of the *in vitro* model [204].

Despite using the same volume of beads and drug doses, the convoluted profile significantly underestimated the plasma concentrations of all three drugs, although the disparity decreases over time and the values begin to converge after 24 h – 48 h. Again, this may be related to the lack of the burst phase and the tight packing and slow flow rate of the system. In particular, doxorubicin was initially very slow to elute from the beads in the flow through model, which may be due to how it is released when packed in a column. Swaine *et al.* (2016) found that dox release from DC bead in a column was based on a process of drug desorption from the near end of the column, followed by resorption by beads further along in the direction of flow [188]. This results in the beads furthest away from the flow source becoming loaded with more drug than the initial loading dose, which may increase drug aggregation and impede ion influx. This effect has resulted in a slow, sustained release of dox in the flow through model, which offset the simulated elimination giving a shallower elimination curve in the convoluted data. *In vivo*, as previously mentioned dox is quickly distributed into tissues and this is not accounted for in the convolution process.

Convolution of *in vitro* data is one approach to develop an IVIVC, however the method used in this study makes several assumptions which may not be suited to controlled release applications. Reported $T_{1/2}$ and V_d for the drugs were found to be variable in the literature, and values obtained for humans may not be applicable to swine. Therefore

apparent $T_{1/2}$ and V_d were obtained from the corresponding DEB pre-clinical studies where possible to improve accuracy. For LUMIDOX they were not able to be calculated and therefore the parameters were taken from a published study which used i.v. infusion of dox solution in swine rather than DEB, which may limit the accuracy of the prediction, as controlled release formulations can cause apparent $T_{1/2}$ and V_d to vary from the standard values. A possible alternative approach would be to de-convolute the *in vivo* data and compare this with the dissolution profiles, but this technique is more complex to realise.

3.5 Conclusions

The models described here have given an insight into how we may start to improve representativeness of *in vitro* elution testing for drug eluting beads. The early phase VFS model allowed a decent estimation of the proportion of drug that would be released during the administration phase of DEB-TACE, which for vandetanib was within a similar range to commonly used drugs irinotecan and doxorubicin therefore this provides encouragement that systemic exposure will remain within acceptably low levels. The flow through model, as intended, seemed more suited to modelling mid to late phase drug release as it did not predict the early burst effect, but instead corresponded better to the drug elimination phase. More sophisticated methods of convoluting or deconvoluting data using multi-compartmental models may improve the IVIVC. It seems that adapting and combining these two methods may be the best way to predict plasma drug concentrations after DEB treatment *in vitro*, and looking forward a third model may be developed based on drug diffusion from DEB into a gel matrix in order to model tissue diffusion, which will complete the picture.

4 CHAPTER FOUR: EFFECT OF HYPOXIA ON VANDETANIB ACTIVITY *IN VITRO*

4.1 Introduction

4.1.1 Vandetanib as an anti-cancer agent

Target	IC ₅₀
VEGFR-2	40nM
VEGFR-1	1.6µM
VEGFR-3	110nM
EGFR	500nM
PDGFRβ	1.1µM
Tie-2	2.5µM
FGFR1	3.6µM

Table 4.1 Tyrosine kinase receptors inhibited by vandetanib and the respective IC₅₀ in enzyme assays. Adapted from Wedge *et al.* (2002)

Vandetanib is a small molecule tyrosine kinase inhibitor that potently inhibits VEGFR-2 and 3, as well as EGFR at a sub-micromolar concentration [84]. Table 4.1 shows the additional targets of vandetanib as well as the *in vitro* IC₅₀ for each target. The VEGFR receptors, platelet derived growth factor receptor (PDGFR) and Tie-2 all have functions in regulating angiogenesis [15, 205, 206]. The mechanism of action of vandetanib against solid tumours is therefore likely to be primarily an anti-angiogenic effect, with inhibition of VEGFR-2

disrupting endothelial cell growth, proliferation and migration, compromising the vascular network supplying the tumour. This effect has been observed in pre-clinical tumour models [207, 208] but has yet to be confirmed using imaging biomarkers in clinical studies on vandetanib [93]. However, vandetanib also exhibits direct anti-proliferative effects on tumour cells via EGFR inhibition and, at higher concentrations, inhibition of FGFR and PDGFR [87, 209]. Therefore, it is of interest to characterise this anti-proliferative effect against HCC cell lines, and specifically in hypoxic conditions in order to identify any effects that inducing ischaemia *via* TACE may have on the anti-tumour activity of vandetanib. The limited available data on use of vandetanib in hypoxic conditions pointed to it being equipotent or slightly hypoxia-selective in non-HCC cell lines [113].

A further purpose for performing *in vitro* viability assays with vandetanib is to confirm the dose at which anti-proliferative effects are seen and cross-reference this with

expected tumour concentrations of drug following DEB injection. As a reference, injection of sunitinib-eluting beads into rabbit livers resulted in average liver concentrations of 14.9 $\mu\text{g/g}$ at 6 hours post treatment [79]. Assuming a liver tissue density of approximately 1 g/mL [210], this equates to a concentration of about 37 μM of sunitinib. Bearing in mind that in this study the dose of sunitinib in the beads was 30 mg per mL of beads, which were delivered non-selectively into the common hepatic artery, there is potential for much higher concentrations in tumour when 100 mg/mL vandetanib-DEB are delivered selectively.

4.1.2 Vandetanib and hypoxia

Figure 4.1 summarises the pathways likely to be implicated in the treatment of liver tumours with vandetanib in a hypoxic environment. Downstream of VEGFR2 and

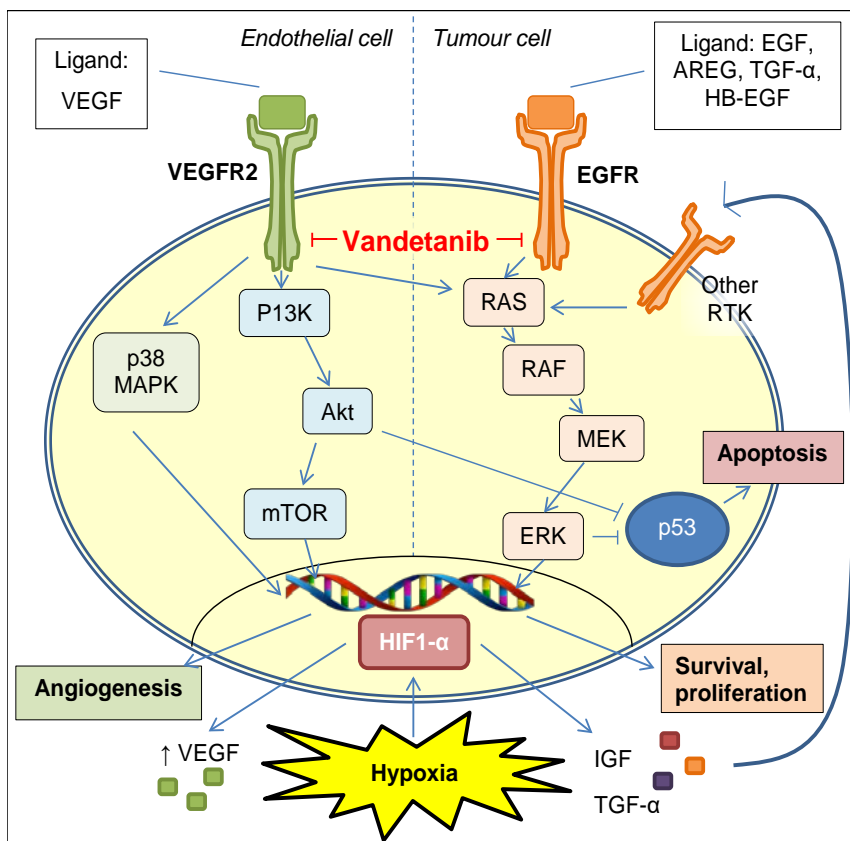


Figure 4.1 Simplified representation of the molecular pathways likely to be implicated in vandetanib-TACE. Vandetanib inhibits the tyrosine kinase domain of VEGFR2 and EGFR, which are normally activated by their ligands VEGF and EGF. This triggers signalling cascades that have functions in promoting angiogenesis, tumour cell survival and proliferation, and inhibition of apoptosis. Additionally, hypoxia induced by embolisation therapy results in stabilisation of HIF-1 α , which switches on expression of target genes that can further encourage cell survival and angiogenesis, including production of growth factors VEGF, IGF and TGF- α [82, 262, 291]. Original in colour.

EGFR, the PI3K/Akt/mTOR and RAF/MEK/ERK (MAP kinase) pathways transduce the signal from tyrosine kinase inhibitors activated by the binding of growth factors such as VEGF and EGF. Ultimately this leads to many cellular responses, including changes in gene expression, inhibition of apoptosis, and an increase in cell proliferation. Both pathways have been shown to be positive regulators of HIF-1 α [211].

4.1.2.1 PI3K/Akt/mTOR pathway

The PI3K/Akt/mTOR pathway coordinates cellular responses to growth factors, nutrients, cytokines, mitogens, and stress. In the presence of growth factors and nutrients, Akt becomes activated *via* PI3K and acts upon a vast number of substrates involved in diverse cellular functions [212]. Activated Akt can directly or indirectly inhibit apoptosis, *via* inhibition of pro-apoptotic proteins such as Bad and p53. Akt can also activate mTOR, which upon forming complexes mTORC1 or mTORC2, results in increased protein synthesis, lipogenesis and cell metabolism, ultimately encouraging cell cycle progression and proliferation [213].

Akt was originally discovered as a proto-oncogene and it is not surprising that the PI3K/Akt/mTOR pathway is deregulated in many forms of cancer, including HCC [214, 215]. One mechanism of deregulation is the loss of expression of PTEN, a tumour suppressor protein that negatively regulates the pathway by suppressing phosphorylation of Akt. PTEN is frequently mutated in HCC, and is known to have low expression in HepG2 and Hep3B cells [216, 217]. The PI3K/Akt/mTOR pathway has been shown to mediate resistance to sorafenib in HCC cells, which was reversible by inhibition of Akt [218].

Hypoxia has been observed to activate the PI3K/Akt/mTOR pathway [219], however mTORC1 should be negatively regulated in hypoxia due to inhibition by the stress-activated protein REDD [220]. Constitutive activation of the pathway by loss of PTEN activity may be sufficient to overcome this inhibition in cancer.

4.1.2.2 MAP Kinase (MAPK) pathway

The MAPK/ERK pathway is stimulated by a number of receptor tyrosine kinases involved in cellular growth and differentiation, including EGFR. The core components of the cascade are Raf, MEK, and ERK, which are serine/threonine protein kinases that phosphorylate each other in turn. Activated ERK1/2 regulates targets within the cytosol

but can also translocate to the nucleus to activate various transcription factors involved in cell proliferation [221].

Activation of the MAPK pathway in human HCC is poorly correlated with prognosis and is present in 50-100% of HCC tumours [222]. ERK has a role in stimulating HIF-1 α translation and can also promote its function as a transcription factor [223]. As well as VEGF, hypoxia can upregulate other ligands that stimulate the MAPK pathway *via* RTK such as insulin-like growth factor (IGF) and PDGF [224, 225].

P38 MAPK is also activated by growth factor signalling, as well as inflammatory cytokines and cellular stressors. Whilst there is a lot of evidence that p38 MAPK suppresses tumorigenesis [226], in hypoxic conditions p38 becomes activated, it can activate HIF-1 α and is involved with the production of VEGF which contributes to angiogenesis [227]. High phospho-p38 levels in human HCC tumours were correlated with large tumours, presence of satellite tumours and poor survival [228].

4.1.3 *Aims of this chapter*

- Determine the IC₅₀ of vandetanib against HCC and endothelial cells in normoxic and hypoxic conditions.
- Investigate the mechanism of action of vandetanib against HCC cell lines by detecting apoptosis.
- Examine expression of key proteins in vandetanib treated cells in normoxic and hypoxic conditions.

4.2 **Materials and Methods**

4.2.1 *Cell lines*

HepG2 cells were purchased from European Collection of Authenticated Cell Cultures (ECACC 85011430) and maintained in Minimum Essential Medium (Gibco) supplemented with 10% fetal bovine serum (FBS) and 1% non-essential amino acids (NEAA, Gibco). Hep3B cells were a gift from Dr. Armand de Gramont at the Department of Oncology, CHUV, Switzerland and were maintained in RPMI 1640 (Gibco) with 10% FBS. JHH6 cells were purchased from the Japanese Collection of Research Bioresources Cell Bank (JCRB1030, original depositor Dr. Seishi Nagamori) and cultured in RPMI 1640 with 10% FBS. Cells used for experiments were below passage number 20.

Pooled donor HUVECs pre-screened for expression of angiogenesis markers (Axl, eNOS, Tie-2, VEGFR-2) were purchased from Lonza (Cat. no. C2519AS) and were cultured in Endothelial Growth Medium (EGM-2, Lonza) consisting of Endothelial Basal Medium supplemented with EGM-2 Bullet Kit containing FBS (final concentration 2%) and endothelial growth supplements.

4.2.2 Cell culture protocols

Cell culture in normoxic conditions was carried out under aseptic conditions inside a laminar flow cell culture hood (HERA Safe, Heraeus). All equipment was sterilised before use, and surfaces were wiped with 70% industrial methylated spirits. Cells were cultured in T75 tissue culture coated flasks (NUNC) and incubated at 37 °C, 95% air and 5% CO₂. Cells were passaged when confluence reached 70-80%. The passage protocol consisted of washing cells once in sterile PBS, before adding 5 mL 0.05% Trypsin-EDTA (Gibco). Once cell detachment was observed, the trypsin was quenched with either 10 mL complete medium containing FBS for HCC cells or 10 mL defined trypsin inhibitor (Gibco) for HUVECs. Cells were transferred to a centrifuge tube and centrifuged for 5 minutes at 500 g (HCC cells) or 200 g (HUVECs). The cell pellet was resuspended in 1 mL of complete medium and an appropriate fraction (dependent on cell confluence and doubling time) was placed into a new flask containing pre-warmed medium.

4.2.3 Hypoxic incubation

4.2.3.1 Baker Ruskinn InvivoO₂ hypoxic workstation

The InvivoO₂ 400 physiological cell culture workstation was purchased from Baker Ruskinn (Figure 4.2). The unit consists of a sealed chamber accessible through gloveless sleeve entry ports. The unit is supplied with lines of nitrogen, oxygen and carbon dioxide. The oxygen sensor is automatically calibrated and allows sensitive control of oxygen levels *via* automatic purging with nitrogen. Internal HEPA filtration permits carrying out experimental manipulation in hypoxic conditions whilst ensuring aseptic conditions.



Figure 4.2 The InvivoO₂ Hypoxia chamber. Original in colour.

For all hypoxic experiments, the atmosphere inside the chamber was maintained at 37 °C, 1% O₂ and 5% CO₂ ($\pm 0.2\%$). Humidity was set at the maximum of 85% and was maintained with the use of provided Aquasorb sachets. Culture plates were introduced to the chamber *via* an interlock which was automatically purged to match the atmosphere inside the main chamber before transfer to the internal culture shelves.

4.2.3.2 Hypoxic cell incubator

A proportion of the cell culture work in this thesis (viability assays on HCC cell lines) was carried out in the University Hospital of Lausanne (CHUV, Switzerland). As a sealed workstation was not available, a multi-gas incubator was used instead (MCO-5M-PE, Panasonic). The atmosphere was maintained in the same conditions of 37 °C, 1% O₂ and 5% CO₂. Care was taken not to open the incubator during incubation periods to avoid fluctuation of oxygen level.

4.2.4 Preparation of drug solutions

For cell based assays, 0.5 mg/mL vandetanib (Astra Zeneca, UK) stock solution was prepared in 0.05M HCl. Doxorubicin (Hisun, China) solution was prepared in ultrapure water at 0.5 mg/mL. The drug stock solutions were sterile filtered using a 0.2 μm pore sterile syringe filter (Corning) and subsequent dilutions of the stock solutions in cell culture medium were performed in sterile conditions prior to use.

4.2.5 Cell viability assays

4.2.5.1 WST-1 assay principle

WST-1 is a water soluble tetrazolium salt used for assessing cell metabolic activity. WST-1 is similar to the widely used MTT assay, with the advantage of being soluble in cell culture medium meaning no additional solubilisation step is required before reading absorbance. WST-1 is reduced by NADH and NADPH enzymes in the presence of intermediate electron acceptors to a soluble formazan, a coloured compound with a maximum absorbance at 440 nm. The reduction of WST-1 occurs extracellularly by electron transport across the plasma membrane of dividing cells [229]. An increase in the number of viable cells results in a rise in overall dehydrogenase activity, and therefore the amount of formazan dye formed is also increased which can be directly correlated to the number of metabolically active cells in the culture. As the WST-1 assay only gives information about the number of viable (metabolically active) cells, complementary assays should be used to provide insights into the mechanism of any changes in cell viability seen as a result of exposure to pharmacologically active compounds, for instance cell cycle arrest, apoptosis, or necrosis.

4.2.5.2 Cell titration experiments and vehicle controls

Prior to exposure of cells to vandetanib, the optimum seeding density for each HCC cell line in hypoxic and normoxic conditions was established by performing a cell titration experiment (data not shown). Briefly, cells were seeded in 96 well plates at a range of densities from 500 – 10,000 cells per well. The plates were cultured in either normoxic or hypoxic conditions for 96 hours after which 20 μ L per well of WST-1 reagent was added, incubated for 30 minutes and OD measured at 440 nm. The seeding density which yielded the optimum absorbance in the linear range of the assay was selected for subsequent experiments: 500 cells per well, 1000 cells per well and 5000 cells per well for JHH6, Hep3B and HepG2 cells respectively.

Preliminary cell viability experiments and background controls were performed using vehicle only (0.05M HCl) diluted in cell culture medium at the relevant concentrations. There were no significant effect on calculated cell viability with any concentration of HCl (amount equivalent to up to 100 μ M vandetanib solution) (data not shown). The buffering properties of the cell culture medium kept the drug solutions in the appropriate pH range for cell culture (7.0-7.7) as there was minimal colour change of

the phenol red indicator. There was no dose dependent effect of vandetanib solution on background WST-1 absorbance (no cells), therefore the highest dose (50 μ M) was selected for the cell-free blank. The UV absorbance maxima of vandetanib were previously determined to be 217, 250 and 330 nm, whereas the WST-1 assay is read at 440nm.

4.2.5.3 WST-1 assay procedure – HCC cell lines

Cells were seeded into 96 well plates (Costar) containing 200 μ L of complete medium per well and allowed to equilibrate in normoxic conditions for 24 hours. At this point, media was aspirated from the cells and replaced with media containing vandetanib of concentrations ranging from 0.1 – 50 μ M. The first column contained cells with media only (control), and the last column used contained no cells with 200 μ l of 50 μ M of vandetanib (blank). Empty wells were filled with sterile PBS to reduce evaporation. Figure 4.3 shows the plate layout used for the assay.

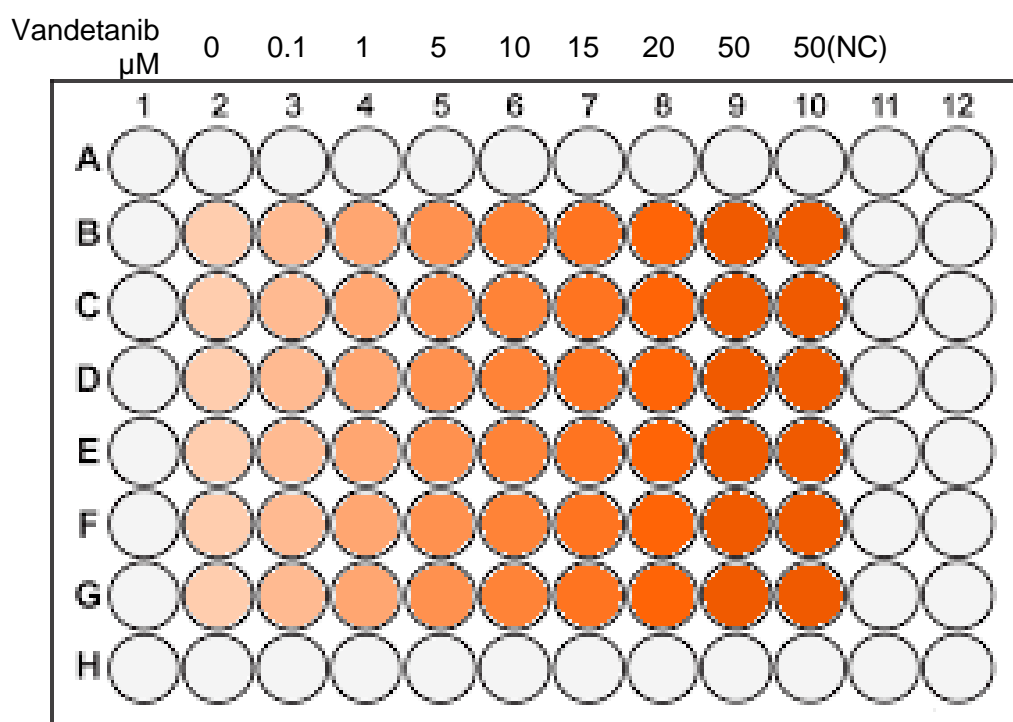


Figure 4.3 WST-1 Assay plate layout. NC = no cells. Original in colour.

After addition of drug, plates were placed in either the normoxic (21% O₂) or hypoxic (1% O₂) incubator for 72 hours. A 72 hour incubation period was selected due to the long 19 day half-life of vandetanib in humans (FDA, 2010). At the end of the incubation period, 20 μ L of WST-1 reagent (Takara) was added to each well and the plate was placed back into the respective incubator for 30 minutes. The absorbance was then read

on a multi-well plate reader after 5 seconds of gentle shaking. The wavelength used was 440 nm with a reference reading at 630 nm which was subtracted from all readings.

4.2.5.4 WST-1 assay procedure – HUVECs

For HUVECs, a similar procedure was followed, however a 72 hour incubation period was not optimal for maintenance of the cells. Significant cell death was observed in untreated samples at various seeding densities. Therefore, a 24 hour incubation period was selected.

HUVECs were seeded in supplemented EGM-2 (2% FBS) at a density of 2500 cells per well in a 96 well plate and allowed to equilibrate for 24 hours in normoxic conditions. The media was removed and replaced with EBM-2 (basal medium) containing 2% FBS and 3 ng/mL VEGF (Peprotech) with vandetanib ranging from 0-20 μ M and incubated for 24 hours in either normoxic or hypoxic conditions. 20 μ L of WST-1 reagent was added to each well and incubated for 1 hour. Absorbance was read in a multi-well plate reader as before.

4.2.5.5 Viability calculations and statistical analysis

The percentage cell viability was calculated as follows:

$$\frac{(S - \text{mean CF})}{(\text{mean NC} - \text{mean CF})} \times 100$$

Where: S = sample absorbance; CF = cell free blank absorbance; NC = negative (media only) control absorbance.

Each experiment was repeated a total of 3 times. In order to calculate IC₅₀ and compare dose-response data between normoxic and hypoxic conditions, a variable slope, four parameter dose-response curve was fitted to log(vandetanib dose) vs percentage viability in Prism 6 software. A comparison of fits was performed using the extra-sum-of-squares F test between normoxic and hypoxic curves which indicated whether normoxic and hypoxic IC₅₀ were significantly different.

4.2.6 *Detection of apoptosis and cell cycle analysis*

4.2.6.1 NucleoCounter® DNA fragmentation assay

During apoptosis, calcium and magnesium-dependent nucleases are activated which degrade DNA. This means that within the DNA there are nicks and double-strand

breaks causing fragmentation. This late event of apoptosis is detected using DNA content analysis to measure cell having less than 1 DNA equivalent (so-called Sub-G1 cells having less than 2C DNA content). Using image analysis, the NucleoCounter® NC-3000™ (ChemoMetec, Denmark) system automates detection of cells with fragmented DNA (sub-G1 cells) by quantifying the intensity of the DNA binding dye, 4',6-diamidino-2-phenylindole (DAPI).

Cells were seeded into T-25 flasks and grown until 70% confluent. The media was removed and replaced with fresh media or media containing 25 µM vandetanib and cells were incubated in normoxic or hypoxic conditions for 24 hours. After incubation, the cells were trypsinised and pooled with the incubation medium containing detached cells. Cells were centrifuged at 500 g for 5 minutes, counted, and resuspended to a concentration of 1-2x10⁶ cells in 0.5 mL PBS. 4.5 mL of ice-cold 70% ethanol was added to fix the cells, which were stored at 4 °C overnight. Cells were centrifuged as before and washed once in PBS to remove low molecular weight DNA that was leached from apoptotic cells. Finally the cell pellet was resuspended in DAPI solution (1 µg/mL DAPI, 0.1% triton X-100 in PBS). Cells were loaded into NC-Slide A8 chamber slides and analysed for DAPI stain intensity, relating to the amount of high molecular weight DNA within the cells. Output data was analysed with FlowJo® flow cytometry software in order to determine cell cycle distribution.

4.2.7 Detection of phospho and total EGFR by western blotting

Composition and origin of materials used in western blotting are listed in Table 4.2.

Table 4.2 Materials used in western blotting.

Material	Composition	Manufacturer
Sample buffer (Laemmli) 2x	4% SDS, 20% glycerol, 10% 2-mercaptoethanol, 0.004% bromophenol blue, 0.125 M Tris HCl	Sigma-Aldrich
Running buffer	25 mM Tris, 192 mM glycine, 0.1% SDS ; pH 8.6	Sigma-Aldrich
Transfer buffer	Tris glycine pH 8.5	Thermo-Fisher
Blocking buffer	5% BSA in TBS 0.025% Tween® 20	Thermo-Fisher
Wash buffer (TBST)	0.15 M sodium chloride, 0.050 M Tris HCl, 0.05% Tween® 20; pH 7.6	Sigma-Aldrich
Mini-PROTEAN® TGX™ Precast Protein Gels	4-20% polyacrylamide	Bio-Rad
Precision Plus Protein™ Dual Color Standards	10-250kDa coloured protein standard ladder	Bio-Rad

HepG2, Hep3B and JHH6 cells were seeded in T-75 flasks and incubated in standard conditions until 70% confluent. Then, the media was removed and replaced with serum-free media containing increasing concentrations of vandetanib (0, 1, 10 and 25 μ M) and cells were incubated in normoxic or hypoxic conditions for 4 hours, followed by stimulation with 100 ng/mL EGF (Peprotech) for 30 minutes. Cells were then washed in ice-cold PBS, harvested by scraping and centrifuged. The cell pellets were lysed on ice in RIPA buffer (Thermo Fisher), which was supplemented with phosphatase inhibitors (PhosSTOP, Roche) and protease inhibitors (cOmplete, Roche) according to the manufacturer's instructions. Lysates were centrifuged at 4 °C at 13000 x g for 15 minutes and the supernatant was collected and stored at -80°C until use.

The protein concentration of cell lysates was determined by Bradford assay (Sigma-Aldrich). 30 μ g of protein per lane was mixed with equal volume of 2x Laemmli sample buffer. Samples were boiled at 90 °C for 5 minutes prior to loading into precast SDS-PAGE gels. Proteins were separated by electrophoresis at 200V for 40 minutes. Proteins were transferred to a nitrocellulose membrane pre-soaked in transfer buffer using a semi-dry transfer apparatus, for 1 hour at 18 V. Membranes were blocked overnight at 4 °C in blocking buffer (5% BSA in TBST). The membranes were then transferred to falcon tubes and probed with primary antibody diluted in blocking buffer, overnight at 4 °C on a carousel mixer. Membranes were washed with wash buffer (TBST) once quickly, then three times for five minutes. Membranes were placed in falcon tubes again and incubated with HRP conjugated secondary antibody diluted in blocking buffer for 1 hour at room temperature on a roller mixer. The membranes were washed as before, then signal was developed using an enhanced chemiluminescence (ECL) kit (Pierce™ ECL Plus, Thermo Fisher) and detected by exposure to autoradiography film (Amersham Hyperfilm ECL, GE Healthcare, UK). Antibody details and dilutions are listed in Table 4.3.

Table 4.3 Antibody pairings and dilutions used in western blotting

Protein of interest	Primary antibody	Secondary antibody
Phospho EGFR (Y1086)	Ab32086 (Abcam) 1:3000	Goat anti-rabbit IgG (HRP) ab6721 (Abcam) 1:50000
EGFR	Ab32077 (Abcam) 1:6000	Goat anti-rabbit IgG (HRP) ab6721 (Abcam) 1:50000
Beta-actin	Ab8226 (Abcam) 1:10000	Rabbit anti-mouse IgG (HRP) ab6728 (Abcam) 1:50000

4.2.8 Measurement of VEGF in cell culture supernatants

HepG2, Hep3B and JHH6 cells were seeded in 24 well plates and allowed to equilibrate for 24 hours or until approximately 70% confluent. After washing cells in PBS, the culture medium was replaced with serum-free medium containing 0, 10 or 25 μM vandetanib or doxorubicin, and cells were incubated in normoxia or hypoxia for 24 hours. Conditioned culture medium was harvested and stored at $-20\text{ }^{\circ}\text{C}$. VEGF levels in the culture medium were quantified by a commercial VEGF ELISA kit (ab100662, Abcam) and normalised to the protein content of each sample as determined by Bradford assay (Sigma Aldrich).

4.2.9 Measurement of HIF-1 α levels

Levels of HIF-1 α were measured using a HIF-1 α ELISA kit (ab171577, Abcam) according to manufacturer's instructions. HepG2, Hep3B and JHH6 cells were seeded in 6 well plates and incubated until 80% confluent. Culture medium was replaced with serum-free medium containing 0, 10 or 25 μM vandetanib or doxorubicin, and cells were incubated in normoxia or hypoxia for 24 hours. To harvest cell extracts, the cells were washed in cold PBS and lysed in lysis buffer supplied with the ELISA kit. Lysates were stored at $-80\text{ }^{\circ}\text{C}$ until use. HIF-1 α levels in the cell extracts were quantified by ELISA and normalised to protein content of each sample as determined by Bradford assay (Sigma Aldrich).

4.2.10 MAPK phosphorylation antibody array

MAPK pathway phosphorylation in vandetanib treated JHH6 cells was screened using a membrane antibody array (ab211071, Abcam). All reagents were provided with the kit unless stated. Cells were grown in T-75 flasks until 70% confluent, then treated with 25 μM vandetanib in complete medium for 4 hours or 24 hours, in either normoxic or hypoxic conditions. Cells were washed in cold PBS, harvested and lysed in lysis buffer containing protease and phosphatase inhibitors for 30 minutes at 4°C . Extracts were centrifuged at $14000 \times g$ for 10 minutes and supernatant was collected for analysis. Protein content was determined by Bradford assay (Sigma-Aldrich). The experiment was performed on a single biological replicate.

In the MAPK phosphorylation antibody array, capture antibodies are supplied arrayed/spotted on a membrane with each pair of spots representing a different analyte. MAPK phosphorylation status in the control and treated cell extracts was determined according to the manufacturer's instructions. Briefly, after blocking the membranes, 300

μg of protein extract diluted in blocking buffer was applied to the membranes and incubated for 2 hours at room temperature. Membranes were washed and then probed with the detection antibody cocktail overnight at 4 °C. The wash step was repeated followed by application of HRP conjugated anti-rabbit IgG antibody for 2 hours at room temperature. After a final wash step the signal was detected using chemiluminescence and developed on x-ray film. The intensity of the spots for each analyte was recorded using densitometry on Image J¹ software, subtracting background signal and normalising to the positive control spots.

4.2.11 Growth factor antibody array

To screen the effect of vandetanib and doxorubicin on the secretion of a panel of growth factors in cell culture supernatant, a membrane antibody array was used (ab134002, Abcam). HepG2 cells were grown until 70% confluent in 6 well plates, and then medium was replaced with serum free medium containing either no drugs, 10 μM vandetanib or 10 μM doxorubicin. After 24 hours incubation in normoxic or hypoxic conditions, the conditioned media was harvested. The undiluted medium was applied to membranes pre-spotted with capture antibodies against 41 human growth factors and assayed according to the manufacturer's instructions using chemiluminescence. The intensity of the spots for each analyte was recorded using densitometry on Image J software, subtracting background signal and normalising to the positive control spots. The experiment was performed on a single biological replicate.

4.3 Results

4.3.1 Effect of vandetanib on HCC cell viability in normoxic and hypoxic conditions

Vandetanib dose-response curves were generated using the WST-1 assay in three HCC cell lines, comparing normoxic and hypoxic conditions over an incubation period of 72 hours. Vandetanib appeared to have a somewhat hormetic effect in all three cell lines with low doses ($\leq 1\mu\text{M}$) showing increased proliferation compared with untreated controls, but this was not consistent between normoxic and hypoxic conditions. Doses of $\geq 5\mu\text{M}$ had an anti-proliferative effect on all three cell lines regardless of oxygen level.

¹ Rasband, W.S., ImageJ, U. S. National Institutes of Health, Bethesda, Maryland, USA, <https://imagej.nih.gov/ij/>, 1997-2016.

4.3.1.1 HepG2

Concentrations of vandetanib above 10 μM consistently decreased HepG2 viability to levels below 10% of the non-treated control regardless of oxygen concentration (Figure 4.4). A variable slope, four parameter normalised dose response curve was fitted to the data using Prism software which enabled calculation of IC_{50} . A comparison of fits (extra-sum-of-squares F test) was performed between normoxic and hypoxic curves which indicated that the normoxic and hypoxic IC_{50} were significantly different (5.6 μM and 2.4 μM respectively, $p=0.0003$). These data show that vandetanib is slightly more potent against HepG2 cells in hypoxic conditions.

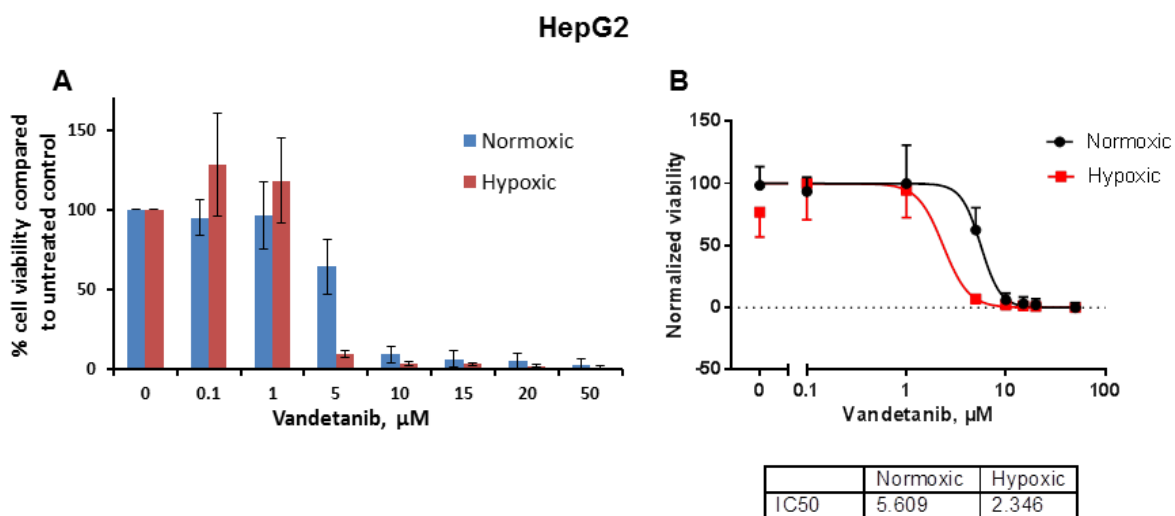


Figure 4.4 HepG2 viability in response to increasing doses of vandetanib as determined by the WST-1 assay. Cells were treated for 72 hours in either normoxic or hypoxic conditions. A) Viable cells at each dose as a percentage of the respective untreated control. B) Non-linear regression curve fitting to normalised dose-response data and the calculated IC_{50} . Data are the mean of three independent experiments \pm SD. Original in colour.

4.3.1.2 Hep3B

Vandetanib concentrations of 0.1 and 1 μM had no effect on Hep3B cell viability, but a decline in viability was seen in concentrations of 5 μM and above, with a complete loss of detectable viable cells at 50 μM (Figure 4.5). Curve fitting and comparison of fits (extra-sum-of-squares F test) between normoxic and hypoxic curves indicated that the normoxic and hypoxic IC_{50} were not significantly different ($p=0.555$). Therefore the IC_{50} for both conditions was calculated to be 3.7 μM .

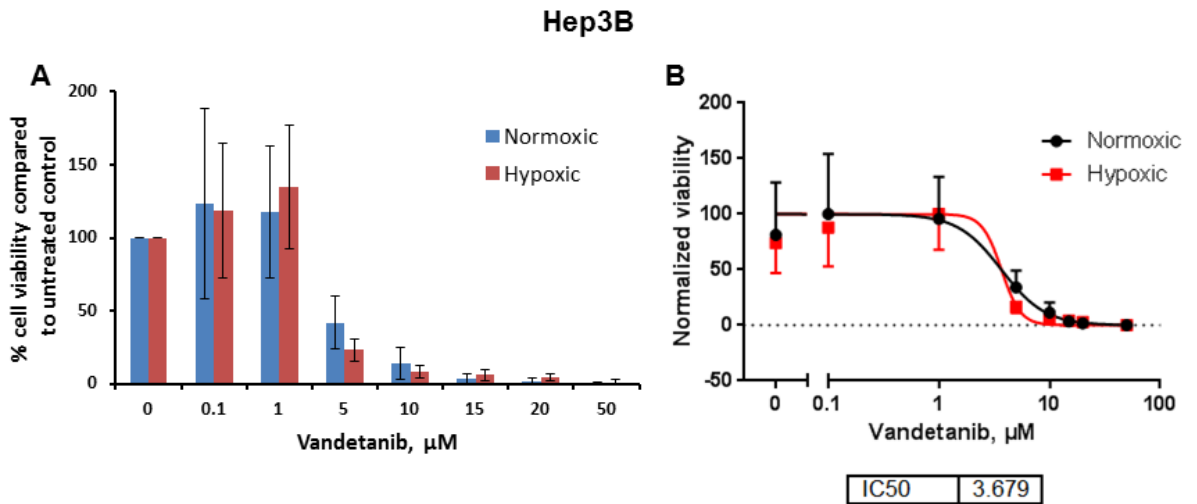


Figure 4.5 Hep3B cell viability in response to increasing doses of vandetanib as determined by the WST-1 assay. Cells were treated for 72 hours in either normoxic or hypoxic conditions. A) Viable cells at each dose as a percentage of the respective untreated control. B) Non-linear regression curve fitting to normalised dose-response data and the calculated IC₅₀. Data are the mean of three independent experiments \pm SD. Original in colour.

4.3.1.3 JHH6

There was a suggestion of an effect of low concentrations of vandetanib (0.1 and 1 μM) on hypoxic JHH6 cell viability however results were variable. At 5 μM viability was greatly reduced in both normoxic and hypoxic conditions and was further reduced with increasing concentrations of vandetanib leading to complete loss in detectable viability

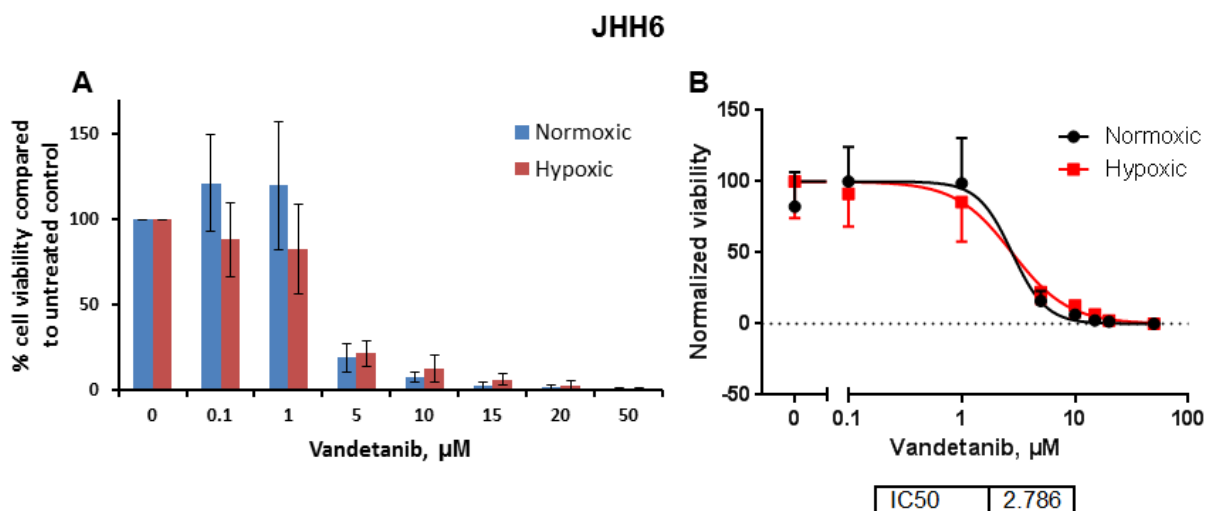


Figure 4.6 JHH6 cell viability in response to increasing doses of vandetanib as determined by the WST-1 assay. Cells were treated for 72 hours in either normoxic or hypoxic conditions. A) Viable cells at each dose as a percentage of the respective untreated control. B) Non-linear regression curve fitting to normalised dose-response data and the calculated IC₅₀. Data are the mean of three independent experiments \pm SD. Original in colour.

at 50 μM (Figure 4.6). Curve fitting and comparison of fits (extra-sum-of-squares F test) between normoxic and hypoxic curves indicated that the normoxic and hypoxic IC_{50} were not significantly different ($p=0.358$). Therefore the IC_{50} for both conditions was calculated to be $2.8\mu\text{M}$.

4.3.2 Effect of vandetanib on HUVEC viability in normoxic and hypoxic conditions

Vandetanib decreased viability of HUVEC after 24 hours incubation, in a dose dependent manner starting from $0.5\ \mu\text{M}$ (Figure 4.7 A). Non-linear regression analysis and comparison of fits (extra-sum-of-squares F test) indicated a significant difference in IC_{50} between normoxic and hypoxic conditions ($p<0.0001$), with HUVEC being slightly more susceptible to vandetanib in normoxic conditions ($\text{IC}_{50} = 2.1\ \mu\text{M}$) compared with hypoxic conditions ($\text{IC}_{50} = 3.1\ \mu\text{M}$) (Figure 4.7 B).

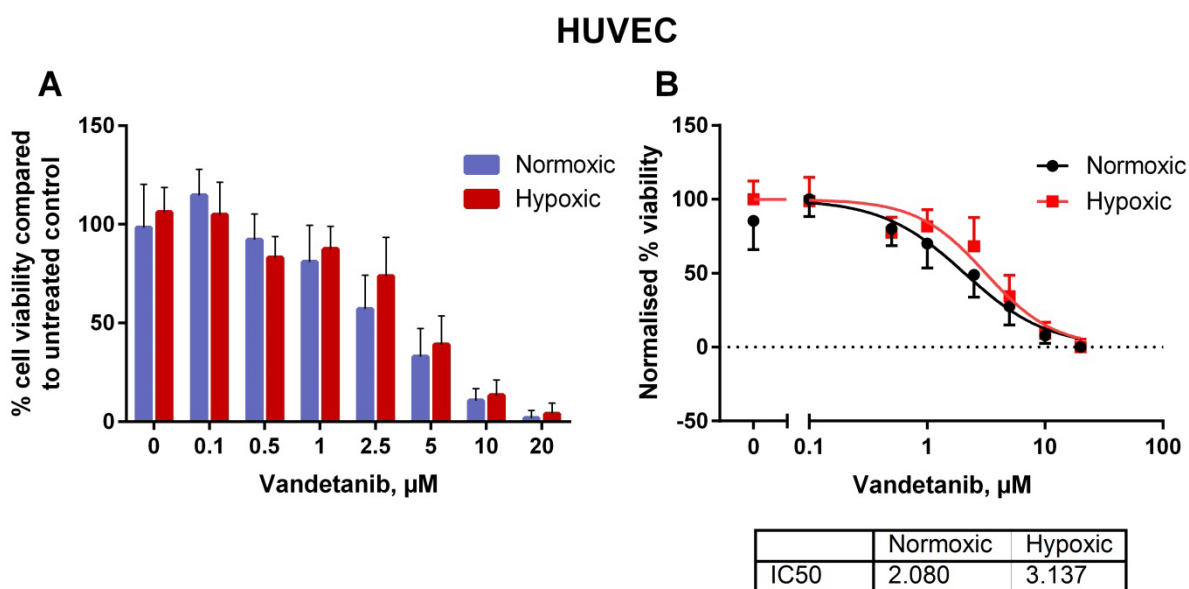


Figure 4.7 HUVEC viability in response to increasing doses of vandetanib as determined by the WST-1 assay. HUVEC were treated for 24 hours in the presence of VEGF in normoxic or hypoxic conditions. A) Viable cells as a percentage of respective untreated controls. B) Non-linear regression curve fitting of normalised dose-response data, and calculated IC_{50} . Data are the mean of three independent experiments \pm SD. Original in colour.

4.3.3 Effects of vandetanib and hypoxia on HCC and HUVEC cell cycle and apoptosis

At 24 hours incubation with 25 μ M vandetanib, a significant accumulation of cells in the subG1 fraction was seen in HepG2 cells and HUVEC, with HUVEC populations being almost entirely in the subG1 fraction (Figure 4.8). In Hep3B and JHH6 cells, although there was a suggestion of an increase in subG1 cells, this did not reach statistical significance. However, in these cell lines there was a significant accumulation of cells in the G1 phase (and subsequent reduction in the S phase) with vandetanib treatment, which suggests that vandetanib induces cell cycle arrest in the G1 phase, which may precede apoptosis with longer incubation times. Hypoxia alone (without vandetanib) did not significantly alter cell cycle distribution in any cell line, nor did it influence vandetanib mediated effects on cell cycle at this time point.

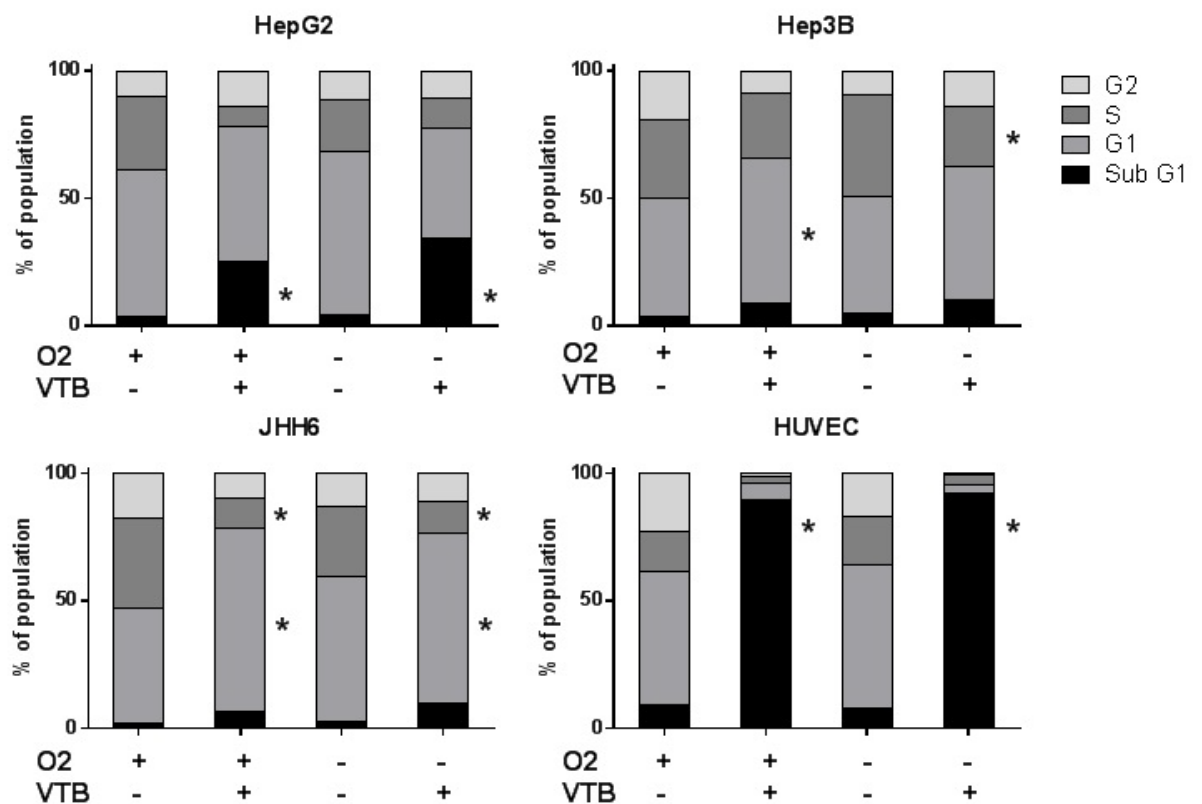


Figure 4.8 Cell cycle analysis of cells treated with vandetanib in normoxic or hypoxic conditions. HepG2, Hep3B, JHH6 HCC cells and HUVECs were incubated for 24 hours in normoxia (O₂ +, 21%) or hypoxia (O₂ -, 1%) in the presence (+) or not (-) of 25 μ M vandetanib (VTB). Bars denote proportions of cells in each cell cycle phase according to the DAPI cell cycle analysis/DNA fragmentation assay. Mean of 3 separate experiments. * denotes a significant difference (p < 0.05) in vandetanib treated samples compared with the respective untreated control.

4.3.4 Effect of hypoxia, vandetanib and doxorubicin on VEGF secretion from HCC cells

Incubation in hypoxic conditions led to a significant increase in secreted VEGF in all cell lines (Figure 4.9). In normoxia, the addition of vandetanib had little effect on the levels of VEGF in the cell culture supernatant. However, in hypoxia, vandetanib caused a dose dependent reduction in VEGF levels compared to the untreated control, with doses of 25 μM bringing VEGF levels back within the range of normoxic levels.

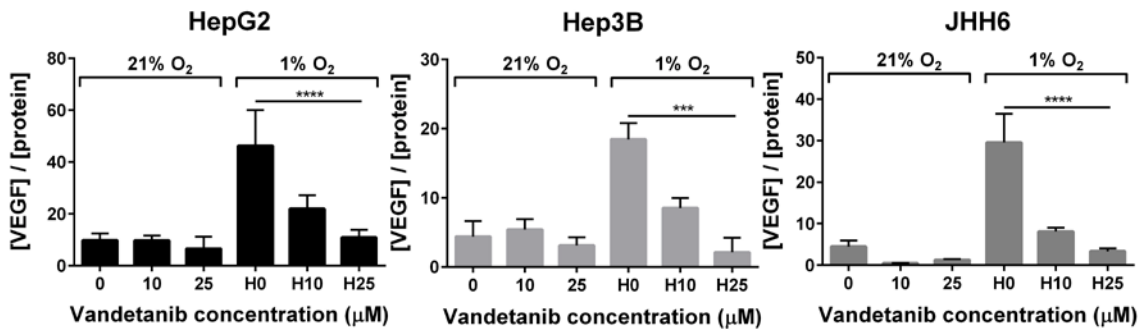


Figure 4.9 Normalised VEGF levels in cell culture supernatant. HepG2, Hep3B and JHH6 cells were exposed to vandetanib in normoxic (21% O₂) or hypoxic (1% O₂) conditions for 24 hours. Conditioned cell culture medium was harvested and VEGF levels were detected via ELISA. Values are presented as VEGF concentration divided by the total protein concentration of each sample. Mean \pm SD, n=3.

In order to ascertain if reduction of VEGF secretion was a unique effect of vandetanib, the assay was repeated with doxorubicin. Interestingly, doxorubicin treatment almost eliminated detectable VEGF from cell culture supernatant of all cell lines, at 10 μM and 25 μM (Figure 4.10). In contrast to vandetanib, the reduction of VEGF was evident in normoxic conditions as well as hypoxic.

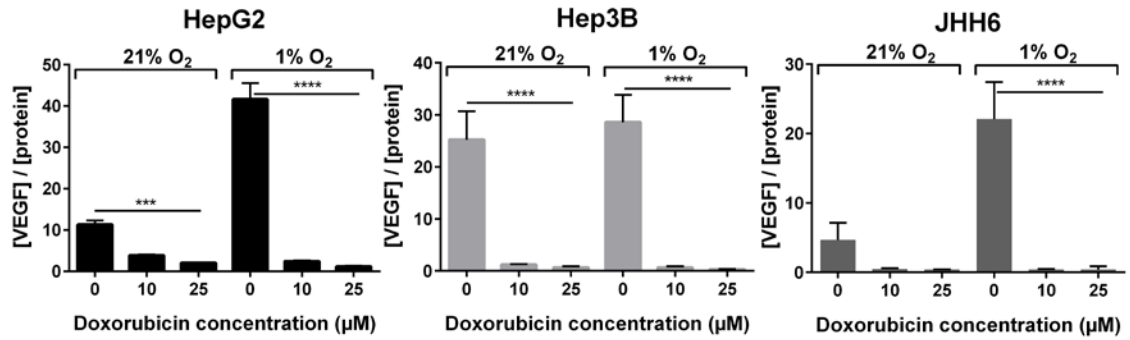


Figure 4.10 Normalised VEGF levels in cell culture supernatant. HepG2, Hep3B and JHH6 cells were exposed to doxorubicin in normoxic (21% O₂) or hypoxic (1% O₂) conditions for 24 hours. Conditioned cell culture medium was harvested and VEGF levels were detected via ELISA. Values are presented as VEGF concentration divided by the total protein concentration of each sample. Mean \pm SD, n=3.

4.3.5 Effect of hypoxia, vandetanib and doxorubicin on HIF-1 α levels in HCC cells

HIF-1 α levels were below the limit of detection in all cells cultured in normoxic conditions. Vandetanib only affected HIF-1 α levels significantly in JHH6 cells, causing a decrease at 25 μ M. In HepG2 and Hep3B cells, doxorubicin treatment at 10 and 25 μ M caused a marked increase in HIF-1 α in the hypoxic cell lysates (Figure 4.11).

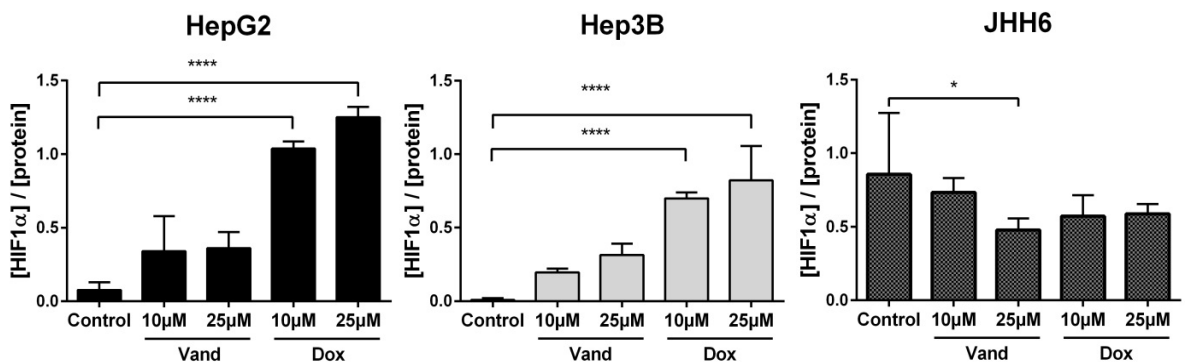


Figure 4.11 Normalised HIF-1 α levels in cell lysates. HepG2, Hep3B and JHH6 cells were exposed to vandetanib or doxorubicin in hypoxic conditions (1% O₂) for 24 hours. Cell lysates were prepared and HIF-1 α levels were detected via ELISA. Values are presented as HIF-1 α concentration divided by the total protein concentration of each sample. Mean \pm SD, n=3.

4.3.6 Phosphorylation of EGFR

The phosphorylation status of EGFR after vandetanib treatment in normoxic and hypoxic conditions was investigated using western blotting (Figure 4.12).

Hep3B and JHH6 cells showed strong expression of EGFR which was unaffected by vandetanib concentration and oxygen level, whereas HepG2 had low EGFR expression. Vandetanib inhibited phosphorylation of EGFR in a dose dependent manner, and the extent of inhibition did not appear to differ between normoxic and hypoxic conditions.

Hep3B cells expressed two phospho-EGFR species, one at ~170 kDa and one at ~130 kDa, visible as two bands in the western blot (Figure 4.12 B). The lower molecular weight form of the protein, possibly an unglycosylated intermediate, appeared more susceptible to inhibition of phosphorylation by vandetanib than the mature receptor.

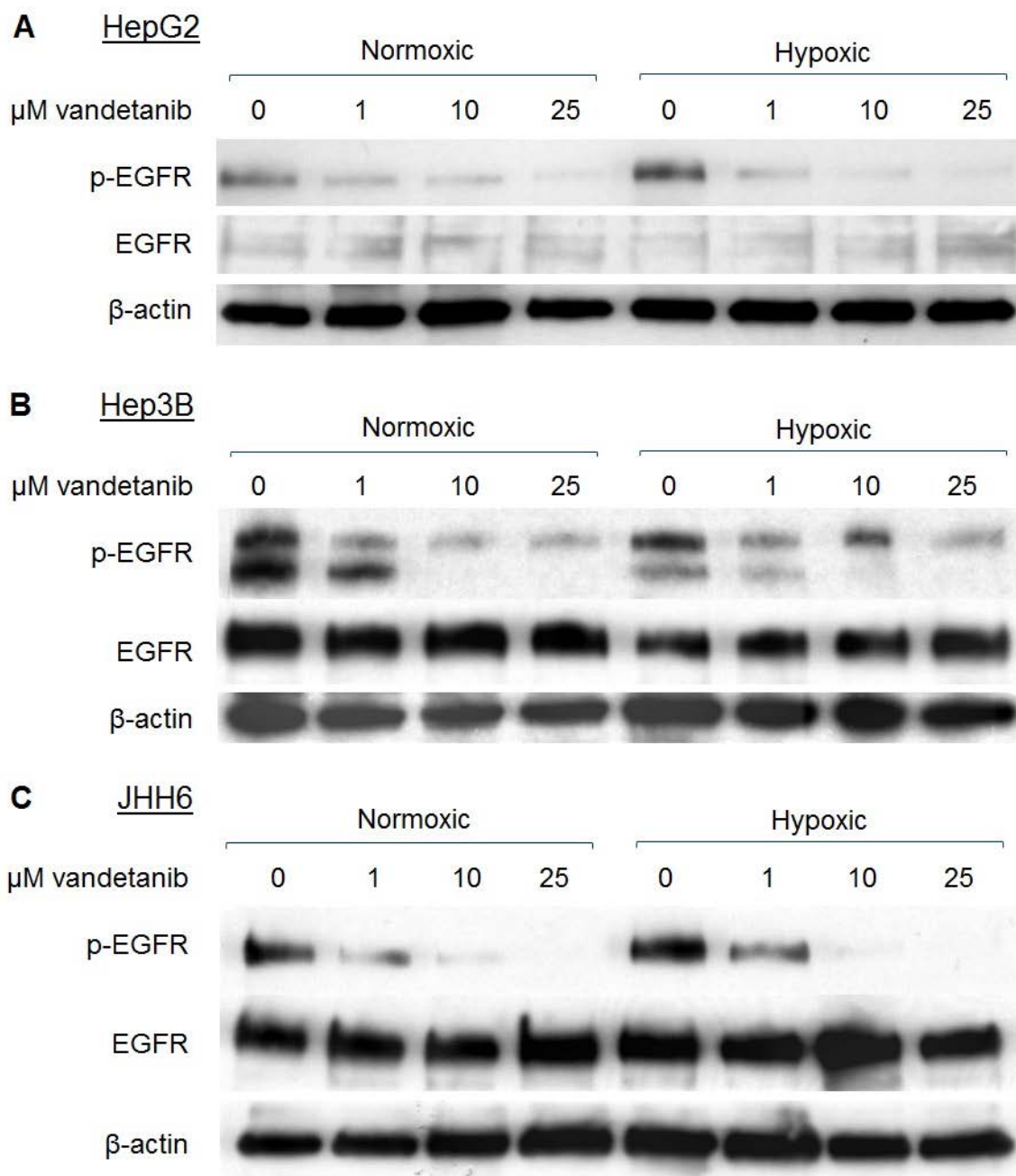


Figure 4.12 Western blots using antibodies against phospho-EGFR, total EGFR and beta-actin (loading control) in A) HepG2, B) Hep3B, and C) JHH6 cell lysates. Serum starved cells were untreated or exposed to 1, 10 or 25 μM vandetanib in normoxic (lanes 1-4) or hypoxic (lanes 5-8) conditions for 4 hours and stimulated with EGF for 30 minutes before lysis. Representative blots of 3 individual experiments.

4.3.7 *MAPK pathway activation*

Figure 4.13 shows the relative signal intensities of a selection of proteins analysed using the MAPK phosphorylation antibody array in JHH6 cell lysates. The results of the array did not suggest that vandetanib caused inhibition of proteins downstream of EGFR. In fact, there was a trend towards increased activation of key kinases such as Akt and ERK1/2 in vandetanib treated cells. This effect was particularly evident after 24 hours incubation with vandetanib in normoxic conditions. The only protein that appeared to show reduced phosphorylation with vandetanib treatment was Mtor, with a modest reduction in signal intensity for vandetanib treated samples compared with controls, in hypoxic conditions only.

The array suggested a trend towards increased baseline phosphorylation of many proteins in the MAPK pathway in hypoxic conditions, with signal intensities for p38, Akt, ERK1/2, MSK2, GSK3a, and Mtor increasing at least two-fold in the hypoxic control sample compared with the normoxic control at the 4 hour time point. This increase was still present at 24 hours albeit less pronounced.

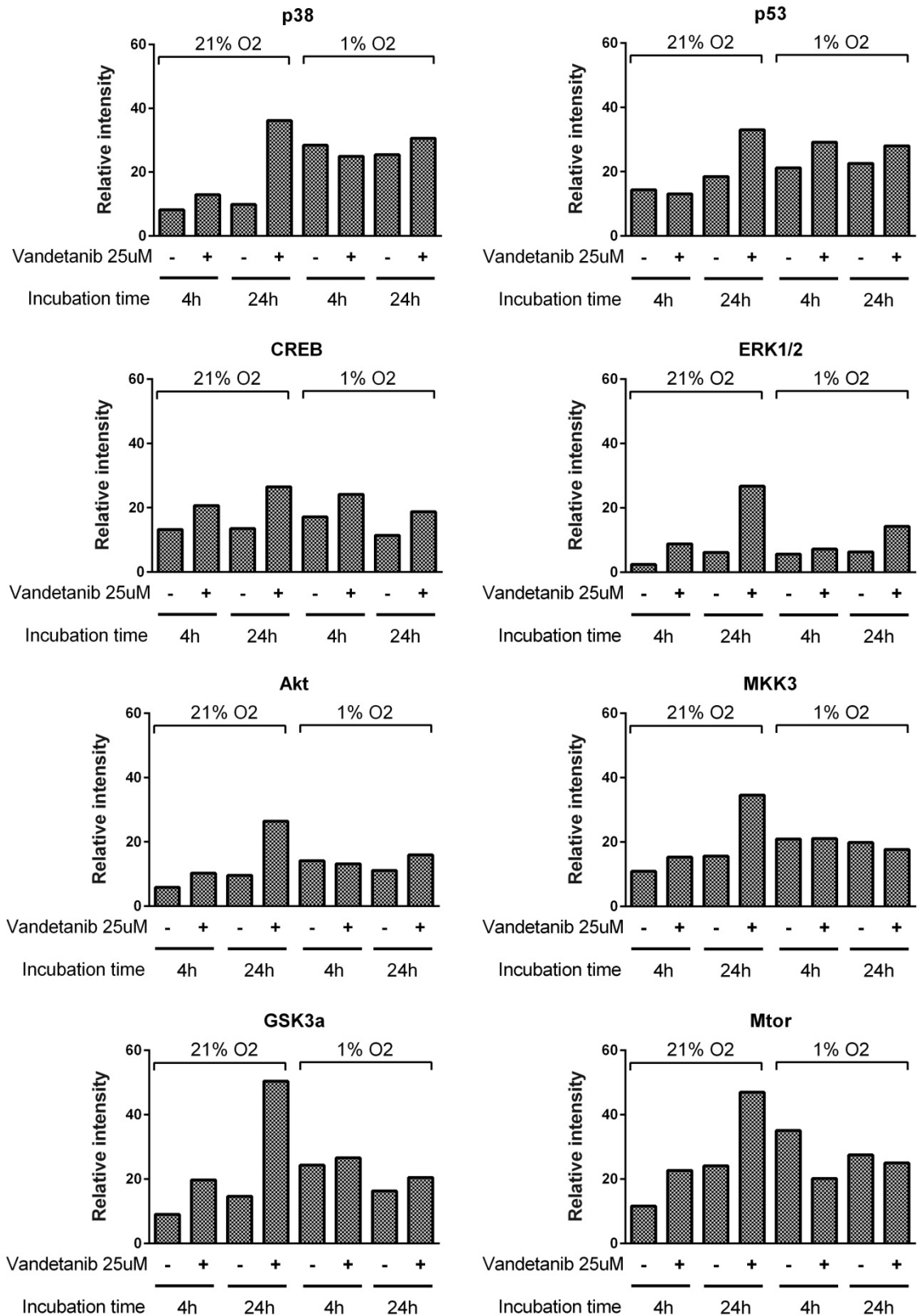


Figure 4.13 Relative spot signal intensities for phosphorylated forms of p38, p53, CREB, ERK1/2, Akt, MKK3, GSK3a, and Mtor in JHH6 cell lysates analysed with a membrane antibody array for MAPK signalling. JHH6 cells cultured in complete medium were untreated or treated with 25 μ M vandetanib for 4 hours or 24 hours, in normoxic (bars 1-4) or hypoxic (bars 5-8) conditions. Data are average of duplicate spots in a single experiment (n=1).

4.3.8 Growth factor secretion

Figure 4.14 shows the relative spot signal intensities for a selection of growth factors that exhibited differences between experimental conditions in a growth factor membrane antibody array. The levels of many growth factors were increased in hypoxic conditions, including IGF-I, IGF Binding proteins (IGFBP) 1 and 2, VEGF and PDGF-AA. Treatment with vandetanib also appeared to increase levels of certain growth factors in hypoxic conditions somewhat further, including IGF-I and II, EGF, some FGF family members, and soluble forms of VEGFR3 and IGFR. Levels of amphiregulin, an alternate ligand to EGFR, were increased by vandetanib in both normoxic and hypoxic conditions.

In keeping with results obtained from the VEGF ELISA, doxorubicin treatment again decreased levels of hypoxia induced VEGF, as well as levels of many other factors, including amphiregulin, IGF-I, IGFBP-1/2, and PDGFAA/BB.

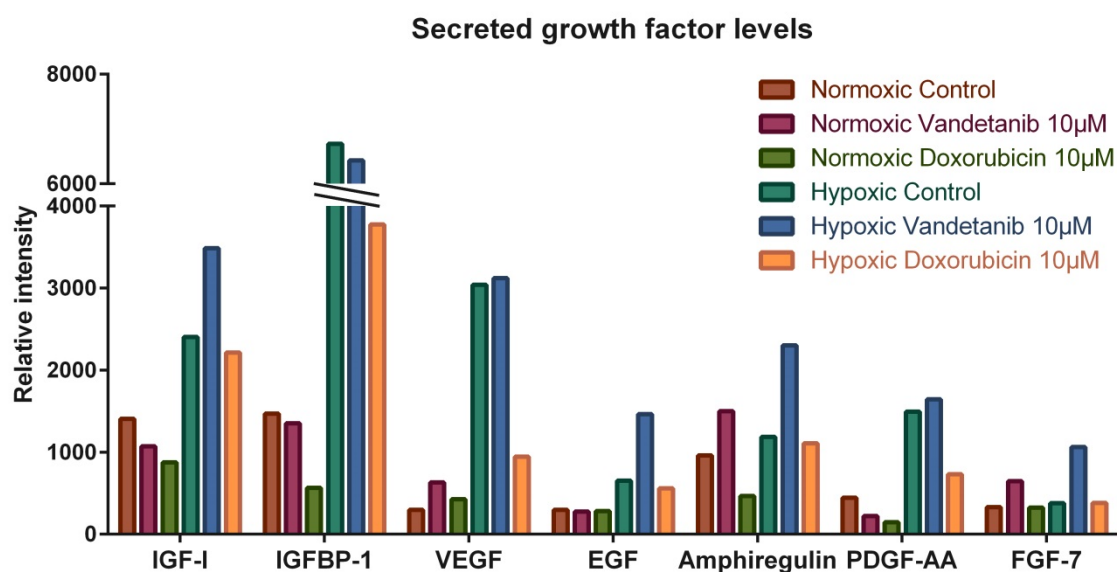


Figure 4.14 Relative spot signal intensities of selected growth factors analysed in the supernatant of HepG2 cells using a membrane antibody array. HepG2 cells were cultured in medium without serum with either no drug, or 10 µM vandetanib or doxorubicin in normoxic or hypoxic conditions. Conditioned medium was collected after 24 hours. Data are average of duplicate spots in a single experiment (n=1). Original in colour.

4.4 Discussion

4.4.1 Vandetanib induces cell cycle arrest and apoptosis in HCC cells and HUVECs with equipotency in normoxia and hypoxia

Hypoxia is known to induce chemoresistance in cancer cells [102]. Ischaemic conditions generated by the embolic effect of TACE may involuntarily promote survival of the remaining viable tumour by inducing HIF-mediated survival pathways such as metastasis, increased proliferation, and resistance to the drugs used in combination with treatment such as doxorubicin. Furthermore, it has been demonstrated that cells undergoing hypoxic stress in response to TACE-like ischaemia had a large increase in the quiescent population [230]. Since doxorubicin targets dividing cells by interfering with DNA replication, it is reasonable to postulate that hypoxic, quiescent cells will be resistant to its effects. Therefore, targeted agents such as vandetanib may be more suitable in the treatment of HCC *via* DEB.

In the present study it has been demonstrated that vandetanib greatly inhibits proliferation of three different HCC cell lines, HepG2, Hep3B and JHH6 at concentrations below 10 μ M. The cell lines used represent a range of phenotypes: hepatoblastoma, epithelial and undifferentiated/aggressive respectively. All cell lines had a similar IC_{50} , however JHH6 cells appeared to be the most susceptible to vandetanib in terms of the viability assay. Hypoxic conditions (1% O_2) had no significant effect on the IC_{50} of vandetanib against Hep3B or JHH6 cell lines, but HepG2 cells were slightly more susceptible to vandetanib in hypoxic conditions.

The IC_{50} achieved for vandetanib are in a similar range to the IC_{50} reported for doxorubicin against HepG2 and Hep3B cells in the literature (1.1-6.5 μ M for HepG2 and 3.5-8.7 μ M for Hep3B) [142, 231, 232]. Furthermore, hypoxia did not induce resistance to vandetanib in these cell lines, in contrast to doxorubicin which has shown to be less potent against HepG2 cells in hypoxic conditions [107].

Low doses of vandetanib (≤ 1 μ M) appeared to have a proliferative effect on HCC cells. This effect, known as hormesis, has been previously observed in a large number of biological systems, and with various anti-cancer compounds, including other tyrosine kinase inhibitors and anti-angiogenic agents [233, 234]. In general terms, it may arise from an 'overcompensation' mechanism, whereby the disruption in cell signalling

homeostasis caused by the inhibitor leads to a response that drives proliferation to a greater than normal extent that is not overcome by low drug doses. Specifically to vandetanib, a proposed mechanism could be that the increased production of VEGF or EGF which is evident following treatment [87, 93] drives cell proliferation which cannot be inhibited by low dose of the drug. This could be an effect to be cautious of as withdrawal of antiangiogenic therapy has been shown to cause a rebound in tumour aggressiveness via this mechanism [235]. Monitoring the vandetanib dose in the tumour over time after TACE will help confirm for how long the drug remains at a therapeutic concentration and when repeat administrations may be required to maintain tumour control.

Cell cycle analysis of vandetanib treated HCC cells gave an insight into the mechanism by which the drug suppresses cell proliferation. Vandetanib induced cell cycle arrest in Hep3B and JHH6 cells, as evident by an increased accumulation of cells in the G1 phase, after only 24 hours of treatment. With sustained vandetanib treatment, cell cycle arrest may lead to induction of apoptosis, as has been seen with other EGFR inhibitors such as erlotinib, mediated by caspase activity [29]. Of the three HCC cell lines, apoptosis induction as measured by the proportion of cells in the sub-G1 fraction was most evident in HepG2 cells after 24 hours of vandetanib treatment. This may be due to differing p53 status between the cell lines. HepG2 cells express wild-type p53, whereas Hep3B and JHH6 are p53-null and mutant, respectively [236, 237]. Functional p53 is involved in G1/S cell cycle arrest and the induction of apoptosis, and is mutated in over 50% of human cancers [238].

HUVEC had a similar vandetanib IC₅₀ to HCC cells, however this was based on 24 hour treatment whereas HCC cells were subjected to 72 hours treatment, therefore HUVEC are likely to be more sensitive to the anti-proliferative effects of the drug. Indeed, they were highly sensitive to high doses of vandetanib, as evident in the massive accumulation of cells (>80%) in the sub-G1 fraction after treatment with 25 µM for 24 hours. Slight differences in the dose-response curves fitted to the normoxic and hypoxic data indicated a marginal resistance to vandetanib for HUVEC in hypoxic conditions, for which the reason was not elucidated, but may be due to a compensatory increase in VEGF production in hypoxia [239]. An increase in hypoxic VEGF secretion was observed in HCC cells, however HCC cells are not dependent on VEGFR2 stimulation for proliferation as is the case for endothelial cells. This slight resistance in hypoxia is

unlikely to be relevant to the clinical setting. As DEB are delivered via the vasculature, endothelial cells are likely to be exposed to the highest concentrations of vandetanib in a TACE procedure. Assuming the majority of tumour feeding vessels are embolised, the vascular network is likely to be compromised due to drug-induced endothelial cell death.

4.4.2 Vandetanib reduces hypoxia induced VEGF secretion from HCC cells independently of HIF-1 α

Vandetanib inhibited secretion of VEGF in hypoxic cells, which is consistent with the studies of Pore *et al* (2006), using EGFR inhibitors gefitinib and erlotinib [117]. In contrast with Pore *et al* however, the effect was not significant in normoxic conditions in our study. HIF-1 α is a direct regulator of VEGF transcription, binding to a hypoxia response element (HRE) on the VEGF gene [240]. Accordingly, Pore *et al* found that VEGF was suppressed at mRNA level as well as protein level and the mechanism of this effect was likely to be a combination of interference with VEGF promoter activity by inhibition of Akt, and a suppression of HIF-1 α protein synthesis also mediated by the PI3/Akt pathway. It has already been demonstrated that HIF-1 α accumulation can be decreased in vandetanib treated HeLa cells [115] so given the lack of effect in normoxic conditions, this initially suggested that the mechanism of VEGF suppression in the HCC cell lines tested was HIF-1 α dependent. However, the effect of vandetanib on HIF-1 α levels in the HCC cells tested did not correlate with VEGF levels – in fact, there was a trend towards slightly increased HIF-1 α levels in hypoxic vandetanib treated HepG2 and Hep3B cells. Therefore, the decrease in VEGF levels may be a result of EGFR inhibition, which in turn suppresses the Sp1 transcription factor binding to VEGF promoter *via* Akt inhibition as was demonstrated with gefitinib [117].

The findings on HIF-1 α levels in this study are in contrast to other studies on the effect of EGFR inhibitors on HIF-1 α . Suppression of HIF-1 α by tyrosine kinase inhibitors has been reported several times, both by VEGFR inhibitors [115, 116] and EGFR inhibitors [117, 241]. VEGFR and EGFR share common downstream signalling pathways, namely PI3/Akt, which was shown to be implicated in the mechanism of HIF-1 α suppression in the aforementioned studies. EGFR activation has been shown to induce HIF-1 α *via* the PI3/Akt pathway [242-244], and blockade of this pathway consequently reduces HIF-1 α translation – Akt is known to directly stimulate the activity of translation initiation factors [245]. The EGFR inhibitor gefitinib was shown to inhibit hypoxia induced total

HIF-1 and prevent HIF-1 nuclear accumulation in breast cancer cells, whereas another EGFR and HER2 inhibitor, lapatinib, had no such effect, highlighting that differential downstream effects of tyrosine kinase inhibitors can occur despite targeting the same receptors [246].

Doxorubicin significantly increased HIF-1 α levels in HepG2 and Hep3B cells compared to untreated controls in hypoxic conditions, which to our knowledge has not been observed before. However, doxorubicin has been reported to increase HIF1- α activity in normoxic conditions in breast cancer cells [247]. Doxorubicin can stimulate MAPK pathway phosphorylation, activating ERK and p38 MAPK, which as previously mentioned can activate HIF-1 α [248]. Many studies have shown that HIF-1 α mediates resistance to doxorubicin and simultaneous inhibition of HIF-1 α improves doxorubicin efficacy [107, 249, 250]. Given that doxorubicin appears to upregulate HIF-1 α , how does this relate to the dramatic decrease in VEGF secretion in doxorubicin treated cells? Lee *et al.* (2009) found that while total HIF-1 α protein levels were unchanged by doxorubicin treatment in HCC cells, transcriptional activity was significantly decreased due to decreased binding of HIF-1 α to DNA. This led to a subsequent decrease in transcription of HIF target genes, including VEGF [251]. Likewise, Duyndam *et al.* (2007) found that doxorubicin suppressed basal and hypoxia induced VEGF at the mRNA, cellular and secreted levels [252]. Given that doxorubicin decreased secretion of several factors in normoxia as well as hypoxia, it is possible that doxorubicin may have had a non-specific dampening effect on overall protein translation *via* introduction of DNA damage, particularly at the higher doses used in this experiment. However, the growth factor array revealed that certainly not all factors tested were suppressed by doxorubicin, and the reduction of hypoxia associated factors such as VEGF or IGFBP-1 was far more pronounced than the other factors in the array.

4.4.3 Insights into potential mechanisms of resistance to vandetanib in the setting of TACE

Vandetanib prevented EGF mediated phosphorylation of EGFR in serum starved HCC cells from 10 μ M, at 4 hours exposure time. However, the MAPK phosphorylation array suggested that downstream effectors of EGFR, such as Akt and ERK1/2, were not inhibited at 4 or 24 h of treatment with a dose of 25 μ M, which is surprising given the clear effect this dose has on HCC cell viability and induction of cell cycle arrest. The reported ability of vandetanib to inhibit phosphorylation of Akt and ERK1/2 varies in

the literature, from complete inhibition at 5 μM [253], modest inhibition at 2 μM [254] and at HCC cell IC_{50} [27], no significant change at 10 μM [255] to vandetanib induced *activation* of Akt [256, 257]. Of course, these studies represent a large variety of doses, incubation conditions/times, and cell lines which can explain the variation in the results, but the finding in our study that vandetanib fails to inhibit Akt or ERK in JHH6 cells is not inconceivable. One possible explanation is that the MAPK array experiment was performed on cells grown in 10% serum conditions, in order to more closely mimic the *in vivo* situation where cells would have access to growth factors and nutrients. Therefore it may be the case that whilst EGFR was inhibited, the presence of growth factors such as IGF could have maintained MAPK pathway activation *via* IGF signalling. Indeed, the growth factor antibody array revealed that IGF was one of the most prevalent growth factors in HepG2 supernatant and was further upregulated in hypoxia.

If Akt and ERK inhibition are not required for inducing cell cycle arrest and apoptosis in HCC cells, this raises questions about how vandetanib causes these effects mechanistically. If the mechanism of action is not wholly dependent on EGFR inhibition, this could explain why HepG2 cells were the most susceptible to vandetanib induced apoptosis despite having the lowest EGFR expression of the cell lines. While EGFR overexpression might be considered a predictor of susceptibility to anti-EGFR therapy in some cases [258], this did not appear to be the case in our study or that of Gianelli *et al.* (2008) wherein the reported IC_{50} of vandetanib in 5 HCC cell lines did not correlate with relative EGFR abundance [27].

As far as vandetanib activating key downstream targets of EGFR, which seemed to be the case particularly in the normoxic 24 hour treatment group, this could be a case of rebound activation as a mechanism of resistance to tyrosine kinase inhibition. This has been observed in cases of resistance to EGFR, MET and FGFR inhibitors [259-261]. Additionally, vandetanib treatment appeared to lead to a slight increase in secretion of ligands capable of binding to EGFR, such as amphiregulin, TGF- α , HB-EGF and EGF, more so in hypoxic conditions, which could be a compensatory response to the receptor inhibition. This may not necessarily be a mechanism of resistance in the setting of vandetanib TACE however, as high sustained doses of the drug may be sufficient to maintain receptor inhibition regardless of the availability of ligands.

Hypoxia had a measurable effect on baseline activation of both MAPK pathways and growth factor secretion, which may be related to each other. Factors that were upregulated in hypoxia were IGF, IGF binding proteins (which can regulate IGF availability and mitogenic potential) and the pro-angiogenic factors VEGF and PDGF, which are known to be induced by HIF-1 α [262, 263]. These factors can all stimulate receptors that activate the P13K/Akt and MAPK pathways, and therefore may contribute to an autocrine growth factor signalling loop that encourages tumour proliferation and angiogenesis.

Overall, it must be kept in mind that the results of the antibody arrays represent one single experiment, so repeating the analysis and confirming with additional techniques is required in future work to ensure robustness and eliminate sources of non-experimental variation.

4.5 Conclusion

This chapter describes the effect of vandetanib on HCC cells and endothelial cells in hypoxic conditions, in order to mimic embolisation-induced hypoxia. Overall, hypoxia does not appear to affect the efficacy of vandetanib against HCC cells and HUVECs, having similar IC₅₀ in each condition and the same capacity to inhibit EGFR phosphorylation, and induce cell cycle arrest and/or apoptosis. However, more detailed investigation of the pathways involved using an antibody array revealed differential expression of certain proteins in hypoxia. These differences converge on the P13K/Akt and MAPK pathways, which may remain active despite vandetanib treatment due to redundancy in tyrosine kinase receptors that activate them and diversion of signalling pathways *via* these other receptors when EGFR is inhibited. The mechanism by which vandetanib induced cell cycle arrest/apoptosis in HCC cells despite having active Akt and ERK remains unclear. The results obtained using the antibody array are the first step towards identifying proteins of interest in the setting of vandetanib TACE and it is clear that more robust analysis is required on the role of Akt, ERK and perhaps cell cycle regulators such as cyclins, upon different cell lines at varying doses of vandetanib and lengths of incubation to gain a clearer picture on how vandetanib mediates its effects. In contrast with doxorubicin, vandetanib had the advantage of not significantly raising HIF-1 α levels nor being less potent in hypoxia, however both treatments suppressed VEGF secretion and doxorubicin also suppressed several other tumorigenic or angiogenic growth factors. Further studies as to whether these effects translate to the

in vivo environment will be of interest to compare the benefits of each drug, but perhaps there is also a rationale for an investigation into the efficacy of a combination of both drugs in the local delivery setting.

5 CHAPTER FIVE: *IN VIVO* EVALUATION OF VANDETANIB LOADED BEADS

5.1 Introduction

Hepatocellular carcinoma is a leading cause of cancer-related death worldwide. The American Cancer Society estimated 42,200 new cases and 30,200 deaths from liver cancer in 2018 in the US alone [264]. The disease has a poor prognosis owing to advanced stage at diagnosis, high rates of tumour recurrence and a lack of effective therapeutic options for tumours where surgical resection is contraindicated [265]. In 2007, the multi-kinase inhibitor sorafenib was approved for the treatment of advanced HCC and became the standard of care for this stage of disease. This demonstrated that the inhibition of growth factor receptors such as VEGFR and interference with MAPK signalling pathways was a viable strategy in combatting liver tumour growth [266]. However, oral sorafenib treatment has only a modest survival benefit and is associated with a high incidence of adverse events (AEs), up to 80%. Several of these AEs can be high grade and affect patient quality of life, including fatigue, diarrhoea and hand-foot skin reaction (painful skin swelling or lesions) and necessitate dose reduction or discontinuation of treatment [267]. As a result, in subsequent years numerous alternative targeted agents have been evaluated in an attempt to match the efficacy of sorafenib or provide a better tolerated treatment, with little success: sunitinib toxicities were more frequent than sorafenib [81], and regorafenib is approved for HCC but only as a second line treatment following failure of sorafenib [268]. Vandetanib, an inhibitor of VEGFR and EGFR kinases, has shown significant inhibition of tumour growth when administered orally in xenograft models of HCC. In a randomised, phase II, double-blind, placebo-controlled clinical study, vandetanib showed a weak signal of improvement in progression-free survival (PFS) and overall survival (OS) in unresectable advanced HCC [93].

Using DEBs in TACE offers potentially improved treatment outcomes by allowing a sustained high dose of anti-cancer agents local to the tumour site, whilst greatly reducing systemic exposure to the drug and therefore the risk of side effects [40, 41]. Vandetanib eluting beads have been developed as a candidate for the treatment of

intermediate stage HCC, offering an alternative delivery mechanism for this targeted drug combined with the anti-tumoral effects of ischaemic embolisation. Vandetanib has shown efficacy against HCC cell lines in hypoxic conditions, which warrants evaluation of the efficacy of vandetanib when delivered *via* DEBs in pre-clinical models of HCC tumours.

5.1.1 *Potential pre-clinical models*

As discussed in the first chapter of this thesis, several animal models of HCC are available for evaluating drug-eluting beads, each with their own advantages and limitations. The most commonly used model for evaluating efficacy of TACE procedures is the rabbit VX2 model. VX2 tumours are fast growing, hypervascular anaplastic squamous cell carcinomas, induced by a papilloma virus [269]. VX2 tumours are first established in the rabbit hind leg from injection of VX2 cell suspension. The developed tumour is then harvested and small fragments of viable tumour are excised for intrahepatic injection, which is usually performed by open surgery to directly expose the liver, which minimizes chance of off target seeding and metastasis. Injection of tumour fragments rather than VX2 cell suspension yields a greater success rate of establishing a liver tumour [270]. After hepatic tumour growth is established, animals must then be anaesthetised, catheterised and the experimental embolisation procedure carried out by a trained interventional radiologist, which makes the study costs high. Another drawback is that VX2 tumours rapid growth means that they are prone to developing a necrotic core, which minimises the amount of viable tumour that can be analysed for its response to chemotherapeutic treatment [271]. Although rabbit hepatic vasculature is sufficiently large to allow catheterisation, it is still significantly smaller than human anatomy which means that bead size and injection volume must be carefully considered. Small beads will penetrate the VX2 tumour more efficiently than larger ones, and the volume required to reach stasis will be much less than in man, meaning that a fraction of the intended chemotherapeutic payload will be delivered.

Mouse models are widely used in drug screening studies due to their ease of use in assessing tumour growth control. Using human tumour cell lines or patient derived xenografts aids in translating drug effect to humans, however depending on the type of model used, tumour microenvironment and host interactions may not be adequately represented [272]. Table 5.1 summarises the types of mouse models that may be used in HCC research. Although mouse vasculature is much too small to allow a TACE

Table 5.1 Summary of mouse models used in HCC research.

Type	Description	Advantages	Disadvantages
Ectopic xenograft	Cultured tumour cells are injected subcutaneously in immunodeficient mice	May be established HCC cell lines or patient derived. Quick and easy to perform. Subcutaneous location allows facile measurement of tumour volume. Proof of concept for drug screening.	No direct interaction with target organ. Unsuitable for examining tumour-host interactions e.g. angiogenesis, metastasis. Response is cell line dependent, multiple lines must be used. Cannot study immune effects.
Hollow fibre	Tumour cells are grown in small semi-permeable tubes which are implanted subcutaneously or intraperitoneally	Multiple fibres may be used for each mouse, allowing multiplexing of cell lines and reducing number of animals. Retrieval of cell lines is possible for post-hoc analysis. Possible to study angiogenesis.	Restricted number of cells. Unable to measure tumour growth. Unrepresentative of tumour physiology and host-tumour interactions.
Orthotopic xenograft	Tumour cells are injected in the organ of origin (e.g. liver for HCC)	Tumours are in contact with intended microenvironment; host-tumour interactions can be studied.	More complicated to perform than ectopic. Response is cell line dependent, multiple cell lines must be used
Genetically engineered	The mouse genome is genetically engineered to allow development of tumours by e.g. overexpression of oncogenes, viral genes or growth factors	Allows investigation of carcinogenic pathways and interplay and dependency on various oncogenes. Mutation expression can be limited by tissue specific promoters, shares molecular similarity with HCC.	Phenotypic outcome may be influenced by multiple genetic and environmental factors. May not correspond to clinical HCC tumours harbouring multiple heterogeneous mutations.
Chemically induced	Mice are dosed with carcinogenic compounds that lead to tumour formation	Allows investigation of carcinogenic pathways induced by external carcinogens, e.g. aflatoxin. Progression to malignancy follows similar pathway to HCC – liver injury, fibrosis/cirrhosis, cancer.	Long time to develop tumours. Response to carcinogens may be species specific. Tumours do not always share genetic similarity with HCC.
Syngeneic models	Immunocompetent mice are inoculated with tumours of murine origin (same strain)	Allows experimentation in an immunocompetent animal.	Both tumour and host have murine biology, may not correspond to human HCC.

procedure, evaluation of DEB in ectopic mouse xenograft models is still possible by altering the route of administration. In previous studies, DEBs were injected adjacent to subcutaneous tumours to provide proof of local release and tumour growth control [107, 137, 156]. Since subcutaneous tissue pressure may force the compressible DEBs back out of the injection site, a viscosity modifier was used to help stabilise the bead bolus *in situ*. Examples of an inert carrier suited to this purpose are alginate solution, as used in the previously referenced studies, or carboxymethylcellulose (CMC) which was used as a vehicle to deliver DEB in an orthotopic rat model of glioma [273].

5.1.2 Aims of this chapter

The aim of this chapter was to use an *in vivo* model to assess the efficacy of vandetanib-eluting bead formulations in controlling HCC tumour growth. For the purposes of this thesis, an ectopic mouse xenograft model was used, requiring development and characterisation of an adapted route of administration for vandetanib beads.

In summary, the aims of this chapter were to:

- Develop a formulation of vandetanib eluting beads suitable for subcutaneous injection in a mouse xenograft model.
- Evaluate efficacy of vandetanib eluting beads as compared with unloaded beads in controlling growth of subcutaneous HepG2 tumour xenografts.

5.2 Materials and methods

5.2.1 Preparation of vandetanib loaded beads

DC Bead LUMI (70-150 μm) was individually loaded in vials at various target doses by incubation with sterile filtered vandetanib solution for a minimum of 3 hours with agitation. Beads were washed twice in ultrapure water to remove unbound drug and neutralise pH (confirmed by pH strip test on representative samples), before resuspending in 5 mL ultrapure water. Vials were sealed with rubber bungs, crimped, and sterilised by autoclave at 121°C for 30 minutes. After autoclaving, the settled bead volume was measured in representative samples to confirm final dose density.

5.2.2 Evaluation of bead formulations for subcutaneous injection

Different delivery vehicles and suspension ratios were considered for their handling properties and effects on drug release from beads. Sterile 0.6% w/v alginate solution was provided in pre-filled syringes (BTG Germany, Alzenau). Carboxymethylcellulose

(CMC) solution was prepared by dissolving CMC sodium salt (medium viscosity, 400-800 cP at 2 % in H₂O) (Sigma Aldrich) in ultrapure water. All CMC solutions were autoclaved for 30 minutes at 121°C.

Drug elution studies on beads or bead suspensions were carried out using an improvised small scale diffusion model. Beads or bead suspensions were placed in the bottom of a plastic semi-micro cuvette. 1.5 mL of PBS was added to the cuvette which was sealed with parafilm and placed on a plate shaker at 100 rpm. At progressive time points, 50 µl of PBS was removed from the cuvette and analysed for vandetanib concentration by HPLC (see section 2.2.2.1 for HPLC method).

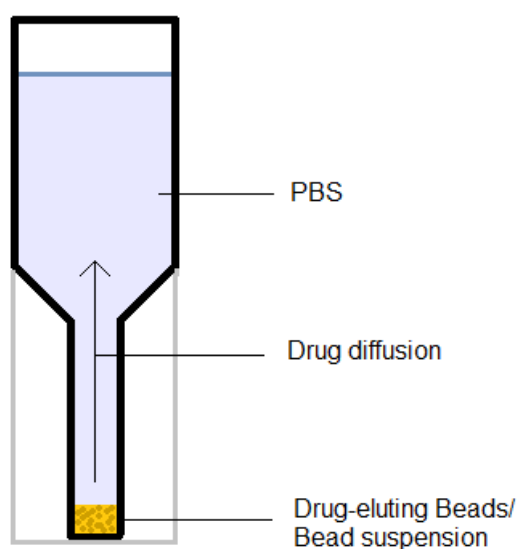


Figure 5.1 Small scale diffusion model of vandetanib release from trial bead formulations. Original in colour.

5.2.3 *Animal study*

All animal studies were carried out at Experimental Pharmacology and Oncology (EPO), Berlin, Germany. The animal experiments were performed in accordance with the UKCCCR regulations for the Welfare of Animals and of the German Animal protection Law and approved by LAGeSo (State Office of Health and Social Affairs), Berlin (License number G0030/15, covers facility and staff). The lead technician was Britta Buettner (EPO GmbH).

5.2.3.1 Mouse species

Animal species and housing conditions are detailed in Table 5.2. Nude mice were selected as a test system due to the ability to grow subcutaneous tumour xenografts. These mice possess an autosomal recessive mutation in the *Foxn1* (forkhead box N1) gene resulting in thymic aplasia, which results in a lack of T-cells and immunodeficiency.

Table 5.2 Test animal details and housing conditions

Animals, gender and strain	NMRI:nu/nu mice, female
Age and bodyweight	At the start of the experiment mice were approximately 8 -10 weeks of age, and at the start of the treatment they had a mean body weight between 28 g and 30 g
Supplier	Janvier, France
Acclimatization	7 to 14 days
Environmental Conditions	Strictly controlled and standardised barrier conditions, IVS System Techniplast DCC (TECNIPLAST DEUTSCHLAND GMBH, Hohenpeißenberg)
Caging	Macrolon Sealsafe 1284L, (TECNIPLAST)
Feed type	Ssniff NM, Soest, Germany
Drinking water	Autoclaved tap water in water bottles (acidified to pH 4 with HCl)
Feeding and drinking time	Ad libitum 24 hours per day
Room temperature	22±1°C
Relative humidity	50±10%
Light period	Artificial; 12-hours dark/12 hours light rhythm (light 06.00 to 18.00 hours)
Health control	The health of the mice was examined at the start of the experiment and twice per day during the experiment.
Identification	Ear mark and cage labels

5.2.3.2 Tumour model

Frozen aliquots of Hep3B cells and JHH6 cells from stocks used for the previous *in vitro* experiments (see section 4.2.1) were supplied to the contract research site to be tested for tumorigenicity in NMRI:nu/nu mice using a standard protocol. Cells were cultured at the study site in RPMI + 10% FBS prior to harvesting and inoculation of 1×10^7 cells in 100 μ l PBS into the left flank of 5 mice per cell line. Tumour growth was

not observed after 6 weeks of monitoring, therefore Hep3B and JHH6 cells were deemed to be non-tumorigenic in this strain.

HepG2 cells are already known to be tumorigenic in NMRI nude mice [274] therefore were used for all studies to generate subcutaneous ectopic tumours. HepG2 cells ATCC (No. HB-8065) were cultured in DMEM + 10% FBS. Cells were harvested and 1×10^7 cells in 100 μ l PBS were inoculated into the left flank and monitored for tumour growth.

5.2.3.3 General study concept

It was proposed that NMRI:nu/nu (nude) mice were inoculated with 1×10^7 HepG2 cells subcutaneously as described above. After tumours became palpable (75-120mm³), mice were randomly assigned to 2 groups: control (unloaded beads), and vandetanib loaded beads. The animals received a subcutaneous injection of drug loaded or unloaded beads adjacent to the tumour once every 7 days (formulations, doses and volumes selected were dependent on the study and are listed in individual study designs). The injection

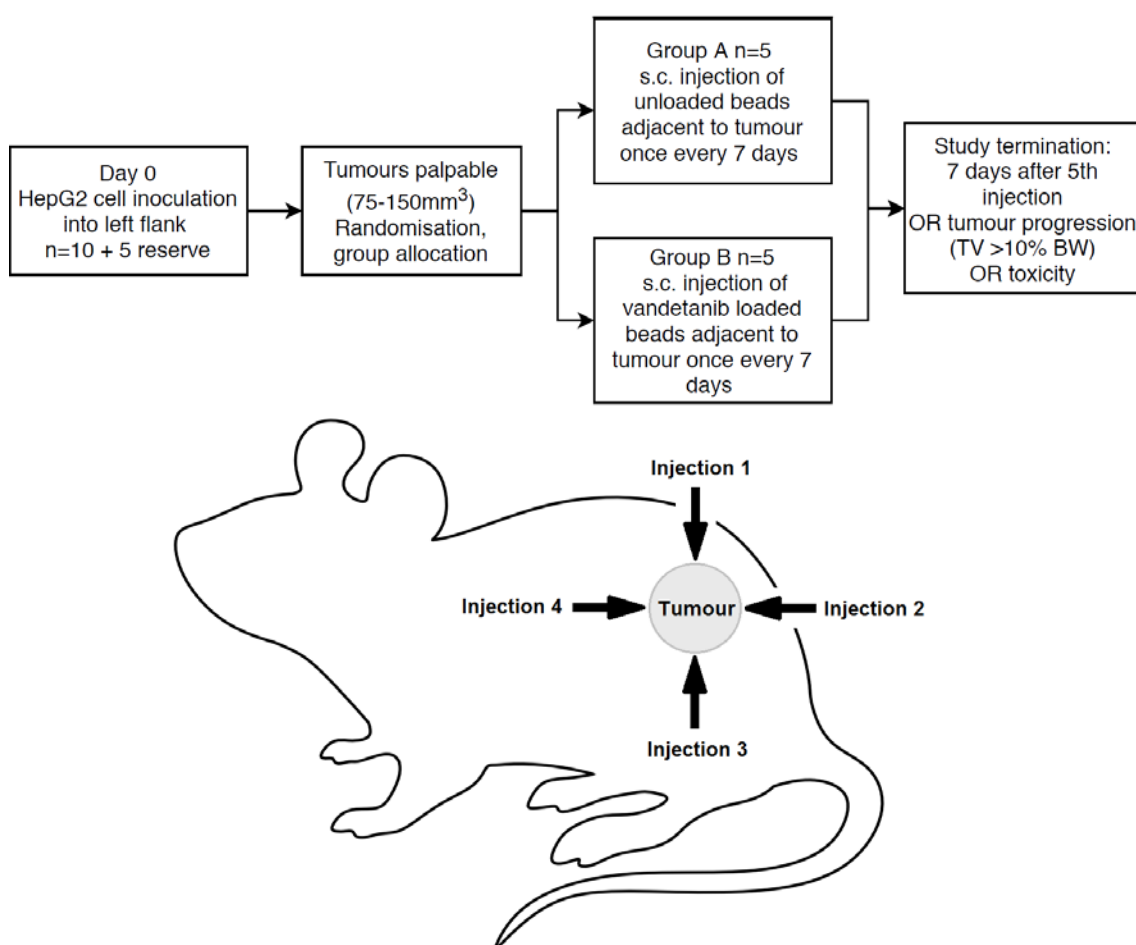


Figure 5.2 Planned study schedule and location of weekly injection of beads around HepG2 tumour xenografts.

site was altered for each weekly treatment by following a North/East/South/West pattern around the tumour to ensure full tumour coverage (Figure 5.2).

5.2.3.4 Animal monitoring and terminal procedures

Mice body weights and tumour volumes were monitored throughout the study period. They were recorded on the first day of treatment (Day 0), twice weekly throughout the treatment period (first and fourth day, relative to Day 0), every subsequent treatment day and the day of necropsy. The size of the tumour was directly measured with callipers on the same days as the body weight measurements. The tumour volume was calculated with following formula:

$$\frac{(\text{length} \times \text{width}^2)}{2}$$

The mice were checked daily for treatment-related toxicity. The onset, intensity and duration of any signs were recorded. Decrease in body weight provides a measure of treatment-related toxicity.

Animals were scheduled to be sacrificed 7 days after the final treatment, with the exception of any animals developing tumours larger than 10% of their body weight or unacceptable toxicities, which were sacrificed early. Following euthanasia, the tumours were removed and weighed. The tumours were divided into halves and snap frozen/paraffin embedded for further examination.

5.2.3.5 Data and statistics

Mouse body weights were recorded throughout the study and mean body weight change from day 0 was calculated as a measure of toxicity.

Tumour growth inhibition was assessed by measurement of subcutaneous tumour volume twice per week. The tumour growth inhibition (T/C %, T= treated tumour volume; C= control tumour volume) was determined, defined as the ratio of the median tumour volumes of the vandetanib bead treated group versus the control bead group.

5.2.3.6 Individual study designs and justification

Study 1: 0.5 mg vandetanib per injection in alginate

The first study followed the concept of previous mouse xenograft studies evaluating drug eluting beads [138, 275]. Historically, an inert viscous delivery vehicle has been

used to suspend beads prior to injection, with the function of facilitating the injection and stabilising the beads *in situ*. This avoids the beads being forced back out of the injection tract by subcutaneous pressure. Based on this assumption, bead formulations in study 1 were prepared for injection by suspension in 0.6% alginate solution in a 1:2 ratio of beads to alginate.

This was the first study to evaluate the effect of subcutaneous application of radiopaque vandetanib loaded beads adjacent to HepG2 xenograft tumours. The dose selected, 15 mg/mL loading equating to 0.5 mg vandetanib per injection (approximately 16.6 mg/kg based on a 30 g mouse), was based on the efficacy of oral vandetanib against various cancer xenografts, showing significant tumour growth inhibition between 12.5-25 mg/kg/day [84]. It was hypothesised that due to the local delivery mechanism of vandetanib loaded beads leading to a high local drug concentration, single weekly injections of 0.5 mg would be sufficient to control tumour growth.

Study 1: 0.5 mg vandetanib per injection in alginate

Treatment Group	Number of animals	Bead loading dose	Administration formulation	Injection volume	Vandetanib dose per injection
A (control)	5	N/A	1:2 suspension of beads in alginate solution	100 µL	N/A
B (vandetanib loaded beads)	5	15 mg/mL	1:2 suspension of beads in alginate solution	100 µL	0.5 mg

Study 2: 5 mg vandetanib per injection, beads alone

A second study was designed with the aim of increasing the dose of vandetanib delivered to the tumours. Subcutaneous test injections of unloaded radiopaque beads in healthy nude mice confirmed that bolus injections of 50 µL settled beads, without a viscosity modifier, were feasibly performed. A drug loading dose of 100 mg/mL was selected which equated to 5 mg vandetanib per injection of beads.

Study 2: 5 mg vandetanib per injection, beads alone

Treatment Group	Number of animals	Bead loading dose	Administration formulation	Injection volume	Vandetanib dose per injection
A (control)	5	N/A	Bolus of settled beads	50 µL	N/A
B (vandetanib loaded beads)	5	100 mg/mL	Bolus of settled beads	50 µL	5 mg

5.3 Results and Discussion

5.3.1 Xenograft study 1 – 15 mg/mL dose

The subcutaneous injection of vandetanib loaded beads, (0.5 mg per injection) close to the tumour nodule did not result in complete or partial remission of the tumours (Figure 5.3). The T/C value at day 46 was 106% (rated at progressive disease by RECIST criteria).

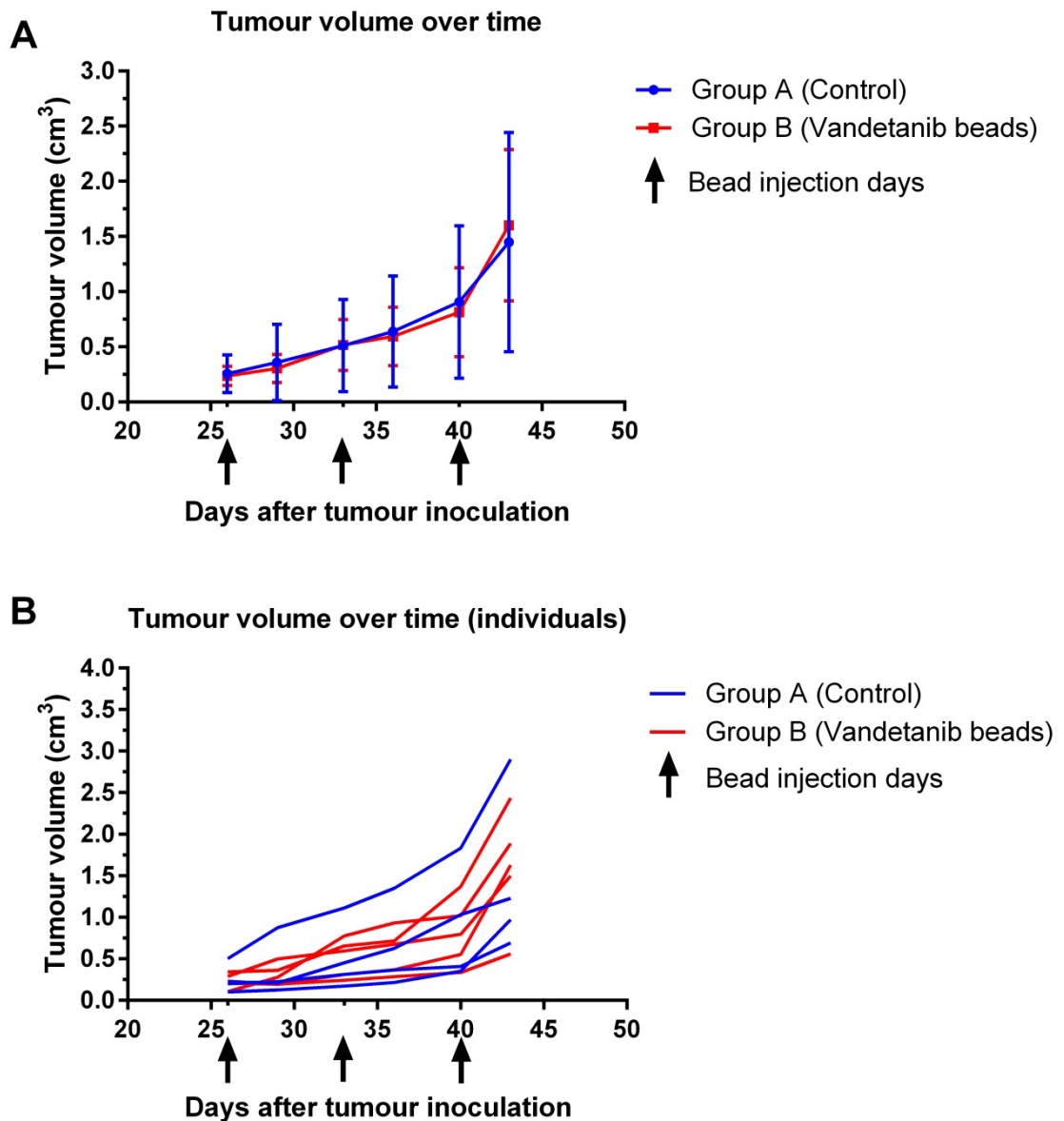


Figure 5.3 Study 1: HepG2 tumour volume over time during treatment with vandetanib loaded beads. A) Mean tumour volume \pm SD; B) individual tumour volumes. Black arrows denote treatment days; mice received an injection of bland beads (Group A, N=4) or beads containing 0.5 mg vandetanib (Group B, N=5) adjacent to the tumour. Original in colour.

5.3.2 Toxicity/Mouse body weight

The treatment was well tolerated and not accompanied by significant side effects. There was no significant decrease in body weight throughout the study in either treatment group (Figure 5.4).

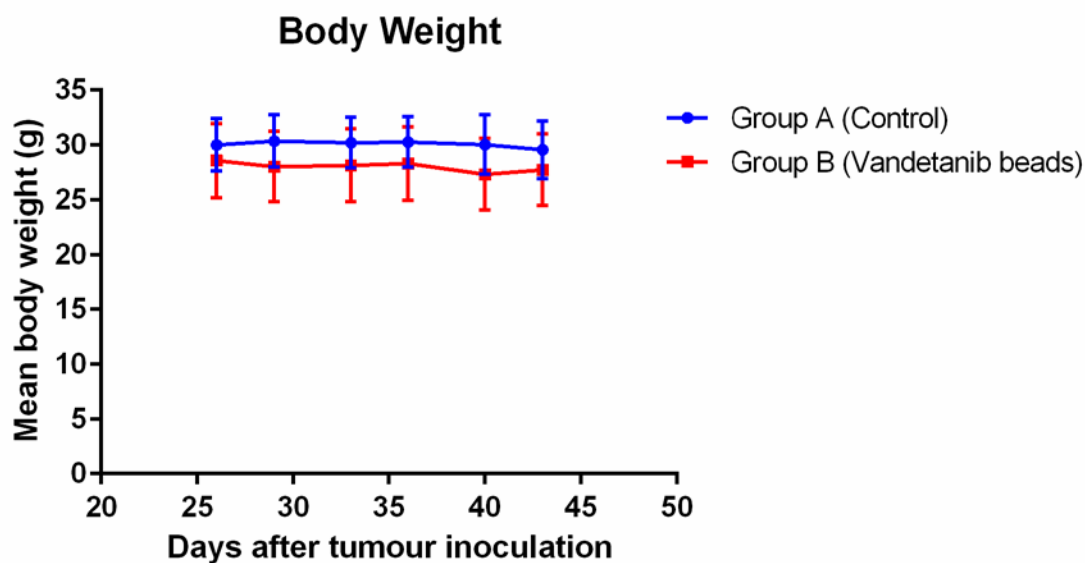


Figure 5.4 Study 1: Mouse body weight over time. Mean \pm SD, Group A N=4, Group B N=5. Original in colour.

5.3.3 Evaluation of bead formulations and alternative vehicles

Following study 1, it was hypothesised that the lack of anti-tumoural efficacy was due to a low dose of vandetanib applied adjacent to the tumour and slow release rate hampered by alginate, leading to insufficient drug accumulation. Traditional elution methods such as described in chapter three are likely to overestimate the rate of drug release in this context. Therefore, a simple diffusion model was envisaged with limited bead movement which enabled comparison of the effect of suspension in alginate, or alternative vehicle 3% CMC on vandetanib release. After 24 hours, more than 3 times the amount of vandetanib was released from beads alone than from beads suspended in alginate (Figure 5.5). Suspension in 3% CMC also had an inhibitory effect on vandetanib release, although this was less marked than alginate. The amounts of vandetanib released in 24 hours from beads alone, beads in alginate and beads in CMC equated to 2.73%, 0.72% and 1.13% of the total dose of 5 mg respectively.

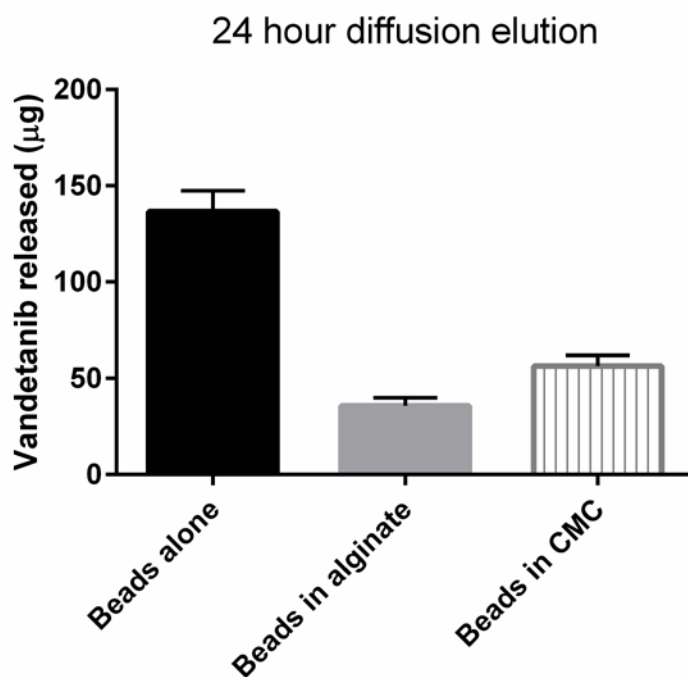


Figure 5.5 The effect of delivery vehicles on vandetanib release in a diffusion model. Beads containing a total of 5mg vandetanib were placed in the bottom of cuvettes alone, with alginate or 3% CMC, and covered with PBS. Vandetanib released in the PBS after 24 hours was quantified by HPLC. Columns show mean of 3 replicates \pm SD.

5.3.4 Xenograft study 2 – 100 mg/mL dose

The subcutaneous injection of vandetanib loaded beads, (5 mg per injection) close to the tumour nodule did not appear to result in significantly complete or partial remission of the tumours (Figure 5.6), however the study was compromised by the incidence of skin toxicity suspected to be related to vandetanib treatment. Some technical issues were experienced with the injection of vandetanib beads in the drug treated group (Vandetanib I): due to the lack of delivery vehicle, beads were prone to blocking the needle. This led to uncertainty in the actual volume administered and whether the procedure was causing undue irritation in the injection site. Therefore, this group was terminated after 2 injections and a new group started using reserve mice (Vandetanib II), taking practical steps to improve the injection process (agitation and priming of beads in the needle prior to injection to minimise blocking). However, these reserve mice had been inoculated with HepG2 cells at the same time as the other groups, and rejected at the study start due to slow growing tumours. Some individuals in this group appeared to have a period of tumour remission after the second injection (Figure 5.6 B); however periods of spontaneous tumour remission also occurred in the control beads group. It is likely that differences in growth rate compared with control are due to unintentional selection of mice bearing slow growing HepG2 xenografts.

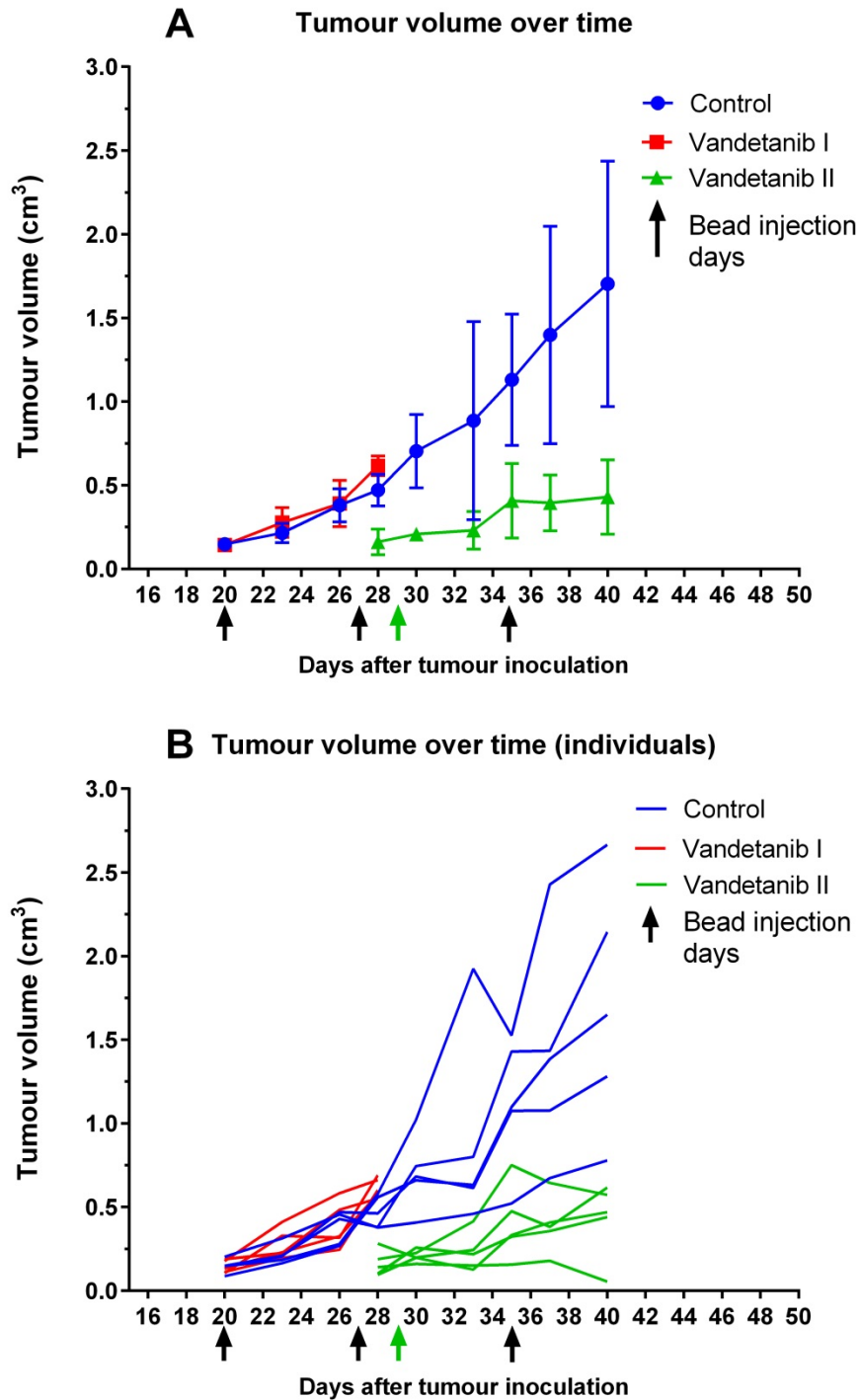


Figure 5.6 Study 2: HepG2 tumour volume over time during treatment with vandetanib loaded beads. A) Mean tumour volume \pm SD; B) individual tumour volumes. Control group (blue) and Vandetanib I group (red) received an injection of bland beads or vandetanib beads (5 mg dose) adjacent to the tumour on days marked with black arrows. Vandetanib II group (green) was formed of reserve mice and received an injection of vandetanib beads (5mg dose) on day 29 (green arrow) and day 35 (black arrow). Original in colour.

5.3.5 Toxicity/ Mouse Body weight

Mouse body weight remained consistent in the control group for the duration of the study. All mice in the Vandetanib II group showed a decrease in body weight after the second treatment, likely due to treatment related toxicity. The mean body weight of mice in the Vandetanib II group was significantly lower than the control group on day 37 (unpaired t-test, $p=0.021$) but not on the day of sacrifice ($p=0.072$).

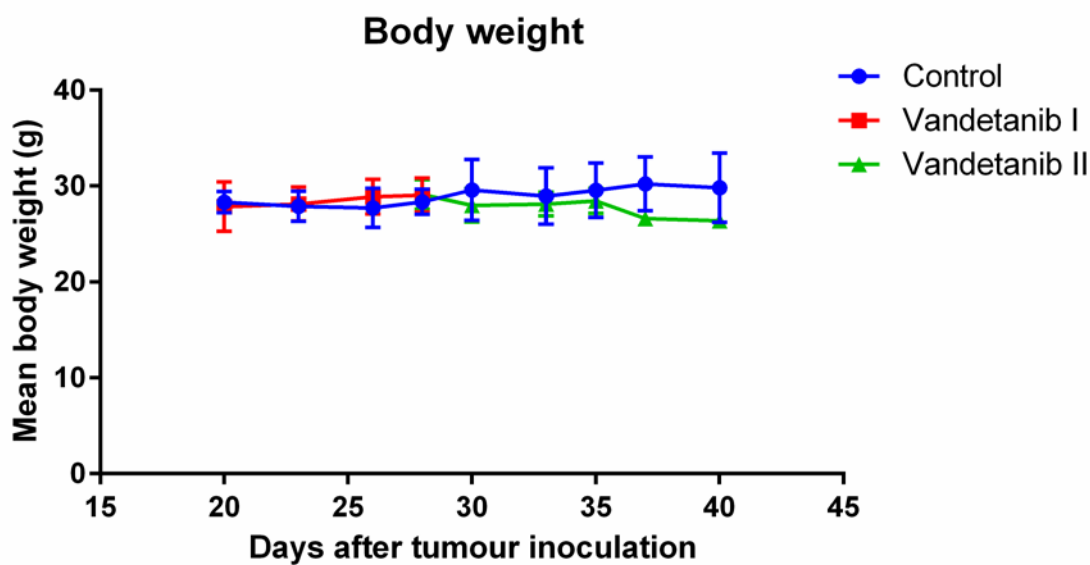


Figure 5.7 Study 2: Mouse body weight over time. Mean \pm SD, N=5. Original in colour.

Both groups of mice receiving the vandetanib loaded beads experienced skin irritation at injection site on the day following the first treatment. The skin lesion was white in colour and 2 mm in diameter. Over time, the inflamed spots increased in size, with a diameter of up to 10 mm 5 days after treatment. The lesions had an inflamed, ulcerated appearance. The mice suffered from pain when touched. The study was terminated 11 days after treatment began due to the skin toxicity. Mice receiving control (unloaded beads) showed no signs of skin toxicity.

The nude mouse ectopic tumour xenograft model is widely used for screening of anti-tumoural treatments, due to relatively low cost and ease of measuring tumour volume. Vandetanib-loaded PVA beads are an embolic drug-device combination product intended to be delivered into tumour vasculature. In the present study, the route of administration of vandetanib-loaded beads was modified to a subcutaneous route to adapt to this model type and demonstrate proof of concept of local drug release and

evaluate effect on tumour growth. This concept was successfully demonstrated using irinotecan loaded DC Bead in a pancreatic tumour xenograft model previously [275], and doxorubicin loaded DC Bead in a HepG2 model [107].

5.3.6 *Limitations of the model – Potential reasons for lack of anti-tumoural activity*

The ectopic implantation of tumours in the mouse xenograft model is a practical approach for treatment administration and measurement of tumour volume, however it is not an accurate representation of the tumour microenvironment. Ectopically implanted tumours have no interaction with liver tissue, which will affect cell phenotype, the supply of nutrients and growth factors, microcirculation, angiogenesis and invasiveness [136, 276, 277]. Hep3B and JHH6 cells were found to be non-tumorigenic in the strain of mice used in this study. Regarding this, Amann *et al.* (2009) also found that Hep3B cells were non-tumorigenic in nude mice, but interestingly were able to form tumours when co-injected with activated hepatic stellate cells (HSC), a normally quiescent pericyte that becomes activated in response to liver injury and plays a role in cirrhosis [274]. This reiterates the importance of replicating the features of the tumour microenvironment when modelling HCC. The studies in this chapter were performed using a single cell line, HepG2. However, responses to any treatment can vary between cell lines. For example, the EGFR inhibitor gefitinib inhibited HCC xenograft growth in a study by Matsuo *et al.* (2003), [278], while in another study by Huynh *et al.* (2006), a panel of 7 patient derived HCC xenografts showed no response to the same drug [279].

The studies performed in this thesis have demonstrated the importance of selecting an appropriate dose and the consequences of drug delivery into non-target tissue or a delivery route that is different than the intended one. In general, administration of vandetanib loaded beads adjacent to a subcutaneous HepG2 tumour had no effect on tumour growth at either low (15 mg/mL) or maximal (100 mg/mL) vandetanib dose despite the drug having effect against HepG2 cells *in vitro*. There are several reasons that this may be the case. In the first study, the lack of anti-tumoural activity was likely a result of insufficient vandetanib concentrations reaching the tumour. Although drug release from DEB is localised and therefore has the potential to reach high concentrations in the target tissue, in reality drug release is fairly slow following implantation as demonstrated in imaging studies using doxorubicin loaded beads.

Namur *et al.* (2010) found that only 43% of the doxorubicin dose contained within DEB (DC Bead, 100-300 μm , 37.5 mg/mL dox) was released in liver tissue 28 days after embolisation of healthy swine liver [159]. Doxorubicin concentrations detected by this method in HCC patient liver explants were on average only 5 μM 8 hours after embolisation and declined thereafter. If we assume a similar rate of release in vandetanib loaded beads, factoring in the effect of alginate, it is likely that with a 15 mg/mL dose the levels of vandetanib released were insufficient to reach therapeutic levels. In the second study, the levels of vandetanib released were likely high due to the high loading dose and the lack of delivery vehicle. No anti-tumoural effect was seen here either, however tumour volume results may have been confounded by the presence of the cutaneous inflammation. In addition, abscess capsules can be a barrier to drug diffusion which may have prevented sufficient drug reaching the tumour [280].

The distance that drug can diffuse through tissue away from DEB is difficult to accurately measure. Several studies using doxorubicin loaded beads have provided an estimate, but results can vary with drug type and loading concentration, bead type and number, tissue integrity and the time of sampling. Namur *et al.* (2010, 2011) found doxorubicin diffused up to 600 μm from beads in a healthy swine liver [159], and as far as 1.2mm away from beads in liver explants of DEB-TACE-treated HCC patients [189], where larger volumes of beads were given. Another study using 75-150 μm sized beads found doxorubicin diffusion distances in swine liver to be up to 600 μm [66]. However, drug concentration decreases sharply as distance from the bead increases, and also as time goes on with maximal drug concentrations usually being found within a few hours of embolisation and decreasing quickly thereafter. The tumours in the HepG2 mouse xenograft studies were on average 0.25 cm^3 in volume when treatment was initiated, and grew to over 1.5 cm^3 at the end of the study. As beads were injected adjacent to the tumour rather than inside, it may be the case that vandetanib diffusion distance was not sufficient to provide drug coverage over the full tumour. In clinical practice, beads would be delivered intra-arterially with the aim of embolising all tumour-feeding vessels and therefore tumour coverage and drug penetration would likely be greater. Indeed, emerging clinical data on the radiopaque DC Bead LUMI indicate good tumour coverage as demonstrated by CT imaging of bead location [281].

Previous mouse xenograft studies using subcutaneously implanted DEB have been carried out using either doxorubicin or irinotecan/topotecan, and showed an immediate inhibition of

tumour growth after the first treatment. These drugs are classed as cytotoxic, in that their mechanism of action directly causes cell death by interference with DNA replication. On the other hand, vandetanib is not classed as cytotoxic. Its mechanism of action is primarily anti-angiogenic, exerting its anti-tumoural effect via disrupting vascular supply to tumours. The secondary effect of EGFR inhibition does have the potential to induce cell cycle arrest and apoptosis, however *in vitro* this was only seen at high doses of 25 μ M. Considering the points mentioned above about slow drug diffusion and incomplete tumour coverage, vandetanib's primarily cytostatic activity could explain differences in efficacy between doxorubicin loaded beads and vandetanib loaded beads in the HepG2 xenograft model.

Another important limitation of the model is the lack of representation of clinical practice. Whilst inherent hypoxia may exist in subcutaneous tumours due to the rate of cancerous growth, the beads were not delivered into blood vessels and as such it is unlikely that their presence caused hypoxia in the tumours as it would during DEB-TACE. This limits the extrapolation of results to human trials as effects of embolisation induced hypoxia and nutrient deprivation cannot be accounted for. Additionally, in clinical practice, vandetanib DEB would not have contact with the skin, so the cutaneous toxicity observed in study 2 is not necessarily expected in animal models or clinical trials where vandetanib beads are delivered *via* TACE in the liver.

5.3.7 *Cutaneous toxicity*

The skin findings observed in the second study are a well-known phenomenon and are consistent with EGF receptor inhibition as EGF is a key regulator of keratinocyte proliferation and differentiation [282, 283]. The administration of EGF caused hyperplasia of the epidermis and adnexa in the cynomolgus monkey [284], dogs and rats. The association of these skin lesions with the pharmacological action of vandetanib is further supported by the reports of similar skin effects in patients treated with a monoclonal antibody to the EGF receptor [285] and small molecule inhibitors of EGF receptor [286].

Folliculitis is the infection and inflammation of one or more hair follicles. The condition may occur anywhere on the skin and is reversible after treatment cessation. Folliculitis appears to be intimately related to microabscess onset following treatment with EGFR inhibitors [287]. Dermatologic toxic effects are the most common side-effects associated with anti-EGFR therapy, including but not limited to acneiform skin rash; pruritus; skin fissures, abscesses and pyogenic granulomas [288]. Additionally a wide

variety of commensal microbes (Gram-positive and Gram-negative bacteria, *Candida albicans*), may have an important role in the development of these skin lesions. In a study conducted by Köpf-Maier *et al.* (1990), the morphological aspect of the skin and the hairs of athymic, macroscopically nude mice (NMRI, nu/nu) was investigated by descriptive light- and electron-microscopy methods and compared with the appearance of the skin and the hairs in normal haired mice (NMRI). These morphological studies revealed that athymic, macroscopically nude mice are not at all hairless, but have about the same number of hair bulbs, embedded in the hypodermis, as normal haired animals [289]. Therefore folliculitis can be observed in nude athymic mice and, subsequently (micro)-abscess can be observed as well.

The severe skin lesions observed in study 2 were associated with pain reactions. As the animals were group-housed, it cannot be excluded that the irritation caused by the treatment led to change in cage hierarchy with dominance-like reactions (licking of damaged skin by a dominant and/or self-mutilation) and/or increased aggressive behaviour towards weak and stressed mice. This may also lead to bacterial infections in immunodeficient mice like the NMRI:nu/nu strain as it can be assumed that an opportunistic bacterial skin infection by commensal microbes in NMRI:nu/nu immunodeficient mice can occur, and that athymic; nude mice are not hairless i.e. prone to develop hair inflammation lesions (folliculitis) and subsequently microabscesses. In addition, this phenomenon can be exaggerated by the normal light conditions within a typical animal room (photo-toxicity) [290].

In study 2 where the toxicity was observed, the beads were delivered subcutaneously (5 mg vandetanib, 100 mg/mL) as a bolus of bead sediment with minimal packing solution. In study 1, they were suspended in an alginate solution (0.5 mg vandetanib, 15 mg/mL), which was shown to slow down the drug release in the drug diffusion model, with no noteworthy clinical signs observed. The absence of a slow-releasing vehicle could lead to a high local dose of vandetanib being released into the surrounding tissue and subsequent development of skin lesions. It is worth noting that when doxorubicin loaded beads were administered subcutaneously in a similar fashion in a previous mouse xenograft study, ulceration of the injection site was also observed [138] which suggests that cutaneous toxicity is likely to be related to the route of administration.

5.3.8 *Alternative models for assessing treatment efficacy*

As mentioned in the introduction of this thesis, rabbits bearing VX2 liver tumours are a frequently used model for TACE procedures, the benefits of this model being that it is orthotopic, bears similarities to human HCC, and is suitable for delivery of DEB through the intended route of hepatic artery catheterisation. Furthermore, several studies using transcatheter arterial embolisation in this model have shown increased tumour hypoxia and HIF-1 expression as a result of this treatment [43, 291-293].

Biocompatibles have carried out VX2 studies to assess the efficacy of vandetanib loaded beads, including an early prototype based on DC Bead [95], and later studies using DC Bead LUMI (manuscript in preparation). In the DC Bead study, vandetanib loaded beads significantly inhibited tumour growth over 21 days following a single TACE treatment. Vandetanib loaded beads showed superior anti-tumoral efficacy compared to unloaded DC Bead, and equivalent anti-tumoral activity compared to oral vandetanib at the doses administered (6.3 mg vs 21 mg/kg/day, respectively). Animals treated with vandetanib loaded beads had a lower plasma concentration and a higher tumour concentration of drug relative to the total dose administered, compared to oral dosing [95]. In the DC Bead LUMI study, the advantage of bead radiopacity was used to confirm the volume of beads present within the tumour after the procedure. The volume of beads in the tumour was identified as a significant prognostic factor for anti-tumoural efficacy, as well as the concentration of vandetanib in the tumour, showing the likelihood that both embolisation and vandetanib contribute to the efficacy of the treatment. In both studies, TACE with vandetanib loaded beads was well tolerated, with limited systemic exposure to vandetanib. In addition, safety pharmacokinetic studies have been carried out using vandetanib beads in healthy swine liver, which demonstrated therapeutic drug concentrations in the liver 30 days after embolisation with no obvious systemic toxicity [193].

5.4 **Conclusion**

The aim of this chapter was to establish a practical *in vivo* model to assess the efficacy of vandetanib-eluting bead formulations in controlling HCC tumour growth. Unfortunately, anti-tumoural activity against ectopic HepG2 xenografts was not observed using subcutaneous injection of vandetanib loaded beads. Treatment with maximally loaded (100 mg/mL) beads induced cutaneous side effects which impeded the analysis of the study and led to early termination. The results obtained here suggest

that mouse xenograft models are not suitable for evaluating efficacy of vandetanib loaded beads. Alternative models, such as the rabbit VX2 model, have been used to evaluate vandetanib loaded beads with signals of significant anti-tumoural effects which seem to be due to a combination of embolisation and the mode of action of vandetanib. TACE with vandetanib loaded beads in rabbits and swine is well tolerated.

6 GENERAL DISCUSSION

Interventional Oncology has been described as the fourth pillar of cancer care in the medical community, owing to its rapidly growing selection of minimally invasive, image-guided cancer therapies that provide patients with treatment options that can minimise side effects and hospital stays. Trans-arterial chemoembolisation with DEB is one such treatment that has proven clinical benefit in treating unresectable HCC [40]. Nonetheless, the aggressive nature of this disease means that tumours can escape treatment by activating hypoxia-induced pathways of neo-angiogenesis and proliferation. Despite over a decade of use of DEBDOX (doxorubicin loaded beads) to treat HCC, there is still discussion as to whether DEB-TACE offers any additional survival benefit compared to cTACE (doxorubicin and Lipiodol emulsion) beyond reduction of side effects [34]. Some schools of thought feel the therapy is limited by doxorubicin's physicochemical properties and its ability to diffuse efficiently throughout the tumour, to reach possible undetected satellite nodules that can act as a site for recurrence. Chemotherapeutic mixtures of cisplatin, doxorubicin and mitomycin C have been administered via cTACE but have not proven more effective than single drug therapy [294].

Newer targeted drugs such as tyrosine kinase inhibitors have shown promise, with the VEGFR inhibitor sorafenib being approved as a first line systemic therapy for advanced HCC [295]. A phase III trial of sunitinib in this patient population was cut short due to high incidence of adverse events [81], but the concept of a sunitinib loaded bead was explored as a method to reduce systemic exposure. Drug distribution imaging revealed that that sunitinib diffused faster and further from occluded vessels than doxorubicin, achieving therapeutic doses over a wide area [80, 158]. Other studies have reported local delivery of sorafenib in imageable microspheres resulting in a local anti-angiogenic effect [72, 73]. This led to the concept and collaboration between Biocompatibles, the manufacturer of the DEBs DC Bead and DC Bead LUMI, and Astra Zeneca, the licence holders at the time of the multi-tyrosine kinase inhibitor vandetanib, to produce a pre-loaded vandetanib DEB capable of delivering locally high doses of the targeted compound to liver tumours and minimising systemic side effects which hindered its use as an oral agent [93]. Therefore, the aim of the work carried out

in thesis was to develop and characterise this novel drug device combination to assess feasibility, optimise formulation, and provide evidence for its efficacy in the hypoxic tumour environment.

At the time of the conception of vandetanib bead, work was underway at Biocompatibles to bring to market a radiopaque embolic bead which would be directly imageable under x-ray: DC Bead LUMI, which is now approved in multiple territories. This raised the question as to whether the vandetanib bead should be developed using standard DC Bead, or its novel radiopaque counterpart. In chapters two and three of this thesis, both platforms were evaluated in terms of their vandetanib loading capacities, their physicochemical properties after loading, and their drug release profiles. DC Bead LUMI showed advantages of having a higher vandetanib loading capacity, resistance to loading induced size changes, and demonstrated uniform drug distribution and radiopacity suitable for *in vivo* imaging. This marked the first report of loading a radiopaque DEB with an anti-angiogenic agent [296]. An additional benefit and function of bead radiopacity is currently being investigated at the National Institutes of Health, USA, whereby radiopacity attenuation in DEB-TACE treated tissue has been found to be directly correlated with released drug concentration [297]. Once we know more about the diffusion behaviour of vandetanib in tissue, this may provide the possibility in the future to create predictive ‘drug maps’ based on the distribution of vandetanib beads in the liver, which is only possible with the use of the radiopaque bead platform.

The third chapter focuses on the release of vandetanib, in comparison with the two most commonly used DEB-TACE drugs doxorubicin and irinotecan, from beads in various *in vitro* models. The vascular flow system allowed the modelling of the early phase of drug release, by replicating the conditions during DEB delivery which lead to an elution burst during which a proportion of drug is rapidly released due to exposure to both contrast agent and free flowing ion-rich blood. The flow through model corresponded better to mid-late phase drug release in the plasma. Relating *in vitro* drug release to tissue levels is more complicated to achieve, and requires development both in the fields of *in vitro* models and *in vivo* drug distribution imaging techniques. Preliminary experiments are planned in order to assess the feasibility of using Raman spectroscopy to detect vandetanib concentrations in tissue sections following DEB-TACE, based techniques in development for cancer diagnostics [298]. Determining the extent of

vandetanib distribution in tissue or tissue mimicking models will also allow us to relate the achieved drug concentrations to the IC_{50} determined in chapter four, as a predictor of the degree of local toxicity and pharmacological effects.

One of the questions raised at the initiation of the vandetanib bead project was how the drug would perform in hypoxic conditions, given that TACE induces hypoxia and therefore can activate HIF-mediated drug resistance pathways [44, 291]. Therefore in chapter four, *in vitro* cell toxicity studies were performed in hypoxic conditions to mimic the embolised tumour environment. Vandetanib was found to be equipotent in normoxic and hypoxic conditions against three HCC cell lines, both in terms of inhibiting cell proliferation and inhibiting EGFR phosphorylation. HUVEC proliferation and VEGF secretion by HCC cells was also inhibited. However, constitutive MAPK pathway activation due to hypoxia and/or pathway redundancy may be a mechanism of resistance to be wary of. Doxorubicin showed its own benefits in this setting, and in future investigations it may be of interest to investigate any synergistic or additive effects of combining doxorubicin with vandetanib in hypoxic cell assays. If this yields positive results, there could be a rationale for using a mixture of doxorubicin and vandetanib loaded beads together in a TACE procedure, or perhaps assessing the feasibility of a dual-drug loaded bead, as has been previously demonstrated with doxorubicin and rapamycin [156].

In vivo evaluation of drug-device combinations such as DEBs in small animal models (e.g. rodents) is difficult to achieve, due to the necessity of using an alternative route of product administration. Subcutaneous injection of vandetanib beads in mouse HCC xenograft models induced cutaneous toxicity and did not demonstrate an anti-tumour effect, but as discussed in chapter five, these results are in contrast to studies where vandetanib beads have been delivered intra-arterially to the liver of VX2 tumour bearing rabbits and demonstrated safety and efficacy (manuscript in preparation). As 3D cell culture techniques become more accessible and attainable, perhaps a more humane and practical way to bridge the gap between 2D cell culture screening and larger animal studies requiring surgical intervention would be to develop spheroid HCC models. This would also allow the incorporation of endothelial cell co-culture, as described in recent work by Chiew, Wei, Sultania, Lim, and Luo (2017) [134], and also hypoxic conditions to screen anti-angiogenic compounds such as vandetanib in the local delivery setting. Taking this idea further, a future concept for toxicity testing in combination with drug

release testing is a microfluidic 3D cell culture system, featuring cancer cells in a 3D matrix perfused by media in microscopic channels, which could also be lined with endothelial cells. Advances in 3D bioprinting have demonstrated capability of producing such vascularised tissue models, with ‘vessels’ as small as 200µm [299] which therefore could be embolised by larger DEBs. Assessing the effects of chemotherapeutic drug release, nutrient deprivation and hypoxia induced by DEB blockage of the channels could also be achieved by fluorescent immunostaining.

In August 2017 the first human patient was treated with vandetanib loaded radiopaque beads as part of the VEROnA trial: a window of opportunity study of vandetanib-eluting radiopaque beads (BTG-002814) in patients with resectable liver malignancies [300]. The purpose of the VEROnA trial is to assess safety and tolerability of vandetanib beads in patients with resectable HCC. The primary aims of VEROnA are to assess the safety and tolerability of treatment with BTG-002814 and to measure the plasma and resected liver tissue concentrations of vandetanib and N-desmethyl vandetanib following treatment with BTG-002814. The secondary aims of VEROnA are: to evaluate the anatomical distribution of BTG-002814 on non-contrast enhanced imaging using 4D CT; evaluate histopathological features in the surgical specimen following treatment with BTG-002814; assess changes in blood flow on dynamic contrast-enhanced magnetic resonance imaging (DCE-MRI) following treatment with BTG-002814.

At the time of writing, three patients have now been successfully screened and treated, going on to have surgical resections. The first procedure was attended by the author, which allowed first-hand experience of the preparation and administration of the product in the cath-lab (Figure 6.1). CT scans of the patient liver post-treatment showed the radiopaque vandetanib beads *in situ*, filling the tumour blood vessels. Resected tumour samples may be available for future analysis of bead and drug distribution in the tumour, pending development of an appropriate imaging method, and could be subjected to biological analysis to determine proof of local pharmacological effect.



Figure 6.1 Interventional Radiologists and BTG team in theatre following the first clinical vandetanib bead procedure. Original in colour.

The future of vandetanib loaded beads as an anti-cancer treatment is promising, and its indication may not necessarily be limited to liver tumour monotherapy. Renal cell carcinoma is often treated with arterial kidney embolisation prior to resection, and evidence suggests that embolisation may play a role in stimulating the immune response [301]. Furthermore, a recent review has highlighted the potential for tyrosine kinase inhibitors to be immunostimulatory agents in the setting of renal cell carcinoma [302]. Inhibition of VEGF and MAPK pathways may augment the tumoural immune response, increasing activity of cytotoxic lymphocytes and interfering with mechanisms of immune tolerance to tumours [303-305]. Given the gathering interest in immunology based treatments such as checkpoint inhibitors, a potential synergy of vandetanib bead with these agents is worthy of future investigation.

In summary, a radiopaque, vandetanib eluting bead has been developed and characterised, showing unique physicochemical properties and release kinetics which have been correlated with pre-clinical pharmacokinetic data. Vandetanib shows activity against hepatocellular carcinoma cells in both hypoxic *in vitro* culture and in animal models. The work carried out in this thesis has supported the transition of this product to first in human clinical trials, the results of which are eagerly anticipated. Novel interventional combinations incorporating targeted drugs are hoped to provide improved treatment outcomes for patients suffering from this difficult to treat disease.

REFERENCES

1. Torre, L.A., F. Bray, R.L. Siegel, J. Ferlay, J. Lortet-Tieulent, and A. Jemal, *Global cancer statistics, 2012*. CA Cancer J Clin, 2015. **65**(2): p. 87-108.
2. Siegel, R.L., K.D. Miller, and A. Jemal, *Cancer statistics, 2016*. CA Cancer J Clin, 2016. **66**(1): p. 7-30.
3. Cancer Research UK. *Risks and Causes of Liver Cancer*. 2014 [19/02/14]; Available from: <http://www.cancerresearchuk.org/cancer-help/type/liver-cancer/about/risks-and-causes-of-liver-cancer>.
4. Forner, A., J.M. Llovet, and J. Bruix, *Hepatocellular carcinoma*. Lancet, 2012. **379**(9822): p. 1245-1255.
5. Bruno, S., T. Stroffolini, M. Colombo, S. Bollani, L. Benvegna, G. Mazzella, A. Ascione, T. Santantonio, F. Piccinino, P. Andreone, A. Mangia, G.B. Gaeta, M. Persico, S. Faggioli, P.L. Almasio, and D. Italian Association of the Study of the Liver, *Sustained virological response to interferon-alpha is associated with improved outcome in HCV-related cirrhosis: a retrospective study*. Hepatology, 2007. **45**(3): p. 579-87.
6. Malarkey, D.E., K. Johnson, L. Ryan, G. Boorman, and R.R. Maronpot, *New Insights into Functional Aspects of Liver Morphology*. Toxicologic Pathology, 2005. **33**(1): p. 27-34.
7. Juza, R.M. and E.M. Pauli, *Clinical and surgical anatomy of the liver: A review for clinicians*. Clinical Anatomy, 2014: p. n/a-n/a.
8. Iwakiri, Y., M. Grisham, and V. Shah, *Vascular Biology and Pathobiology of the Liver: Report of a Single Topic Symposium*. Hepatology, 2008. **47**(5): p. 1754-1763.
9. Frevert, U., S. Engelmann, S. Zougbedé, J. Stange, B. Ng, K. Matuschewski, L. Liebes, and H. Yee, *Intravital Observation of Plasmodium berghei Sporozoite Infection of the Liver*. PLOS Biology, 2005. **3**(6): p. e192.
10. Longo, D.L. and A.S. Fauci, *Harrison's Gastroenterology and Hepatology 2010*: The McGraw-Hill Companies, Inc.
11. Caldwell, S. and S.H. Park, *The epidemiology of hepatocellular cancer: from the perspectives of public health problem to tumor biology*. Journal of Gastroenterology, 2009. **44**: p. 96-101.
12. Whittaker, S., R. Marais, and A.X. Zhu, *The role of signaling pathways in the development and treatment of hepatocellular carcinoma*. Oncogene, 2010. **29**(36): p. 4989-5005.
13. Kim, S. and G.K. Abou-Alfa, *The role of tyrosine kinase inhibitors in hepatocellular carcinoma*. Clin Adv Hematol Oncol, 2014. **12**(1): p. 36-41.
14. Al-Husein, B., M. Abdalla, M. Trepte, D.L. DeRemer, and P.R. Somanath, *Anti-angiogenic therapy for cancer: An update*. Pharmacotherapy, 2012. **32**(12): p. 1095-1111.
15. Hoeben, A., B. Landuyt, M.S. Highley, H. Wildiers, A.T. Van Oosterom, and E.A. De Bruijn, *Vascular Endothelial Growth Factor and Angiogenesis*. Pharmacological Reviews, 2004. **56**(4): p. 549-580.
16. Soulen, G., *Interventional Oncology: Principles and Practice 2008*, USA: Cambridge University Press. 615.
17. Wang, G.L., B.H. Jiang, E.A. Rue, and G.L. Semenza, *Hypoxia-inducible factor 1 is a basic-helix-loop-helix-PAS heterodimer regulated by cellular O₂ tension*. Proceedings of the National Academy of Sciences of the United States of America, 1995. **92**(12): p. 5510-5514.
18. Semenza, G.L., *Targeting HIF-1 for cancer therapy*. Nature reviews.Cancer, 2003. **3**(10): p. 721-732.

19. von Marschall, Z., T. Cramer, M. Hocker, G. Finkenzeller, B. Wiedenmann, and S. Rosewicz, *Dual mechanism of vascular endothelial growth factor upregulation by hypoxia in human hepatocellular carcinoma*. *Gut*, 2001. **48**(1): p. 87-96.
20. Iavarone, M., P. Lampertico, F. Iannuzzi, E. Manenti, M.F. Donato, E. Arosio, F. Bertolini, M. Primignani, A. Sangiovanni, and M. Colombo, *Increased expression of vascular endothelial growth factor in small hepatocellular carcinoma*. *Journal of Viral Hepatitis*, 2007. **14**(2): p. 133-139.
21. Buckley, A.F., L.J. Burgart, V. Sahai, and S. Kakar, *Epidermal growth factor receptor expression and gene copy number in conventional hepatocellular carcinoma*. *Am J Clin Pathol*, 2008. **129**(2): p. 245-51.
22. Yoneda, N., Y. Sato, A. Kitao, H. Ikeda, S. Sawada-Kitamura, M. Miyakoshi, K. Harada, M. Sasaki, O. Matsui, and Y. Nakanuma, *Epidermal growth factor induces cytokeratin 19 expression accompanied by increased growth abilities in human hepatocellular carcinoma*. *Lab Invest*, 2011. **91**(2): p. 262-72.
23. Hooper, C. *EGFR interactions, roles and cancer therapy options*. [cited 2016 12/02/16]; Available from: <http://www.abcam.com/index.html?pageconfig=resource&rid=10723#affil>.
24. Zhang, Z., A.L. Stiegler, T.J. Boggon, S. Kobayashi, and B. Halmos, *EGFR-mutated lung cancer: a paradigm of molecular oncology*. *Oncotarget*, 2010. **1**(7): p. 497-514.
25. Su, M.C., H.C. Lien, and Y.M. Jeng, *Absence of epidermal growth factor receptor exon 18-21 mutation in hepatocellular carcinoma*. *Cancer Lett*, 2005. **224**(1): p. 117-21.
26. Lee, S.-C., S.-G. Lim, R. Soo, W.-S. Hsieh, J.-Y. Guo, T. Putti, Q. Tao, R. Soong, and B.-C. Goh, *Lack of somatic mutations in EGFR tyrosine kinase domain in hepatocellular and nasopharyngeal carcinoma*. *Pharmacogenetics and genomics*, 2006. **16**(1): p. 73-74.
27. Giannelli, G., C. Sgarra, L. Porcelli, A. Azzariti, S. Antonaci, and A. Paradiso, *EGFR and VEGFR as potential target for biological therapies in HCC cells*. *Cancer Letters*, 2008. **262**(2): p. 257-264.
28. Hopfner, M., A.P. Sutter, A. Huether, D. Schuppan, M. Zeitz, and H. Scherubl, *Targeting the epidermal growth factor receptor by gefitinib for treatment of hepatocellular carcinoma*. *J Hepatol*, 2004. **41**(6): p. 1008-16.
29. Huether, A., M. Hopfner, A.P. Sutter, D. Schuppan, and H. Scherubl, *Erlotinib induces cell cycle arrest and apoptosis in hepatocellular cancer cells and enhances chemosensitivity towards cytostatics*. *J Hepatol*, 2005. **43**(4): p. 661-9.
30. Sherman, M., *Staging for hepatocellular carcinoma: An embarrassment of riches*. *Journal of Hepatology*, 2015.
31. Ackerman, N.B., *Experimental studies on the circulatory dynamics of intrahepatic tumor blood supply*. *Cancer*, 1972. **29**(2): p. 435-439.
32. Park, Y.N., C.P. Yang, G.J. Fernandez, O. Cubukcu, S.N. Thung, and N.D. Theise, *Neoangiogenesis and sinusoidal "capillarization" in dysplastic nodules of the liver*. *Am J Surg Pathol*, 1998. **22**(6): p. 656-62.
33. Cazejust, J., B. Bessoud, N. Colignon, C. Garcia-Alba, O. Planché, and Y. Menu, *Hepatocellular carcinoma vascularization: From the most common to the lesser known arteries*. *Diagnostic and Interventional Imaging*, 2014. **95**(1): p. 27-36.
34. Facciorusso, A., *Drug-eluting beads transarterial chemoembolization for hepatocellular carcinoma: Current state of the art*. *World Journal of Gastroenterology*, 2018. **24**(2): p. 161-169.
35. Carter, S. and R.C.G. Martin Li, *Drug-eluting bead therapy in primary and metastatic disease of the liver*. *HPB : The Official Journal of the International Hepato Pancreato Biliary Association*, 2009. **11**(7): p. 541-550.
36. de Baere, T., S. Plotkin, R. Yu, A. Sutter, Y. Wu, and G.M. Cruise, *An In Vitro Evaluation of Four Types of Drug-Eluting Microspheres Loaded with Doxorubicin*. *Journal of Vascular and Interventional Radiology*, 2016. **27**(9): p. 1425-1431.

37. Hidaka, K., L. Moine, G. Collin, D. Labarre, J. Louis Grossiord, N. Huang, K. Osuga, S. Wada, and A. Laurent, *Elasticity and viscoelasticity of embolization microspheres*. Journal of the Mechanical Behavior of Biomedical Materials, 2011. **4**(8): p. 2161-2167.
38. Ashrafi, K., Y. Tang, H. Britton, O. Domenge, D. Blino, A.J. Bushby, K. Shuturminska, M. den Hartog, A. Radaelli, A.H. Negussie, A.S. Mikhail, D.L. Woods, V. Krishnasamy, E.B. Levy, B.J. Wood, S.L. Willis, M.R. Dreher, and A.L. Lewis, *Characterization of a novel intrinsically radiopaque Drug-eluting Bead for image-guided therapy: DC Bead LUMI™*. Journal of Controlled Release, 2017. **250**: p. 36-47.
39. Lewis, A.L., *DC Bead(TM): a major development in the toolbox for the interventional oncologist*. Expert Review of Medical Devices, 2009. **6**(4): p. 389-400.
40. Lammer, J., K. Malagari, T. Vogl, F. Pilleul, A. Denys, A. Watkinson, M. Pitton, G. Sergent, T. Pfammatter, S. Terraz, Y. Benhamou, Y. Avajon, T. Gruenberger, M. Pomoni, H. Langenberger, M. Schuchmann, J. Dumortier, C. Mueller, P. Chevallier, and R. Lencioni, *Prospective Randomized Study of Doxorubicin-Eluting-Bead Embolization in the Treatment of Hepatocellular Carcinoma: Results of the PRECISION V Study*. Cardiovascular and Interventional Radiology, 2010. **33**(1): p. 41-52.
41. Varela, M., M.I. Real, M. Burrel, A. Forner, M. Sala, M. Brunet, C. Ayuso, L. Castells, X. Montañá, J.M. Llovet, and J. Bruix, *Chemoembolization of hepatocellular carcinoma with drug eluting beads: Efficacy and doxorubicin pharmacokinetics*. Journal of Hepatology, 2007. **46**(3): p. 474-481.
42. Liu, K., X. Zhang, W. Xu, J. Chen, J. Yu, J.R. Gamble, and G.W. McCaughan, *Targeting the vasculature in hepatocellular carcinoma treatment: Starving versus normalizing blood supply*. Clinical And Translational Gastroenterology, 2017. **8**: p. e98.
43. Liang, B., C.-s. Zheng, G.-s. Feng, H.-p. Wu, Y. Wang, H. Zhao, J. Qian, and H.-m. Liang, *Correlation of Hypoxia-Inducible Factor 1[alpha] with Angiogenesis in Liver Tumors After Transcatheter Arterial Embolization in an Animal Model*. Cardiovascular and Interventional Radiology, 2010. **33**(4): p. 806-12.
44. Jia, Z.-z., G.-m. Jiang, and Y.-l. Feng, *Serum HIF-1 α and VEGF Levels Pre- and Post-TACE in Patients with Primary Liver Cancer*. Chinese Medical Sciences Journal, 2011. **26**(3): p. 158-162.
45. Kim, Y.B., Y.N. Park, and C. Park, *Increased proliferation activities of vascular endothelial cells and tumour cells in residual hepatocellular carcinoma following transcatheter arterial embolization*. Histopathology, 2001. **38**(2): p. 160-166.
46. Li, X., G.-S. Feng, C.-S. Zheng, C.-K. Zhuo, and X. Liu, *Expression of plasma vascular endothelial growth factor in patients with hepatocellular carcinoma and effect of transcatheter arterial chemoembolization therapy on plasma vascular endothelial growth factor level*. World Journal of Gastroenterology, 2004. **10**(19): p. 2878-2882.
47. Wang, B., XU, H., GAO, Z. Q., NING, H. F., SUN, Y. Q. & CAO, G. W., *Increased expression of vascular endothelial growth factor in hepatocellular carcinoma after transcatheter arterial chemoembolization*. Acta Radiologica, 2008. **49**(5): p. 523-529.
48. Xiong, Z.P., S.R. Yang, Z.Y. Liang, E.H. Xiao, X.P. Yu, S.K. Zhou, and Z.S. Zhang, *Association between vascular endothelial growth factor and metastasis after transcatheter arterial chemoembolization in patients with hepatocellular carcinoma*. Hepatobiliary Pancreat Dis Int, 2004. **3**(3): p. 386-90.
49. Poon, R.T., Lau, C., Yu, W., Fan, S., Wong, J., *High serum levels of vascular endothelial growth factor predict poor response to transarterial chemoembolization in hepatocellular carcinoma: A prospective study*. Oncology Reports, 2004. **11**(5): p. 1077-1084.
50. Sergio, A., C. Cristofori, R. Cardin, G. Pivetta, R. Ragazzi, A. Baldan, L. Girardi, U. Cillo, P. Burra, A. Giacomini, and F. Farinati, *Transcatheter arterial*

- chemoembolization (TACE) in hepatocellular carcinoma (HCC): the role of angiogenesis and invasiveness.* Am J Gastroenterol, 2008. **103**(4): p. 914-21.
51. Shim, J.H., J.-W. Park, J.H. Kim, M. An, S.-Y. Kong, B.-H. Nam, J.-I. Choi, H.B. Kim, W.J. Lee, and C.-M. Kim, *Association between increment of serum VEGF level and prognosis after transcatheter arterial chemoembolization in hepatocellular carcinoma patients.* Cancer Science, 2008. **99**(10): p. 2037-2044.
 52. Zhu, A.X., *Systemic Therapy of Advanced Hepatocellular Carcinoma: How Hopeful Should We Be?* The Oncologist, 2006. **11**(7): p. 790-800.
 53. Villanueva, A., V. Hernandez-Gea, and J.M. Llovet, *Medical therapies for hepatocellular carcinoma: a critical view of the evidence.* Nature Reviews Gastroenterology & Hepatology, 2013. **10**(1): p. 34-42.
 54. Hsu, C.-H., Y. Shen, Y. Shao, C. Hsu, and A. Cheng, *Sorafenib in advanced hepatocellular carcinoma: current status and future perspectives.* Journal of Hepatocellular Carcinoma, 2014. **1**: p. 85-99.
 55. Fang, P., J.H. Hu, Z.G. Cheng, Z.F. Liu, J.L. Wang, and S.C. Jiao, *Efficacy and safety of bevacizumab for the treatment of advanced hepatocellular carcinoma: a systematic review of phase II trials.* PLoS ONE, 2012. **7**(12): p. e49717.
 56. Eskens, F.A.L.M. and J. Verweij, *The clinical toxicity profile of vascular endothelial growth factor (VEGF) and vascular endothelial growth factor receptor (VEGFR) targeting angiogenesis inhibitors; A review.* European Journal of Cancer, 2006. **42**(18): p. 3127-3139.
 57. Hebbbar, M., A. Heurgue-Berlot, V. Boige, K. Le Malicot, B. Bernard-Chabert, C. Marcus, S. Dharancy, G. Sergent, J.M. Perarnau, F. Ehrhard, I. Ollivier-Hourmand, J. Vergniol, P. Michel, J. Edeline, Y. Rinaldi, J.F. Seitz, C. Lepage, and T. De Baere, *2305 Randomized phase 2/3 trial of transcatheter arterial chemoembolization (TACE) plus sunitinib or placebo in patients with hepatocellular carcinoma (HCC) (PRODIGE 16/SATURNE study): Results of the Phase II part.* European Journal of Cancer. **51**: p. S434.
 58. Zhang, L., P. Hu, X. Chen, and P. Bie, *Transarterial Chemoembolization (TACE) plus Sorafenib Versus TACE for Intermediate or Advanced Stage Hepatocellular Carcinoma: A Meta-Analysis.* PLoS ONE, 2014. **9**(6): p. e100305.
 59. Chan, S.L., W. Yeo, F. Mo, A.W.H. Chan, J. Koh, L. Li, E.P. Hui, C.C.N. Chong, P.B.S. Lai, T.S.K. Mok, and S.C.H. Yu, *A phase 2 study of the efficacy and biomarker on the combination of transarterial chemoembolization and axitinib in the treatment of inoperable hepatocellular carcinoma.* Cancer, 2017. **123**(20): p. 3977-3985.
 60. Liu, C., W. Xing, T. Si, H. Yu, and Z. Guo, *Efficacy and safety of apatinib combined with transarterial chemoembolization for hepatocellular carcinoma with portal venous tumor thrombus: a retrospective study.* Oncotarget, 2017. **8**(59): p. 100734-100745.
 61. Britten, C.D., A.S. Gomes, Z.A. Wainberg, D. Elashoff, R. Amado, Y. Xin, R.W. Busuttil, D.J. Slamon, and R.S. Finn, *Transarterial chemoembolization plus or minus intravenous bevacizumab in the treatment of hepatocellular cancer: a pilot study.* BMC cancer, 2012. **12**: p. 16.
 62. Chan, S.L. and W. Yeo, *Targeted therapy of hepatocellular carcinoma: Present and future.* Journal of Gastroenterology and Hepatology, 2012. **27**(5): p. 862-872.
 63. Lencioni, R., J.M. Llovet, G. Han, W.Y. Tak, J. Yang, A. Guglielmi, S.W. Paik, M. Reig, Y. Kim do, G.Y. Chau, A. Luca, L.R. del Arbol, M.A. Leberre, W. Niu, K. Nicholson, G. Meinhardt, and J. Bruix, *Sorafenib or placebo plus TACE with doxorubicin-eluting beads for intermediate stage HCC: The SPACE trial.* J Hepatol, 2016. **64**(5): p. 1090-8.
 64. Kudo, M., K. Imanaka, N. Chida, K. Nakachi, W.-Y. Tak, T. Takayama, J.-H. Yoon, T. Hori, H. Kumada, N. Hayashi, S. Kaneko, H. Tsubouchi, D.J. Suh, J. Furuse, T. Okusaka, K. Tanaka, O. Matsui, M. Wada, I. Yamaguchi, T. Ohya, G. Meinhardt, and K. Okita, *Phase III study of sorafenib after transarterial chemoembolisation in Japanese*

- and Korean patients with unresectable hepatocellular carcinoma. *European Journal of Cancer*. **47**(14): p. 2117-2127.
65. Geschwind, J.F., M. Kudo, J.A. Marrero, A.P. Venook, X.P. Chen, J.P. Bronowicki, L. Dagher, J. Furuse, L. Ladron de Guevara, C. Papandreou, A.J. Sanyal, T. Takayama, S.L. Ye, S.K. Yoon, K. Nakajima, R. Lehr, S. Heldner, and R. Lencioni, *TACE Treatment in Patients with Sorafenib-treated Unresectable Hepatocellular Carcinoma in Clinical Practice: Final Analysis of GIDEON*. *Radiology*, 2016. **279**(2): p. 630-40.
 66. Dreher, M.R., K.V. Sharma, D.L. Woods, G. Reddy, Y. Tang, W.F. Pritchard, O.A. Chiesa, J.W. Karanian, J.A. Esparza, D. Donahue, E.B. Levy, S.L. Willis, A.L. Lewis, and B.J. Wood, *Radiopaque Drug-Eluting Beads for Transcatheter Embolotherapy: Experimental Study of Drug Penetration and Coverage in Swine*. *Journal of Vascular and Interventional Radiology*, 2012. **23**(2): p. 257-264.e4.
 67. Sharma, K.V., M.R. Dreher, Y. Tang, W. Pritchard, O.A. Chiesa, J. Karanian, J. Peregoy, B. Orandi, D. Woods, D. Donahue, J. Esparza, G. Jones, S.L. Willis, A.L. Lewis, and B.J. Wood, *Development of Image-able Beads for Transcatheter Embolotherapy*. *J Vasc Interv Radiol*, 2010. **21**(6): p. 865-876.
 68. Thanoo, B.C. and A. Jayakrishnan, *Radiopaque hydrogel microspheres*. *J Microencapsul*, 1989. **6**(2): p. 233-44.
 69. Mawad, D., L.A. Poole-Warren, P. Martens, L.H. Koole, T.L.B. Slots, and C.S.J.v. Hooy-Corstjens, *Synthesis and Characterization of Radiopaque Iodine-containing Degradable PVA Hydrogels*. *Biomacromolecules*, 2008. **9**(1): p. 263-268.
 70. Duran, R., K. Sharma, M.R. Dreher, K. Ashrafi, S. Mirpour, M. Lin, R.E. Scherthaner, T.R. Schlachter, V. Tacher, A.L. Lewis, S. Willis, M. den Hartog, A. Radaelli, A.H. Negussie, B.J. Wood, and J.F. Geschwind, *A Novel Inherently Radiopaque Bead for Transarterial Embolization to Treat Liver Cancer - A Pre-clinical Study*. *Theranostics*, 2016. **6**(1): p. 28-39.
 71. Park, W., J. Chen, S. Cho, S.-j. Park, A.C. Larson, K. Na, and D.-H. Kim, *Acidic pH-Triggered Drug-Eluting Nanocomposites for Magnetic Resonance Imaging-Monitored Intra-arterial Drug Delivery to Hepatocellular Carcinoma*. *ACS Applied Materials & Interfaces*, 2016. **8**(20): p. 12711-12719.
 72. Chen, J., S.B. White, K.R. Harris, W. Li, J.W.T. Yap, D.-H. Kim, R.J. Lewandowski, L.D. Shea, and A.C. Larson, *Poly(lactide-co-glycolide) microspheres for MRI-monitored delivery of sorafenib in a rabbit VX2 model*. *Biomaterials*, 2015. **61**: p. 299-306.
 73. Chen, J., A.Y. Sheu, W. Li, Z. Zhang, D.-H. Kim, R.J. Lewandowski, R.A. Omary, L.D. Shea, and A.C. Larson, *Poly(lactide-co-glycolide) Microspheres for MRI-Monitored Transcatheter Delivery of Sorafenib to Liver Tumors*. *Journal of controlled release : official journal of the Controlled Release Society*, 2014. **184**: p. 10-17.
 74. Wang, Y., A. Benzina, D.G.M. Molin, N.v.d. Akker, M. Gagliardi, and L.H. Koole, *Preparation and structure of drug-carrying biodegradable microspheres designed for transarterial chemoembolization therapy*. *Journal of Biomaterials Science, Polymer Edition*, 2015. **26**(2): p. 77-91.
 75. Wang, Y., D.G. Molin, C. Sevrin, C. Grandfils, N.M. van den Akker, M. Gagliardi, M.L. Knetsch, T. Delhaas, and L.H. Koole, *In vitro and in vivo evaluation of drug-eluting microspheres designed for transarterial chemoembolization therapy*. *Int J Pharm*, 2016. **503**(1-2): p. 150-62.
 76. Lahti, S.J., D. Zeng, J.B. Jia, M. Xing, and H.S. Kim, *Sorafenib loaded drug-eluting beads: loading and eluting kinetics and in vitro viability study*. *Journal of Vascular and Interventional Radiology*, 2015. **26**(2): p. S80-S81.
 77. Lahti, S.J., D. Zeng, J.B. Jia, M. Xing, and H.S. Kim, *Sunitinib loaded drug-eluting beads: loading and eluting kinetics and in vitro viability study*. *Journal of Vascular and Interventional Radiology*, 2017. **26**(2): p. S81-S82.
 78. Fuchs, K., P.E. Bize, A. Denys, G. Borchard, and O. Jordan, *Sunitinib-eluting beads for chemoembolization: Methods for in vitro evaluation of drug release*. *International Journal of Pharmaceutics*, 2015. **482**(1-2): p. 68-74.

79. Fuchs, K., P.E. Bize, O. Dormond, A. Denys, E. Doelker, G. Borchard, and O. Jordan, *Drug-Eluting Beads Loaded with Antiangiogenic Agents for Chemoembolization: In Vitro Sunitinib Loading and Release and In Vivo Pharmacokinetics in an Animal Model*. *Journal of Vascular and Interventional Radiology*, 2014. **25**(3): p. 379-387.
80. Bize, P., R. Duran, K. Fuchs, O. Dormond, J. Namur, L.A. Decosterd, O. Jordan, E. Doelker, and A. Denys, *Antitumoral Effect of Sunitinib-eluting Beads in the Rabbit VX2 Tumor Model*. *Radiology*, 2016. **280**(2): p. 150361.
81. Cheng, A.-L., Y.-K. Kang, D.-Y. Lin, J.-W. Park, M. Kudo, S. Qin, H.-C. Chung, X. Song, J. Xu, G. Poggi, M. Omata, S.P. Lowenthal, S. Lanzalone, L. Yang, M.J. Lechuga, and E. Raymond, *Sunitinib Versus Sorafenib in Advanced Hepatocellular Cancer: Results of a Randomized Phase III Trial*. *Journal of Clinical Oncology*, 2013. **31**(32): p. 4067-4075.
82. Morabito, A., M.C. Piccirillo, F. Falasconi, G. De Feo, A. Del Giudice, J. Bryce, M. Di Maio, E. De Maio, N. Normanno, and F. Perrone, *Vandetanib (ZD6474), a Dual Inhibitor of Vascular Endothelial Growth Factor Receptor (VEGFR) and Epidermal Growth Factor Receptor (EGFR) Tyrosine Kinases: Current Status and Future Directions*. *Oncologist*, 2009. **14**(4): p. 378-390.
83. Weil, A., P. Martin, R. Smith, S. Oliver, P. Langmuir, J. Read, and K.-H. Molz, *Pharmacokinetics of Vandetanib in Subjects with Renal or Hepatic Impairment*. *Clinical Pharmacokinetics*, 2010. **49**(9): p. 607-18.
84. Wedge, S.R., D.J. Ogilvie, M. Dukes, J. Kendrew, R. Chester, J.A. Jackson, S.J. Boffey, P.J. Valentine, J.O. Curwen, H.L. Musgrove, G.A. Graham, G.D. Hughes, A.P. Thomas, E.S.E. Stokes, B. Curry, G.H.P. Richmond, P.F. Wadsworth, A.L. Bigley, and L.F. Hennequin, *ZD6474 Inhibits Vascular Endothelial Growth Factor Signaling, Angiogenesis, and Tumor Growth following Oral Administration*. *Cancer research*, 2002. **62**(16): p. 4645-4655.
85. Huang, P.X., X.J. Xu, L.Y. Wang, B.J. Zhu, X.D. Wang, and J.L. Xia, *The role of EGF-EGFR signalling pathway in hepatocellular carcinoma inflammatory microenvironment*. *Journal of Cellular and Molecular Medicine*, 2014. **18**(2): p. 218-230.
86. Eng, C., *RET Proto-Oncogene in the Development of Human Cancer*. *Journal of Clinical Oncology*, 1999. **17**(1): p. 380.
87. Inoue, K., T. Torimura, T. Nakamura, H. Iwamoto, H. Masuda, M. Abe, O. Hashimoto, H. Koga, T. Ueno, H. Yano, and M. Sata, *Vandetanib, an Inhibitor of VEGF Receptor-2 and EGF Receptor, Suppresses Tumor Development and Improves Prognosis of Liver Cancer in Mice*. *Clinical Cancer Research*, 2012. **18**(14): p. 3924-3933.
88. Brave, S., G. Marshall, A. Wainwright, N. James, N. Acheson, Z. Howard, K. Ratcliffe, G. Speake, S. Barry, D. Hickinson, and A. Ryan, *In vitro effects of vandetanib on VEGFR2, EGFR and RET phosphorylation, endothelial cell tube formation, and tumor cell growth and survival*. *Molecular Cancer Therapeutics*, 2014. **6**(11 Supplement): p. C189.
89. Wang, J., H. Wang, J. Li, Z. Liu, H. Xie, X. Wei, D. Lu, R. Zhuang, X. Xu, and S. Zheng, *iRGD-Decorated Polymeric Nanoparticles for the Efficient Delivery of Vandetanib to Hepatocellular Carcinoma: Preparation and in Vitro and in Vivo Evaluation*. *ACS Applied Materials & Interfaces*, 2016. **8**(30): p. 19228-19237.
90. Lee, S.H., J.K. Lee, M.J. Ahn, D.W. Kim, J.M. Sun, B. Keam, T.M. Kim, D.S. Heo, J.S. Ahn, Y.L. Choi, H.S. Min, Y.K. Jeon, and K. Park, *Vandetanib in pretreated patients with advanced non-small cell lung cancer-harboring RET rearrangement: a phase II clinical trial*. *Ann Oncol*, 2017. **28**(2): p. 292-297.
91. De Luca, A., A. D'Alessio, M.R. Maiello, M. Gallo, S. Bevilacqua, D. Frezzetti, A. Morabito, F. Perrone, and N. Normanno, *Vandetanib as a potential treatment for breast cancer*. *Expert Opin Investig Drugs*, 2014. **23**(9): p. 1295-303.
92. Stamatakis, L., B. Shuch, E.A. Singer, J. Nix, H. Truong, J.C. Friend, S. Fowler, G. Bratslavsky, A.R. Metwalli, J.H. Shih, W.M. Linehan, and R. Srinivasan, *Phase II trial*

- of vandetanib in Von Hippel-Lindau-associated renal cell carcinoma.* Journal of Clinical Oncology, 2013. **31**(15_suppl): p. 4584-4584.
93. Hsu, C., T.-S. Yang, T.-I. Huo, R.-K. Hsieh, C.-W. Yu, W.-S. Hwang, T.-Y. Hsieh, W.-T. Huang, Y. Chao, R. Meng, and A.-L. Cheng, *Vandetanib in patients with inoperable hepatocellular carcinoma: A phase II, randomized, double-blind, placebo-controlled study.* Journal of Hepatology, 2012. **56**(5): p. 1097-1103.
 94. Ton, G.N., M.E. Banaszynski, and J.M. Kolesar, *Vandetanib: a novel targeted therapy for the treatment of metastatic or locally advanced medullary thyroid cancer.* Am J Health Syst Pharm, 2013. **70**(10): p. 849-55.
 95. Hagan, A., W. Macfarlane, A. Lloyd, G. Phillips, R. Holden, Z. Bascal, R. Whomsley, H. Kilpatrick, Y. Tang, A. Lewis, J. Namur, F. Pascale, and J. Pelage, *In vitro and in vivo characterisation of a multiple tyrosine kinase inhibitor drug eluting bead.* Journal of Vascular and Interventional Radiology, 2016. **27**(3): p. S84.
 96. Takahashi, S., M. Kudo, H. Chung, T. Inoue, E. Ishikawa, S. Kitai, C. Tatsumi, T. Ueda, Y. Minami, K. Ueshima, and S. Haji, *Initial treatment response is essential to improve survival in patients with hepatocellular carcinoma who underwent curative radiofrequency ablation therapy.* Oncology, 2007. **72 Suppl 1**: p. 98-103.
 97. Jungermann, K. and T. Kietzmann, *Oxygen: Modulator of metabolic zonation and disease of the liver.* Hepatology, 2000. **31**(2): p. 255-260.
 98. Talks, K.L., H. Turley, K.C. Gatter, P.H. Maxwell, C.W. Pugh, P.J. Ratcliffe, and A.L. Harris, *The Expression and Distribution of the Hypoxia-Inducible Factors HIF-1 α and HIF-2 α in Normal Human Tissues, Cancers, and Tumor-Associated Macrophages.* The American Journal of Pathology, 2000. **157**(2): p. 411-421.
 99. Wilson, G.K., D.A. Tennant, and J.A. McKeating, *Hypoxia inducible factors in liver disease and hepatocellular carcinoma: Current understanding and future directions.* Journal of Hepatology, 2014. **61**(6): p. 1397-1406.
 100. Wong, C.C.-L., A.K.-L. Kai, and I.O.-L. Ng, *The impact of hypoxia in hepatocellular carcinoma metastasis.* Frontiers of Medicine, 2014. **8**(1): p. 33-41.
 101. Wu, X.Z., G.R. Xie, and D. Chen, *Hypoxia and hepatocellular carcinoma: The therapeutic target for hepatocellular carcinoma.* J Gastroenterol Hepatol, 2007. **22**(8): p. 1178-82.
 102. Rohwer, N. and T. Cramer, *Hypoxia-mediated drug resistance: Novel insights on the functional interaction of HIFs and cell death pathways.* Drug Resistance Updates, 2011. **14**(3): p. 191-201.
 103. Gewirtz, D.A., *A critical evaluation of the mechanisms of action proposed for the antitumor effects of the anthracycline antibiotics adriamycin and daunorubicin.* Biochem Pharmacol, 1999. **57**(7): p. 727-41.
 104. Shen, F., S. Chu, A.K. Bence, B. Bailey, X. Xue, P.A. Erickson, M.H. Montrose, W.T. Beck, and L.C. Erickson, *Quantitation of doxorubicin uptake, efflux, and modulation of multidrug resistance (MDR) in MDR human cancer cells.* J Pharmacol Exp Ther, 2008. **324**(1): p. 95-102.
 105. Comerford, K.M., T.J. Wallace, J. Karhausen, N.A. Louis, M.C. Montalto, and S.P. Colgan, *Hypoxia-inducible factor-1-dependent regulation of the multidrug resistance (MDR1) gene.* Cancer Res, 2002. **62**(12): p. 3387-94.
 106. Shen, D.W., Y.G. Lu, K.V. Chin, I. Pastan, and M.M. Gottesman, *Human hepatocellular carcinoma cell lines exhibit multidrug resistance unrelated to MDR1 gene expression.* J Cell Sci, 1991. **98 (Pt 3)**: p. 317-22.
 107. Bowyer, C., A.L. Lewis, A.W. Lloyd, G.J. Phillips, and W.M. Macfarlane, *Hypoxia as a target for drug combination therapy of liver cancer.* Anticancer Drugs, 2017.
 108. Cox, J. and S. Weinman, *Mechanisms of doxorubicin resistance in hepatocellular carcinoma.* Hepatic Oncology, 2015. **3**(1): p. 57-59.
 109. Manov, I., Y. Pollak, R. Broneshter, and T.C. Iancu, *Inhibition of doxorubicin-induced autophagy in hepatocellular carcinoma Hep3B cells by sorafenib – the role of*

- extracellular signal-regulated kinase counteraction*. FEBS Journal, 2011. **278**(18): p. 3494-3507.
110. Jovelet, C., J. Bénard, F. Forestier, R. Farinotti, J.M. Bidart, and S. Gil, *Inhibition of P-glycoprotein functionality by vandetanib may reverse cancer cell resistance to doxorubicin*. European journal of pharmaceutical sciences : official journal of the European Federation for Pharmaceutical Sciences, 2012. **46**(5): p. 484.
 111. El-Kenawi, A.E. and A.B. El-Remessy, *Angiogenesis inhibitors in cancer therapy: mechanistic perspective on classification and treatment rationales*. British Journal of Pharmacology, 2013. **170**(4): p. 712-729.
 112. Pàez-Ribes, M., E. Allen, J. Hudock, T. Takeda, H. Okuyama, F. Viñals, M. Inoue, G. Bergers, D. Hanahan, and O. Casanovas, *Antiangiogenic Therapy Elicits Malignant Progression of Tumors to Increased Local Invasion and Distant Metastasis*. Cancer cell, 2009. **15**(3): p. 220-231.
 113. Ahmadi, M., Z. Ahmadihosseini, S.J. Allison, S. Begum, K. Rockley, M. Sadiq, S. Chintamaneni, R. Lokwani, N. Hughes, and R.M. Phillips, *Hypoxia modulates the activity of a series of clinically approved tyrosine kinase inhibitors*. British Journal of Pharmacology, 2014. **171**(1): p. 224-236.
 114. Liang, Y., T. Zheng, R. Song, J. Wang, D. Yin, L. Wang, H. Liu, L. Tian, X. Fang, X. Meng, H. Jiang, J. Liu, and L. Liu, *Hypoxia-mediated sorafenib resistance can be overcome by EF24 through Von Hippel-Lindau tumor suppressor-dependent HIF-1 α inhibition in hepatocellular carcinoma*. Hepatology, 2013. **57**(5): p. 1847-57.
 115. Ban, H.S., M. Uno, and H. Nakamura, *Suppression of hypoxia-induced HIF-1 α accumulation by VEGFR inhibitors: Different profiles of AAL993 versus SU5416 and KRN633*. Cancer Letters, 2010. **296**(1): p. 17-26.
 116. Nilsson, M.B., P.E. Zage, L. Zeng, L. Xu, T. Cascone, H.K. Wu, B. Saigal, P.A. Zweidler-McKay, and J.V. Heymach, *Multiple receptor tyrosine kinases regulate HIF-1[α] and HIF-2[α] in normoxia and hypoxia in neuroblastoma: implications for antiangiogenic mechanisms of multikinase inhibitors*. Oncogene, 2010. **29**(20): p. 2938-2949.
 117. Pore, N., Z. Jiang, A. Gupta, G. Cerniglia, G.D. Kao, and A. Maity, *EGFR Tyrosine Kinase Inhibitors Decrease VEGF Expression by Both Hypoxia-Inducible Factor (HIF)-1-Independent and HIF-1-Dependent Mechanisms*. Cancer research, 2006. **66**(6): p. 3197-3204.
 118. Yang, Z.F., R.T.P. Poon, Y. Liu, C.K. Lau, D.W. Ho, K.H. Tam, C.T. Lam, and S.T. Fan, *High doses of tyrosine kinase inhibitor PTK787 enhance the efficacy of ischemic hypoxia for the treatment of hepatocellular carcinoma: dual effects on cancer cell and angiogenesis*. Molecular Cancer Therapeutics, 2006. **5**(9): p. 2261-2270.
 119. Martinez, I., G.I. Nedredal, C.I. Øie, A. Warren, O. Johansen, D.G. Le Couteur, and B. Smedsrød, *The influence of oxygen tension on the structure and function of isolated liver sinusoidal endothelial cells*. Comparative Hepatology, 2008. **7**(1): p. 1-11.
 120. McKeown, S.R., *Defining normoxia, physoxia and hypoxia in tumours—implications for treatment response*. The British Journal of Radiology, 2014. **87**(1035): p. 20130676.
 121. Wu, D. and P. Yotnda, *Induction and Testing of Hypoxia in Cell Culture*. Journal of Visualized Experiments : JoVE, 2011(54): p. 2899.
 122. López-Terrada, D., S.W. Cheung, M.J. Finegold, and B.B. Knowles, *Hep G2 is a hepatoblastoma-derived cell line*. Human Pathology, 2009. **40**(10): p. 1512-1515.
 123. Zhao, P., X. Yang, S. Qi, H. Liu, H. Jiang, S. Hoppmann, Q. Cao, M.-S. Chua, S.K. So, and Z. Cheng, *Molecular Imaging of Hepatocellular Carcinoma Xenografts with Epidermal Growth Factor Receptor Targeted Affibody Probes*. Biomed Res Int, 2013. **2013**: p. 11.
 124. Itabashi, H., C. Maesawa, H. Oikawa, K. Kotani, E. Sakurai, K. Kato, H. Komatsu, H. Nitta, H. Kawamura, G. Wakabayashi, and T. Masuda, *Angiotensin II and epidermal growth factor receptor cross-talk mediated by a disintegrin and metalloprotease*

- accelerates tumor cell proliferation of hepatocellular carcinoma cell lines*. *Hepatol Res*, 2008. **38**(6): p. 601-13.
125. Costantini, S., G. Di Bernardo, M. Cammarota, G. Castello, and G. Colonna, *Gene expression signature of human HepG2 cell line*. *Gene*, 2013. **518**(2): p. 335-345.
 126. Hoffmann, K., Z. Xiao, C. Franz, E. Mohr, S. Serba, M.W. Büchler, and P. Schemmer, *Involvement of the epidermal growth factor receptor in the modulation of multidrug resistance in human hepatocellular carcinoma cells in vitro*. *Cancer Cell International*, 2011. **11**(1): p. 40.
 127. Jo, M., D.B. Stolz, J.E. Espren, K. Dorko, G.K. Michalopoulos, and S.C. Strom, *Cross-talk between Epidermal Growth Factor Receptor and c-Met Signal Pathways in Transformed Cells*. *Journal of Biological Chemistry*, 2000. **275**(12): p. 8806-8811.
 128. Pang, R.T.K., T.C.W. Poon, N. Wong, P.B.S. Lai, N.L.Y. Wong, C.M.L. Chan, J.W.S. Yu, A.T.C. Chan, and J.J.Y. Sung, *Comparison of protein expression patterns between hepatocellular carcinoma cell lines and a hepatoblastoma cell line*. *Clinical Proteomics*, 2004. **1**(3): p. 313-331.
 129. Knowles, B.B., C.C. Howe, and D.P. Aden, *Human hepatocellular carcinoma cell lines secrete the major plasma proteins and hepatitis B surface antigen*. *Science*, 1980. **209**(4455): p. 497-9.
 130. Sánchez-Elsner, T., L.M. Botella, B. Velasco, A. Corbí, L. Attisano, and C. Bernabéu, *Synergistic Cooperation between Hypoxia and Transforming Growth Factor- β Pathways on Human Vascular Endothelial Growth Factor Gene Expression*. *Journal of Biological Chemistry*, 2001. **276**(42): p. 38527-38535.
 131. Hung, W., M. Yang, C. Chang, J. Tsai, and L. Chuang, *Differential regulation of EGF production, EGF receptor-binding, and cellular growth by sodium-butyrate in hep3b and plc/prf/5 human hepatoma-cells*. *Int J Oncol*, 1995. **7**(5): p. 1089-93.
 132. Sukowati, C.H.C., B. Anfusio, G. Torre, P. Francalanci, L.S. Crocè, and C. Tiribelli, *The Expression of CD90/Thy-1 in Hepatocellular Carcinoma: An In Vivo and In Vitro Study*. *PLoS ONE*, 2013. **8**(10): p. e76830.
 133. Hoarau-Véchet, J., A. Rafii, C. Touboul, and J. Pasquier, *Halfway between 2D and Animal Models: Are 3D Cultures the Ideal Tool to Study Cancer-Microenvironment Interactions?* *International Journal of Molecular Sciences*, 2018. **19**(1): p. 181.
 134. Chiew, G.G.Y., N. Wei, S. Sultania, S. Lim, and K.Q. Luo, *Bioengineered three-dimensional co-culture of cancer cells and endothelial cells: A model system for dual analysis of tumor growth and angiogenesis*. *Biotechnology and Bioengineering*, 2017. **114**(8): p. 1865-1877.
 135. Jung, H.-R., H.M. Kang, J.-W. Ryu, D.-S. Kim, K.H. Noh, E.-S. Kim, H.-J. Lee, K.-S. Chung, H.-S. Cho, N.-S. Kim, D.-S. Im, J.H. Lim, and C.-R. Jung, *Cell Spheroids with Enhanced Aggressiveness to Mimic Human Liver Cancer In Vitro and In Vivo*. *Scientific Reports*, 2017. **7**(1): p. 10499.
 136. Heindryckx, F., I. Colle, and H. Van Vlierberghe, *Experimental mouse models for hepatocellular carcinoma research*. *Int J Exp Pathol*, 2009. **90**(4): p. 367-86.
 137. Forster, R.E., S.A. Small, Y. Tang, C.L. Heaysman, A.W. Lloyd, W. Macfarlane, G.J. Phillips, M.D. Antonijevic, and A.L. Lewis, *Comparison of DC Bead-irinotecan and DC Bead-topotecan drug eluting beads for use in locoregional drug delivery to treat pancreatic cancer*. *J Mater Sci Mater Med*, 2010. **21**(9): p. 2683-90.
 138. Bowyer, C., *Hypoxia as a target for drug combination therapy of liver cancer*, in *School of Pharmacy and Biomolecular Sciences 2011*, University of Brighton.
 139. Tennant, B.C., *Hepatocellular carcinoma in the woodchuck model of hepatitis B virus infection*. *Gastroenterology*, 2004. **127**(5 Suppl 1): p. S283-93.
 140. Wilkins, L.R., J.R. Stone, J. Mata, A. Hawrylack, E. Kubicka, and D.L. Brautigan, *The Use of the Woodchuck as an Animal Model for Evaluation of Transarterial Embolization*. *Journal of Vascular and Interventional Radiology*, 2017. **28**(10): p. 1467-1471.

141. Iyer, R., B. Tennant, R. Brekken, L. Rivera, L. Pendyala, J. Wu, G. Fetterly, C. Johnson, and D. Trump, *Woodchuck hepatocellular cancer (HCC): a translational model for developing anti-angiogenic therapies for human hepatocellular cancer*. *Cancer research*, 2008. **68**(9 Supplement): p. 2916-2916.
142. Pascale, F., L. Bedouet, M. Baylatry, J. Namur, and A. Laurent, *Comparative Chemosensitivity of VX2 and HCC Cell Lines to Drugs Used in TACE*. *Anticancer Res*, 2015. **35**(12): p. 6497-503.
143. Hong, K., A. Khwaja, E. Liapi, M.S. Torbenson, C.S. Georgiades, and J.F. Geschwind, *New intra-arterial drug delivery system for the treatment of liver cancer: preclinical assessment in a rabbit model of liver cancer*. *Clin Cancer Res*, 2006. **12**(8): p. 2563-7.
144. Vossen, J.A., M. Buijs, L. Syed, F. Kutiyawala, M. Kutiyawala, J.F. Geschwind, and M. Vali, *Development of a new orthotopic animal model of metastatic liver cancer in the rabbit VX2 model: effect on metastases after partial hepatectomy, intra-arterial treatment with 3-bromopyruvate and chemoembolization*. *Clin Exp Metastasis*, 2008. **25**(7): p. 811-7.
145. Choi, J.W., H.-J. Cho, J.-H. Park, S.Y. Baek, J.W. Chung, D.-D. Kim, and H.-C. Kim, *Comparison of Drug Release and Pharmacokinetics after Transarterial Chemoembolization Using Diverse Lipiodol Emulsions and Drug-Eluting Beads*. *PLoS ONE*, 2014. **9**(12): p. e115898.
146. Martin, R., J. Irurzun, J. Munchart, I. Trofimov, A. Scupchenko, C. Tatum, and G. Narayanan, *Optimal technique and response of doxorubicin beads in hepatocellular cancer: bead size and dose*. *Korean J Hepatol*, 2011. **17**(1): p. 51-60.
147. Geschwind, J.F., D.E. Ramsey, B. Cleffken, B.C. van der Wal, H. Kobeiter, K. Juluru, G.G. Hartnell, and M.A. Choti, *Transcatheter arterial chemoembolization of liver tumors: effects of embolization protocol on injectable volume of chemotherapy and subsequent arterial patency*. *Cardiovasc Intervent Radiol*, 2003. **26**(2): p. 111-7.
148. Reyes, D.K., J.A. Vossen, I.R. Kamel, N.S. Azad, T.A. Wahlin, M.S. Torbenson, M.A. Choti, and J.-F.H. Geschwind, *Single-Center Phase II Trial of Transarterial Chemoembolization With Drug-Eluting Beads for Patients With Unresectable Hepatocellular Carcinoma: Initial Experience in the United States*. *Cancer journal (Sudbury, Mass.)*, 2009. **15**(6): p. 526-532.
149. Lewis, A.L., M.V. Gonzalez, S.W. Leppard, J.E. Brown, P.W. Stratford, G.J. Phillips, and A.W. Lloyd, *Doxorubicin eluting beads - 1: effects of drug loading on bead characteristics and drug distribution*. *J Mater Sci Mater Med*, 2007. **18**(9): p. 1691-9.
150. Taylor, R.R., Y. Tang, M.V. Gonzalez, P.W. Stratford, and A.L. Lewis, *Irinotecan drug eluting beads for use in chemoembolization: in vitro and in vivo evaluation of drug release properties*. *Eur J Pharm Sci*, 2007. **30**(1): p. 7-14.
151. Kerr, D.J., *Microparticulate drug delivery systems as an adjunct to cancer treatment*. *Cancer Drug Deliv*, 1987. **4**(1): p. 55-61.
152. Lewis, A.L. and M.R. Dreher, *Locoregional Drug Delivery Using Image-guided Intra-arterial Drug Eluting Bead Therapy*. *Journal of Controlled Release*, 2012. **161**(2): p. 338-350.
153. Taylor, R.R., Y. Tang, M.V. Gonzalez, P.W. Stratford, and A.L. Lewis, *Irinotecan drug eluting beads for use in chemoembolization: In vitro and in vivo evaluation of drug release properties*. *European Journal of Pharmaceutical Sciences*, 2007. **30**(1): p. 7-14.
154. Keese, M., L. Gasimova, K. Schwenke, V. Yagublu, E. Shang, R. Faissner, A. Lewis, S. Samel, and M. Löhr, *Doxorubicin and mitoxantrone drug eluting beads for the treatment of experimental peritoneal carcinomatosis in colorectal cancer*. *International Journal of Cancer*, 2009. **124**(11): p. 2701-2708.

155. Lahti, S.J., D. Zeng, J.B. Jia, M. Xing, and H.S. Kim, *Sorafenib loaded drug-eluting beads: loading and eluting kinetics and in vitro viability study*. Journal of Vascular and Interventional Radiology, 2015. **26**(2 (Suppl.)): p. S80-S81.
156. Forster, R.E., Y. Tang, C. Bowyer, A.W. Lloyd, W. Macfarlane, G.J. Phillips, and A.L. Lewis, *Development of a combination drug-eluting bead: towards enhanced efficacy for locoregional tumour therapies*. Anticancer Drugs, 2012. **23**(4): p. 355-69.
157. Biondi, M., S. Fusco, A.L. Lewis, and P.A. Netti, *New insights into the mechanisms of the interactions between doxorubicin and the ion-exchange hydrogel DC Bead for use in transarterial chemoembolization (TACE)*. J Biomater Sci Polym Ed, 2012. **23**(1-4): p. 333-54.
158. Fuchs, K., A. Kiss, P.E. Bize, R. Duran, A. Denys, G. Hopfgartner, G. Borchard, and O. Jordan, *Mapping of drug distribution in the rabbit liver tumor model by complementary fluorescence and mass spectrometry imaging*. J Control Release, 2017. **269**: p. 128-135.
159. Namur, J., M. Wassef, J.M. Millot, A.L. Lewis, M. Manfait, and A. Laurent, *Drug-eluting beads for liver embolization: concentration of doxorubicin in tissue and in beads in a pig model*. J Vasc Interv Radiol, 2010. **21**(2): p. 259-67.
160. Prajapati, H.J., M. Xing, J.R. Spivey, S.I. Hanish, B.F. El-Rayes, J.S. Kauh, Z. Chen, and H.S. Kim, *Survival, efficacy, and safety of small versus large doxorubicin drug-eluting beads TACE chemoembolization in patients with unresectable HCC*. AJR Am J Roentgenol, 2014. **203**(6): p. W706-14.
161. Tam, K.Y., K.C.-F. Leung, and Y.-X.J. Wang, *Chemoembolization agents for cancer treatment*. European Journal of Pharmaceutical Sciences, 2011. **44**(1-2): p. 1-10.
162. Poon, R.T., W.K. Tso, R.W. Pang, K.K. Ng, R. Woo, K.S. Tai, and S.T. Fan, *A phase I/II trial of chemoembolization for hepatocellular carcinoma using a novel intra-arterial drug-eluting bead*. Clin Gastroenterol Hepatol, 2007. **5**(9): p. 1100-8.
163. Lencioni, R., T. de Baere, M. Burrel, J.G. Caridi, J. Lammer, K. Malagari, R.C.G. Martin, E. O'Grady, M.I. Real, T.J. Vogl, A. Watkinson, and J.-F.H. Geschwind, *Transcatheter Treatment of Hepatocellular Carcinoma with Doxorubicin-loaded DC Bead (DEBDOX): Technical Recommendations*. Cardiovascular and Interventional Radiology, 2012. **35**(5): p. 980-985.
164. Lewis, A.L., M.R. Dreher, V. O'Byrne, D. Grey, M. Caine, A. Dunn, Y. Tang, B. Hall, K.D. Fowers, C.G. Johnson, K.V. Sharma, and B.J. Wood, *DC BeadM1™: towards an optimal transcatheter hepatic tumour therapy*. Journal of Materials Science. Materials in Medicine, 2016. **27**: p. 13.
165. Bonomo, G., V. Pedicini, L. Monfardini, P. Della Vigna, D. Poretti, G. Orgera, and F. Orsi, *Bland embolization in patients with unresectable hepatocellular carcinoma using precise, tightly size-calibrated, anti-inflammatory microparticles: first clinical experience and one-year follow-up*. Cardiovasc Intervent Radiol, 2010. **33**(3): p. 552-9.
166. Brown, K.T., *Fatal pulmonary complications after arterial embolization with 40-120-microm tris-acryl gelatin microspheres*. J Vasc Interv Radiol, 2004. **15**(2 Pt 1): p. 197-200.
167. Jordan, O., A. Denys, T. De Baere, N. Boulens, and E. Doelker, *Comparative Study of Chemoembolization Loadable Beads: In vitro Drug Release and Physical Properties of DC Bead and Hepasphere Loaded with Doxorubicin and Irinotecan*. Journal of Vascular and Interventional Radiology, 2010. **21**(7): p. 1084-1090.
168. Khurana, I., *Textbook of Medical Physiology* 2006: Elsevier.
169. Guiu, B., A. Schmitt, S. Reinhardt, A. Fohlen, T. Pohl, M. Wendremaire, A. Denys, J. Blummel, and M. Boulin, *Idarubicin-loaded ONCOZONE drug-eluting embolic agents for chemoembolization of hepatocellular carcinoma: in vitro loading and release and in vivo pharmacokinetics*. J Vasc Interv Radiol, 2015. **26**(2): p. 262-70.
170. Lewis, A.L., *DC Bead™: a major development in the toolbox for the interventional oncologist*. Expert Review of Medical Devices, 2009. **6**(4): p. 389-400.

171. Lewis, A.L. and M.R. Dreher, *Locoregional drug delivery using image-guided intra-arterial drug eluting bead therapy*. J Control Release, 2012.
172. Namur, J., *Microsphères d'embolisation pour la vectorisation de principes actifs: étude de la libération in vivo par microspectroscopies optiques*, 2009, Reims.
173. Malagari, K., E. Emmanouil, M. Pomoni, and D. Kelekis, *Chemoembolization with DC Bead™ for the treatment of hepatocellular carcinoma: an update*. Hepatic Oncology, 2014. **1**(2): p. 205-214.
174. Aliberti, C., R. Carandina, D. Sarti, E. Pizzirani, G. Ramondo, U. Cillo, S. Guadagni, and G. Fiorentini, *Transarterial chemoembolization with DC Bead LUMI radiopaque beads for primary liver cancer treatment: preliminary experience*. Future Oncol, 2017. **13**(25): p. 2243-2252.
175. Levy, E.B., V.P. Krishnasamy, A.L. Lewis, S. Willis, C. Macfarlane, V. Anderson, I.M. van der Bom, A. Radaelli, M.R. Dreher, K.V. Sharma, A. Negussie, A.S. Mikhail, J.F. Geschwind, and B.J. Wood, *First Human Experience with Directly Image-able Iodinated Embolization Microbeads*. Cardiovasc Intervent Radiol, 2016. **39**(8): p. 1177-86.
176. Ahnfelt, E., E. Sjögren, P. Hansson, and H. Lennernäs, *In Vitro Release Mechanisms of Doxorubicin From a Clinical Bead Drug-Delivery System*. Journal of Pharmaceutical Sciences, 2016. **105**(11): p. 3387-3398.
177. Rusu, M.C., I.C. Ichim, M. Popa, and M. Rusu, *New radiopaque acrylic bone cement. II. Acrylic bone cement with bromine-containing monomer*. J Mater Sci Mater Med, 2008. **19**(7): p. 2609-17.
178. Justaniah, A.I., S.I. Iqbal, M.M. Hakky, C.P. Molgaard, H. Ahari, B.D. Davison, and S. Flacke, *Influence of bead size on tumor response rate after drug-eluting bead transcatheter arterial chemoembolization in hepatocellular carcinoma*. Journal of Vascular and Interventional Radiology, 2014. **25**(3): p. S116-S117.
179. Spreafico, C., T. Cascella, A. Facciorusso, C. Sposito, L. Rodolfo, C. Morosi, E.M. Civelli, M. Vaiani, S. Bhoori, A. Pellegrinelli, A. Marchiano, and V. Mazzaferro, *Transarterial chemoembolization for hepatocellular carcinoma with a new generation of beads: clinical-radiological outcomes and safety profile*. Cardiovasc Intervent Radiol, 2015. **38**(1): p. 129-34.
180. Brown, K.T., R.K. Do, M. Gonen, A.M. Covey, G.I. Getrajdman, C.T. Sofocleous, W.R. Jarnagin, M.I. D'Angelica, P.J. Allen, J.P. Erinjeri, L.A. Brody, G.P. O'Neill, K.N. Johnson, A.R. Garcia, C. Beattie, B. Zhao, S.B. Solomon, L.H. Schwartz, R. DeMatteo, and G.K. Abou-Alfa, *Randomized Trial of Hepatic Artery Embolization for Hepatocellular Carcinoma Using Doxorubicin-Eluting Microspheres Compared With Embolization With Microspheres Alone*. Journal of Clinical Oncology, 2016.
181. Boulin, M. and B. Guiu, *Chemoembolization or Bland Embolization for Hepatocellular Carcinoma: The Question Is Still Unanswered*. Journal of Clinical Oncology, 2017. **35**(2): p. 256-257.
182. Boulin, M., S. Guiu, B. Chauffert, S. Aho, J.-P. Cercueil, F. Ghiringhelli, D. Krause, P. Fagnoni, P. Hillon, L. Bedenne, and B. Guiu, *Screening of anticancer drugs for chemoembolization of hepatocellular carcinoma*. Anti-Cancer Drugs, 2011. **22**(8): p. 741-748.
183. Lewis, A.L., *DC Bead™: a major development in the toolbox for the interventional oncologist*. Expert Rev Med Devices, 2009. **6**(4): p. 389-400.
184. Biondi, M., S. Fusco, A.L. Lewis, and P.A. Netti, *Investigation of the mechanisms governing doxorubicin and irinotecan release from drug-eluting beads: mathematical modeling and experimental verification*. Journal of Materials Science: Materials in Medicine, 2013. **24**(10): p. 2359-2370.
185. Lewis, A.L., M.V. Gonzalez, A.W. Lloyd, B. Hall, Y. Tang, S.L. Willis, S.W. Leppard, L.C. Wolfenden, R.R. Palmer, and P.W. Stratford, *DC bead: in vitro characterization of a drug-delivery device for transarterial chemoembolization*. J Vasc Interv Radiol, 2006. **17**(2 Pt 1): p. 335-42.

186. Gonzalez, M.V., Y. Tang, G.J. Phillips, A.W. Lloyd, B. Hall, P.W. Stratford, and A.L. Lewis, *Doxorubicin eluting beads-2: methods for evaluating drug elution and in-vitro:in-vivo correlation*. J Mater Sci Mater Med, 2008. **19**(2): p. 767-75.
187. Amyot, F.B., V.; Jurski, K.; Chaumeil, J.-C.; Counourd, J.-L.; Guiffant, G.; Dufaux, J., *A new experimental methods for the evaluation of the release profiles of drug-loaded microbeads designed for embolisation*. ITBM-RBM, 2002. **23**(5): p. 285-289.
188. Swaine, T., Y. Tang, P. Garcia, J. John, L.J. Waters, and A.L. Lewis, *Evaluation of ion exchange processes in drug-eluting embolization beads by use of an improved flow-through elution method*. European Journal of Pharmaceutical Sciences, 2016. **93**: p. 351-359.
189. Namur, J., S.J. Citron, M.T. Sellers, M.H. Dupuis, M. Wassef, M. Manfait, and A. Laurent, *Embolization of hepatocellular carcinoma with drug-eluting beads: doxorubicin tissue concentration and distribution in patient liver explants*. J Hepatol, 2011. **55**(6): p. 1332-8.
190. Caine, M., *Gel Phantom for Real-Time In Vitro Spatiotemporal Diffusion of Doxorubicin from Radiopaque and Non-Radiopaque Drug Eluting Beads Introduction*. Journal of Vascular and Interventional Radiology, 2017. **28**(6): p. e47-e48.
191. Zhang, Y., M. Huo, J. Zhou, A. Zou, W. Li, C. Yao, and S. Xie, *DDSolver: An Add-In Program for Modeling and Comparison of Drug Dissolution Profiles*. The AAPS Journal, 2010. **12**(3): p. 263-271.
192. FDA, *Guidance for Industry: Dissolution Testing of Immediate Release Solid Oral Dosage Forms*, 1997, FDA.
193. Denys, A., P. Czuczman, D. Grey, Z. Bascal, R. Whomsley, H. Kilpatrick, and A.L. Lewis, *Vandetanib-eluting Radiopaque Beads: In vivo Pharmacokinetics, Safety and Toxicity Evaluation following Swine Liver Embolization*. Theranostics, 2017. **7**(8): p. 2164-2176.
194. Qureshi, S.A., *In Vitro-In Vivo Correlation (IVIVC) and Determining Drug Concentrations in Blood from Dissolution Testing - A Simple and Practical Approach*. The Open Drug Delivery Journal, 2010. **4**: p. 38-47.
195. Dubbelboer, I.R., E. Lilienberg, M. Hedeland, U. Bondesson, M. Piquette-Miller, E. Sjögren, and H. Lennernäs, *The Effects of Lipiodol and Cyclosporin A on the Hepatobiliary Disposition of Doxorubicin in Pigs*. Molecular Pharmaceutics, 2014. **11**(4): p. 1301-1313.
196. Gustafson, D.L., J.C. Rastatter, T. Colombo, and M.E. Long, *Doxorubicin pharmacokinetics: Macromolecule binding, metabolism, and excretion in the context of a physiologic model*. J Pharm Sci, 2002. **91**(6): p. 1488-501.
197. Reich, S.D., F. Steinberg, N.R. Bachur, C.E. Riggs, Jr., R. Goebel, and M. Berman, *Mathematical model for adriamycin (doxorubicin) pharmacokinetics*. Cancer Chemother Pharmacol, 1979. **3**(2): p. 125-31.
198. FDA, *Guidance for Industry. Extended Release Oral Dosage Forms: Development, Evaluation, and Application of In Vitro/In Vivo Correlations*, 1997.
199. Padia, S.A., G. Shivaram, S. Bastawrous, P. Bhargava, N.J. Vo, S. Vaidya, K. Valji, W.P. Harris, D.S. Hippe, and M.J. Kogut, *Safety and efficacy of drug-eluting bead chemoembolization for hepatocellular carcinoma: comparison of small-versus medium-size particles*. J Vasc Interv Radiol, 2013. **24**(3): p. 301-6.
200. Chao, M., H. Wu, K. Jin, B. Li, J. Wu, G. Zhang, G. Yang, and X. Hu, *A nonrandomized cohort and a randomized study of local control of large hepatocarcinoma by targeting intratumoral lactic acidosis*. eLife, 2016. **5**: p. e15691.
201. Hecq, J.-D., A.L. Lewis, D. Vanbeckbergen, A. Athanosopoulos, L. Galanti, J. Jamart, P. Czuczman, and T. Chung, *Doxorubicin-loaded drug-eluting beads (DC Bead®) for use in transarterial chemoembolization: A stability assessment*. Journal of Oncology Pharmacy Practice, 2013. **19**(1): p. 65-74.

202. Drugbank. *Doxorubicin*. 2017 09/01/2018]; Available from: <https://www.drugbank.ca/drugs/DB00997>.
203. Andhariya, J.V., J. Shen, S. Choi, Y. Wang, Y. Zou, and D.J. Burgess, *Development of in vitro-in vivo correlation of parenteral naltrexone loaded polymeric microspheres*. J Control Release, 2017. **255**: p. 27-35.
204. Cardot, J.M. and B.M. Davit, *In vitro-In Vivo Correlations: Tricks and Traps*. The AAPS Journal, 2012. **14**(3): p. 491-499.
205. Mitsuhashi, N., H. Shimizu, M. Ohtsuka, Y. Wakabayashi, H. Ito, F. Kimura, H. Yoshidome, A. Kato, Y. Nukui, and M. Miyazaki, *Angiopoietins and Tie-2 expression in angiogenesis and proliferation of human hepatocellular carcinoma*. Hepatology, 2003. **37**(5): p. 1105-13.
206. Wang, H., Y. Yin, W. Li, X. Zhao, Y. Yu, J. Zhu, Z. Qin, Q. Wang, K. Wang, W. Lu, J. Liu, and L. Huang, *Over-Expression of PDGFR- β Promotes PDGF-Induced Proliferation, Migration, and Angiogenesis of EPCs through PI3K/Akt Signaling Pathway*. PLoS ONE, 2012. **7**(2): p. e30503.
207. Bradley, D.P., J.L. Tessier, D. Checkley, H. Kuribayashi, J.C. Waterton, J. Kendrew, and S.R. Wedge, *Effects of AZD2171 and vandetanib (ZD6474, Zactima) on haemodynamic variables in an SW620 human colon tumour model: an investigation using dynamic contrast-enhanced MRI and the rapid clearance blood pool contrast agent, P792 (gadomelitol)*. NMR in Biomedicine, 2008. **21**(1): p. 42-52.
208. Tai, J.H., J. Tessier, A.J. Ryan, L. Hoffman, X. Chen, and T.-Y. Lee, *Assessment of Acute Antivasular Effects of Vandetanib with High-Resolution Dynamic Contrast-Enhanced Computed Tomographic Imaging in a Human Colon Tumor Xenograft Model in the Nude Rat*. Neoplasia, 2010. **12**(9): p. 697-707.
209. Liu, S., J. Gong, A. Morishita, T. Nomura, H. Miyoshi, J. Tani, K. Kato, H. Yoneyama, A. Deguchi, H. Mori, S. Mimura, K. Nomura, T. Himoto, K. Deguchi, K. Okano, K. Izuishi, Y. Suzuki, Y. Kushida, R. Haba, H. Iwama, and T. Masaki, *Use of protein array technology to investigate receptor tyrosine kinases activated in hepatocellular carcinoma*. Experimental and Therapeutic Medicine, 2011. **2**(3): p. 399-403.
210. Overmoyer, B.A., C.E. McLaren, and G.M. Brittenham, *Uniformity of liver density and nonheme (storage) iron distribution*. Arch Pathol Lab Med, 1987. **111**(6): p. 549-54.
211. Bárdos, J.I. and M. Ashcroft, *Negative and positive regulation of HIF-1: A complex network*. Biochimica et Biophysica Acta (BBA) - Reviews on Cancer, 2005. **1755**(2): p. 107-120.
212. Hers, I., E.E. Vincent, and J.M. Tavaré, *Akt signalling in health and disease*. Cell Signal, 2011. **23**(10): p. 1515-27.
213. Laplante, M. and David M. Sabatini, *mTOR Signaling in Growth Control and Disease*. Cell, 2012. **149**(2): p. 274-293.
214. Matter, M.S., T. Decaens, J.B. Andersen, and S.S. Thorgeirsson, *Targeting the mTOR pathway in hepatocellular carcinoma: Current state and future trends*. Journal of Hepatology, 2014. **60**(4): p. 855-865.
215. Zhou, Q., V. Lui, and W. Yeo, *Targeting the PI3K/Akt/mTOR pathway in hepatocellular carcinoma*. Future Oncology, 2011. **7**(10): p. 1149-1167.
216. Tian, T., K.J. Nan, S.H. Wang, X. Liang, C.X. Lu, H. Guo, W.J. Wang, and Z.P. Ruan, *PTEN regulates angiogenesis and VEGF expression through phosphatase-dependent and -independent mechanisms in HepG2 cells*. Carcinogenesis, 2010. **31**(7): p. 1211-9.
217. Augello, G., R. Puleio, M.R. Emma, A. Cusimano, G.R. Loria, J.A. McCubrey, G. Montalto, and M. Cervello, *A PTEN inhibitor displays preclinical activity against hepatocarcinoma cells*. Cell Cycle, 2016. **15**(4): p. 573-583.
218. Chen, K.-F., H.-L. Chen, W.-T. Tai, W.-C. Feng, C.-H. Hsu, P.-J. Chen, and A.-L. Cheng, *Activation of Phosphatidylinositol 3-Kinase/Akt Signaling Pathway Mediates Acquired Resistance to Sorafenib in Hepatocellular Carcinoma Cells*. Journal of Pharmacology and Experimental Therapeutics, 2011. **337**(1): p. 155-161.

219. Alvarez-Tejado, M., S. Naranjo-Suárez, C. Jiménez, A.C. Carrera, M.O. Landázuri, and L. del Peso, *Hypoxia Induces the Activation of the Phosphatidylinositol 3-Kinase/Akt Cell Survival Pathway in PC12 Cells: PROTECTIVE ROLE IN APOPTOSIS*. Journal of Biological Chemistry, 2001. **276**(25): p. 22368-22374.
220. Brugarolas, J., K. Lei, R.L. Hurley, B.D. Manning, J.H. Reiling, E. Hafen, L.A. Witters, L.W. Ellisen, and W.G. Kaelin, *Regulation of mTOR function in response to hypoxia by REDD1 and the TSC1/TSC2 tumor suppressor complex*. Genes & Development, 2004. **18**(23): p. 2893-2904.
221. Dhillon, A.S., S. Hagan, O. Rath, and W. Kolch, *MAP kinase signalling pathways in cancer*. Oncogene, 2007. **26**(22): p. 3279-90.
222. Delire, B. and P. Stärkel, *The Ras/MAPK pathway and hepatocarcinoma: pathogenesis and therapeutic implications*. Eur J Clin Invest, 2015. **45**(6): p. 609-623.
223. Sang, N., D.P. Stiehl, J. Bohensky, I. Leshchinsky, V. Srinivas, and J. Caro, *MAPK Signaling Up-regulates the Activity of Hypoxia-inducible Factors by Its Effects on p300*. Journal of Biological Chemistry, 2003. **278**(16): p. 14013-14019.
224. Liu, Q., Z. Xu, S. Mao, W. Chen, R. Zeng, S. Zhou, and J. Liu, *Effect of hypoxia on hypoxia inducible factor-1 α , insulin-like growth factor I and vascular endothelial growth factor expression in hepatocellular carcinoma HepG2 cells*. Oncology Letters, 2015. **9**(3): p. 1142-1148.
225. Schito, L., S. Rey, M. Tafani, H. Zhang, C.C.-L. Wong, A. Russo, M.A. Russo, and G.L. Semenza, *Hypoxia-inducible factor 1-dependent expression of platelet-derived growth factor B promotes lymphatic metastasis of hypoxic breast cancer cells*. Proceedings of the National Academy of Sciences, 2012. **109**(40): p. E2707-E2716.
226. Loesch, M. and G. Chen, *The p38 MAPK stress pathway as a tumor suppressor or more?* Frontiers in bioscience : a journal and virtual library, 2008. **13**: p. 3581-3593.
227. Koul, H.K., M. Pal, and S. Koul, *Role of p38 MAP Kinase Signal Transduction in Solid Tumors*. Genes & Cancer, 2013. **4**(9-10): p. 342-359.
228. Wang, S.N., K.T. Lee, C.J. Tsai, Y.J. Chen, and Y.T. Yeh, *Phosphorylated p38 and JNK MAPK proteins in hepatocellular carcinoma*. Eur J Clin Invest, 2012. **42**(12): p. 1295-301.
229. Berridge, M.V., P.M. Herst, and A.S. Tan, *Tetrazolium dyes as tools in cell biology: new insights into their cellular reduction*. Biotechnol Annu Rev, 2005. **11**: p. 127-52.
230. Gade, T.P., E. Tucker, S. Hunt, M. Nakazawa, B. Krock, W. Wong, G. Nadolski, T. Clark, E. Furth, M. Schnall, M.C. Soulen, and C. Simon, *Targeting the metabolic stress response in hepatocellular carcinoma to potentiate TACE-induced ischemia*. Journal of Vascular and Interventional Radiology, 2015. **26**(2): p. S17.
231. Khan, M.A., M. Singh, M.S. Khan, A.K. Najmi, and S. Ahmad, *Caspase mediated synergistic effect of Boswellia serrata extract in combination with doxorubicin against human hepatocellular carcinoma*. Biomed Res Int, 2014. **2014**: p. 294143.
232. Hu, Q.-D., W. Chen, T.-L. Yan, T. Ma, C.-L. Chen, C. Liang, Q. Zhang, X.-F. Xia, H. Liu, X. Zhi, X.-X. Zheng, X.-L. Bai, X.-Z. Yu, and T.-B. Liang, *NSC 74859 enhances doxorubicin cytotoxicity via inhibition of epithelial-mesenchymal transition in hepatocellular carcinoma cells*. Cancer Letters, 2012. **325**(2): p. 207-213.
233. Calabrese, E.J., *Cancer Biology and Hormesis: Human Tumor Cell Lines Commonly Display Hormetic (Biphasic) Dose Responses*. Critical Reviews in Toxicology, 2005. **35**(6): p. 463-582.
234. Reynolds, A.R., *Potential Relevance of Bell-Shaped and U-Shaped Dose-Responses for the Therapeutic Targeting of Angiogenesis in Cancer*. Dose-Response, 2010. **8**(3): p. dose-response.09-049.Reynolds.
235. Yang, Y., Y. Zhang, H. Iwamoto, K. Hosaka, T. Seki, P. Andersson, S. Lim, C. Fischer, M. Nakamura, M. Abe, R. Cao, P.V. Skov, F. Chen, X. Chen, Y. Lu, G. Nie, and Y. Cao,

- Discontinuation of anti-VEGF cancer therapy promotes metastasis through a liver revascularization mechanism.* Nature Communications, 2016. **7**: p. 12680.
236. Qiu, G.-H., X. Xie, F. Xu, X. Shi, Y. Wang, and L. Deng, *Distinctive pharmacological differences between liver cancer cell lines HepG2 and Hep3B.* Cytotechnology, 2015. **67**(1): p. 1-12.
 237. Barretina, J., G. Caponigro, N. Stransky, K. Venkatesan, A.A. Margolin, S. Kim, C.J. Wilson, J. Lehár, G.V. Kryukov, D. Sonkin, A. Reddy, M. Liu, L. Murray, M.F. Berger, J.E. Monahan, P. Morais, J. Meltzer, A. Korejwa, J. Jané-Valbuena, F.A. Mapa, J. Thibault, E. Bric-Furlong, P. Raman, A. Shipway, I.H. Engels, J. Cheng, G.K. Yu, J. Yu, P. Aspesi, M. de Silva, K. Jagtap, M.D. Jones, L. Wang, C. Hatton, E. Palesscandolo, S. Gupta, S. Mahan, C. Sougnez, R.C. Onofrio, T. Liefeld, L. MacConaill, W. Winckler, M. Reich, N. Li, J.P. Mesirov, S.B. Gabriel, G. Getz, K. Ardlie, V. Chan, V.E. Myer, B.L. Weber, J. Porter, M. Warmuth, P. Finan, J.L. Harris, M. Meyerson, T.R. Golub, M.P. Morrissey, W.R. Sellers, R. Schlegel, and L.A. Garraway, *The Cancer Cell Line Encyclopedia enables predictive modeling of anticancer drug sensitivity.* Nature, 2012. **483**(7391): p. 603-607.
 238. Ozaki, T. and A. Nakagawara, *Role of p53 in Cell Death and Human Cancers.* Cancers, 2011. **3**(1): p. 994-1013.
 239. Namiki, A., E. Brogi, M. Kearney, E.A. Kim, T. Wu, T. Couffinhal, L. Varticovski, and J.M. Isner, *Hypoxia Induces Vascular Endothelial Growth Factor in Cultured Human Endothelial Cells.* Journal of Biological Chemistry, 1995. **270**(52): p. 31189-31195.
 240. Forsythe, J.A., B.H. Jiang, N.V. Iyer, F. Agani, S.W. Leung, R.D. Koos, and G.L. Semenza, *Activation of vascular endothelial growth factor gene transcription by hypoxia-inducible factor 1.* Mol Cell Biol, 1996. **16**(9): p. 4604-13.
 241. Wang, W.-M., Z.-L. Zhao, S.-R. Ma, G.-T. Yu, B. Liu, L. Zhang, W.-F. Zhang, A.B. Kulkarni, Z.-J. Sun, and Y.-F. Zhao, *Epidermal Growth Factor Receptor Inhibition Reduces Angiogenesis via Hypoxia-Inducible Factor-1 α and Notch1 in Head Neck Squamous Cell Carcinoma.* PLoS ONE, 2015. **10**(2): p. e0119723.
 242. Peng, X.H., P. Karna, Z. Cao, B.H. Jiang, M. Zhou, and L. Yang, *Cross-talk between epidermal growth factor receptor and hypoxia-inducible factor-1 α signal pathways increases resistance to apoptosis by up-regulating survivin gene expression.* J Biol Chem, 2006. **281**(36): p. 25903-14.
 243. Lee, S.H., K.H. Koo, J.W. Park, H.J. Kim, S.K. Ye, J.B. Park, B.K. Park, and Y.N. Kim, *HIF-1 is induced via EGFR activation and mediates resistance to anoikis-like cell death under lipid rafts/caveolae-disrupting stress.* Carcinogenesis, 2009. **30**(12): p. 1997-2004.
 244. Déry, M.-A.C., M.D. Michaud, and D.E. Richard, *Hypoxia-inducible factor 1: regulation by hypoxic and non-hypoxic activators.* The International Journal of Biochemistry & Cell Biology, 2005. **37**(3): p. 535-540.
 245. Ruggero, D. and N. Sonenberg, *The Akt of translational control.* Oncogene, 2005. **24**(50): p. 7426-34.
 246. El Guerrab, A., R. Zegrour, C.-C. Nemlin, F. Vigier, A. Cayre, F. Penault-Llorca, F. Rossignol, and Y.-J. Bignon, *Differential Impact of EGFR-Targeted Therapies on Hypoxia Responses: Implications for Treatment Sensitivity in Triple-Negative Metastatic Breast Cancer.* PLoS ONE, 2011. **6**(9): p. e25080.
 247. Cao, Y., J.M. Eble, E. Moon, H. Yuan, D.H. Weitzel, C.D. Landon, C.Y.-C. Nien, G. Hanna, J.N. Rich, J.M. Provenzale, and M.W. Dewhirst, *Tumor Cells Upregulate Normoxic HIF-1 α in Response to Doxorubicin.* Cancer research, 2013. **73**(20): p. 6230-6242.
 248. Navarro, R., R. Martinez, I. Busnadiego, M.B. Ruiz-Larrea, and J.I. Ruiz-Sanz, *Doxorubicin-induced MAPK activation in hepatocyte cultures is independent of oxidant damage.* Ann N Y Acad Sci, 2006. **1090**: p. 408-18.
 249. Liu, F., P. Wang, X. Jiang, G. Tan, H. Qiao, H. Jiang, G.W. Krissansen, and X. Sun, *Antisense hypoxia-inducible factor 1 α gene therapy enhances the therapeutic efficacy*

- of doxorubicin to combat hepatocellular carcinoma. Cancer Science, 2008. 99(10): p. 2055-2061.*
250. Zhang, H., C.C.L. Wong, H. Wei, D.M. Gilkes, P. Korangath, P. Chaturvedi, L. Schito, J. Chen, B. Krishnamachary, P.T. Winnard, V. Raman, L. Zhen, W.A. Mitzner, S. Sukumar, and G.L. Semenza, *HIF-1-dependent Expression of Angiopoietin-like 4 and L1CAM Mediates Vascular Metastasis of Hypoxic Breast Cancer Cells to the Lungs. Oncogene, 2012. 31(14): p. 1757-1770.*
 251. Lee, K., D.Z. Qian, S. Rey, H. Wei, J.O. Liu, and G.L. Semenza, *Anthracycline chemotherapy inhibits HIF-1 transcriptional activity and tumor-induced mobilization of circulating angiogenic cells. Proceedings of the National Academy of Sciences of the United States of America, 2009. 106(7): p. 2353-2358.*
 252. Duyndam, M.C.A., M.P.A. van Berkel, J.C. Dorsman, D.A.P. Rockx, H.M. Pinedo, and E. Boven, *Cisplatin and doxorubicin repress Vascular Endothelial Growth Factor expression and differentially down-regulate Hypoxia-inducible Factor 1 activity in human ovarian cancer cells. Biochemical Pharmacology, 2007. 74(2): p. 191-201.*
 253. Siegfried, J.M., C.T. Gubish, M.E. Rothstein, C. Henry, and L.P. Stabile, *Combining the Multitargeted Tyrosine Kinase Inhibitor Vandetanib with the Antiestrogen Fulvestrant Enhances Its Antitumor Effect in Non-small Cell Lung Cancer. Journal of Thoracic Oncology, 2012. 7(3): p. 485-495.*
 254. Jane, E.P., D.R. Premkumar, S.O. Addo-Yobo, and I.F. Pollack, *Abrogation of Mitogen-Activated Protein Kinase and Akt Signaling by Vandetanib Synergistically Potentiates Histone Deacetylase Inhibitor-Induced Apoptosis in Human Glioma Cells. J Pharmacol Exp Ther, 2009. 331(1): p. 327-337.*
 255. Yoshikawa, D., H. Ojima, A. Kokubu, T. Ochiya, S. Kasai, S. Hirohashi, and T. Shibata, *Vandetanib (ZD6474), an inhibitor of VEGFR and EGFR signalling, as a novel molecular-targeted therapy against cholangiocarcinoma. British journal of cancer, 2009. 100(8): p. 1257-1266.*
 256. Zhou, Y., Y. Zhang, H. Zou, N. Cai, X. Chen, L. Xu, X. Kong, and P. Liu, *The multi-targeted tyrosine kinase inhibitor vandetanib plays a bifunctional role in non-small cell lung cancer cells. Scientific Reports, 2015. 5: p. 8629.*
 257. Fujishiro, Y., M. Tonogi, H. Ochiai, K. Matsuzaka, G.Y. Yamane, and T. Azuma, *The receptor tyrosine kinase inhibitor vandetanib activates Akt and increases side population in a salivary gland tumor cell line (A253). Int J Oncol, 2012. 41(1): p. 362-8.*
 258. Hirsch, F.R., M. Varella-Garcia, and F. Cappuzzo, *Predictive value of EGFR and HER2 overexpression in advanced non-small-cell lung cancer. Oncogene, 2009. 28: p. S32.*
 259. Pupo, E., N. Ducano, B. Lupo, E. Vigna, D. Avanzato, T. Perera, L. Trusolino, L. Lanzetti, and P.M. Comoglio, *Rebound Effects Caused by Withdrawal of MET Kinase Inhibitor Are Quenched by a MET Therapeutic Antibody. Cancer research, 2016. 76(17): p. 5019-5029.*
 260. Adachi, Y., K. Watanabe, K. Kita, H. Kitai, H. Kotani, Y. Sato, N. Inase, S. Yano, and H. Ebi, *Resistance mediated by alternative receptor tyrosine kinases in FGFR1-amplified lung cancer. Carcinogenesis, 2017. 38(11): p. 1063-1072.*
 261. Ma, P., Y. Fu, M. Chen, Y. Jing, J. Wu, K. Li, Y. Shen, J.-X. Gao, M. Wang, X. Zhao, and G. Zhuang, *Adaptive and Acquired Resistance to EGFR Inhibitors Converge on the MAPK Pathway. Theranostics, 2016. 6(8): p. 1232-1243.*
 262. Krock, B.L., N. Skuli, and M.C. Simon, *Hypoxia-Induced Angiogenesis: Good and Evil. Genes & Cancer, 2011. 2(12): p. 1117-1133.*
 263. Feldser, D., F. Agani, N.V. Iyer, B. Pak, G. Ferreira, and G.L. Semenza, *Reciprocal positive regulation of hypoxia-inducible factor 1alpha and insulin-like growth factor 2. Cancer Res, 1999. 59(16): p. 3915-8.*
 264. Siegel, R.L., K.D. Miller, and A. Jemal, *Cancer statistics, 2018. CA Cancer J Clin, 2018. 68(1): p. 7-30.*

265. Takayasu, K., S. Arii, I. Ikai, M. Omata, K. Okita, T. Ichida, Y. Matsuyama, Y. Nakanuma, M. Kojiro, M. Makuuchi, and Y. Yamaoka, *Prospective Cohort Study of Transarterial Chemoembolization for Unresectable Hepatocellular Carcinoma in 8510 Patients*. *Gastroenterology*, 2006. **131**(2): p. 461-469.
266. Llovet, J.M., S. Ricci, V. Mazzaferro, P. Hilgard, E. Gane, J.F. Blanc, A.C. de Oliveira, A. Santoro, J.L. Raoul, A. Forner, M. Schwartz, C. Porta, S. Zeuzem, L. Bolondi, T.F. Greten, P.R. Galle, J.F. Seitz, I. Borbath, D. Haussinger, T. Giannaris, M. Shan, M. Moscovici, D. Voliotis, and J. Bruix, *Sorafenib in advanced hepatocellular carcinoma*. *N Engl J Med*, 2008. **359**(4): p. 378-90.
267. Li, Y., Z.-H. Gao, and X.-J. Qu, *The Adverse Effects of Sorafenib in Patients with Advanced Cancers*. *Basic & Clinical Pharmacology & Toxicology*, 2015. **116**(3): p. 216-221.
268. Bruix, J., S. Qin, P. Merle, A. Granito, Y.-H. Huang, G. Bodoky, M. Pracht, O. Yokosuka, O. Rosmorduc, V. Breder, R. Gerolami, G. Masi, P.J. Ross, T. Song, J.-P. Bronowicki, I. Ollivier-Hourmand, M. Kudo, A.-L. Cheng, J.M. Llovet, R.S. Finn, M.-A. LeBerre, A. Baumhauer, G. Meinhardt, and G. Han, *Regorafenib for patients with hepatocellular carcinoma who progressed on sorafenib treatment (RESORCE): a randomised, double-blind, placebo-controlled, phase 3 trial*. *The Lancet*, 2016. **389**(10064): p. 56-66.
269. Kidd, J.G. and P. Rous, *A TRANSPLANTABLE RABBIT CARCINOMA ORIGINATING IN A VIRUS-INDUCED PAPILLOMA AND CONTAINING THE VIRUS IN MASKED OR ALTERED FORM*. *J Exp Med*, 1940. **71**(6): p. 813-38.
270. Parvinian, A., L.C. Casadaban, and R.C. Gaba, *Development, growth, propagation, and angiographic utilization of the rabbit VX2 model of liver cancer: a pictorial primer and "how to" guide*. *Diagnostic and Interventional Radiology*, 2014. **20**(4): p. 335-340.
271. Luo, W., X. Zhou, X. Zheng, G. He, M. Yu, Q. Li, and Q. Liu, *Role of sonography for implantation and sequential evaluation of a VX2 rabbit liver tumor model*. *J Ultrasound Med*, 2010. **29**(1): p. 51-60.
272. Heindryckx, F., I. Colle, and H. Van Vlierberghe, *Experimental mouse models for hepatocellular carcinoma research*. *Int J Exp Pathol*, 2009. **90**(4): p. 367-386.
273. Vinchon-Petit, S., D. Jarnet, S. Michalak, A. Lewis, J.P. Benoit, and P. Menei, *Local implantation of doxorubicin drug eluting beads in rat glioma*. *International Journal of Pharmaceutics*, 2010. **402**(1): p. 184-189.
274. Amann, T., F. Bataille, T. Spruss, M. Mühlbauer, E. Gäbele, J. Schölmerich, P. Kiefer, A.-K. Bosserhoff, and C. Hellerbrand, *Activated hepatic stellate cells promote tumorigenicity of hepatocellular carcinoma*. *Cancer Science*, 2009. **100**(4): p. 646-653.
275. Forster, R.E.J., S.A. Small, Y. Tang, C.L. Heaysman, A.W. Lloyd, W. Macfarlane, G.J. Phillips, M.D. Antonijevic, and A.L. Lewis, *Comparison of DC Bead-irinotecan and DC Bead-topotecan drug eluting beads for use in locoregional drug delivery to treat pancreatic cancer*. *Journal of Materials Science: Materials in Medicine*, 2010. **21**(9): p. 2683-2690.
276. Ho, K.S., P.C. Poon, S.C. Owen, and M.S. Shoichet, *Blood vessel hyperpermeability and pathophysiology in human tumour xenograft models of breast cancer: a comparison of ectopic and orthotopic tumours*. *BMC cancer*, 2012. **12**: p. 579-579.
277. Cespedes, M.V., I. Casanova, M. Parreno, and R. Mangués, *Mouse models in oncogenesis and cancer therapy*. *Clin Transl Oncol*, 2006. **8**(5): p. 318-29.
278. Matsuo, M., H. Sakurai, and I. Saiki, *ZD1839, a Selective Epidermal Growth Factor Receptor Tyrosine Kinase Inhibitor, Shows Antimetastatic Activity Using a Hepatocellular Carcinoma Model*. *Molecular Cancer Therapeutics*, 2003. **2**(6): p. 557-561.

279. Huynh, H., K.C. Soo, P.K. Chow, L. Panasci, and E. Tran, *Xenografts of human hepatocellular carcinoma: a useful model for testing drugs*. Clin Cancer Res, 2006. **12**(14 Pt 1): p. 4306-14.
280. Wagner, C., R. Sauermann, and C. Joukhadar, *Principles of antibiotic penetration into abscess fluid*. Pharmacology, 2006. **78**(1): p. 1-10.
281. Levy, E.B., V.P. Krishnasamy, A.L. Lewis, S. Willis, C. Macfarlane, V. Anderson, I.M. van der Bom, A. Radaelli, M.R. Dreher, K.V. Sharma, A. Negussie, A.S. Mikhail, J.-F.H. Geschwind, and B.J. Wood, *First Human Experience with Directly Image-able Iodinated Embolization Microbeads*. Cardiovascular and Interventional Radiology, 2016. **39**(8): p. 1177-1186.
282. Murillas, R., F. Larcher, C.J. Conti, M. Santos, A. Ullrich, and J.L. Jorcano, *Expression of a dominant negative mutant of epidermal growth factor receptor in the epidermis of transgenic mice elicits striking alterations in hair follicle development and skin structure*. EMBO J, 1995. **14**(21): p. 5216-23.
283. Lacouture, M.E., *Mechanisms of cutaneous toxicities to EGFR inhibitors*. Nat Rev Cancer, 2006. **6**(10): p. 803-12.
284. Reindel, J.F., A.W. Gough, G.D. Pilcher, W.F. Bobrowski, G.P. Sobocinski, and F.A.D.L. Iglesia, *Systemic Proliferative Changes and Clinical Signs in Cynomolgus Monkeys Administered a Recombinant Derivative of Human Epidermal Growth Factor*. Toxicologic Pathology, 2001. **29**(2): p. 159-173.
285. Busam, K.J., P. Capodici, R. Motzer, T. Kiehn, D. Phelan, and A.C. Halpern, *Cutaneous side-effects in cancer patients treated with the anti-epidermal growth factor receptor antibody C225*. British Journal of Dermatology, 2001. **144**(6): p. 1169-1176.
286. Hidalgo, M., L.L. Siu, J. Nemunaitis, J. Rizzo, L.A. Hammond, C. Takimoto, S.G. Eckhardt, A. Tolcher, C.D. Britten, L. Denis, K. Ferrante, D.D.V. Hoff, S. Silberman, and E.K. Rowinsky, *Phase I and Pharmacologic Study of OSI-774, an Epidermal Growth Factor Receptor Tyrosine Kinase Inhibitor, in Patients With Advanced Solid Malignancies*. Journal of Clinical Oncology, 2001. **19**(13): p. 3267-3279.
287. Bachet, J.B., L. Peuvrel, C. Bachmeyer, Z. Reguiai, P.A. Gourraud, O. Bouche, M. Ychou, R.J. Bensadoun, B. Dreno, and T. Andre, *Folliculitis induced by EGFR inhibitors, preventive and curative efficacy of tetracyclines in the management and incidence rates according to the type of EGFR inhibitor administered: a systematic literature review*. Oncologist, 2012. **17**(4): p. 555-68.
288. Ehmann, L.M., T. Ruzicka, and A. Wollenberg, *Cutaneous side-effects of EGFR inhibitors and their management*. Skin Therapy Lett, 2011. **16**(1): p. 1-3.
289. Kopf-Maier, P., V.F. Mboneko, and H.J. Merker, *Nude mice are not hairless. A morphological study*. Acta Anat (Basel), 1990. **139**(2): p. 178-90.
290. Son, Y.-M., J.-Y. Roh, E.-K. Cho, and J.-R. Lee, *Photosensitivity Reactions to Vandetanib: Redevelopment after Sequential Treatment with Docetaxel*. Ann Dermatol, 2011. **23**(Suppl 3): p. S314-S318.
291. Rhee, T.K., J.Y. Young, A.C. Larson, G.K. Haines Iii, K.T. Sato, R. Salem, M.F. Mulcahy, L.M. Kulik, T. Paunesku, G.E. Woloschak, and R.A. Omary, *Effect of Transcatheter Arterial Embolization on Levels of Hypoxia-inducible Factor-1 α in Rabbit VX2 Liver Tumors*. Journal of Vascular and Interventional Radiology, 2007. **18**(5): p. 639-645.
292. Virmani, S., T.K. Rhee, R.K. Ryu, K.T. Sato, R.J. Lewandowski, M.F. Mulcahy, L.M. Kulik, B. Szolc-Kowalska, G.E. Woloschak, G.Y. Yang, R. Salem, A.C. Larson, and R.A. Omary, *Comparison of hypoxia-inducible factor-1 α expression before and after transcatheter arterial embolization in rabbit VX2 liver tumors*. J Vasc Interv Radiol, 2008. **19**(10): p. 1483-9.
293. Dai, F., X. Zhang, W. Shen, J. Chen, L. Liu, and G. Gao, *Liposomal curcumin inhibits hypoxia-induced angiogenesis after transcatheter arterial embolization in VX2 rabbit liver tumors*. Onco Targets Ther, 2015. **8**: p. 2601-11.

294. Gomes, A.S., P.A. Monteleone, J.W. Sayre, R.S. Finn, S. Sadeghi, M.J. Tong, C.D. Britten, and R.W. Busuttill, *Comparison of Triple-Drug Transcatheter Arterial Chemoembolization (TACE) With Single-Drug TACE Using Doxorubicin-Eluting Beads: Long-Term Survival in 313 Patients*. *AJR Am J Roentgenol*, 2017. **209**(4): p. 722-732.
295. Rimassa, L. and A. Santoro, *Sorafenib therapy in advanced hepatocellular carcinoma: the SHARP trial*. *Expert Rev Anticancer Ther*, 2009. **9**(6): p. 739-45.
296. Hagan, A., G.J. Phillips, W.M. Macfarlane, A.W. Lloyd, P. Czuczman, and A.L. Lewis, *Preparation and characterisation of vandetanib-eluting radiopaque beads for locoregional treatment of hepatic malignancies*. *European Journal of Pharmaceutical Sciences*, 2017. **101**: p. 22-30.
297. Mikhail, A., E. Levy, V. Krishnasamy, A. Negussie, W. Pritchard, D. Woods, J. Thompson, D. Amchin, I. Bakhutashvili, J. Esparza-Trujillo, F. Banovac, J. Karanian, Y. Tang, C. Macfarlane, S. Willis, A. Lewis, and B. Wood, *Drug dose mapping using radiopaque, drug-eluting embolic beads following DEBTACE in rabbit VX2 using MDCT and micro CT*. *Journal of Vascular and Interventional Radiology*. **28**(2): p. S158.
298. Kong, K., C. Kendall, N. Stone, and I. Notingher, *Raman spectroscopy for medical diagnostics — From in-vitro biofluid assays to in-vivo cancer detection*. *Advanced Drug Delivery Reviews*, 2015. **89**: p. 121-134.
299. Kolesky, D.B., K.A. Homan, M.A. Skylar-Scott, and J.A. Lewis, *Three-dimensional bioprinting of thick vascularized tissues*. *Proceedings of the National Academy of Sciences*, 2016. **113**(12): p. 3179-3184.
300. ClinicalTrials.gov. *Vandetanib-eluting Radiopaque Embolic Beads in Patients With Resectable Liver Malignancies (VEROnA)*. 2017 [cited 2018 19/01/2018]; Available from: <https://clinicaltrials.gov/ct2/show/NCT03291379>.
301. Zielinski, H.S., T.; Szmigielski, S, *Renal Artery Embolization in Treatment of Renal Cancer with Emphasis on Response of Immune System*, in *Renal Tumour*, P.J. Chen, Editor 2013, InTech.
302. Tannir, N., H. Hammers, and A. Amin, *First-line vascular endothelial growth factor-targeted therapy in renal cell carcinoma: priming the tumor microenvironment for immunotherapy*. *Current Medical Research and Opinion*, 2018: p. 1-15.
303. Seliger, B., C. Massa, B. Rini, J. Ko, and J. Finke, *Antitumour and immune-adjuvant activities of protein-tyrosine kinase inhibitors*. *Trends in Molecular Medicine*, 2010. **16**(4): p. 184-192.
304. Sun, X., Q. Sui, C. Zhang, Z. Tian, and J. Zhang, *Targeting Blockage of STAT3 in Hepatocellular Carcinoma Cells Augments NK Cell Functions via Reverse Hepatocellular Carcinoma-Induced Immune Suppression*. *Molecular Cancer Therapeutics*, 2013. **12**(12): p. 2885.
305. Yang, J., J. Yan, and B. Liu, *Targeting VEGF/VEGFR to Modulate Antitumor Immunity*. *Frontiers in Immunology*, 2018. **9**(978).

APPENDICES

Micro-CT protocol (RSSL)

The samples were opened and a small amount of MilliQ purified water was carefully decanted into each sample tube. Each sample was then analysed by X-Ray Micro-Computer Tomography (μ -CT) using a single scan, to include the water reference and the beads. The samples were then reconstructed using NRecon and calibrated against a volume of interest (VOI) of the purified water reference. A region of interest (ROI) of air and water was analysed after calibration to verify the Hounsfield calibration. The samples were reconstructed (NRecon) and analysed (CT Analyser) using the same instrument and acquisition parameters (Table A1).

Table A1 Micro-CT instrument and acquisition parameters as supplied by RSSL.

Instrument	SkyScan 1172
Software	SkyScan1172 Version 1.5 (build 14)
NRecon version	1.6.9.6
CT Analyser version	1.13.5.1
Source Type	10Mp Hamamatsu 100/250
Camera Resolution (pixel)	4000 x 2096
Camera Binning	1 x 1
Source Voltage kV	65
Source Current μ A	153
Image Pixel Size (μ m)	3.96
Filter	Al 0.5 mm
Rotation Step (deg.)	0.280
Output Format	8bit BMP
Dynamic Range	0.000 – 0.140
Smoothing	0
Beam Hardening	0
Post Alignment	Corrected
Ring Artefacts	16

PUBLICATIONS & PRESENTATIONS

Peer reviewed publications (attached)

Hagan, A., et al., Preparation and characterisation of vandetanib-eluting radiopaque beads for locoregional treatment of hepatic malignancies. *European Journal of Pharmaceutical Sciences*, 2017. 101: p. 22-30.

Conference presentations

Hagan, A., et al., In vitro and in vivo characterisation of a multiple tyrosine kinase inhibitor drug eluting bead. *Journal of Vascular and Interventional Radiology*, 2016. 27(3): p. S84.

Hagan, A., et al., Novel drug-eluting beads (DEBs) containing tyrosine kinase inhibitors (TKIs) for cancer therapy. *Journal of Biotechnology and Biomaterials*, 2016. 6(1(Suppl)): p. 38.

Hagan, A., et al., Novel in vitro models for predicting drug release from radiopaque embolic beads, in *Controlled Release Society (CRS) 44th Annual Meeting & Exposition 2017: Boston, USA*.

Publications in preparation

Hagan, A. et al., Prediction of the Pharmacokinetic Behavior of Different Drugs Released from Radiopaque Drug-eluting Embolization Beads using Novel in vitro Elution Methods. 2018.

Hagan, A. et al., Physicochemical Evaluation and Insights into the Biological Efficacy of Vandetanib-eluting Radiopaque Beads. 2018.



Preparation and characterisation of vandetanib-eluting radiopaque beads for locoregional treatment of hepatic malignancies



Alice Hagan^{a,b,*}, Gary J. Phillips^a, Wendy M. Macfarlane^a, Andrew W. Lloyd^a, Peter Czuczman^b, Andrew L. Lewis^b

^a School of Pharmacy and Biomolecular Sciences, University of Brighton, Moulsecoomb, Brighton BN2 4GJ, UK

^b Biocompatibles UK Ltd., BTG International Group Company, Lakeview, Riverside Way, Watchmoor Park, Camberley GU15 3YL, UK

ARTICLE INFO

Article history:

Received 30 November 2016

Received in revised form 24 January 2017

Accepted 25 January 2017

Available online 27 January 2017

Keywords:

Vandetanib

Tyrosine kinase inhibitors

Drug-eluting beads

Transarterial chemoembolization

ABSTRACT

Since their introduction around a decade ago, embolic drug-eluting beads (DEBs) have become a well-established treatment option for the locoregional transarterial treatment of hepatic malignancies. Despite this success, the therapy is seen to be limited by the choice of drug and more effective options are therefore being sought. These include the small molecule multi-tyrosine kinase inhibitors (MTKi), which exert an anti-angiogenic and anti-proliferative effect that could be highly beneficial in combating some of the unwanted downstream consequences of embolization. Vandetanib is an MTki which acts against such targets as vascular endothelial growth factor receptor (VEGFR) and epithelial growth factor receptor (EGFR) and has demonstrated modest activity against hepatocellular carcinoma (HCC), albeit with some dose-limiting cardiac toxicity. This makes this compound an interesting candidate for DEB-based locoregional delivery. In this study we describe the preparation and characterisation of vandetanib DEBs made from DC Bead™ and its radiopaque counterpart, DC Bead LUMI™. Drug loading was shown to be dependent upon the pH of the drug loading solution, as vandetanib has multiple sites for protonation, with the bead platform also having a fundamental influence due to differences in binding capacities and bead shrinkage effects. Fourier transform infrared (FTIR) spectroscopy and energy dispersive X-ray (EDX) Spectroscopy confirmed drug interaction is by ionic interaction, and in the case of the radiopaque DEB, the drug is distributed uniformly inside the bead and contributes slightly to the overall radiopacity by virtue of a bromine atom on the vandetanib structure. Drug release from both bead platforms is controlled and sustained, with a slightly slower rate of release from the radiopaque bead due to its more hydrophobic nature. Vandetanib DEBs therefore have suitable characteristics for intra-arterial delivery and site-specific sustained release of drug into liver tumours.

© 2017 The Author(s). Published by Elsevier B.V. This is an open access article under the CC BY-NC-ND license (<http://creativecommons.org/licenses/by-nc-nd/4.0/>).

1. Introduction

The current standard of care for intermediate hepatocellular carcinoma (HCC) is transarterial chemoembolization (TACE), an image guided procedure in which a chemotherapeutic agent is injected via the hepatic artery into the tumour feeding blood vessels. This is followed by an embolic material which occludes the vessels, with the aim of starving the tumour of oxygen and nutrients (Bruix et al., 2004). TACE may also be performed using drug eluting beads (DEB): embolic microspheres capable of loading positively charged drugs and releasing them local to the tumour site via ion exchange, thus reducing systemic drug exposure (Lewis and Holden, 2011).

The drug of choice for loading into DEB is usually doxorubicin, a cytotoxic agent which intercalates with DNA, interfering with replication (Gewirtz, 1999). However, it has been shown that hypoxic conditions can lead to doxorubicin resistance in HCC cells (Cox and Weinman, 2015). Moreover, tumour hypoxia induced by embolization therapy leads to upregulation of pro-angiogenic pathways contributing to the formation of new blood vessels (Liang et al., 2010; Rhee et al., 2007). Anti-angiogenic strategies are therefore being considered in combination with DEBs to improve treatment outcomes.

Several trials combining TACE with oral anti-angiogenic therapy such as sorafenib, sunitinib or bevacizumab are underway or completed with some promising results, however there remain toxicity issues associated with oral use of these agents (Lencioni et al., 2016; Erhardt et al., 2014). DEBs provide an opportunity for local delivery of these agents, allowing for high local doses and reduced toxicity compared with oral treatment. Forster et al. were the first to demonstrate that DEBs could be loaded with a combination of drugs (Forster et al.,

Abbreviations: MTki, multi-tyrosine kinase inhibitor; RODEB, radiopaque drug-eluting bead; HCC, hepatocellular carcinoma.

* Corresponding author at: School of Pharmacy and Biomolecular Sciences, University of Brighton, Moulsecoomb, Brighton BN2 4GJ, UK.

E-mail address: alice.hagan@btgplc.com (A. Hagan).

2012), not only to provide the benefit of local delivery of a cytotoxic drug such as doxorubicin, but also concomitant delivery of an agent with a complimentary mode of action such as rapamycin in order to downregulate expression of Hypoxia Inducible Factor Alpha (HIF-1 α) and consequently induction of angiogenesis. Sakr et al. have more recently described a layer-by-layer process for loading bevacizumab onto DC Bead™ (Sakr et al., 2016) for controlled locoregional delivery of a monoclonal antibody that inhibits Vascular Endothelial Growth Factor-A (VEGF-A), a chemical signal for angiogenesis. It is however, the small molecule multi-tyrosine kinase inhibitors that have attracted most interest, given the approval of sorafenib (Nexavar®, Bayer-Onyx) for the treatment of advanced HCC. Sorafenib drug-eluting peptide nanocomposites (Park et al., 2016) and poly(lactide-co-glycolide) microspheres (Chen et al., 2014; Chen et al., 2015), both with magnetic resonance imaging (MRI) capability have been described for intra-arterial delivery to treat HCC. Poly(D,L-lactic acid) microspheres have also been prepared and loaded with either sorafenib or together with cisplatin and showed that the drug combination had a faster release rate (Wang et al., 2015) and was more efficacious in cell assays (Wang et al., 2016) compared to either drug alone. Lahti et al. described the loading of LC Bead with both sorafenib (Lahti et al., 2015a) and sunitinib (Lahti et al., 2015b) but both processes were inefficient. Fuchs et al. have reported on a much more comprehensive appraisal of sunitinib loading into DC Bead™ (Fuchs et al., 2015), correlation of *in vitro* release with *in vivo* pharmacokinetics (Fuchs et al., 2014) and evaluation of antitumor effects in a rabbit VX2 embolization model (Bize et al., 2016). Whilst these studies show great promise and demonstrate feasibility for the locoregional delivery of MTKis from DEBs, concerns remain over the severe toxicity of sunitinib in the liver (Cheng et al., 2013) and alternative suitable MTKi candidates have been sought.

Table 1 outlines a short selection from a broad list of options that have been considered for MTKi loading into DEBs, taking into account drug structure, properties and mode of action. Herein we describe a feasibility study undertaken with one of these candidates, vandetanib. Vandetanib is a multi-tyrosine kinase inhibitor (MTKi) which selectively inhibits vascular endothelial growth factor receptor 2 (VEGFR-2), epidermal growth factor receptor (EGFR), and rearranged during transfection (RET) tyrosine kinase (Morabito et al., 2009). Common adverse events associated with the oral delivery of vandetanib include diarrhoea and rash, which can occasionally be severe. Prolongation of the QT interval (a measure of the time between the start of the Q wave and the end of the T wave in the heart's electrical cycle and a marker for the potential of ventricular tachyarrhythmias) has also been observed (Tsang et al., 2016). The VEGF and EGF pathways have both been implicated in the pathogenesis of HCC, and a phase II trial of vandetanib in advanced unresectable HCC patients showed a suggestion of improvement in progression free survival and overall survival (Hsu et al., 2012). There is therefore, a strong rationale for the locoregional delivery of this drug.

In this study the feasibility of loading vandetanib into DEB was investigated using both DC Bead™ and the recently approved radiopaque DEB DC Bead LUMI™ (Biocompatibles UK Ltd., Farnham, UK). This has resulted in an understanding of the interactions between vandetanib and the hydrogel network of the microspheres and the physicochemical characteristics of the resulting vandetanib-eluting beads in terms of maximum drug loading capacity, morphology, drug distribution and release.

2. Materials and methods

2.1. Materials

DC Bead™ and DC Bead LUMI™, both of diameter range 70–150 μ m, were provided by Biocompatibles Ltd. (Farnham, UK). Vandetanib base was provided by Astra Zeneca (Macclesfield, UK, >99% purity).

Table 1
Selection of MTKis and their mode of action and properties.

Compound	Mode of action	Properties ^a
Axitinib	Potent VEGF inhibitor, inhibits breast cancer growth, prevents neoangiogenesis in 9 L tumours, activity in refractory met renal cell	DMSO + DMF soluble Solubility of over 0.2 μ g/mL in aq media with a pH 1.1–7.8, pKa 4.8
Bosutinib	Active inhibitor of Bcr-Abl, inhibits tumour cell growth, angiogenesis, growth factor expression	DMSO + EtOH soluble, poorly water soluble Basic pKas 8.04, 4.80, 3.77
Canertinib diHCl	Potent pan-erb B tyrosine kinase inhibitor, irreversible TK inhibitor, radiosensitiser	10 mg/mL water solubility, DMSO \geq 5.6 mg/mL, logPc 3.05
Dasatinib	SRC and BCR/ABL tyrosine kinase inhibitor, Lyn & Src kinase inhibitor	Very poorly water soluble (0.0128 mg/mL), pKas 3.1, 6.8, logP 1.8
Dovitinib	MTKi of FGFR 3, inhibits tumour growth in xenograft models of colon cancer	DMSO soluble, poorly EtOH soluble
Erlotinib HCl	Targets EGFR TK, potent inhibitor of JAK2-V617F. "Tarceva" approved for NSCLC, pancreatic and others	Slight water and methanol solubility, pKa 5.42, logP 2.7
Gefitinib	EGFR TK inhibitor. "Iressa" approved for NSCLC	Solubility 0.027 mg/mL, sparingly water soluble at pH 3, pKas 5.4, 7.2, logP 3.2
Imatinib methane-sulfonate	Inhibits particular TK enzymes, used to decrease bcr-abl TK activity. Gleevec®, indicated for chronic myelogenous leukemia, GI stromal tumours	DMSO and water soluble, poorly EtOH soluble, logP 3
Lapatinib toluene-sulfonate	EGFR and HER2/neu dual TK inhibitor, potent EGFR kinase inhibitor, can restore tamoxifen sensitivity. "Tykerb®" for advanced met breast cancer	Poorly water soluble (0.0223 mg/mL), DMSO soluble, logP 5.4
Lestaurtinib	Potent inhibitor of several TKs FLT-3, TrkA, clinical activity in AML pts. with FLT-3 mutations	Very poorly water soluble
Masitinib	Protein TK inhibitor, phase III in dogs with canine mast cell tumours	Soluble in DMSO \geq 95 mg/mL, water < 1.2 mg/mL
Nilotinib	Selective BCR-ABL inhibitor and of proliferation of haematopoietic cells in CML and ALL. TK inhibitor Ph I in CML "Tasigna®"	Poorly water (0.00201 mg/mL) and poorly EtOH soluble, DMSO soluble, logPc 4.51
Pazopanib	Selective multitargeted TK inhibitor, targets VEGFR, PDGFR and c-kit	Limited solubility in warm DMSO, poorly water soluble (0.0433 mg/mL) logPc 3.59
Sorafenib toluene-sulfonate	Biaryl urea inhibits ERK pathway and angiogenesis by targeting VEGFR-2 and PDGFR-b. "Nexavar®" approved renal cell carcinoma and HCC	Poorly water (0.00171 mg/mL) and EtOH soluble, DMSO soluble, logP 3.8
Sunitinib Malate	Selective inhibitors of MTKs, inhibits FLT3-ITD phosphorylation, CSF-1 rK. "Sutent®" for renal cell carcinoma	Water soluble at pH 1.2–6.8, fluorescent, weak base pKa 8.95, logP 5.2
Vandetanib	VEGFR-dependent tumour angiogenesis inhibitor, EGFR & RET-dependent proliferation inhibitor. "Zactima®" for follicular, medullary, anaplastic, adv/met papillary thyroid cancer	DMSO soluble, poorly water soluble (0.008 mg/mL), soluble at lower pHs, logPc 5.01
Vatalanib diHCl	Selective inhibitor for	Water soluble (10 mg/mL),

Table 1 (continued)

Compound	Mode of action	Properties ^a
	VEGFR-1&2 TK + PDGFR- β , c-KIT & c-FMS	DMSO soluble (85 mg/mL)

^a Information sourced from www.drugbank.ca or individual drug FDA labels.

2.2. Loading of beads with vandetanib solution

As vandetanib exhibits pH dependent solubility, solutions were prepared by first dissolving the powdered drug in 0.1 M hydrochloric acid to 70% of the required volume. The solution was then adjusted to the required pH by dropwise addition of sodium hydroxide, before making up to volume with purified water. By this protocol, solutions at pH 2.1 and 4.4 were prepared at a concentration of 20 mg/mL. Solutions at pH 6.8 were prepared at a concentration of 5 mg/mL due to limits in solubility.

To load beads with vandetanib, the packing solution was removed from bead vials and vandetanib solution was added. Incubation with the loading solution was performed at room temperature under agitation for a minimum of 2 h. Depleted loading solution was removed and the beads washed 3 times in deionised water. To determine loading efficiency, vandetanib concentration in the depleted loading solution and washings was quantified by HPLC, using a Hypersil Gold C18 column (Thermo Scientific, UK) and PDA detector at a wavelength of 254 nm. Mobile phase was a gradient of 0.1% TFA v/v in purified water and 0.1% TFA v/v in methanol; flow rate 1 mL/min.

2.3. Bead morphometry

Bead samples before and after vandetanib loading were examined using an Olympus BX50 optical microscope with attached Colorview III camera. The diameter of 200 beads per sample was recorded using Stream software (Olympus, Southend on Sea, UK). Bead density was determined using a displacement assay described in detail previously (Duran et al., 2016).

2.4. Elemental mapping using SEM-EDX

DC Bead LUMI™ was loaded with the maximum vandetanib dose of 135 mg/mL of sedimented beads. Bead samples were embedded in Tissue-Tek optimum cutting temperature compound (Sakura, Thatcham, UK) on liquid nitrogen and transferred to $-80\text{ }^{\circ}\text{C}$ to ensure thorough freezing. Samples were sectioned in a cryostat (Leica, Milton Keynes, UK) in 10 μm thick sections and mounted on SEM stubs with carbon pads. Samples were coated with 4 nm platinum using a Q150T turbo molecular-pumped sputter coating system (Quorum, Lewes, UK) prior to SEM-EDX analysis. SEM imaging was carried out on a Zeiss SIGMA FEG-SEM (Zeiss, Cambridge, UK) scanning electron microscope equipped with an Oxford Instruments 80 mm² X-Max energy dispersive X-ray analysis system. The sample was left in the SEM for several minutes prior to imaging to ensure the small amount of water present in the section was removed under the high vacuum. Elemental mapping and spectra were acquired for iodine, bromine, fluorine and sulfur on unloaded DC Bead LUMI™ and DC Bead LUMI™ loaded with vandetanib at maximum capacity.

2.5. Vandetanib-bead interactions using Fourier transform infra-red microscopy

DC Bead LUMI™ loaded with different doses of vandetanib were embedded and sectioned into 10 μm slices as described in Section 2.4. These were subjected to FTIR microscopy point analysis across a 10–15 different regions of interest across the samples surface. The spectra were collated and the position of the S=O stretching frequency around 1040–1050 cm^{-1} was averaged for each sample. The effect of differing

concentrations of drug loading on the stretching absorption of the sulfonate binding groups on the beads could then be evaluated.

2.6. X-ray micro-computer tomography (μ -CT) analysis for bead radiopacity

Unloaded LUMI™ and LUMI™ loaded with vandetanib at concentrations of 30, 60 and 100 mg/mL were uniformly suspended in 1% agarose solution in nunc tubes. μ -CT 3D scanning was performed to quantify individual bead radiopacity in Hounsfield units (HU) of each bead in the sample. μ -CT analysis was performed by Reading Scientific Services Ltd., Reading, UK.

2.7. Vandetanib release from beads

DC Bead™ and DC Bead LUMI™ were loaded with 20 mg/mL and 40 mg/mL of vandetanib respectively. The volume of DC Bead™ decreased by 50% following loading leading to a final dose density of 40 mg/mL. Aliquots of 0.3 mL of beads each containing 12 mg vandetanib were placed in amber jars containing 1 L of pH 7 PBS (Source Bioscience, Nottingham, UK), stirring at 200 rpm. At determined time points, stirring was stopped to allow beads to settle before removing a 5 mL sample of PBS for vandetanib quantification by HPLC as described in Section 2.2. 5 mL of fresh PBS was replaced after each timepoint.

2.8. Evaluation of suspension, handling and administration of vandetanib loaded DC Bead LUMI™

A series of evaluations were conducted to ensure that loading of vandetanib into the beads did not adversely affect their handling and delivery through a microcatheter. DC Bead LUMI™ (70–150 μm) was loaded with 100 mg/mL of vandetanib as described in Section 2.2, excess loading solution removed and the bead slurry (1 mL) mixed with contrast agent (9 mL Omnipaque 350®, GE Healthcare, Oslo, Norway). After transferring into a 20 mL Luer-lok™ syringe (BD Plastipak, Temse, Belgium) a three-way stopcock (Discofix®, B. Braun, Melsungen, Germany) was attached to the syringe and another syringe attached to enable transfer between them for suspension. Beads were transferred between two syringes in injection mixture of Omnipaque 350® and water 20 times. Suspension time was measured by the time it took for 25% of the solution to be free from beads, *i.e.* time taken for the top of the bead suspension to fall to 75% of the internal height of the syringe ($n = 3$). The suspension was passed through a 2.4 Fr catheter (Progreat®, Terumo Corp., Tokyo, Japan) and the beads assessed visually for any signs of deformation of their shape or presence of fragmentation using optical microscopy as in Section 2.3.

2.9. Stability of vandetanib loaded DC Bead LUMI™ contrast agent suspension

When used in hospital, on occasion DEBs are often prepared in the hospital pharmacy the night before and stored in a refrigerator. Drug elution from vandetanib loaded DC Bead LUMI™ (70–150 μm) suspended in contrast agent was therefore investigated by taking aliquots of the delivery media supernatant over a period of 24 h and analysing them using the HPLC method described in Section 2.2 to determine the amount of vandetanib eluted ($n = 3$). The chromatographic peak was also analysed to determine if there was any drug degradation during this period.

3. Results

3.1. Vandetanib loading and maximum capacity

At acidic pH, positively charged amines on vandetanib molecules interact with negatively charged sulfonate groups within the microsphere

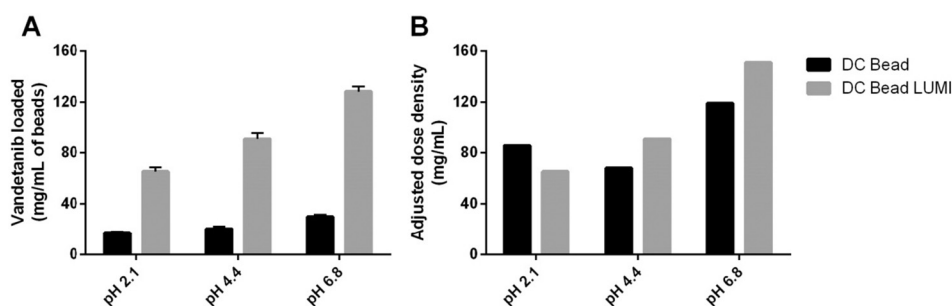


Fig. 1. Maximum loading of vandetanib in DC Bead™ and DC Bead LUMI™ at varying pH. A) Amount of drug uptake per mL of beads (initial volume), bars represent mean \pm SD, $n = 5$; B) dose density per mL of beads after adjustment for loading induced bead shrinkage.

hydrogel network, enabling drug loading. From the theoretical prediction shown in Fig. 8, the major vandetanib microspecies, a 2+ charged form and a 1+ charged form, are predominant at pH 2.1 and pH 6.8 respectively, with a 50:50 proportion of each form at pH 4.4. Vandetanib solutions were prepared at each of these pHs and added to beads in excess to assess the effect on maximum loading capacity.

Maximum vandetanib capacity increased with pH (proportion of 1+ form) as expected, with maximum capacity at 30 mg/mL for DC Bead™ and 135 mg/mL for DC Bead LUMI™ (Fig. 1). Initial analysis of depleted loading solution from DC Bead™ showed a higher than expected loading efficiency, but with subsequent washes in water the actual loading dose was found to be lower suggesting that some drug was weakly associated with the bead surface and able to be removed with water. This effect was less pronounced with DC Bead LUMI™. Below maximum capacity, a loading efficiency of >99% was achieved after 2 h of incubation with loading solution, suggesting fast adsorption of vandetanib into beads. When considering the respective chemical compositions of both beads, the theoretical maximum loading capacity based upon the content of sulfonic acid drug binding residues is higher for both DC Bead™ and DC Bead LUMI™ than the actual experimentally determined maximum drug binding capacity. For DC Bead, the maximum amount of drug loaded varies from 81 to 91.2% of the theoretical, compared to 74.5–80.4% for DC Bead LUMI™, both dependent upon the pH of the loading solution.

3.2. Bead morphology, size and density after loading

After loading with vandetanib, beads retained a smooth, spherical appearance (Fig. 2A–D). Loading DC Bead M1™ at maximum vandetanib capacity caused a significant decrease in mean diameter (35%, $p < 0.0001$) as well as a narrowing of the size distribution (Fig. 2E). The size decrease showed a trend with decreasing pH. The size reduction corresponded with a reduction in settled bead volume of over 60%. The bead density increase from $1.03 \pm 0.03 \text{ g/cm}^3$ (unloaded) to $1.15 \pm 0.09 \text{ g/cm}^3$ (loaded at 30 mg/mL), this small increase due to the decrease in size and contraction of the matrix. In contrast, the mean diameter of DC Bead LUMI™ loaded at maximum capacity did not significantly decrease at any pH (Fig. 2F), despite a 15% reduction in the settled bead volume at pH 6.8 only. The density increased only minimally from $1.29 \pm 0.03 \text{ g/cm}^3$ (unloaded) to $1.31 \pm 0.09 \text{ g/cm}^3$ when loaded at 100 mg/mL due to the marginal size change.

3.3. Vandetanib distribution in beads

Scanning electron microscopy showed the sectioned internal structure of DC Bead LUMI™ to be homogeneous and devoid of any visible pores (Fig. 3(a)). SEM-EDX analysis was used to detect vandetanib distribution in sectioned sample loaded at maximum capacity of 135 mg/mL. Bromine was selected as the element of interest for the

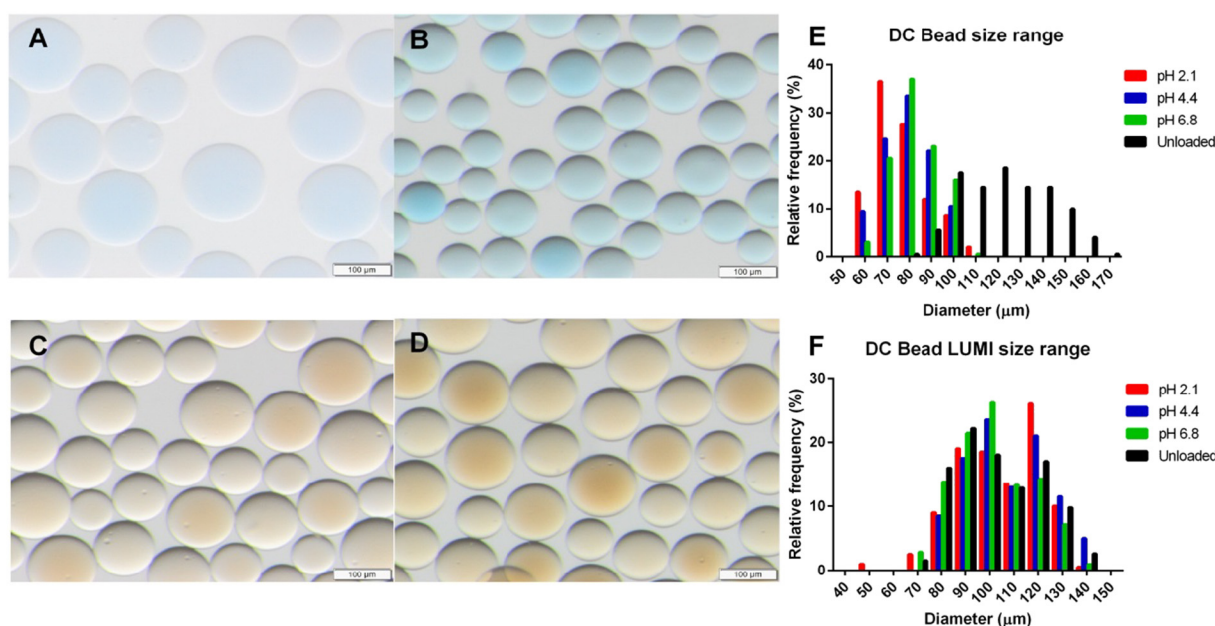


Fig. 2. (A) Unloaded DC Bead™; (B) vandetanib-loaded DC Bead™ (30 mg/mL, pH 4.6); (C) unloaded DC Bead LUMI™; (D) vandetanib-loaded DC Bead LUMI™ (100 mg/mL, pH 4.6). Scale bars 100 μm. (E) DC Bead™ and (F) DC Bead LUMI™ size decrease after vandetanib loading at differing pHs.

drug distribution, being present in vandetanib molecules but not in DC Bead LUMI™. The sulfur and iodine distributions were also mapped to gain insight into the bead internal structure. Elemental mapping revealed that bromine was evenly distributed throughout the sectioned beads (Fig. 3(b)), the bromine peak seen in the EDX spectrum (arrow, Fig. 3(e)) being absent in the spectrum for control (unloaded) beads (data not shown). Sulfur and iodine distributions also appeared to be evenly distributed within the bead structure (Fig. 3(c) and (d)) (Duran et al., 2016). The table insert in Fig. 3(e) shows there is an excellent agreement between the measured weight percent of elements by

EDX compared with the theoretical calculated weight percentage expected based upon 135 mg/mL loading of vandetanib into DC Bead LUMI™, the latter which possesses 177 mg/mL iodine (Duran et al., 2016).

3.4. Evaluation of drug-bead interactions using FTIR microscopy

As the dose of vandetanib loaded into DC Bead LUMI™ was increased, the frequency of the S=O stretch from the sulfonate groups of the beads was seen to shift steadily to lower wavenumber (Fig. 4).

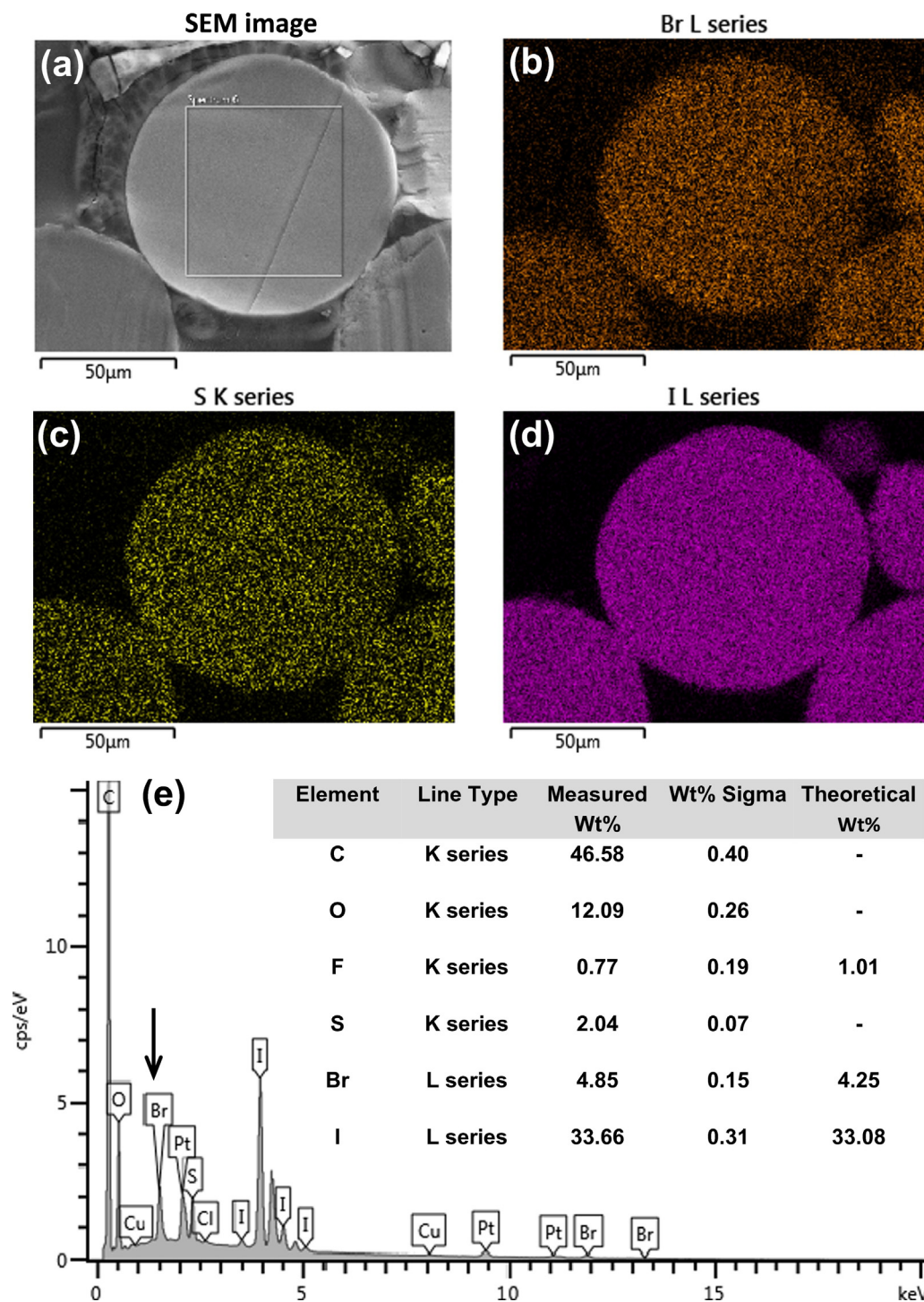


Fig. 3. (a) Scanning electron microscopy image of a sectioned vandetanib-loaded DC Bead LUMI™ sample; (b) bromine elemental mapping distribution image; (c) sulfur elemental mapping distribution image; (d) iodine elemental mapping distribution image; (e) EDX elemental spectrum showing bromine peak for the vandetanib loaded bead and elemental analysis (table inset).

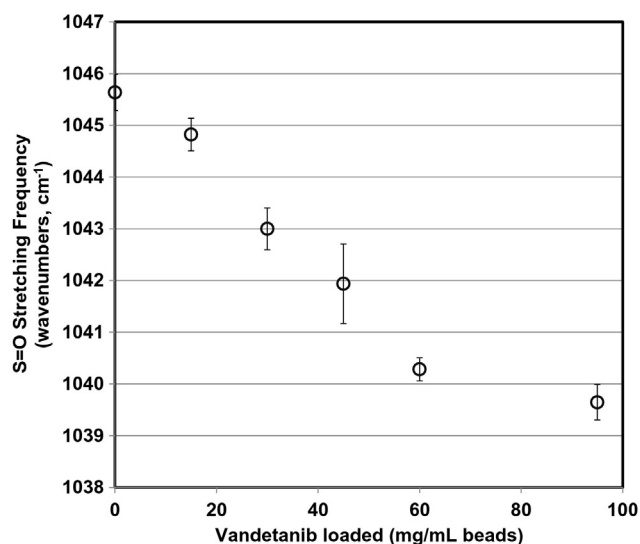


Fig. 4. Effect of vandetanib loading dose on the S=O stretching frequency from the sulfonate groups on the beads (error bars = SEM).

This is indicative of an increasing interaction between drug and bead as all of the bead binding sites become progressively occupied. Samples loaded using a target loading of 60 mg/mL at pH 6.8, 4.4 and 2.1 gave rise to similar S=O stretching frequencies at 1041.6 cm⁻¹, 1040.3 cm⁻¹ and 1040.4 cm⁻¹ respectively.

3.5. Radiopacity of vandetanib loaded DC Bead LUMI™

Micro-CT analysis of DC Bead LUMI™ shows it to possess an inherent radiopacity due to the triodobenzyl moieties attached to the bead structure (Duran et al., 2016; Levy et al., 2016; Sharma et al., 2016), giving rise to a baseline radiopacity of 4454 ± 225 Hounsfield units. The level of radiopacity is seen to increase linearly with increasing loading of vandetanib into the beads (Fig. 5) until at a loading of 100 mg/mL of vandetanib, the radiopacity is seen to have increased by 621 Hounsfield Units.

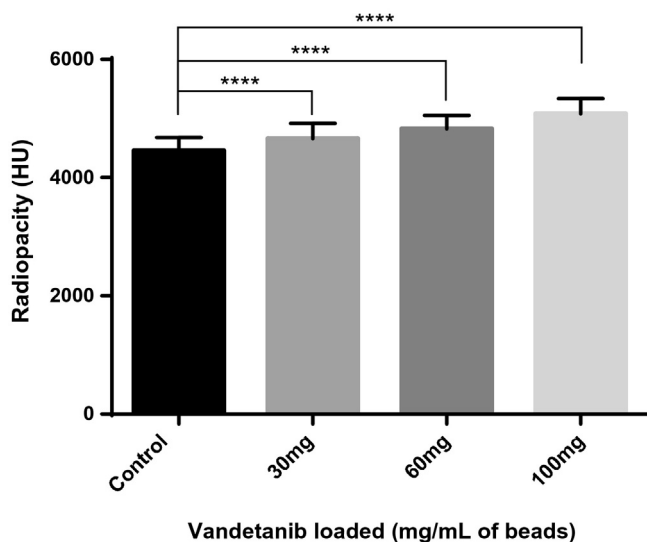


Fig. 5. Effect of vandetanib loading into DC Bead LUMI™ on radiopacity of the beads. Bars represent mean of all beads in a single scan of the sample (>6000 beads per sample) ± SD. **** = p < 0.0001 by 1 way ANOVA + Holm-Sidak's multiple comparisons test between doses.

3.6. Vandetanib release from beads

The elution of vandetanib from DC Bead™ and DC Bead LUMI™ into PBS was analysed using an *in vitro* USP type II dissolution model, using 0.3 mL aliquots of beads that had been loaded at equivalent dose densities of 40 mg/mL at pH 4.4 (12 mg per aliquot). Drug release showed a rapid burst phase in the first 2 h, after which it began to plateau (Fig. 6). The total percentage release of vandetanib over the test period was higher from DC Bead™ than from DC Bead LUMI™, achieving on average 85% drug release in 24 h, compared to an average of 50% from DC Bead LUMI™.

3.7. Evaluation of suspension, handling, delivery and stability of vandetanib loaded DC Bead LUMI™

When DC Bead LUMI loaded with 100 mg of vandetanib was suspended in Omnipaque 350® (Section 2.8) the beads formed a uniform suspension and showed no signs of bead agglomeration. The bead suspension did not adhere onto the surface of the vial and was easily transferred into a syringe for delivery. The average time in suspension within the syringe was >6.5 min which is more than sufficient for practical usage. The bead suspension was delivered through a 2.4 Fr microcatheter with ease and there was no occurrence of catheter blockage during bead delivery. The beads remained spherical with no signs of fragmentation post-delivery.

The amount of vandetanib released from the beads into the contrast medium 15 min after mixing was 3.3 mg, which increased to just 3.5 mg in total after 24 h storage. The drug was seen to be unaltered and remained within specification, >98.0% purity with no single impurity >0.2%. This shows that a bead suspension could be potentially prepared in advance and stored overnight without significant elution of drug into the delivery medium and without risk of drug degradation.

4. Discussion

Drug candidates that have been loaded into DC Bead™ have conventionally been water soluble cationic salt forms that allow for diffusion and ion-exchange into the anionically-charged hydrogel matrix of the bead (Forster et al., 2010; Guiu et al., 2015; Lewis, 2009; Lewis et al., 2007; Taylor et al., 2007). MTKis represent a group of small molecules with widely differing structures that impact drug solubility, lipophilicity and ionization potential. Different process strategies may therefore be required when considering how to load sufficient amounts of these compounds in an efficient way into the bead matrix, and subsequently what intermolecular drug-bead interactions will control the release of the molecule.

The chemical structures of a selection of MTKis considered for combining with DEBs are presented in Fig. 7. Sorafenib loading into DC Bead™ has been reported but the low solubility of the drug in aqueous media requires a loading process of several sequential sessions of loading from low drug concentration solution to achieve sufficient quantities of loaded drug (Lahti et al., 2015a). This can be overcome by use of a DMSO swelling process in which drug dissolved in DMSO can be used to swell the beads, followed by a precipitation step as the drug swollen beads are immersed in water (Forster et al., 2012). This however, leaves the drug in a microprecipitated form in which its elution is dependent upon the dissolution of the particulates. The partial ethanol solubility of sorafenib can be used to produce suitable loading solutions in ethanol:water mixtures in which the drug can be exchanged into the bead matrix. Sorafenib however, unlike, many of the other MTKis, has no protonatable amine group and relies upon strong hydrogen bonding of the amines on the urea group to interact with carboxylate residues in at its target site. This may also provide a source of interaction between drug and bead to ensure controlled release.

Sunitinib on the other hand has a pendant tertiary diethyl substituted amine that can be protonated to provide a ionic interaction with the

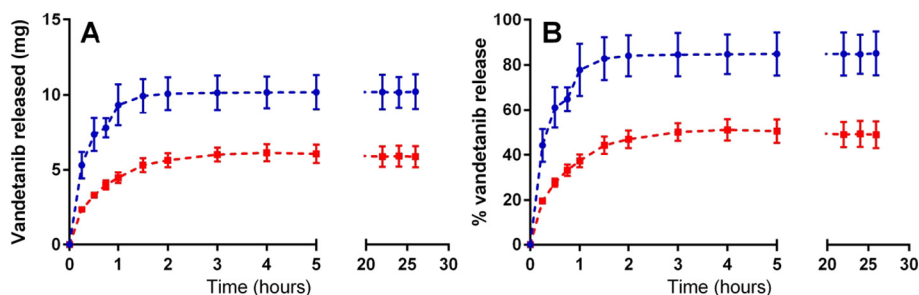


Fig. 6. Vandetanib release from DC Bead™ (●) and DC Bead LUMI™ (■) as A) amount released in mg; B) percentage of available dose. 0.3 mL aliquots of beads containing equivalent of 12 mg vandetanib were stirred in 1 L PBS, pH 7. Mean \pm SD, n = 3.

beads (Lahti et al., 2015b.). Solubility is improved below pH 6.8 and is further enhanced with the addition of a sugar or polyol additive to aid loading (Fuchs et al., 2015). Vandetanib, erlotinib, gefitinib and dasatinib all share a common secondary amine bridging function attached to a pyrimidine ring, providing additional sites of ionization to aid in ion-exchange and increase the solubility of these compounds in water at reduced pH. The positive charge residing on this aromatic portion of the molecule however, can be significantly delocalised across the conjugated ring system, which lessens its capability for charge-charge interaction (Lewis, 2009).

Based on the theoretical ionization of vandetanib in solution at different pH (Fig. 8) and therefore the relative concentrations of different vandetanib charge forms, the drug loading maximum capacity should be influenced by the pH of the loading solution, which has been confirmed in Fig. 1. For both DC Bead™ and DC Bead LUMI™, there was a positive relationship between pH of the loading solution and the maximum amount of vandetanib that could be loaded into the beads. This is due to the fact that as pH decreases, a greater proportion of vandetanib molecules in solution have 2 positive charges, and can therefore occupy 2 sulfonate binding sites within the beads, shifting towards a 2:1 binding ratio. Regardless of the pH, neither bead was able to load the theoretical maximum drug loading based upon sulfonic acid group content, although DC Bead™ was seen to load closer to the theoretical maximum (91.2%) than DC Bead LUMI™ (80.4%), the latter having a denser, more hydrophobic gel matrix in which access to all binding sites may be more restricted.

In DC Bead™, a slight decrease in size range was observed with decreasing pH. This is in keeping with previously observed effects of

loading the antineoplastic mitoxantrone, which has 2 positively charged sites, and thus exerts an increased shrinking effect on DC Bead™ which is suggested to be an effect of 'pulling' the hydrogel network closer together by interacting with multiple sites (Lewis, 2009). The drug-bead charge-charge interaction through the sulfonate groups was confirmed by the shift of the S=O stretching frequency to lower wavenumber with increasing drug dose, a phenomenon also observed for both doxorubicin and irinotecan binding to DC Bead™ (Lewis and Dreher, 2012; Namur, 2009). Interestingly, when 60 mg/mL loading was performed at pH 2.1, 4.4 and 6.8, the S=O frequency was seen not to change significantly, even though at this dose the DC Bead LUMI™ is only at about 50% binding capacity. At pH 2.1 it is expected that vandetanib would carry two positive charges and hence capable of interaction with nearly all binding sites in the beads. The second charge residing on the conjugated ring system would not be expected to interact as strongly as that on the piperidine ring as indicated by the lack of change in the S=O stretching frequency.

Furthermore, although it could be expected that vandetanib molecules binding to 2 sites may be released more slowly in an elution model, the release profile of vandetanib from DC Bead LUMI™ did not vary significantly depending on the pH of the loading solution (data not shown). Possible reasons for this are that the ionic interactions are not strong enough to be affected in this manner, or perhaps the neutral pH of the elution medium negates this pH dependent effect as soon as the ion exchange process begins.

Release of vandetanib from DC Bead LUMI™ was incomplete, despite maximum concentrations reached in the elution vessel remaining lower than the theoretical solubility of 0.008 mg/mL (Fig. 6A). The higher

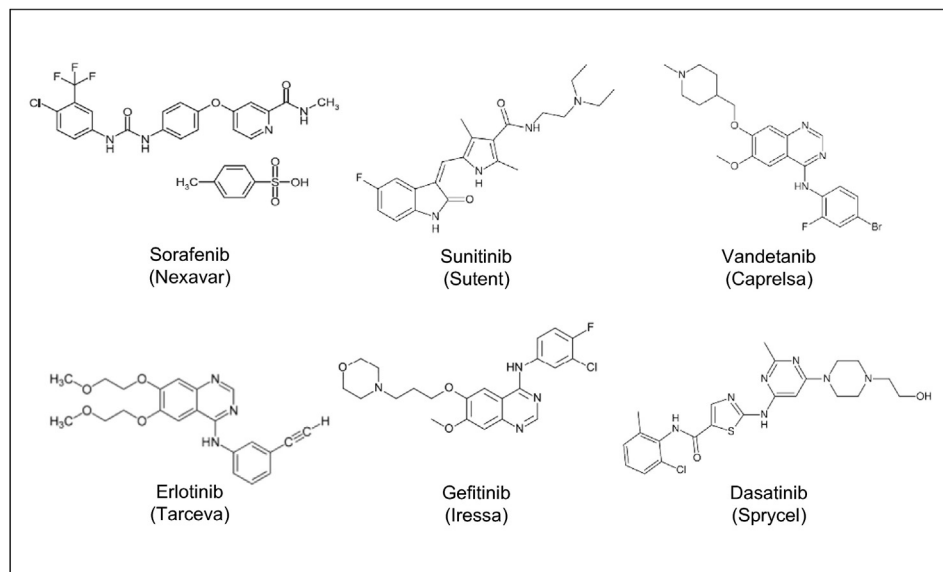


Fig. 7. Structure of a selection of approved MTKi.

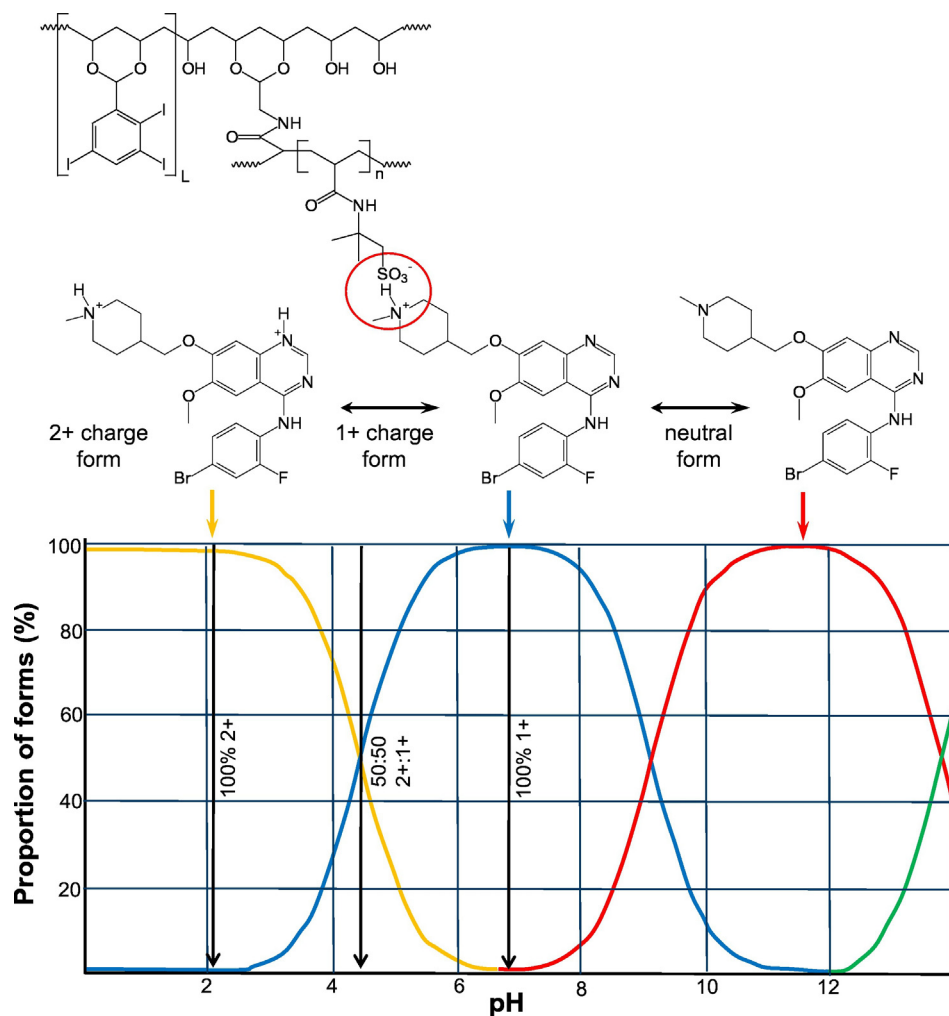


Fig. 8. Ionic interaction of DC Bead™ (L groups are present in DC Bead LUMI™) with vandetanib (top); structure of the ionised forms of vandetanib at different pH (middle); (c) theoretical proportion of the various forms of vandetanib present with pH (adapted from chemicalize.org).

density and therefore less ‘open’ structure of DC Bead LUMI™ likely limits movement of drug molecules out of the beads. However, by adjusting the pH of the PBS elution medium to 5, vandetanib release rate from LUMI™ was slightly improved with total drug release increasing by 10% to 60% (data not shown). Hypoxic tumours are known to be acidotic due to production of lactic acid by anaerobic glycolysis. Moreover efficient arterial embolization will impede clearance of lactic acid from tumoural tissues, contributing to the acidic microenvironment (Chao et al., 2016), which may somewhat facilitate release in the case of acidic-soluble drugs. Similarly to doxorubicin (Hecq et al., 2013), vandetanib binding to DEB has been shown to be fully reversible as the total dose can be extracted using a solution of potassium chloride and ethanol. Using improved elution models with open-loop flow through conditions as described by Swaine et al. may facilitate the modelling of full extended vandetanib release by preventing saturation of elution medium and more closely mimicking the *in vivo* situation (Swaine et al., 2016).

The addition of the iodinated moiety that renders DC Bead LUMI™ radiopaque increases the solid content of the beads (Duran et al., 2016) and introduces hydrophobic portions to the bead structure which may interact with various drugs thereby altering drug loading and release properties. Increasing loading of vandetanib also leads to a proportional increase in the radiopacity of the DC Bead LUMI™ (Fig. 4) which is not attributable to a densification of the internal structure as the mean diameter of the beads are essentially unchanged with drug loading (Fig. 2F). The existence of a bromine atom on the vandetanib

structure is the likely source of the added radiopacity, which increases by approximately 25–26 Hounsfield units per mg of radiodense atom (iodine and bromine) present.

The data presented in this study has confirmed that DC Bead LUMI™ has desirable physicochemical characteristics suitable for use as an anti-angiogenic DEB. Firstly, maximum vandetanib loading capacity is high, reaching maximum doses of over 120 mg/mL at pH 6.8 and even when decreasing pH to maintain vandetanib solubility doses of 100 mg/mL are still feasible. The increased solid content leads to a higher density of drug binding sites than standard DC Bead™. This increased capacity may compensate for the slower drug release rate. Secondly, DC Bead LUMI™ was more resistant to size changes after loading with vandetanib, compared with DC Bead™ which had a significant reduction in bead size and volume. Although there has been a trend towards using smaller size beads in recent years (Lencioni et al., 2012), it has been observed that particles of around 40 μm pose a risk of potentially fatal complications resulting from off-target embolisation (Bonomo et al., 2010; Brown, 2004). The radiopacity of DC Bead LUMI™ may also provide advantages in this respect due to the potential for intra and post-procedural feedback on bead delivery (Duran et al., 2016). Finally, loading of the drug did not adversely affect the properties of the beads in terms of their suspension, handling and delivery in contrast agent. When mixed into suspension only a small amount of drug (3.5 mg) was released into Omnipaque contrast agent and the drug was shown to be stable in this mixture over the 24 h storage condition selected for the test. These preliminary evaluations confirm that

vandetanib loaded DC Bead LUMI™ performs in a manner amenable for a DEB-TACE procedure.

Recent investigations have been performed using DC Bead™ loaded with the VEGFR inhibitor sunitinib (Fuchs et al., 2015; Fuchs et al., 2014), which have shown significant effects on endothelial cell proliferation, apoptosis and migration, with both sunitinib beads and free sunitinib having similar activity *in vitro*. Sunitinib beads had modest anti-proliferative effects against a range of cancer cell lines, with lack of direct cytotoxicity due to the mechanism of action of sunitinib being VEGFR inhibition. As well as inhibiting VEGFR, vandetanib also targets EGFR and therefore has the potential to also directly impede cancer cell proliferation and induce apoptosis. *In vitro* assays have revealed that vandetanib has a significant anti-proliferative effect on endothelial cells and induces apoptosis in hepatoma cell lines at a concentration of <10 μmol/L (4.75 μg/ml) (Inoue et al., 2012). The elution studies performed here indicate that the release of vandetanib levels in excess of this concentration is feasible. In support of this preliminary data we have recently reported on a safety and pharmacokinetics study of vandetanib DEB-TACE in healthy swine liver which demonstrated that the treatment was well tolerated and confirmed the presence of therapeutic concentrations of vandetanib up to 30 days after administration (Czuczman et al., 2016).

5. Conclusions

Vandetanib can be efficiently loaded and released from DC Bead™ and DC Bead LUMI™ whilst maintaining microsphere integrity and properties suitable for use as an embolization agent. The inclusion of vandetanib in a DEB warrants further characterisation *in vitro* and *in vivo* to determine its efficacy in models of HCC.

Acknowledgements

A. Hagan would like to thank the Royal Commission for the Exhibition of 1851 for provision of funding for an Industrial Fellowship.

References

- Bize, P., et al., 2016. Antitumoral effect of sunitinib-eluting beads in the rabbit VX2 tumor model. *Radiology* 280 (2), 425–435.
- Bonomo, G., et al., 2010. Bland embolization in patients with unresectable hepatocellular carcinoma using precise, tightly size-calibrated, anti-inflammatory microparticles: first clinical experience and one-year follow-up. *Cardiovasc. Intervent. Radiol.* 33 (3), 552–559.
- Brown, K.T., 2004. Fatal pulmonary complications after arterial embolization with 40–120-micron tris-acryl gelatin microspheres. *J. Vasc. Interv. Radiol.* 15 (2 Pt 1), 197–200.
- Bruix, J., Sala, M., Llovet, J.M., 2004. Chemoembolization for hepatocellular carcinoma. *Gastroenterology* 127 (5, Supplement 1), S179–S188.
- Chao, M., et al., 2016. A nonrandomized cohort and a randomized study of local control of large hepatocarcinoma by targeting intratumoral lactic acidosis. *Elife* 5, e15691.
- Chen, J., et al., 2014. Poly(lactide-co-glycolide) microspheres for MRI-monitored transcatheter delivery of sorafenib to liver tumors. *J. Control. Release* 184, 10–17.
- Chen, R., et al., 2015. Poly(lactide-co-glycolide) microspheres for MRI-monitored delivery of sorafenib in a rabbit VX2 model. *Biomaterials* 61, 299–306.
- Cheng, A.L., et al., 2013. Sunitinib versus sorafenib in advanced hepatocellular cancer: results of a randomized phase III trial. *J. Clin. Oncol.* 31 (32), 4067–4075.
- Cox, J., Weinman, S., 2015. Mechanisms of doxorubicin resistance in hepatocellular carcinoma. *Hepat. Oncol.* 3 (1), 57–59.
- Czuczman, P., et al., 2016. Elution of vandetanib from radiopaque drug-eluting beads *in vitro* and pharmacokinetics of vandetanib in swine following administration in radiopaque drug-eluting beads. CIRSE Annual Congress. Springer, Barcelona, Spain.
- Duran, R., et al., 2016. A novel inherently radiopaque bead for transarterial embolization to treat liver cancer - a pre-clinical study. *Theranostics* 6 (1), 28–39.
- Erhardt, A., et al., 2014. TACE plus sorafenib for the treatment of hepatocellular carcinoma: results of the multicenter, phase II SOCRATES trial. *Cancer Chemother. Pharmacol.* 74 (5), 947–954.
- Forster, R.E., et al., 2010. Comparison of DC Bead-irinotecan and DC Bead-topotecan drug eluting beads for use in locoregional drug delivery to treat pancreatic cancer. *J. Mater. Sci. Mater. Med.* 21 (9), 2683–2690.
- Forster, R.E., et al., 2012. Development of a combination drug-eluting bead: towards enhanced efficacy for locoregional tumour therapies. *Anti-Cancer Drugs* 23 (4), 355–369.
- Fuchs, K., et al., 2014. Drug-eluting beads loaded with antiangiogenic agents for chemoembolization: *in vitro* sunitinib loading and release and *in vivo* pharmacokinetics in an animal model. *J. Vasc. Interv. Radiol.* 25 (3), 379–387.
- Fuchs, K., et al., 2015. Sunitinib-eluting beads for chemoembolization: methods for *in vitro* evaluation of drug release. *Int. J. Pharm.* 482 (1–2), 68–74.
- Gewirtz, D.A., 1999. A critical evaluation of the mechanisms of action proposed for the antitumor effects of the anthracycline antibiotics adriamycin and daunorubicin. *Biochem. Pharmacol.* 57 (7), 727–741.
- Guiu, B., et al., 2015. Idarubicin-loaded ONCOZONE drug-eluting embolic agents for chemoembolization of hepatocellular carcinoma: *in vitro* loading and release and *in vivo* pharmacokinetics. *J. Vasc. Interv. Radiol.* 26 (2), 262–270.
- Hecq, J.-D., et al., 2013. Doxorubicin-loaded drug-eluting beads (DC Bead®) for use in transarterial chemoembolization: a stability assessment. *J. Oncol. Pharm. Pract.* 19 (1), 65–74.
- Hsu, C., et al., 2012. Vandetanib in patients with inoperable hepatocellular carcinoma: a phase II, randomized, double-blind, placebo-controlled study. *J. Hepatol.* 56 (5), 1097–1103.
- Inoue, K., et al., 2012. Vandetanib, an inhibitor of VEGF receptor-2 and EGF receptor, suppresses tumor development and improves prognosis of liver cancer in mice. *Clin. Cancer Res.* 18 (14), 3924–3933.
- Lahti, S.J., et al., 2015a. Sorafenib loaded drug-eluting beads: loading and eluting kinetics and *in vitro* viability study. *J. Vasc. Interv. Radiol.* 26 (2 (Suppl.)), S80–S81.
- Lahti, S.J., et al., 2015b. Sunitinib loaded drug-eluting beads: loading and eluting kinetics and *in vitro* viability study. *J. Vasc. Interv. Radiol.* 26 (2 (Suppl.)), S81–S82.
- Lencioni, R., et al., 2012. Transcatheter treatment of hepatocellular carcinoma with doxorubicin-loaded DC Bead (DEBDOX): technical recommendations. *Cardiovasc. Intervent. Radiol.* 35 (5), 980–985.
- Lencioni, R., et al., 2016. Sorafenib or placebo plus TACE with doxorubicin-eluting beads for intermediate stage HCC: the SPACE trial. *J. Hepatol.* 64 (5), 1090–1098.
- Levy, E.B., et al., 2016. First human experience with directly image-able iodinated embolization microbeads. *Cardiovasc. Intervent. Radiol.* 39 (8), 1177–1186.
- Lewis, A.L., 2009. DC Bead™: a major development in the toolbox for the interventional oncologist. *Expert Rev. Med. Devices* 6 (4), 389–400.
- Lewis, A.L., Dreher, M.R., 2012. Locoregional drug delivery using image-guided intra-arterial drug eluting bead therapy. *J. Control. Release*.
- Lewis, A.L., Holden, R.R., 2011. DC Bead embolic drug-eluting bead: clinical application in the locoregional treatment of tumours. *Expert Opin. Drug Deliv.* 8 (2), 153–169.
- Lewis, A.L., et al., 2007. Doxorubicin eluting beads - 1: effects of drug loading on bead characteristics and drug distribution. *J. Mater. Sci. Mater. Med.* 18 (9), 1691–1699.
- Liang, B., et al., 2010. Correlation of hypoxia-inducible factor 1[alpha] with angiogenesis in liver tumors after transcatheter arterial embolization in an animal model. *Cardiovasc. Intervent. Radiol.* 33 (4), 806–812.
- Morabito, A., et al., 2009. Vandetanib (ZD6474), a dual inhibitor of vascular endothelial growth factor receptor (VEGFR) and epidermal growth factor receptor (EGFR) tyrosine kinases: current status and future directions. *Oncologist* 14 (4), 378–390.
- Namur, J., 2009. Microsphères d'embolisation Pour la Vectorisation de Principes Actifs: Étude de la Libération *In Vivo* par Microspectroscopies Optiques (Reims).
- Park, W., et al., 2016. Acidic pH-triggered drug-eluting nanocomposites for magnetic resonance imaging-monitored intra-arterial drug delivery to hepatocellular carcinoma. *ACS Appl. Mater. Interfaces* 8 (20), 12711–12719.
- Rhee, T.K., et al., 2007. Effect of transcatheter arterial embolization on levels of hypoxia-inducible factor-1α in rabbit VX2 liver tumors. *J. Vasc. Interv. Radiol.* 18 (5), 639–645.
- Sakr, O.S., et al., 2016. Arming embolic beads with anti-VEGF antibodies and controlling their release using IBL technology. *J. Control. Release* 224, 199–207.
- Sharma, K.V., et al., 2016. Long-term biocompatibility, imaging appearance and tissue effects associated with delivery of a novel radiopaque embolization bead for image-guided therapy. *Biomaterials* 103, 293–304.
- Swaine, T., et al., 2016. Evaluation of ion exchange processes in drug-eluting embolization beads by use of an improved flow-through elution method. *Eur. J. Pharm. Sci.* 93, 351–359.
- Taylor, R.R., et al., 2007. Irinotecan drug eluting beads for use in chemoembolization: *in vitro* and *in vivo* evaluation of drug release properties. *Eur. J. Pharm. Sci.* 30 (1), 7–14.
- Tsang, V.H., Robinson, B.G., Learoyd, D.L., 2016. The safety of vandetanib for the treatment of thyroid cancer. *Expert Opin. Drug Saf.* 15 (8), 1107–1113.
- Wang, Y., et al., 2015. Preparation and structure of drug-carrying biodegradable microspheres designed for transarterial chemoembolization therapy. *J. Biomater. Sci. Polym. Ed.* 26 (2), 77–91.
- Wang, Y., et al., 2016. *In vitro* and *in vivo* evaluation of drug-eluting microspheres designed for transarterial chemoembolization therapy. *Int. J. Pharm.* 503 (1–2), 150–162.